NEURAL TECHNOLOGY EDITORS' PICK 2021

EDITED BY: Laura Ballerini and Michele Giugliano
PUBLISHED IN: Frontiers in Neuroscience

frontiers Research Topics

frontiers

ISSN 1664-8714
ISBN 978-2-88971-103-1
DOI 10.3389/978-2-88971-103-1

About Frontiers

Frontiers is more than just an open-access publisher of scholarly articles: it is a pioneering approach to the world of academia, radically improving the way scholarly research is managed. The grand vision of Frontiers is a world where all people have an equal opportunity to seek, share and generate knowledge. Frontiers provides immediate and permanent online open access to all its publications, but this alone is not enough to realize our grand goals.

Frontiers Journal Series

The Frontiers Journal Series is a multi-tier and interdisciplinary set of open-access, online journals, promising a paradigm shift from the current review, selection and dissemination processes in academic publishing. All Frontiers journals are driven by researchers for researchers; therefore, they constitute a service to the scholarly community. At the same time, the Frontiers Journal Series operates on a revolutionary invention, the tiered publishing system, initially addressing specific communities of scholars, and gradually climbing up to broader public understanding, thus serving the interests of the lay society, too.

Dedication to Quality

Each Frontiers article is a landmark of the highest quality, thanks to genuinely collaborative interactions between authors and review editors, who include some of the world's best academicians. Research must be certified by peers before entering a stream of knowledge that may eventually reach the public - and shape society; therefore, Frontiers only applies the most rigorous and unbiased reviews.
Frontiers revolutionizes research publishing by freely delivering the most outstanding research, evaluated with no bias from both the academic and social point of view. By applying the most advanced information technologies, Frontiers is catapulting scholarly publishing into a new generation.

What are Frontiers Research Topics?

Frontiers Research Topics are very popular trademarks of the Frontiers Journals Series: they are collections of at least ten articles, all centered on a particular subject. With their unique mix of varied contributions from Original Research to Review Articles, Frontiers Research Topics unify the most influential researchers, the latest key findings and historical advances in a hot research area! Find out more on how to host your own Frontiers Research Topic or contribute to one as an author by contacting the Frontiers Editorial Office: frontiersin.org/about/contact

NEURAL TECHNOLOGY EDITORS' PICK 2021

Topic Editors:
Laura Ballerini, International School for Advanced Studies (SISSA), Italy
Michele Giugliano, International School for Advanced Studies (SISSA), Italy

Citation: Ballerini, L., Giugliano, M., eds. (2021). Neural Technology Editors' Pick 2021. Lausanne: Frontiers Media SA. doi: 10.3389/978-2-88971-103-1

Table of Contents

04 ***An Observational Study With the Janssen Autism Knowledge Engine (JAKE®) in Individuals With Autism Spectrum Disorder***
Seth L. Ness, Abigail Bangerter, Nikolay V. Manyakov, David Lewin, Matthew Boice, Andrew Skalkin, Shyla Jagannatha, Meenakshi Chatterjee, Geraldine Dawson, Matthew S. Goodwin, Robert Hendren, Bennett Leventhal, Frederick Shic, Jean A. Frazier, Yvette Janvier, Bryan H. King, Judith S. Miller, Christopher J. Smith, Russell H. Tobe and Gahan Pandina

23 ***Experimental and Computational Methods for the Study of Cerebral Organoids: A Review***
Daniele Poli, Chiara Magliaro and Arti Ahluwalia

36 ***Multimodal Evaluation of TMS - Induced Somatosensory Plasticity and Behavioral Recovery in Rats With Contusion Spinal Cord Injury***
Vijai S. Krishnan, Samuel S. Shin, Visar Belegu, Pablo Celnik, Mark Reimers, Kylie R. Smith and Galit Pelled

45 **In vivo *Two-Photon Imaging of Anesthesia-Specific Alterations in Microglial Surveillance and Photodamage-Directed Motility in Mouse Cortex***
Weilun Sun, Kunimichi Suzuki, Dmytro Toptunov, Stoyan Stoyanov, Michisuke Yuzaki, Leonard Khiroug and Alexander Dityatev

57 ***A Biohybrid Setup for Coupling Biological and Neuromorphic Neural Networks***
Hanna Keren, Johannes Partzsch, Shimon Marom and Christian G. Mayr

68 **In vivo *Recording Quality of Mechanically Decoupled Floating Versus Skull-Fixed Silicon-Based Neural Probes***
Laetitia Chauvière, Frederick Pothof, Kai S. Gansel, Johanna Klon-Lipok, Arno A. A. Aarts, Tobias Holzhammer, Oliver Paul, Wolf J. Singer and Patrick Ruther

80 ***Low-Frequency Pulsed Magnetic Field Improves Depression-Like Behaviors and Cognitive Impairments in Depressive Rats Mainly via Modulating Synaptic Function***
Jiajia Yang, Ling Wang, Faqi Wang, Xiaoxuan Tang, Peng Zhou, Rong Liang, Chenguang Zheng and Dong Ming

92 ***New Vision for Visual Prostheses***
Alexander Farnum and Galit Pelled

103 ***EEG Biomarkers Related With the Functional State of Stroke Patients***
Marc Sebastián-Romagosa, Esther Udina, Rupert Ortner, Josep Dinarès-Ferran, Woosang Cho, Nensi Murovec, Clara Matencio-Peralba, Sebastian Sieghartsleitner, Brendan Z. Allison and Christoph Guger

119 ***Functional Near-Infrared Spectroscopy and Its Clinical Application in the Field of Neuroscience: Advances and Future Directions***
Wei-Liang Chen, Julie Wagner, Nicholas Heugel, Jeffrey Sugar, Yu-Wen Lee, Lisa Conant, Marsha Malloy, Joseph Heffernan, Brendan Quirk, Anthony Zinos, Scott A. Beardsley, Robert Prost and Harry T. Whelan

frontiers in Neuroscience

ORIGINAL RESEARCH
published: 27 February 2019
doi: 10.3389/fnins.2019.00111

An Observational Study With the Janssen Autism Knowledge Engine (JAKE®) in Individuals With Autism Spectrum Disorder

Seth L. Ness[1], Abigail Bangerter[1], Nikolay V. Manyakov[2], David Lewin[3], Matthew Boice[1], Andrew Skalkin[4], Shyla Jagannatha[5], Meenakshi Chatterjee[6], Geraldine Dawson[7], Matthew S. Goodwin[8], Robert Hendren[9], Bennett Leventhal[9], Frederick Shic[10,11], Jean A. Frazier[12], Yvette Janvier[13], Bryan H. King[9], Judith S. Miller[14], Christopher J. Smith[15], Russell H. Tobe[16] and Gahan Pandina[17]*

[1] Neuroscience Therapeutic Area, Janssen Research & Development, Titusville, FL, United States, [2] Computational Biology, Discovery Sciences, Janssen Research & Development, Beerse, Belgium, [3] Statistically Speaking Consulting, LLC, Chicago, IL, United States, [4] Informatics, Janssen Research & Development, Spring House, PA, United States, [5] Statistical Decision Sciences, Janssen Research & Development, Titusville, NJ, United States, [6] Computational Biology, Discovery Sciences, Janssen Research & Development, Spring House, PA, United States, [7] Departments of Psychiatry and Behavioral Sciences, Duke Center for Autism and Brain Development, Duke University School of Medicine, Durham, NC, United States, [8] Department of Health Sciences, Northeastern University, Boston, MA, United States, [9] Department of Psychiatry, School of Medicine, University of California, San Francisco, San Francisco, CA, United States, [10] Center for Child Health, Behavior and Development, Seattle Children's Research Institute, Seattle, WA, United States, [11] Department of Pediatrics, University of Washington, Seattle, WA, United States, [12] Eunice Kennedy Shriver Center and Department of Psychiatry, University of Massachusetts Medical School, Worcester, MA, United States, [13] Department of Developmental-Behavioral Pediatrics, Children's Specialized Hospital, Toms River, NJ, United States, [14] Center for Autism Research, Perelman School of Medicine, Children's Hospital of Philadelphia, University of Pennsylvania, Philadelphia, PA, United States, [15] Southwest Autism Research & Resource Center, Phoenix, AZ, United States, [16] Department of Outpatient Research, Nathan Kline Institute for Psychiatric Research, Orangeburg, NY, United States, [17] Neuroscience Therapeutic Area, Janssen Research & Development, Pennington, NJ, United States

OPEN ACCESS

Edited by:
Stephen Louis Macknik,
SUNY Downstate Medical Center,
United States

Reviewed by:
Brent Winslow,
Design Interactive, United States
Emilia Biffi,
Eugenio Medea (IRCCS), Italy

***Correspondence:**
Seth L. Ness
SNess@its.jnj.com

Specialty section:
This article was submitted to Neural Technology, a section of the journal Frontiers in Neuroscience

Received: 29 October 2018
Accepted: 30 January 2019
Published: 27 February 2019

Citation:
Ness SL, Bangerter A, Manyakov NV, Lewin D, Boice M, Skalkin A, Jagannatha S, Chatterjee M, Dawson G, Goodwin MS, Hendren R, Leventhal B, Shic F, Frazier JA, Janvier Y, King BH, Miller JS, Smith CJ, Tobe RH and Pandina G (2019) An Observational Study With the Janssen Autism Knowledge Engine (JAKE®) in Individuals With Autism Spectrum Disorder. Front. Neurosci. 13:111. doi: 10.3389/fnins.2019.00111

Objective: The Janssen Autism Knowledge Engine (JAKE®) is a clinical research outcomes assessment system developed to more sensitively measure treatment outcomes and identify subpopulations in autism spectrum disorder (ASD). Here we describe JAKE and present results from its digital phenotyping (My JAKE) and biosensor (JAKE Sense) components.

Methods: An observational, non-interventional, prospective study of JAKE in children and adults with ASD was conducted at nine sites in the United States. Feedback on JAKE usability was obtained from caregivers. JAKE Sense included electroencephalography, eye tracking, electrocardiography, electrodermal activity, facial affect analysis, and actigraphy. Caregivers of individuals with ASD reported behaviors using My JAKE. Results from My JAKE and JAKE Sense were compared to traditional ASD symptom measures.

Results: Individuals with ASD (N =144) and a cohort of typically developing (TD) individuals (N = 41) participated in JAKE Sense. Most caregivers reported that overall use and utility of My JAKE was "easy" (69%, 74/108) or "very easy" (74%, 80/108). My JAKE could detect differences in ASD symptoms as measured by traditional methods. The majority of biosensors included in JAKE Sense captured sizable amounts of quality data (i.e., 93–100% of eye tracker, facial affect analysis, and electrocardiogram data

was of good quality), demonstrated differences between TD and ASD individuals, and correlated with ASD symptom scales. No significant safety events were reported.

Conclusions: My JAKE was viewed as easy or very easy to use by caregivers participating in research outside of a clinical study. My JAKE sensitively measured a broad range of ASD symptoms. JAKE Sense biosensors were well-tolerated. JAKE functioned well when used at clinical sites previously inexperienced with some of the technologies. Lessons from the study will optimize JAKE for use in clinical trials to assess ASD interventions. Additionally, because biosensors were able to detect features differentiating TD and ASD individuals, and also were correlated with standardized symptom scales, these measures could be explored as potential biomarkers for ASD and as endpoints in future clinical studies.

Clinical Trial Registration: https://clinicaltrials.gov/ct2/show/NCT02668991 identifier: NCT02668991

Keywords: autism spectrum disorder (ASD), biosensor, web and mobile application, mood report, assessment

INTRODUCTION

Widely accepted, standardized tools for diagnosing autism spectrum disorder (ASD) include the Autism Diagnostic Observation Schedule, 2nd edition (ADOS-2) and the Autism Diagnostic Interview-Revised (Falkmer et al., 2013). However, physiological and psychological instruments designed to detect change over time in core and associated symptoms of ASD are lacking. As ASD is a neurodevelopmental disorder with its roots in brain structure and function, it is reasonable that physiological and psychological measurements that assess this structure and function would be useful. In addition, monitoring of ASD symptoms in naturalistic settings will likely both improve care of people with ASD and yield insights into the condition. Such tools are needed to address significant unmet medical needs for improved diagnosis and expanded treatment options in ASD, and to develop novel therapies that target core and associated symptoms.

Global efforts to identify potential biomarkers for use in ASD research have been noted in the European Union (EU) and US. The EU-AIMS initiative consists of a large public-private partnership between academia, pharma, and foundations (Loth et al., 2016) to carry out several large-scale studies involving children, adolescents, and adults. In the US, the Autism Biomarkers Consortium Clinical Trial (ABC-CT) is engaged in a similar effort to examine change over time in a younger cohort of children and adolescents with ASD (McPartland, 2018). These large-scale consortia utilize a select group of expert academic sites and employ high-density tools (e.g., 128 lead electroencephalogram [EEG] and magnetic resonance imaging) to help identify biomarkers to stratify subgroups of individuals with ASD that might be more responsive to a particular therapy, and to measure change in symptoms and behavior over time.

Biomarker Development in ASD

Biosensor research is relatively new in its development and application to ASD. Sensor-based biomarkers (e.g., EEG and eye tracking) have the potential to measure progress objectively and facilitate development of novel therapies for ASD core and associated symptoms (Murias et al., 2018). Biomarkers may be used to characterize participants who share common pathophysiology, as well as being an objective measure for clinical outcomes (Loth et al., 2017).

Wearable Biosensors

Actigraphy

An actigraph measures physical activity and can be worn on a participant's wrist like a watch. Data recorded during the day can be used to identify time periods of sedentary, light, moderate, and moderate-to-vigorous activity. An ASD population is expected to spend more time engaged in sedentary activity, less time exposed to ambient light, and less moderate and moderate-to-vigorous activity than typically developing (TD) children of the same age (Vaughan Van Hecke et al., 2009). Additionally, it has been reported that sleep problems occur in ∼50–80% of children with ASD, compared with 9–50% for a TD group (Richdale and Schreck, 2009). The use of actigraphy for sleep monitoring, with ∼90% sensitivity of sleep estimation using curated data approaches, provides a valid, more tolerable, and efficient potential alternative to polysomnography (PSG) (Meltzer et al., 2012). Although PSG, of course, remains the gold-standard for sleep measurements, we feel the far greater versatility and practicality of actigraphy makes it a reasonable choice for use in clinical studies. The ability to automatically detect repetitive motor movements using actigraphy and machine learning has also been demonstrated (Goodwin et al., 2011, 2014; Großekathöfer et al., 2017).

Electrodermal Activity

ASD is partially characterized by sensory differences and atypical affective responses, symptoms included in standard diagnostic tools such as the ADOS-2 (Lord et al., 2012), Autism Diagnostic Interview (Lord et al., 1994), and the Diagnostic and Statistical Manual of Mental Disorders, 5th Edition (DSM-5) (American

Psychiatric Association, 2013). Dysregulated emotional and atypical physiological responses may underlie these features (Woodard et al., 2012; Mazefsky et al., 2013; Levine et al., 2014; Klusek et al., 2015; Lydon et al., 2016). Similarly, individuals with ASD often demonstrate difficulties regulating their internal emotional states (Mazefsky et al., 2013). As such, electrodermal activity (EDA), a peripheral index of sympathetic nervous system arousal (Boucsein, 2012), may be informative in ASD populations (McCormick et al., 2014; Prince et al., 2017). For instance, processing of social stimuli may differentiate ASD and TD populations in terms of autonomic nervous system responsivity (Louwerse et al., 2014).

Lab-Based Biosensors

Multiple brain systems are implicated in the formation and maintenance of core deficits in ASD. Establishing peripheral, non-intrusive methods such as EEG or eye tracking to interrogate these deficits would allow for *in vivo* study and potentially quantify ASD core deficits, as well as links to underlying ASD neurobiology (Black et al., 2017). EEG may be well-suited for detecting the alterations in brain connectivity found in ASD, through the use of coherence measurements and other paradigms (O'Reilly et al., 2017). Translational research suggests direct links between ASD neurobiology and social deficits. For example, EEG has been utilized in mouse models of Fragile X to link to neurobiological substrates (Goswami et al., 2019). Significant differences in EEG activity have been widely demonstrated in studies to distinguish individuals with ASD from TD controls (Gurau et al., 2017). Studies using eye tracking and event-related potentials (ERPs) to examine emotional face processing suggest that the neural correlates of gaze direction processing may be delayed in young children with ASD (Grice et al., 2005; Wang et al., 2013; Shou et al., 2017), and that individuals with ASD show an atypical pattern of emotional face processing and a reduced relationship between gaze behavior and neural processing of faces (Wagner et al., 2013).

Visual information processing in TD individuals is reinforced by additional speech information, demonstrating that TD children's ability to integrate multimodal input enables faster encoding and recognition of faces (Bahrick, 1987; Carpenter et al., 1998; Lydon et al., 2016). There is also evidence that face detection is facilitated when combined with directed speech in TD infants (Yirmiya et al., 1989). In contrast, children with ASD are characterized by limited attention to faces combined with under-responsivity to speech (Dawson et al., 2004; Wetherby et al., 2004; Chawarska et al., 2012). Limited attention to faces in individuals with ASD is particularly prominent when viewing dynamic videos presented in complex naturalistic contexts (Speer et al., 2007). It is possible that such limited attention to faces is a direct result of increased salience of objects, which are of high autism interest (HAI) (Senju et al., 2004; Sasson et al., 2008, 2011). It is also expected that differences between ASD and TD populations become apparent when dyadic cues consisting of directed speech and eye contact are introduced (Chawarska et al., 2016; Wang et al., 2018). Individuals with ASD assessed by eye tracking show diminished attention to scenes where an actress emulates bids for dyadic engagement, and spend less time monitoring the speaker's face in general and mouth in particular. Instead, their attention is directed toward toys as well as hand/action areas (Chawarska et al., 2012).

In contrast, when passively observing the interactions of others, children with ASD exhibit diminished attention to others' functional play activities, in addition to limited attention to faces (Shic et al., 2011). In combination, these studies provide evidence that eye tracking can identify and measure variables associated with limited social information processing in ASD, limitations likely reflecting fundamental social deficits in ASD and difficulties in subsequent social learning (Bushwick, 2001; Klin et al., 2003). Several studies have also suggested that eye tracking can be used to monitor the effects of pharmacological agents. For example, eye tracking studies have shown that individuals with ASD look more at eyes subsequent to administration of intranasal oxytocin (Andari et al., 2010; Auyeung et al., 2015); another study found increased orienting to biological motion subsequent to administration of a novel V1a antagonist (Umbricht et al., 2017). Murias et al. used eye tracking to demonstrate that improvements in social behavior were correlated with increased attention to social stimuli (Murias et al., 2018).

In the TD population, facial expressions activated via automatic or intentional mimicry appear to influence corresponding emotions, whereas the influence is impaired in the ASD population (Tomasello et al., 2005). Consequently, it is expected that individuals with ASD will show fewer facial emotional reactions (i.e., less variance in emotion) compared to TD individuals in response to videos designed to elicit overt emotional states, such as humorous or funny videos. A more neutral flatness of affect has been found in the activated facial expressions of children with autism (Yirmiya et al., 1989). It is also expected that facial expressions activated in the ASD population will be diminished compared to those of TD participants.

Finally, as suggested above, recent large scale trials (Bazelmans et al., 2018), and systematic reviews (Klusek et al., 2015; Lydon et al., 2016) of the literature on physiological reactivity to sensory, social, and emotional stimuli indicate that differences in cardiovascular arousal exist for many individuals with ASD.

Deep Phenotyping Tools in ASD

ASD interventions are frequently evaluated using caregiver-reported measures administered during study visits. Two common caregiver measurements of behavior change in ASD are the Aberrant Behavior Checklist–Community (ABC) (Aman et al., 2004; Aman and Singh, 2017) that measures general behaviors, and the Social Responsiveness Scale 2™ (SRS-2) that measures symptoms associated with social behaviors (Constantino et al., 2003). While informative, these surveys are retrospective, which can reduce rating accuracy. For example, caregivers may report ASD symptoms as being worse in the past compared to real-time reporting, even in the absence of an intervention (Jones et al., 2015). Deficits in social communication (SC) may be a risk factor for the development of mood and anxiety disorders in ASD (De-la-Iglesia and Olivar, 2015; Gotham et al., 2015). Some interventions directed at SC (6 of 10

tested), led to improvements in depression and anxiety symptoms in ASD (Rumney and MacMahon, 2017). Understanding relationships between mental health and core ASD symptoms could help identify specific interventions to improve quality of life for individuals with ASD and their caregivers.

The Janssen Autism Knowledge Engine (JAKE®) system is an initiative to standardize physiological and psychological instruments to reliably identify and measure core and associated symptoms of ASD. A preliminary study was performed with 29 participants with ASD to test the feasibility of the JAKE system and the learnings regarding logistics, data collection, data quality, and analysis have been published (Ness et al., 2017). The results obtained for the performance of the system allowed for further refinement and validation of JAKE in this follow-up study in a completely independent sample. As compared to the initial study the system was complete and able to gather useable data. System reliability, quality, user feedback, and representative examples of results from the various components of JAKE are described herein as well as participant demographics and safety. Detailed methodology and results of the ABI, other components of My JAKE, and the various sensors and tasks are published elsewhere (Bangerter et al., 2017, In press; Manfredonia et al., 2018; Manyakov et al., 2018; Jagannatha et al., In press) or are in preparation.

MATERIALS AND METHODS

Study Design

JAKE is a dynamically updated clinical research system developed to provide quantifiable and reproducible measures for use in assessing treatment outcomes, potentially including detection of change in ASD symptoms and ASD subgroup identification. JAKE is a three-part investigational system consisting of: My JAKE (a web and mobile application for use by caregivers and clinicians to log symptoms, record treatments, track progress, and gather comprehensive medical information); JAKE Sense (research biosensors and tasks designed to detect and monitor changes in experimental, proof-of-concept ASD biomarkers); and JAKE Stream (a system designed to collect, time-synchronize, and process data from both My JAKE [My JAKE Data Pipeline] and JAKE Sense [JAKE Sense Data Pipeline]).

This prospective, observational, non-interventional study was conducted from 06 July 2015 to 14 October 2016 at 9 study sites in the US and was completely independent from a previous study on the use of JAKE (Ness et al., 2017). The study consisted of a 14-day screening phase followed by an 8-to-10-week data-collection phase. Study visits were performed at baseline, Week 4, and study endpoint (8–10 weeks). Evaluations throughout the study encompassed several categories within the

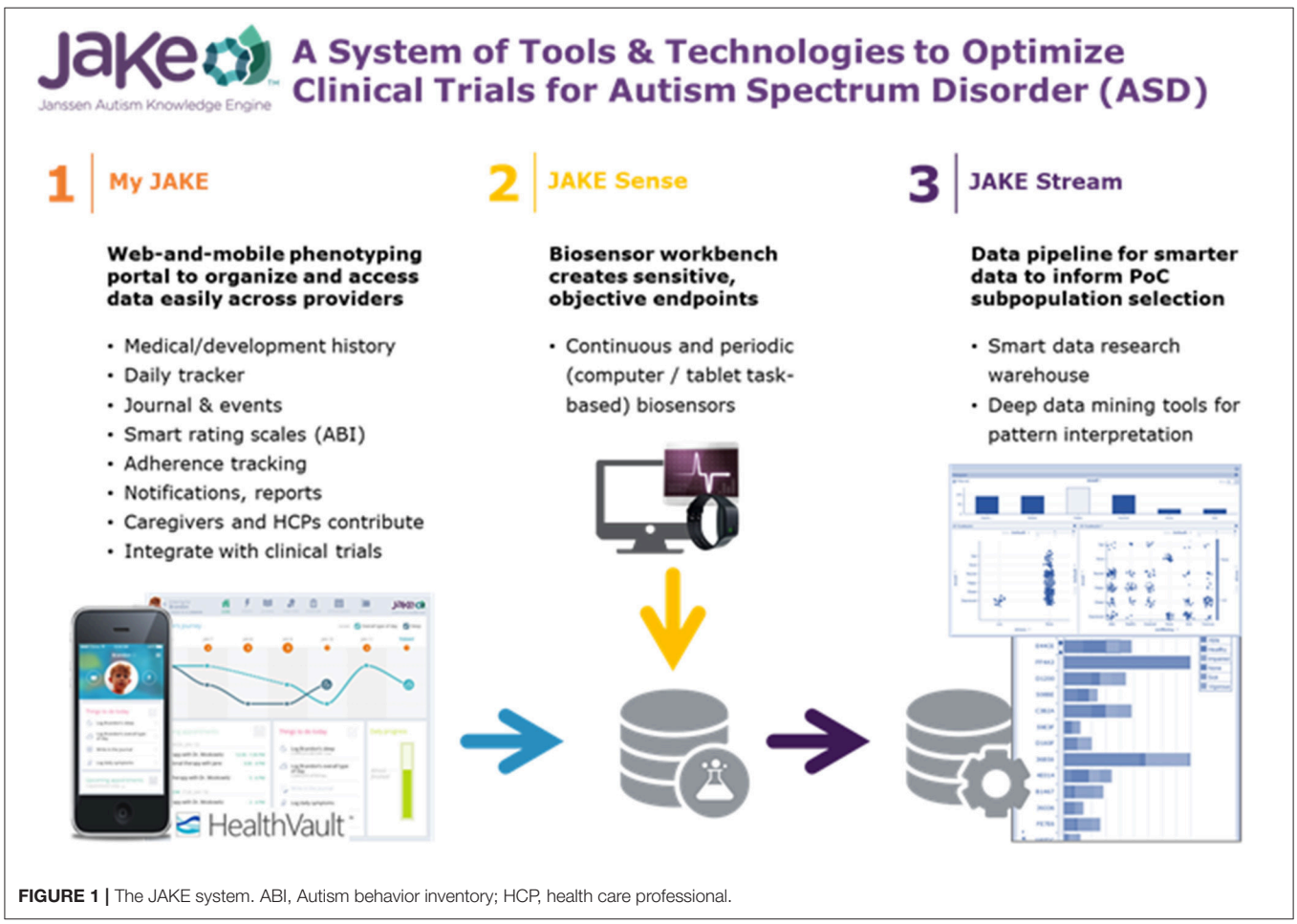

FIGURE 1 | The JAKE system. ABI, Autism behavior inventory; HCP, health care professional.

JAKE system (**Figure 1**). Though this was a non-interventional study, participants received treatment as usual, and there was some anticipated change in reported behaviors measured at baseline and endpoint. Observed improvements or worsening of behavior over the course of the study were used to assess JAKE's ability to detect change. This study was registered with clinicaltrials.gov (NCT02668991).

Participants

The study enrolled males and females aged ≥6 years with an ADOS-2-confirmed diagnosis of ASD. Participants were permitted to receive behavioral and/or pharmacologic treatments for ASD and comorbid disorders during the study, but this was not required. Participants lived with a parent or primary caregiver (or a guardian or support provider, referred to as "caregiver" throughout this publication) or, if not, spent at least 3 h a day for at least 4 days each week or at least 3 weekends a month with a parent or primary caregiver. Key exclusion criteria were a measured composite score on the Kaufmann Brief Intelligence Test-2 (KBIT-2) (Kaufman, 2004) of <60 during screening (or other recent IQ evaluation), history of or current significant medical illness, and documented psychological and/or emotional problems.

The study also enrolled a TD cohort comprised of males and females, aged ≥6 years, with a score in the normal range on the Social Communication Questionnaire (SCQ) (Rutter et al., 2003), no mental disorders as defined in the DSM-5, no significant medical illness, or current psychotropic medication. The TD cohort provided normative data for comparison with ASD participants, completed standard instruments and scales, a paper version of the ABI, and lab-based JAKE Sense assessments, but did not use My JAKE. Planned study cohorts are presented in **Table 1**.

Institutional Review Boards approved the study protocol and its amendments. The study was conducted in accordance with the ethical principles originating in the Declaration of Helsinki, consistent with Good Clinical Practices and applicable regulatory requirements. Participants, their caregivers (for participants <18 years old), or legally authorized representatives provided written informed consent before participating in the study. The study is registered at clinicaltrials.gov (NCT02668991).

TABLE 1 | Planned study cohorts.

ASD Cohort	TD Cohort
Approximately 150 individuals with ASD aged ≥6 years	Approximately 30 normally developing individuals with ASD aged ≥6 years, with ∼5 individuals in each subgroup of ages 6–9 years, 10–12 years, 13–17 years, and ≥18 years
No requirements or restrictions regarding concurrent therapies or treatments	Single visit and single session with JAKE Task Battery and JAKE Sense
A 14-day screening phase, and an 8–10-week data collection phase extending from Day 0 (Baseline) to endpoint was planned	
Optional: After the endpoint visit, participants may continue to use My JAKE and the Microsoft® HealthVault pHR to contribute data to the study until the end of the study	

ASD, autism spectrum disorder; JAKE, Janssen Autism Knowledge Engine; pHR, personal healthcare record.

Study Assessment Instruments and Scales

Throughout the study, data collected through My JAKE and JAKE Sense were compared against psychometrically standardized scales (completed outside the JAKE system) to assess validity of the system as a tool for measuring clinical outcomes in ASD (**Table 2**).

Deep Phenotyping Tools-My JAKE

My JAKE is a web and mobile application (iOS+/Android+) consisting of various modules to help caregivers and healthcare providers who support individuals with ASD to log symptoms, demarcate events of interest, record treatments and medical information, and track overall study progress. My JAKE was developed, in part, to enhance the ability to understand the phenotypic underpinnings of individuals with ASD and to address both a lack of appropriate measures and convenient methods of use. The purpose of My JAKE is to provide a robust and sensitive set of integrated outcome measures for ASD clinical trials and other interventional studies in place of or in addition to current measures that do not necessarily assess the full range of ASD symptoms or were not designed to measure change over time.

All data created and accessed by My JAKE were saved to a caregiver's Microsoft HealthVault account, a publicly-available Class 1 electronic personal health record system. As the sole storage mechanism for all My JAKE data, the use of HealthVault permitted caregivers to own and control their dependent's study data, even after the study ended. Additionally, caregivers controlled which people and applications could access their HealthVault account at any time. The My JAKE application server is hosted on Microsoft Azure.

My JAKE is accessible through most web browsers, as well as mobile devices, and was used throughout the present study. The My JAKE home page includes a "Journey" chart for visualizing change of ASD "events" and selected symptoms, a study tasks tracker (the "To-Do" list) to help caregivers monitor required items, and a list of upcoming appointments (the Therapy Tracker) (**Figure 2**). Other My JAKE components included:

Medical/Developmental History

A comprehensive medical and developmental history filled out by caregivers during the screening/on boarding phase of the study and edited throughout.

The Autism Behavior Inventory (ABI)

An important element of My JAKE is the Autism Behavior Inventory (ABI), a web-based caregiver-rated scale for assessing ASD core diagnostic symptoms and associated behavior. The development of the ABI component of My JAKE have been previously published (Bangerter et al., 2017). The ABI consisted of 73 items divided into five domains: two ASD core symptom domains, SC, and restricted and repetitive behaviors (RRB); and three symptom co-occurrence domains, mental health (MH),

TABLE 2 | Study assessment instruments and scales.

Test	Description
DIAGNOSTIC AND CLASSIFICATION INSTRUMENTS ADMINISTERED AT SCREENING[a]	
Autism Diagnostic Observation Schedule, 2nd edition (ADOS-2)	Used to accurately assess and diagnose autism spectrum disorders across age, developmental level, and language skills in ASD participants
Kaufman Brief Intelligence Test, Second Edition (KBIT-2)	A validated test used to obtain a quick estimate of intelligence, administered at screening in order both to help select participants capable of performing the required tasks and for analysis of data in ASD participants
The Mini International Neuropsychiatric Interview 7.0 (MINI 7.0) or pediatric component (MINI KID)	Used to rule out any major psychiatric diagnosis in TD participants, and to identify any psychiatric comorbidities in ASD participants
Social Communication Questionnaire, current form (SCQ)	A 40-item scale that evaluates social functioning and communication skills over the last 3 months, administered at screening. It was administered only to the TD cohort, to help rule out ASD
STANDARD INSTRUMENTS FOR MEASURING CHANGE[b]	
Aberrant Behavior Checklist (ABC)	A 58-item behavior rating scale, used to measure behavior problems across 5 subscales: irritability, lethargy (social withdrawal), stereotypy, hyperactivity, and inappropriate speech (Aman et al., 2004; Aman and Singh, 2017)
Zarit Burden Interview–Short Version (ZBI)	A 22-item scale assessed the psychological burden experienced by a caregiver, for both patients with dementia and children and adults with ASD (Zarit et al., 1980; Cadman et al., 2012)
Social Responsiveness Scale 2 (SRS-2)	Distinguishes autism spectrum conditions from other child psychiatric conditions by identifying the presence and extent of autistic social impairment (Constantino et al., 2003)
Child Adolescent Symptom Inventory – Anxiety (CASI-Anx)	A 21-point anxiety scale used as a possible outcome measure for autism (Sukhodolsky et al., 2008; Hallett et al., 2013)
Repetitive Behavior Scale—Revised (RBS-R) (caregiver)	A 43-item report scale used to indicate occurrence of repetitive behaviors and degree to which a behavior is a problem (Bodfish et al., 1999).

[a] *Instruments used to establish the diagnosis of autism or help rule it out, to help classify participants by intelligence quotient (IQ), or to rule out or rule in the presence of other psychiatric disorders in participants.*

[b] *Caregiver-reported rating scales used to assess change over time in particular domains of ASD symptoms and to validate components of the JAKE system. They were administered only to ASD participants at baseline, midpoint and endpoint visits. Scales were selected based on previous use in clinical trials for ASD, or recommendations in reviews of scales for use in measuring change in ASD core and associated behavior (Lecavalier et al., 2014; Anagnostou et al., 2015; Scahill et al., 2015) ASD, autism spectrum disorder; TD, typically developing.*

self-regulation (SR), and challenging behavior. The ABI yields a score in each domain, plus a core score combining SC and RRB, based on behaviors that occurred within the last 7 days. The ABI can be downloaded in the USA from https://www.janssenmd.com/ (in the tools/psychiatry section) and accessed outside the USA via email request to autismbehaviorinventory@its.jnj.com. Questions were asked on two 4-point scales and consisted of either frequency and intensity ratings, frequency and context, or quality and context. The full ABI was completed by the primary caregiver at baseline, midpoint (Week 4), and endpoint. A short (35-item) form of the ABI (ABI-S) was completed by the investigator or delegate at baseline, Week 4, and endpoint. The primary caregiver completed the ABI-S on weeks when they were not required to complete the full ABI (Weeks 2, 3, 5, 6, and 7).

The Daily Tracker

The Daily Tracker consisted of several questions answered by caregivers of ASD participants. In this study, all caregivers were asked in the morning "How was (participant name)'s sleep last night?" and in the evening "How was (participant name)'s day?" Caregivers could also choose up to three additional behaviors to track, but only the two standard questions were analyzed. Questions could be answered by dragging a card along an 8-point scale ranging from "troubling" to "encouraging" either on the My JAKE mobile application or in a web browser. Responses to these questions were tracked and displayed over a 2-week period on the web site home page to provide feedback to caregivers and increase engagement in the study.

Mood Report

The affective circumplex model of affect reporting has a long and widespread history in measuring affective/emotional states, including those with ASD (Kring et al., 2003; Tseng et al., 2014). A digital version of the classical affective circumplex was created for the My JAKE mobile application for this study. The x-axis represents arousal, termed "activity," and the y-axis represents valence, termed "mood." The model was divided into "Quadrants" of activity and mood relationships. Caregivers moved the icon to a location on the screen that represented their child's perceived mood at the moment; they were asked to do this twice a day but could do so as many times as desired.

Event Tracker and Journal

Caregivers tracked all items of interest, including sleep and diet, on a daily basis. They were also able to provide free text entries *ad-hoc* to track both positive and negative events as they occurred.

Therapy Tracker

This module allowed tracking of participants' medical treatments or therapies, using a calendar-like interface. Caregivers had the option to export their created appointments to the calendaring system of their choice.

Biosensor Data-JAKE Sense

JAKE Sense is based on the use of experimental biosensors to assess physiological characteristics and behavior related to core and associated symptoms of ASD. The biometric devices can be divided into two categories: lab-based biosensors, which measure biometric information in a laboratory setting (usually paired with challenge tasks or stimuli presented on a computer screen) and continuous biosensors, designed for daily wearable use to

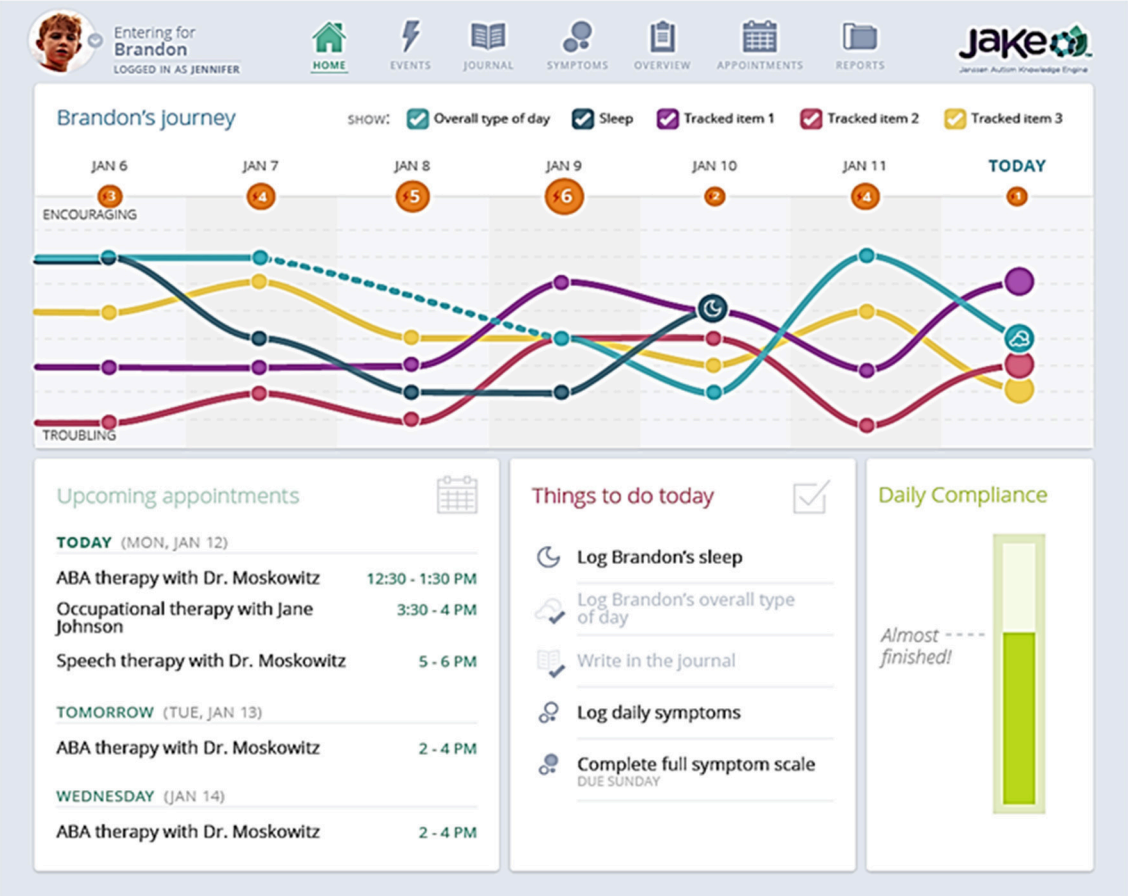

FIGURE 2 | Sample My JAKE home page. ABA, Applied behavior analysis.

collect real-world biometric information about the participant. The selected biosensors (and their output) were used strictly for exploratory research purposes and were not used to diagnose, treat, or prevent any disease or disorder. All devices were used in compliance with their documented intended use.

Biosensors

Continuous Biosensors

The "daytime biosensor" (Empatica E4™ Wristband) is a commercially-available wireless wristband biosensor that records EDA, skin surface temperature, blood volume pulse and inter-beat interval (producing an approximation of heart rate and heart rate variability), and 3-axis acceleration. The E4 has been used in previously published research (Goodwin et al., 2018) involving youth with ASD in the current study's participant age range (≥6 years of age) and did not require alterations to the band in either study to acquire quality signals. Both the EDA (Poh et al., 2010; Sano et al., 2014) and photoplethysmography sensors (McCarthy et al., 2016) in the E4 have been independently validated. It was worn during waking hours, at minimum for the afternoon until bedtime on weekdays, at periodic lab visits, and the entire day on weekends.

A "nighttime biosensor," the commercially-available Ambulatory Monitoring, Inc. (AMI) Motionlogger® Actigraph was worn at bed-time for the entire night's sleep. Each night's sleep start time, number of awakenings during sleep, time duration of sleep, and sleep efficiency were derived from measurements recorded by the sensor (Acebo et al., 1999; Wiggs and Stores, 2004; Souders et al., 2009; Gringras et al., 2012; Meltzer et al., 2012), and have been validated in children with ASD.

Lab-Based Biosensors

These biosensors were used at a study visit while participants were exposed to specific visual or auditory stimuli or asked to perform a task (**Table 3**). Tasks and stimuli for use with lab-based biosensors comprised a battery of ∼40 min for use at laboratory sites. Participants were asked to wear or use all the lab-based biosensors (in addition to the daytime continuous biosensor described above) during presentation of all tasks and stimuli. Tasks and stimuli were presented on a computer monitor using the iMotions® Biometric Research Platform (formerly called Attention Tool). The continuous and lab-based sensors were found to be tolerable (Ness et al., 2017).

TABLE 3 | Tasks or stimuli (the JAKE Task Battery) for use with lab-based biosensors.

Task/Stimulus	Description	Biosensor				
		Eye tracking	EEG	FACET	ECG	EDA
Resting state-eyes open (Murias et al., 2007)	Video of sand falling through an hourglass for 1 min	x	*		x	x
Resting state-eyes closed (Murias et al., 2007)	Participant asked to close their eyes for 45 s		*		x	x
Event related potentials (Grice et al., 2005)	Static facial stimuli with averted or direct gaze	x	*		x	x
Social orienting task (Chawarska et al., 2012; Plesa-Skwerer et al., 2016)	Video of male or female actor presented in random order; actor engages participant in direct speech (dyadic bid) and joint attention, toward or away from a moving toy	*			x	x
Social vs. non-social videos (Pitcher et al., 2011)	Dynamic videos of children's faces (social) or toys (non-social)	x	*		x	x
Visual exploration task (Sasson et al., 2008, 2011)	Free viewing of Arrays of 24 images (including social images, HAI and LAI objects)	*			x	x
Biological motion (Umbricht et al., 2017)	2 side by side videos, in random left-right order. Each video contains dynamic point-light displays. One video is derived from human actor's performance; the other video is a computer-generated animation of moving dots	*	x		x	x
NimStim emotional faces (Wagner et al., 2013)	Static images of happy, angry, fear, and neutral faces	x	*		x	x
Activity monitoring (Shic et al., 2011, 2014; Umbricht et al., 2017)	Video recording of multiple human actors performing a social activity, with visually salient distracters in the background; actors focus on each other or on the activity only in 2 conditions	*			x	x
Funny videos	Funny videos, or videos designed to elicit an emotional response of surprise or joy			*	x	x
Expression of emotional faces	Participants asked to make faces to reflect basic emotions: Happy, Sad, Surprise, Scared, Angry, Yucky (disgust).			*	x	x
Auditory stimuli	3 sets of auditory stimuli (toilet flush, a ticking clock, or an 880 hz tone) presented for 3 s duration each, with ISI of 8–12 s each. Screen displayed bubbles screen saver and a progress bar indicating time until the presentation was complete.			x	*	*

**primary hypotheses.*

x, additional hypotheses.

ECG, electrocardiogram; EDA, electrodermal activity; EEG, electroencephalogram; FACET, FACial Expression; HAI, high autism interest; ISI, interstimulus interval; LAI,low autism interest.

Eye tracking data were collected using the Tobii X2-30 and synchronized with stimuli and facial affect data through the iMotions® eye tracking module.

EEG data were collected using the Brain Vision actiCHamp 32 and its proprietary software (BrainVision Recorder). A total of 20 electrodes were placed in accordance with the standard 10–20 electrode system. The use of a photodiode attached to the lower-right corner of the computer monitor allowed the software to precisely timestamp stimuli slide changes.

Electrocardiogram (ECG) data were collected using the CamNtech Actiwave Cardio Single-Channel ECG and used to assess heart rate and heart rate variability.

Facial affect detection was evaluated using the iMotions® FACial Expression Analysis (FACET) module and a high definition web camera.

An assembled JAKE Sense setup is shown in **Figure 3**.

JAKE Stream

JAKE Stream was designed to collect and process data from both My JAKE and JAKE Sense. JAKE Stream is divided into two physically distinct subcomponent sets of Microsoft.NET command line utilities hosted on Janssen servers: "My JAKE Data Pipeline" and "JAKE Sense Data Pipeline."

The My JAKE Data Pipeline was designed to capture and process a daily archive of My JAKE data stored in a caregiver's and/or participant's Microsoft HealthVault account (described earlier). After the My JAKE Data Pipeline processed daily capture, data were directed to an internal Janssen server for traceability archiving/auditing and then ultimately to the Janssen data management team (via secure file transfer server) for incorporation into final study results. A site manager dashboard was used to view a read-only copy of My JAKE data stored on the internal Janssen server for monitoring participant, caregiver, and clinical site usage of web and mobile applications.

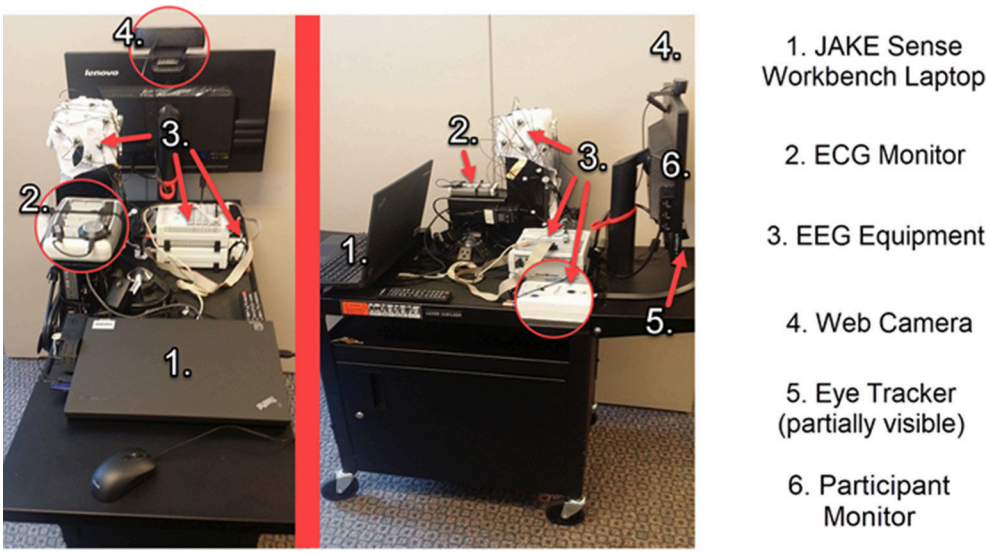

FIGURE 3 | Assembled JAKE Sense workbench cart. ECG, electrocardiogram; EEG, electroencephalogram.

Similarly, the JAKE Sense Data Pipeline was designed to process and extract biometric features from data packages provided by JAKE Sense. Examples of the types of features that were extracted are shown in **Table 4**. After packages were archived to ensure traceability of derived analyses, a collection of MATLAB utilities scanned the packages to produce a series of extracted features (as flat.CSV-formatted files). Finally, the files were stored in a secured datastore server ("JAKE Sense Data Pipeline Features Archive") for exploratory, proof-of-concept data mining; data are not used for clinical trial endpoints or for clinical decision-making.

Data Quality Control

All features extracted from data collected by JAKE were assessed and labeled according to their fidelity and quality (Webb et al., 2015), with analyses performed only on features reaching the following criteria:

As an automatic first step, EEG and eye tracking features were estimated on three levels, with data designated as "excellent," "excellent+good," and "any" quality. These three levels were defined as follows:

For eye tracking: "excellent" corresponds to the related value of calibration as defined by the iMotions® Biometric Research Platform software; "excellent+good" combines recordings with "excellent" and "good" calibration as defined by the software; and "any" corresponds to "excellent," "good," or "bad" calibration results as defined by the software.

For EEG: "excellent" corresponds to impedance below 25 kOhm; "excellent+good" corresponds to impedance below 50 kOhm; and "any" corresponds to any value of impedance. Additionally, we considered information from the eye tracker relating to times when participants were attending to the screen during EEG processing, allowing EEG segments corresponding to an absence of attention to be excluded from feature estimation. The use of "recalibration" videos embedded in the stimuli battery also allowed eye tracker calibration consistency to be checked throughout experiments. EEG data were further evaluated for eye-blinking artifacts and consequences of bridging electrodes. Corresponding EEG segments per channel (or data from a whole channel) were labeled accordingly.

Feature estimation algorithms incorporated information from these labels, wherein features were only estimated when no artifacts were identified. Artifact identification was performed by assessing mean, SD, maximum, minimum, median, mode, skewness, and kurtosis of EEG data values by applying sliding windows and comparing obtained distributions between channels with preset parameters in order to identify outliers. Since EEG follows 1/f distribution (pink noise) in the frequency domain, model slope, and model intercept for power spectrum density were estimated in sliding window segments and also checked for outliers via comparison of distributions between channels and with preset parameters. As a result of this artifact rejection step, diagnostic plots were created and visually inspected during subsequent manual quality checks.

After all features were automatically extracted, an expert manually checked the diagnostic plots produced during the automatic quality check including 1/f pink noise shape for spectra, presence of components for ERP, signal-to-noise ratio, detection of N peaks for ECG, and valid time for eye tracking to make additional quality determinations. This assessment resulted in modification of files with questionable data quality information and sometimes resulted in re-estimation of all features if necessary.

EDA data were manually and automatically inspected according to established guidelines (Dawson et al., 2007; Boucsein et al., 2012; Kleckner et al., 2018). This enabled identification of parts of recordings or whole recordings where data were missing (e.g., straight line at zero level), had poor signal

TABLE 4 | Example features.

Eye-tracking	EEG	ECG	EDA	Actigraphy	FACET
Tobii X2-30	Brain Vision ActiCHamp 32	CamNtech Actiwave Cardio Single-Channel ECG	Empatica E4™	AMI Motionlogger® Actigraph	iMotions® FACial Expression
General features • Fixations and saccades (using velocity based binocular algorithms) • % valid time on screen • % on ROIs (also normalized to % valid time) • Pupil size Specific features • Biological Motion preference (%), first saccade orienting (%) saccade latency, fixation orienting (%), fixation latency • VET exploration, preservation, detail orientation, RQA features	Induced EEG activity (estimated for each electrode and different brain region) • Power spectra at different bands (delta, theta, alpha, beta, gamma) • Normalized power spectra at different bands • Brain asymmetry index for different bands • Coherence between at different bands ERP • Components' amplitudes with peak- and area-based methods • Components' latencies with peak- and area-based methods	• HR • SDNN • SDSD • rMSSD • NN50 • pNN50 • ApEn • SpEn • LF HRV • Normalized LF HRV • HF HRV • Normalized HF HRV • LF/HF HRV	Tonic activity • SCL Phasic activity: • SCRR	• Sleep duration • Sleep start • Sleep end • # awakenings • Sleep efficiency	For each emotion (joy, anger, surprise, fear, contempt, disgust, sadness, confusion, frustration) and action unit defined according to FACS • Average evidence • Variance of evidence • Area under evidence curve

ApEn, approximate entropy; ECG, electrocardiography; EEG, electroencephalograpy; EDA, electrodermal activity; ERP, event-related potentials; FACET, iMotions® FACial Expression analysis; FACS, Facial Action Coding System; HF, high frequency; HR, heart rate; HRV, heart rate variability; LF, low frequency; NN50, number of pairs of successive NNs that differ by more than 50 ms; pNN50, proportion of NN50 divided by total number of NNs); rMSSD, root mean square of successive differences; ROI, Region of interest (such as eye region, mouth region, face region, and so on); RQA, recurrence quantification analysis; SCL, skin conductance level; SCRR, skin conductance response rate; SDNN, standard deviation of normal to normal R-R intervals; SDSD, standard deviation of successive differences; SpEn, sample entropy; VET, visual exploration task.

quality, or were otherwise noisy. These values were subsequently excluded from analyses.

Exit Interview

Caregivers were asked to provide final feedback on their experience with JAKE in an exit interview and a 36-question on-line survey. Examples of questions were "which JAKE components would you like to use outside of a clinical trial" and "how easy were the following tasks to complete."

Genomic Assessment

A genomic cheek swab sample was collected from ASD participants who consented separately to this component of the study. Participation in genomic research was optional.

Safety Evaluations

All reported study events (intercurrent illnesses, changes in signs/symptoms, early discontinuations, device-related events, etc.) with onset during study participation were included in evaluations. For each event, percentages of participants who experienced at least one occurrence were summarized.

Data Quality Assurance

Steps taken to ensure accuracy and reliability of clinical study data included selection of qualified investigators and appropriate study sites, review of protocol procedures with investigators and associated study-site personnel prior to study start, and periodic monitoring visits by the sponsor or their delegate.

Data Analyses

All analyses performed for this study were exploratory. Pre-specified hypotheses relating to My JAKE and JAKE Sense were developed prior to conducting analyses. The overall Type I error rate for testing each hypothesis when two variables were assessed for correlation or the difference between ASD and TD participants involved a 2-sided or 1-sided significance level of 0.05. No adjustments for collinearity, multiplicity, or experiment-wise error were made as results were intended for hypothesis generation, not confirmation. Where presented, all confidence intervals are 2-sided at 95%, which correspond to a 2-sided significance level of 0.05 and a 1-sided significance level of 0.025. Descriptive statistics were provided for all study evaluations at baseline, Week 4, and study endpoint.

RESULTS

Study Population

A total of 144 participants with a diagnosis of ASD were enrolled. Of these, 136 (94.4%) participants completed the study and 8 (5.6%) discontinued. The most common reason for discontinuation was self-withdrawal from the study (6 [4.2%]). The reasons for self-withdrawal were not reported. A total of 41 TD participants were enrolled and all (100%) completed the single visit of the study.

The ASD study population was primarily male (77.8%), consistent with higher male:female ratios for ASD (Loomes et al., 2017). The mean (SD) age of ASD participants was 14.6 (7.83) years compared with a mean (SD) age of 16.3 (13.18) years

for TD participants. Mean (SD) ADOS total score of the ASD participants was 7.6 (1.7), their IQ was 99.2 (19.6), and all were verbal (**Table 5**).

Data Capture and Quality

My JAKE

Overall, My JAKE was used an average of four times a day by each primary caregiver throughout the course of the study for over 34,000 distinct interactions.

As designed, My JAKE used at study sites captured the ABI with no missing items. On rare occasions, a few items were missing when a paper alternative was used due to internet failure at the sites.

The average (SD) number of reports for all participants for mood and overall type of day were 61.2 (35.9) and 29.8 (17.3), respectively, per caregiver over the course of the study.

JAKE Sense

Automated and manual curation of JAKE Sense data was used to assess amount and quality of data obtained from the various sensors and to exclude poor quality data from analyses. **Table 6** shows the percentage of total features captured and the percentage of captured features classified as suitable for analysis (good) by sensor and experiment for ASD participants at the baseline visit using the current version of the data quality algorithms and feature extractors.

The proportion of good features obtained (93.2–100%) was generally high for most of the experiments, although a lower overall proportion (45.6–83.8%) was seen in all EEG variables (biological motion, ERP, resting state, social vs. non-social videos, and NimStim) and EDA experiments (80.1–83.8%). Additionally, many of the EEG and EDA experiments had a relatively lower percentage of captured features than seen in the ECG, eye tracking, and facial affect experiments.

Autism Behavior Inventory (ABI)

While full results of the ABI have been submitted as a separate manuscript, in short, the ABI performed well, with excellent test-retest reliability and strong correlations between domains and scales prospectively hypothesized to measure similar constructs (the core ABI Pearson correlation with the SRS-2 (0.81), ABI restrictive behaviors with RBS-R (0.77), ABI mental health with CASI-anx (0.78), ABI self-regulation with ABC hyperactivity (0.88), and ABI challenging behavior with ABC irritability (0.81). Conversely, as expected, lower correlations were observed where different symptom clusters were assessed, such as between the ABI challenging behaviors domain and the SRS-2 social communication and interaction score (0.32) (**Table 7**).

Test-retest reliability of each domain score 3 to 5 days after baseline was excellent, with Intraclass correlation coefficient values ranging from 0.85 to 0.95. Means did not change significantly between test and retest (**Table 8**).

My JAKE

Representative examples of results from My JAKE are shown in **Figure 4**. The mood report positive valence percentage showed a negative correlation with the ABI challenging behavior subscale at endpoint visit ($r = -0.30$, $p = 0.004$) indicating that more positively perceived mood correlated with a more favorable

TABLE 5 | Participant characteristics.

Characteristic	ASD $N = 144$	TD $N = 41$
GENDER, *n* (%)		
Male	112 (77.8)	27 (65.9)
Female	32 (22.2)	14 (34.1)
AGE		
Mean (SD)	14.6 (7.83)	16.3 (13.18)
Median (Range)	12.5 (6–54)	11.0 (6–63)
RACE, *n* (%)		
White	118 (81.9)	34 (82.9)
Black or African American	6 (4.2)	2 (4.9)
Asian	4 (2.8)	0
Multiple	10 (6.9)	3 (7.3)
Other	4 (2.8)	0
Missing/unknown	2 (1.4)	2 (4.9)
ADOS CSS Total Score, mean (SD)	7.6 (1.7)	–
KBIT-2 IQ Composite Score, mean (SD)	99.2 (19.6)	–

ADOS, autism diagnostic observation schedule; ASD, autism spectrum disorder; CSS, calibrated severity score; KBIT-2 IQ, Kaufman brief intelligence test, second edition; IQ, intelligence quotient; SD, standard deviation; TD, typical developing.

TABLE 6 | Quantity and quality of data obtained from JAKE Sense biosensors (using current data quality algorithms and feature extractors).

Sensor	Experiment	Features Captured (%)	Good Features (%)
ECG	Eyes closed	97	98
ECG	Eyes open	94.8	97.9
EDA	Ticking clock	75.4	81.3
EDA	Toilet flush	75.4	83.8
EDA	Tone	76.3	80.1
EEG	BioMotion	80.5	60.7
EEG	ERP experiment	81.3	75.7
EEG	Social vs. non-social video	82.3	63.6
EEG	NimStim	80.3	45.6
EEG	Resting state	81.4	49.2
EYE	Activity monitoring	83.1	99.9
EYE	Biological motion	85.9	100
EYE	Social orienting task video	70.3	99.8
EYE	ERP experiment	86.7	100
EYE	Social vs. non-social video	91.1	100
EYE	NimStim	81.5	100
EYE	VET	89.9	99.9
FACET	Facial expression production	95.3	93.2
FACET	Funny videos	95.5	98.3

ECG, electrocardiogram; EDA, electrodermal activity; EEG, electroencephalogram; ERP, event-related potential; FACET, FACial Expression; VET, visual exploratory task.

TABLE 7 | Pearson correlations between ABI scales and subscales and related patient reported outcome measures.

Analysis time point related PRO measure	Core ASD symptoms	Social communication	Restrictive repetitive behaviors	Mental health	Self-regulation	Challenging behavior
ABI SCALE						
Baseline ($N = 139$)						
SRS-2 (Caregiver)						
Total score	0.81	0.65	0.74	0.50	0.47	0.35
Social communication and interaction	0.80	0.68	0.69	0.48	0.43	0.32
Restricted interests/repetitive behavior	0.71	0.46	0.76	0.49	0.52	0.41
CASI-Anx						
Anxiety scale score	0.54	0.34	0.58	0.78	0.38	0.25
RBS-R						
Overall score	0.68	0.40	0.77	0.45	0.52	0.42
ABC-Community						
Irritability/agitation	0.50	0.26	0.61	0.56	0.68	0.81
Lethargy/social withdrawal	0.70	0.69	0.52	0.35	0.17	0.19
Stereotypic behavior	0.60	0.40	0.64	0.36	0.53	0.42
Hyperactivity/non-compliance	0.44	0.23	0.54	0.30	0.88	0.54
Inappropriate speech	0.59	0.33	0.69	0.40	0.65	0.48

ABC, Aberrant Behavior Checklist; ABI, autism behavior inventory; ASD, autism spectrum disorder; CASI-Anx, Child Adolescent Symptom Inventory – Anxiety; PRO, Patient Reported Outcome; RBS-R, Repetitive Behavior Scale – Revised; SRS-2, Social Responsiveness Scale 2; ZBI, Zarit Burden Interview.

TABLE 8 | Test-retest correlations for all ABI subscales based on caregiver responses to ABI.

	Core ASD $n = 88$	Social communication $n = 87$	Restrictive repetitive behaviors $n = 88$	Mental health $n = 88$	Self-regulation $n = 88$	Challenging behavior $n = 88$
ICC estimate	0.91	0.91	0.88	0.85	0.92	0.95
p-value	< 0.0001	< 0.0001	< 0.0001	< 0.0001	< 0.0001	< 0.0001
95% CI	(0.88, 0.94)	(0.87, 0.94)	(0.83, 0.92)	(0.78, 0.90)	(0.88, 0.95)	(0.92, 0.97)

p-value for difference from a one-sample t-test. Pearson correlation based on test and retest values. ICC was 2, 1 variant. ICC, intraclass correlation coefficient.

challenging behavior score (**Figure 4A**). **Figure 4B** illustrates that average perceived type of day negatively correlated with ABI Core score at baseline ($r = -0.42$, $p < 0.001$), indicating that a better day correlated with a better ABI Core score.

JAKE Sense

Examples of results generated by the EEG (A), FACET (B), and eye tracking components (C) of JAKE Sense are shown in **Figure 5**. The N170 amplitude (a measure of face processing in the ERP direct and averted gaze paradigm) displayed a difference between TD and ASD participants (**Figure 5A**). TD participants showed greater evidence of "happy" facial expression production in response to being asked to produce a happy face (**Figure 5B**). Also, the more time ASD participants spent looking at the eye region of images of faces in the direct and averted gaze paradigm, the better they scored on the ABI social communications domain (**Figure 5C**). Detailed presentations of results on FACET and eye-tracking are available elsewhere (Manfredonia et al., 2018; Manyakov et al., 2018) and manuscripts of additional results from these and other sensors are in preparation.

Caregiver Feedback

Most caregivers provided positive feedback on overall ease of use and utility using My JAKE for reporting and monitoring behaviors (**Figure 6**). Caregivers viewed the website as "easy" or "very easy" to use (69%, 74/108). Mobile application use by caregivers was rated as "easy" or "very easy" to use (74%, 80/108). Fifty-five percent (59/107) of caregivers were "likely" or "very likely" to use My JAKE outside of a clinical trial. Overall reaction to My JAKE was "positive" or "very positive" from 79% (85/108) of caregivers. For the majority of caregivers, their impression of use of the AMI Motionlogger actigraph by the participant was very comfortable (37%, 22/103) or comfortable (55%, 57/103). Participant's use of the Empatica E4 was reported as comfortable (34%, 23/68), neutral (26.5%, 18/68), or very comfortable (24%, 16/68).

Safety

No significant device-related study events were reported. Approximately 40% of participants (57/144) with ASD had at least 1 event during the study (**Table 9**). The most frequently reported study events (≥1.0% of participants) were upper respiratory tract infection 6.9% (10/144), headache 4.2% (6/144),

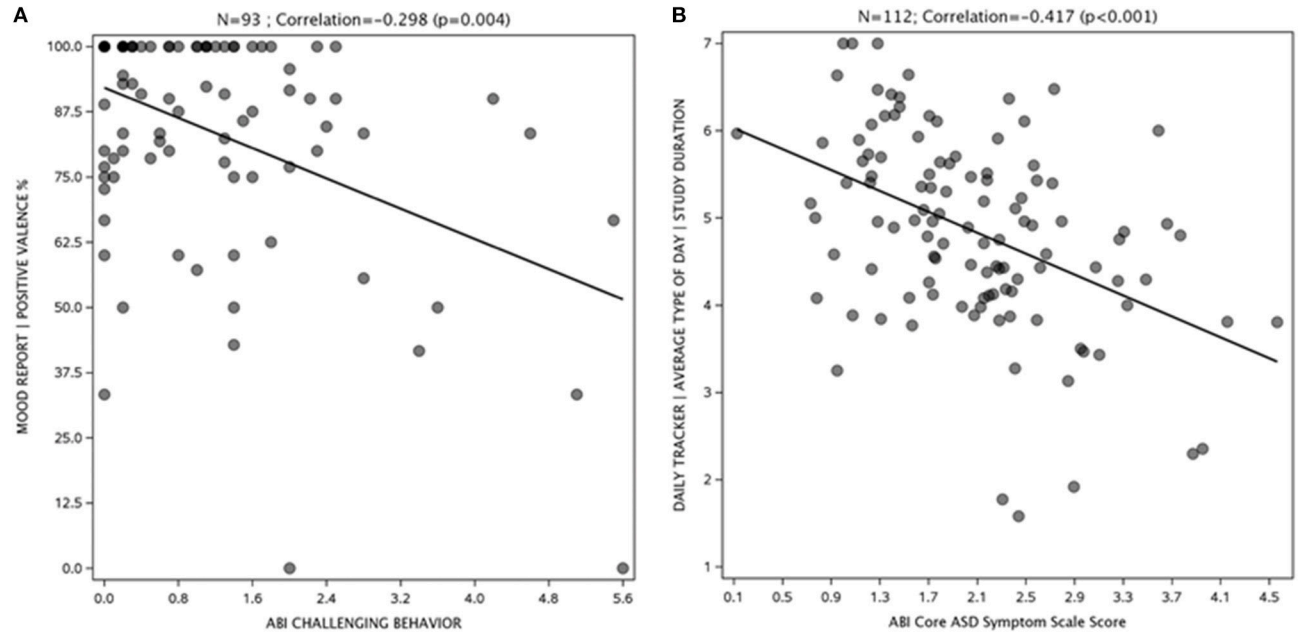

FIGURE 4 | Mood report **(A)** and daily tracker **(B)** correlations with ASD symptoms. ABI, Autism Behavior Inventory; ASD, autism spectrum disorder; TD, typically developing.

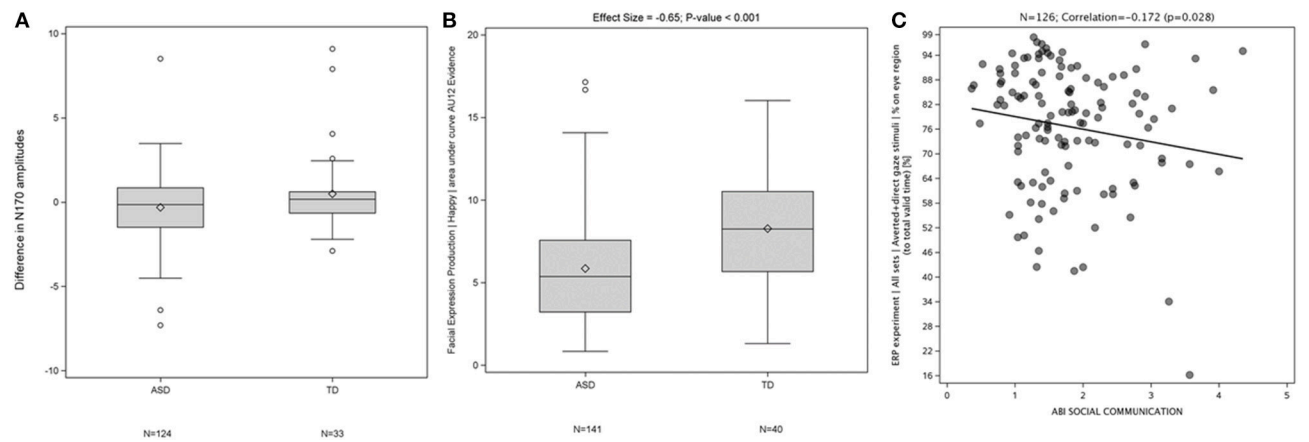

FIGURE 5 | Difference in N170 amplitudes between ERP responses to direct and averted gaze stimuli at electrode T7 in TD and ASD participants ($p = 0.053$) **(A)**, Difference in production of "Happy" facial expressions between TD and ASD participants **(B)**, and Correlation between percentage of time spent by a participant looking at eye region (across both averted and direct gaze stimuli) corrected for total valid time (time on screen) and ABI social communication scales **(C)**. ABI, Autism Behavior Inventory; ASD, autism spectrum disorder; ERP, event-related potentials; TD, typically developing.

and nasopharyngitis 3.5% (5/144). No events were reported with the TD participants.

Three of 144 ASD participants (2.1%) reported study events which were moderate or severe in intensity and designated as serious by the investigator. One participant reported an event of abdominal pain on study Day 40, which was of moderate intensity and resolved after 6 days. One participant reported an event of suicidal ideation on study Day 1, which was of severe intensity and resulted in psychiatric hospitalization. The participant was discontinued from the study due to this event. One participant reported two episodes of severe psychiatric decompensation. The first event occurred on study Day 23 and resolved after 8 days. The other event occurred on study Day 39 and resolved after 9 days.

DISCUSSION

The complexity and heterogeneity of ASD has contributed to difficulties finding effective and scalable therapies to treat core symptoms. Emerging tools and technologies have the potential to improve our ability to measure change more sensitively and to identify subgroups of individuals potentially responsive to

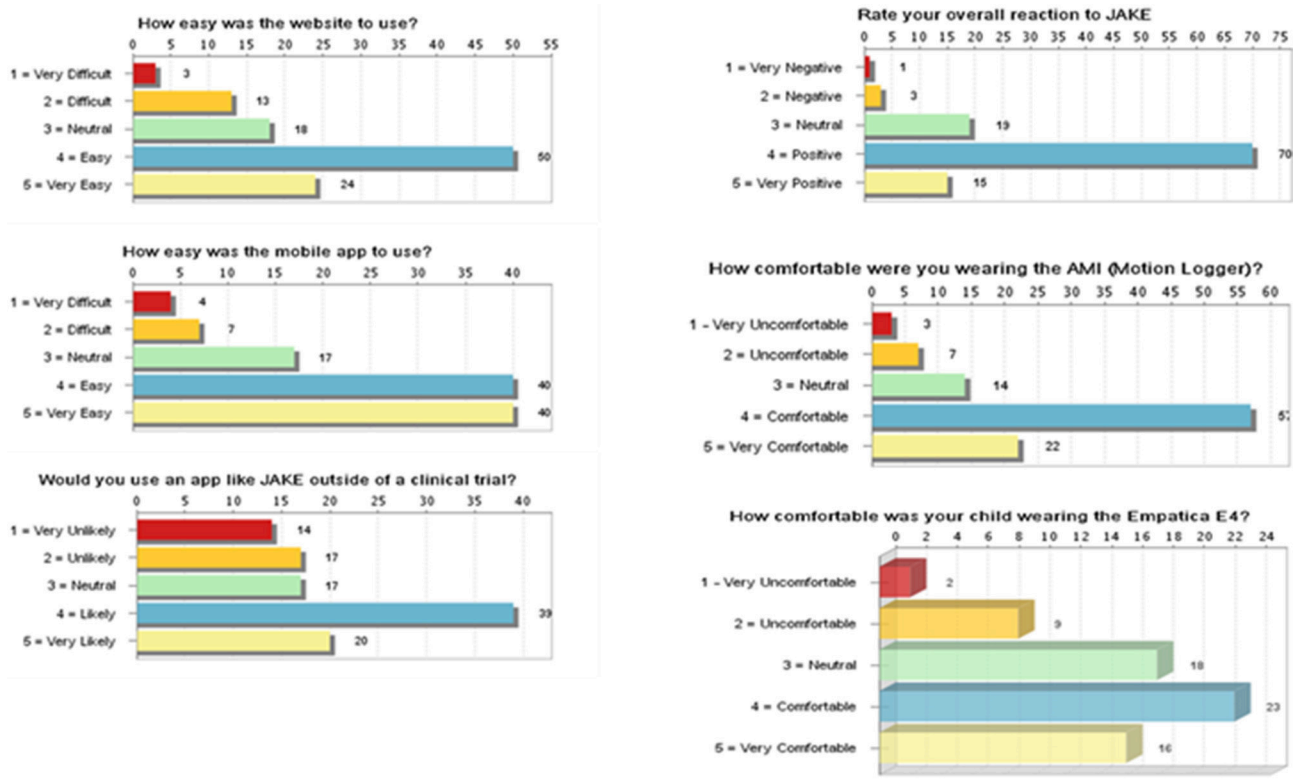

FIGURE 6 | Results of exit survey completed by caregivers of children with ASD. ASD, autism spectrum disorder.

novel therapies. In this study, we report on the practicality of combining and scaling multiple methodologies including biosensors and clinician and caregiver reporting to measure outcomes in a multisite study of children, adolescents, and adults with ASD. Recently, results from specific features of My JAKE and JAKE sense have been reported (Bangerter et al., 2017, In press; Manfredonia et al., 2018; Manyakov et al., 2018; Jagannatha et al., In press; Sargsyan et al., In press).

Data Capture and Quality

An important feasibility metric is the amount and quality of data collected. Both JAKE Sense and My JAKE demonstrated high levels of performance as indicated by user feedback and the capture and quality metrics presented.

Capturing quality data in clinical trials for ASD is difficult due to cost and complexity, particularly when biosensors are included as outcome measures. Sample sizes are therefore often small, which prevents development of approaches for within-group stratification (Loth et al., 2017; Howes et al., 2018). There is a need for big data rich in features, gathered across a large sample, and at multiple levels across the same individuals (Lombardo et al., 2018). This study represents a successful attempt to gather this type of data in a large number of individuals with ASD across a range of levels of development and ages. Of particular importance is the number of sites involved (9) and the range of expertise of the sites in the use of biosensors (some sites had never used an EEG or eye tracker prior to this program), as well as the use of portable devices scalable to larger numbers of sites in a manner not prohibited by size or cost.

JAKE Sense

The collection of hardware and software known as JAKE Sense enables collection of a wealth of synchronized data across multiple sensor modalities and stimulus paradigms. The ECG, eye tracker, and FACET sensors had minimal poor or missing data while data quality was more problematic for EDA and EEG.

Because of technical difficulties encountered in gathering EDA data from the home (for example connectivity issues) and the relatively lower quality of this data compared to other metrics when it was obtained at the sites, EDA has been removed from regular use in future studies within the JAKE system. Rather, participants will be given a single actigraphy device for continuous wear (day+sleep). EDA devices using adhesive wet electrodes may be another option for clinical studies.

The Brain Vision EEG collected reliable and valid data, but the proportion of test sets with acceptable data still needs improvement. Based on direct communication with study sites and analysis of session flow, a number of improvements are being implemented: (a) EEG will be integrated directly into the iMotions® Biometric Research Platform so as not to require separate recording software running simultaneously; (b) the process to ensure the photodiode is connected and functioning

TABLE 9 | Incidence of study events in ≥1.0% of participants.

	ASD (*N* = 144) *n* (%)	TD (*N* = 41) *n* (%)
Participants with at least one study event	57 (39.6)	0
Upper respiratory tract infection	10 (6.9)	0
Nasopharyngitis	5 (3.5)	0
Otitis media	3 (2.1)	0
Sinusitis	3 (2.1)	0
Gastroenteritis	2 (1.4)	0
Influenza	2 (1.4)	0
Respiratory tract infection viral	2 (1.4)	0
Urinary tract infection	2 (1.4)	0
Cough	2 (1.4)	0
Nasal congestion	2 (1.4)	0
Rhinorrhea	2 (1.4)	0
Headache	6 (4.2)	0
Migraine	2 (1.4)	0
Vomiting	3 (2.1)	0
Abdominal pain	2 (1.4)	0
Aggression	3 (2.1)	0
Seasonal allergy	4 (2.8)	0
Rash	2 (1.4)	0
Pyrexia	2 (1.4)	0

ASD, autism spectrum disorder; TD, typically developing.

will be improved; (c) increased training in EEG setup and cap/electrode/impedance procedures, and (d) components of the EEG will be made more water-resistant to prevent damage.

Compared to our previous study where useable data was only gathered from ECG and FACET (Ness et al., 2017), the version of JAKE Sense used in this study, as described in Methods, represents a significant improvement in data collection. Even for EEG data which is often reported as more difficult to obtain (Gurau et al., 2017), and which had relatively lower success rates then our other sensors, substantial amounts of good quality data was obtained. Method changes that were implemented in this study such as better training of site personnel and change of EEG device contributed to the improved quality of data.

Based on feedback from sites and analysis of results, shortening the stimuli battery would also improve tolerability and attention of participants. Considering the length of various stimuli together with the proportion of high-quality data they provide, it is likely that ERP eye gaze, NimStim, and social vs. non-social video stimuli will be removed from the battery. Other tasks, for example biological motion, will be reduced in duration. "Funny videos" will be retained and refined, including the inclusion of sound, as these were reported to maintain interest of participants. The auditory task will be revised and an additional physical challenge (orthostasis) task will be added to specifically probe for changes in ECG measures. The result will be a task battery with two parts, each lasting <15 min.

A novel ERP task that compares EEG response to social and non-social still images of HAI will also be added (Benning et al., 2016). ERP tasks are lengthy in nature, and the EEG set up is more arduous than other biosensors, but these assessments might indicate biological differences in ASD vs. TD individuals. Similar stimuli designed to elicit differences in brain-based responses are also a key component of other leading biomarker studies in ASD. For example, EU-AIMS includes EEG resting state and social and non-social videos in their battery of tasks (Loth et al., 2017). The ABC-CT, a longitudinal study of school-age children with ASD and typical development, is making similar efforts by evaluating a wide range of EEG and eye tracking biomarkers and their associations with caregiver-report and clinician-administered assessments of social communication skills (McPartland, 2018). A key distinction is the restriction of these studies to expert, academic sites. Furthermore, the ABC-CT focuses specifically on social communication skills as the primary endpoint, whereas JAKE includes a wider range of clinical endpoints, such as RRB, challenging behaviors, and mood.

My JAKE

My JAKE was effective in engaging caregivers during the study and successfully captured data encompassing a broad range of demographic, medical, developmental, educational, and psychological aspects of ASD. The website and mobile applications were extensively used by caregivers throughout the study. Caregivers were prompted by My JAKE to complete the ABI and were able to use the web application to enter data on a full range of ASD symptoms.

User Experience

Another important feasibility metric is user experience. Feedback from caregivers, both systematic (through the Exit Survey) and informal (through communication with study centers) was positive. The majority of caregivers found the system easy to use, helpful, and of interest to use again, even outside of a study. Though no major changes in My JAKE other than those discussed above are anticipated prior to deployment in interventional studies in autism, further refinements are planned, including improving charting features, enhancing the mood report, and modifying requirements for frequency of completing various components. These refinements are intended to increase acceptability to and use by caregivers.

To improve caregiver experience completing the ABI, analyses of data obtained in this study will focus on further decreasing user burden and simplifying scoring. Possible options under consideration include changing the number of anchors and altering the item filtering logic.

It is also anticipated that a decrease in duration of the JAKE Sense task battery will improve participant experience and tolerability. Consolidation of wearable home-based sensors to a single wrist-worn actigraph, rather than a different device for night time (actigraph) and day time (actigraph + EDA), may also improve compliance.

Clinical Significance

Perhaps most importantly, clinical relevance of data acquired must be examined. We have reported on biosensor data analysis from facial expressions (Manfredonia et al., 2018) and eye tracking (Manyakov et al., 2018) and found both

have the potential to aid with diagnosis and evaluation of clinical symptoms of ASD. Data mining methods of biosensor data were investigated as an approach to enable objective discrimination between ASD and TD individuals to potentially subgroup ASD participants based on phenotypic data gathered by JAKE (Jagannatha et al., In press). In addition, predictive modeling using biosensor-based feature selection was explored to examine how changes in these features correlated with clinical assessments (Sargsyan et al., In press). We are preparing additional results obtained by the various components of JAKE Sense, focusing on differences between TD and ASD participants' correlations between sensors and ASD severity and symptoms as measured by the ABI, and on changes over time. Genomic analysis will attempt to correlate polymorphisms in distinct genetic pathways with differences in autism phenotype.

In this study, we demonstrated the domains of the ABI were highly correlated with standard scales measuring the same constructs while comprising far fewer items than the combined battery of these scales. A complete presentation of results of the ABI from this study has been submitted for publication.

Similarly, the utility of My JAKE for capturing real-time daily reports was demonstrated, and further exploration of system elements and relationships of reports to other measures are underway. Clinical endpoints measured by components of My JAKE, such as the Daily Tracker and Mood Report, showed that even simple methods may be useful for measuring the effectiveness of interventional therapy.

Limitations

Limitations of this study include a caregiver burden that was sometimes considerable, and the task battery being stressful for some participants. Technical failures with various sensors of JAKE Sense such as EDA and EEG also limited data capture. Improved algorithms for use in analyses of various sensor data and in data cleaning will also be explored.

A recent study (Anusha et al., 2018) suggests that dry electrodes on dry skin should be worn for at least 27 min before a sufficient moisture barrier is built up to produce stable EDA values. Although sites were requested to implement this warm-up time not all sites may have done so for all data collection sessions.

While a relatively heterogeneous group of individuals with ASD participated in the study, data from more individuals spanning autism severity and IQ is needed to determine whether there are meaningfully different profiles. This would necessarily require a much larger sample than allowed by this initial observational study. Also, individuals with ASD and particular symptoms, for instance prominent sensory sensitivities or inattention, may not have been able to tolerate portions of JAKE Sense.

Data were generally provided by the primary caregiver. It will be important to have data from other collateral sources such as school or program staff and more self-reported data from individuals with ASD who are capable of providing feedback on their own cognition, affect, and behavior.

As the primary purpose of the study was to assess the system in ASD participants, the size of the TD sample was relatively small in comparison. My JAKE was also not used by the TD cohort.

CONCLUSIONS

JAKE is a dynamic system being developed to identify subpopulations of individuals with ASD and to sensitively measure ASD intervention outcomes. The use of JAKE in future interventional trials has the potential to advance novel treatments for ASD core and associated symptoms. In this study, JAKE demonstrated the ability to capture a broad range of high-quality data on ASD. Interventional studies will be needed to demonstrate the ability of JAKE to serve as a robust and sensitive measurement tool.

DATA AVAILABILITY

The datasets generated for this study are available on request to the corresponding author.

AUTHOR CONTRIBUTIONS

SN, AB, JF, NM, DL, MB, AS, SJ, GD, MG, RH, BL, FS, YJ, BK, RT, JM, CS, and GP were involved in study design and/or data collection. DL, SJ, MC, and NM were responsible for the statistical analyses. SN, AB, NM, AS, and GP were involved in data analysis. All authors were involved in interpretation of the results and review of the manuscript.

FUNDING

The authors declare that this study received funding from Janssen Research & Development, LLC. The funder was not involved in the study design or collection, analysis, or interpretation of the data.

ACKNOWLEDGMENTS

Stacey E. Shehin, Ph.D. of PRA Health Sciences provided medical writing assistance, which was funded by Janssen Research & Development. Ellen Baum, Ph.D. of Janssen Global Services provided additional editorial support. The authors thank all staff at the research sites involved in data collection. Above all, the authors thank all research participants, their families and support providers for their contributions.

REFERENCES

Acebo, C., Sadeh, A., Seifer, R., Tzischinsky, O., Wolfson, A. R., Hafer, A., et al. (1999). Estimating sleep patterns with activity monitoring in children and adolescents: how many nights are necessary for reliable measures? *Sleep* 22, 95–103. doi: 10.1093/sleep/22.1.95

Aman, M. G., Novotny, S., Samango-Sprouse, C., Lecavalier, L., Leonard, E., Gadow, K. D., et al. (2004). Outcome measures for clinical drug

trials in autism. *CNS Spectr.* 9, 36–47. doi: 10.1017/S1092852900008348

Aman, M. G., and Singh, N. N. (2017). *Aberrant Behavior Checklist Manual, Second Edition.* East Aurora, NY: Slosson Educational Publications, Inc.,

American Psychiatric Association (2013). *Diagnostic and Statistical Manual of Mental Disorders, 5th Edition: DSM-5*. Arlinglton, TX: American Psychiatric Publishing. doi: 10.1176/appi.books.9780890425596

Anagnostou, E., Jones, N., Huerta, M., Halladay, A. K., Wang, P., Scahill, L., et al. (2015). Measuring social communication behaviors as a treatment endpoint in individuals with autism spectrum disorder. *Autism* 19, 622–636. doi: 10.1177/1362361314542955

Andari, E., Duhamel, J. R., Zalla, T., Herbrecht, E., Leboyer, M., and Sirigu, A. (2010). Promoting social behavior with oxytocin in high-functioning autism spectrum disorders. *Proc. Natl. Acad. Sci. U.S.A.* 107, 4389–4394. doi: 10.1073/pnas.0910249107

Anusha, A. S., Preejith, S. P., Akl, T. J., Joseph, J., and Sivaprakasam, M. (2018). "Dry Electrode Optimization for Wrist-based Electrodermal Activity Monitoring", in 2018 *IEEE International Symposium on Medical Measurements and Applications (MeMeA)* (Rome), 1–6.

Auyeung, B., Lombardo, M. V., Heinrichs, M., Chakrabarti, B., Sule, A., Deakin, J. B., et al. (2015). Oxytocin increases eye contact during a real-time, naturalistic social interaction in males with and without autism. *Transl. Psychiatry* 5:e507. doi: 10.1038/tp.2014.146

Bahrick, L. E. (1987). Infants' intermodal perception of two levels of temporal structure in natural events. *Infant Behav. Dev.* 10, 387–416. doi: 10.1016/0163-6383(87)90039-7

Bangerter, A., Manyakov, N. V., Lewin, D., Boice, M., Skalkin, A., Jagannatha, S., et al. (In press). Caregiver daily reporting of symptoms in autism spectrum disorder: an observational study using web and mobile applications. *JMIR Ment. Health*. doi: 10.2196/11365

Bangerter, A., Ness, S., Aman, M. G., Esbensen, A. J., Goodwin, M. S., Dawson, G., et al. (2017). Autism behavior inventory: a novel tool for assessing core and associated symptoms of autism spectrum disorder. *J. Child Adolesc. Psychopharmacol.* 27, 814–822. doi: 10.1089/cap.2017.0018

Bazelmans, T., Jones, E. J., Ghods, S., Corrigan, S., Toth, K., Charman, T., et al. (2018). Heart rate mean and variability as a biomarker for phenotypic variation in preschoolers with autism spectrum disorder. *Autism Res.* 12, 39–52. doi: 10.1002/aur.1982

Benning, S. D., Kovac, M., Campbell, A., Miller, S., Hanna, E. K., Damiano, C. R., et al. (2016). Late positive potential ERP responses to social and nonsocial stimuli in youth with autism spectrum disorder. *J. Autism Dev. Disord.* 46, 3068–3077. doi: 10.1007/s10803-016-2845-y

Black, M. H., Chen, N. T. M., Iyer, K. K., Lipp, O. V., Bolte, S., Falkmer, M., et al. (2017). Mechanisms of facial emotion recognition in autism spectrum disorders: insights from eye tracking and electroencephalography. *Neurosci. Biobehav. Rev.* 80, 488–515. doi: 10.1016/j.neubiorev.2017.06.016

Bodfish, J., Symons, F., and Lewis, M. (1999). *The Repetitive Behavior Scale (Western Carolina Center Research Reports)*. Morganton, NC: Western Carolina Center.

Boucsein, W. (2012). *Electrodermal Activity*. New York, NY: Springer doi: 10.1007/978-1-4614-1126-0

Boucsein, W., Fowles, D. C., Grimnes, S., Ben-Shakhar, G., Roth, W. T., Dawson, M. E., et al. (2012). Publication recommendations for electrodermal measurements. *Psychophysiology* 49, 1017–1034. doi: 10.1111/j.1469-8986.2012.01384.x

Bushwick, N. L. (2001). Social learning and the etiology of autism. *N Ideas Psychol.* 19, 49–75. doi: 10.1016/S0732-118X(00)00016-7

Cadman, T., Eklund, H., Howley, D., Hayward, H., Clarke, H., Findon, J., et al. (2012). Caregiver burden as people with autism spectrum disorder and attention-deficit/hyperactivity disorder transition into adolescence and adulthood in the United Kingdom. *J. Am. Acad. Child. Adolesc. Psychiatry* 51, 879–888. doi: 10.1016/j.jaac.2012.06.017

Carpenter, M., Nagell, K., Tomasello, M., Butterworth, G., and Moore, C. (1998). Social cognition, joint attention, and communicative competence from 9 to 15 months of age. *Monogr. Soc. Res. Child Dev.* 68:142–143. doi: 10.2307/1166214

Chawarska, K., Macari, S., and Shic, F. (2012). Context modulates attention to social scenes in toddlers with autism. *J. Child. Psychol. Psychiatry* 53, 903–913. doi: 10.1111/j.1469-7610.2012.02538.x

Chawarska, K., Ye, S., Shic, F., and Chen, L. (2016). Multilevel differences in spontaneous social attention in toddlers with autism spectrum disorder. *Child Dev.* 87, 543–557. doi: 10.1111/cdev.12473

Constantino, J. N., Davis, S. A., Todd, R. D., Schindler, M. K., Gross, M. M., Brophy, S. L., et al. (2003). Validation of a brief quantitative measure of autistic traits: comparison of the social responsiveness scale with the autism diagnostic interview-revised. *J. Autism Dev. Disord.* 33, 427–433. doi: 10.1023/A:1025014929212

Dawson, G., Toth, K., Abbott, R., Osterling, J., Munson, J., Estes, A., et al. (2004). Early social attention impairments in autism: social orienting, joint attention, and attention to distress. *Dev. Psychol.* 40:271. doi: 10.1037/0012-1649.40.2.271

Dawson, M., Schell, A., and Filllion, D. (2007). *The Electrodermal System.* New York, NY: Cambridge University Press. doi: 10.1017/CBO9780511546396.007

De-la-Iglesia, M., and Olivar, J. S. (2015). Risk factors for depression in children and adolescents with high functioning autism spectrum disorders. *Sci. World J.* 2015:127853. doi: 10.1155/2015/127853

Falkmer, T., Anderson, K., Falkmer, M., and Horlin, C. (2013). Diagnostic procedures in autism spectrum disorders: a systematic literature review. *Eur. Child Adolesc. Psychiatry* 22, 329–340. doi: 10.1007/s00787-013-0375-0

Goodwin, M. S., Haghighi, M., Tang, Q., Akcakaya, M., Erdogmus, D., and Intille, S. (2014). "Moving towards a real-time system for automatically recognizing stereotypical motor movements in individuals on the autism spectrum using wireless accelerometry," in *Proceedings of the 2014 ACM International Joint Conference on Pervasive and Ubiquitous Computing* (ACM), 861–872.

Goodwin, M. S., Intille, S. S., Albinali, F., and Velicer, W. F. (2011). Automated detection of stereotypical motor movements. *J. Autism Dev. Disord.* 41, 770–782. doi: 10.1007/s10803-010-1102-z

Goodwin, M. S., Özdenizci, O., Cumpanasoiu, C., Tian, P., Guo, Y., Stedman, A., et al. (2018). Predicting imminent aggression onset in minimally-verbal youth with autism spectrum disorder using preceding physiological signals. *Int. Conf. Pervasive Comput. Technol. Healthc.* 2018, 201–207. doi: 10.1145/3240925.3240980

Goswami, S., Cavalier, S., Sridhar, V., Huber, K. M., and Gibson, J. R. (2019). Local cortical circuit correlates of altered EEG in the mouse model of Fragile X syndrome. *Neurobiol. Dis.* 9, S0969–S9961. doi: 10.1016/j.nbd.2019.01.002

Gotham, K., Unruh, K., and Lord, C. (2015). Depression and its measurement in verbal adolescents and adults with autism spectrum disorder. *Autism* 19, 491–504. doi: 10.1177/1362361314536625

Grice, S. J., Halit, H., Farroni, T., Baron-Cohen, S., Bolton, P., and Johnson, M. H. (2005). Neural correlates of eye-gaze detection in young children with autism. *Cortex* 41, 342–353. doi: 10.1016/S0010-9452(08)70271-5

Gringras, P., Gamble, C., Jones, A. P., Wiggs, L., Williamson, P. R., Sutcliffe, A., et al. (2012). Melatonin for sleep problems in children with neurodevelopmental disorders: randomised double masked placebo controlled trial. *BMJ* 345:e6664. doi: 10.1136/bmj.e6664

Großekathöfer, U., Manyakov, N. V., Mihajlović, V., Pandina, G., Skalkin, A., Ness, S., et al. (2017). Automated detection of stereotypical motor movements in autism spectrum disorder using recurrence quantification analysis. *Front. Neuroinform.* 11:9. doi: 10.3389/fninf.2017.00009

Gurau, O., Bosl, W. J., and Newton, C. R. (2017). How useful is electroencephalography in the diagnosis of autism spectrum disorders and the delineation of subtypes: a systematic review. *Front. Psychiatry* 8:121. doi: 10.3389/fpsyt.2017.00121

Hallett, V., Lecavalier, L., Sukhodolsky, D. G., Cipriano, N., Aman, M. G., McCracken, J. T., et al. (2013). Exploring the manifestations of anxiety in children with autism spectrum disorders. *J. Autism Dev. Disord.* 43, 2341–2352. doi: 10.1007/s10803-013-1775-1

Howes, O. D., Rogdaki, M., Findon, J. L., Wichers, R. H., Charman, T., King, B. H., et al. (2018). Autism spectrum disorder: consensus guidelines on assessment, treatment and research from the British Association for Psychopharmacology. *J. Psychopharmacol.* 32, 3–29. doi: 10.1177/0269881117741766

Jagannatha, S., Sargsyan, D., Manyakov, N. V., Skalkin, A., Bangerter, A., Ness, S., et al. (In press). A practical application of data mining methods to build predictive models for autism spectrum disorder based on biosensor data from JAKEtm. *Stat. Biopharm. Res*. doi: 10.1080/19466315.2018.1527247

Jones, R. M., Risi, S., Wexler, D., Anderson, D., Corsello, C., Pickles, A., et al. (2015). How interview questions are placed in time influences caregiver description of social communication symptoms on the ADI-R. *J. Child Psychol. Psychiatry* 56, 577–585. doi: 10.1111/jcpp.12325

Kaufman, A. (2004). *KBIT-2: Kaufman Brief Intelligence Test–Second Edition*. Bloomington, MN: Pearson.

Kleckner, I. R., Jones, R. M., Wilder-Smith, O., Wormwood, J. B., Akcakaya, M., Quigley, K. S., et al. (2018). Simple, transparent, and flexible automated quality assessment procedures for ambulatory electrodermal activity data. *IEEE Trans. Biomed. Eng.* 65, 1460–1467. doi: 10.1109/TBME.2017.2758643

Klin, A., Jones, W., Schultz, R., and Volkmar, F. (2003). The enactive mind, or from actions to cognition: lessons from autism. *Philos. Trans. R. Soc. Lond. Ser. B* 358, 345–360. doi: 10.1098/rstb.2002.1202

Klusek, J., Roberts, J. E., and Losh, M. (2015). Cardiac autonomic regulation in autism and Fragile X syndrome: a review. *Psychol. Bull.* 141, 141–175. doi: 10.1037/a0038237

Kring, A. M., Barrett, L. F., and Gard, D. E. (2003). On the broad applicability of the affective circumplex: representations of affective knowledge among schizophrenia patients. *Psychol. Sci.* 14, 207–214. doi: 10.1111/1467-9280.02433

Lecavalier, L., Wood, J. J., Halladay, A. K., Jones, N. E., Aman, M. G., Cook, E. H., et al. (2014). Measuring anxiety as a treatment endpoint in youth with autism spectrum disorder. *J. Autism Dev. Disord.* 44, 1128–1143. doi: 10.1007/s10803-013-1974-9

Levine, T. P., Conradt, E., Goodwin, M. S., Sheinkopf, S. J., and Lester, B. (2014). "Psychophysiological arousal to social stress in autism spectrum disorders," in *Comprehensive Guide to Autism*, eds V. B. Patel, V. R. Preedy, and C. R. Martin (New York, NY: Springer), 1177–1193.

Lombardo, M. V., Lai, M. C., and Baron-Cohen, S. (2018). Big data approaches to decomposing heterogeneity across the autism spectrum. *bioRxiv*, 278788. doi: 10.1101/278788

Loomes, R., Hull, L., and Mandy, W. P. L. (2017). What is the male-to-female ratio in autism spectrum disorder? A systematic review and meta-analysis. *J. Am. Acad. Child Adolesc. Psychiatry* 56, 466–474. doi: 10.1016/j.jaac.2017.03.013

Lord, C., Rutter, M., DiLavore, P., Risi, S., Gotham, K., and Bishop, S. (2012). *Autism Diagnostic Observation Schedule–Second Edition (ADOS-2)*. Los Angeles, CA: Western Psychological Services.

Lord, C., Rutter, M., and Le Couteur, A. (1994). Autism diagnostic interview-revised: a revised version of a diagnostic interview for caregivers of individuals with possible pervasive developmental disorders. *J. Autism Dev. Disord.* 24, 659–685. doi: 10.1007/BF02172145

Loth, E., Charman, T., Mason, L., Tillmann, J., Jones, E. J. H., Wooldridge, C., et al. (2017). The EU-AIMS Longitudinal European Autism Project (LEAP): design and methodologies to identify and validate stratification biomarkers for autism spectrum disorders. *Mol. Autism* 8:24. doi: 10.1186/s13229-017-0146-8

Loth, E., Spooren, W., Ham, L. M., Isaac, M. B., Auriche-Benichou, C., Banaschewski, T., et al. (2016). Identification and validation of biomarkers for autism spectrum disorders. *Nat. Rev. Drug Dis.* 15:70. doi: 10.1038/nrd.2015.7

Louwerse, A., Tulen, J. H., van der Geest, J. N., van der Ende, J., Verhulst, F. C., and Greaves-Lord, K. (2014). Autonomic responses to social and nonsocial pictures in adolescents with autism spectrum disorder. *Autism Res.* 7, 17–27. doi: 10.1002/aur.1327

Lydon, S., Healy, O., Reed, P., Mulhern, T., Hughes, B. M., and Goodwin, M. S. (2016). A systematic review of physiological reactivity to stimuli in autism. *Dev. Neurorehabil.* 19, 335–355. doi: 10.3109/17518423.2014.971975

Manfredonia, J., Bangerter, A., Manyakov, N. V., Ness, S., Lewin, D., Skalkin, A., et al. (2018). Automatic recognition of posed facial expression of emotion in individuals with autism spectrum disorder. *J. Autism Dev. Disord.* 49, 279–293. doi: 10.1007/s10803-018-3757-9

Manyakov, N. V., Bangerter, A., Chatterjee, M., Mason, L., Ness, S., Lewin, D., et al. (2018). Visual exploration in autism spectrum disorder: exploring age differences and dynamic features using recurrence quantification analysis. *Autism Res.* 11, 1554–1566. doi: 10.1002/aur.2021

Mazefsky, C. A., Herrington, J., Siegel, M., Scarpa, A., Maddox, B. B., Scahill, L., et al. (2013). The role of emotion regulation in autism spectrum disorder. *J. Am. Acad. Child Adolesc. Psychiatry* 52, 679–688. doi: 10.1016/j.jaac.2013.05.006

McCarthy, C., Pradhan, N., Redpath, C., and Adler, A. (2016). "Validation of the Empatica E4 wristband," in *2016 IEEE EMBS International Student Conference (ISC)*, 1–4.

McCormick, C., Hessl, D., Macari, S. L., Ozonoff, S., Green, C., and Rogers, S. J. (2014). Electrodermal and behavioral responses of children with autism spectrum disorders to sensory and repetitive stimuli. *Autism Res.* 7, 468–480. doi: 10.1002/aur.1382

McPartland, J. (2018). *Autism Biomarkers Consortium for Clinical Trials*. Available online at: https://medicine.yale.edu/ycci/researchers/autism/ (Accessed December 12, 2018).

Meltzer, L. J., Walsh, C. M., Traylor, J., and Westin, A. M. (2012). Direct comparison of two new actigraphs and polysomnography in children and adolescents. *Sleep* 35, 159–166. doi: 10.5665/sleep.1608

Murias, M., Major, S., Davlantis, K., Franz, L., Harris, A., Rardin, B., et al. (2018). Validation of eye-tracking measures of social attention as a potential biomarker for autism clinical trials. *Autism Res.* 11, 166–174. doi: 10.1002/aur.1894

Murias, M., Webb, S. J., Greenson, J., and Dawson, G. (2007). Resting state cortical connectivity reflected in EEG coherence in individuals with autism. *Biol. Psychol.* 62, 270–273. doi: 10.1016/j.biopsych.2006.11.012

Ness, S. L., Manyakov, N. V., Bangerter, A., Lewin, D., Jagannatha, S., Boice, M., et al. (2017). JAKE(R) multimodal data capture system: insights from an observational study of autism spectrum disorder. *Front. Neurosci.* 11:517. doi: 10.3389/fnins.2017.00517

O'Reilly, C., Lewis, J. D., and Elsabbagh, M. (2017). Is functional brain connectivity atypical in autism? A systematic review of EEG and MEG studies. *PLoS ONE* 12:e0175870. doi: 10.1371/journal.pone.0175870

Pitcher, D., Dilks, D. D., Saxe, R. R., Triantafyllou, C., and Kanwisher, N. (2011). Differential selectivity for dynamic versus static information in face-selective cortical regions. *Neuroimage* 56, 2356–2363. doi: 10.1016/j.neuroimage.2011.03.067

Plesa-Skwerer, D., Chu, A., Brukilacchio, B., and Tager-Flusberg, H. (2016). "Exploring visual social attention in minimally verbal children and adolescents with ASD," in *International Meeting for Autism Research (IMFAR)*. Available online at: www.autism-insar.org.

Poh, M., Swenson, N. C., and Picard, R. W. (2010). A wearable sensor for unobtrusive, long-term assessment of electrodermal activity. *IEEE Trans. Biomed. Eng.* 57, 1243–1252. doi: 10.1109/TBME.2009.2038487

Prince, E. B., Kim, E. S., Wall, C. A., Gisin, E., Goodwin, M. S., Simmons, E. S., et al. (2017). The relationship between autism symptoms and arousal level in toddlers with autism spectrum disorder, as measured by electrodermal activity. *Autism* 21, 504–508. doi: 10.1177/1362361316648816

Richdale, A. L., and Schreck, K. A. (2009). Sleep problems in autism spectrum disorders: prevalence, nature, & possible biopsychosocial aetiologies. *Sleep Med. Rev.* 13, 403–411. doi: 10.1016/j.smrv.2009.02.003

Rumney, H. L., and MacMahon, K. (2017). Do social skills interventions positively influence mood in children and young people with autism? A systematic review. *Mental Health Prev.* 5, 12–20. doi: 10.1016/j.mhp.2016.12.001

Rutter, M., Bailey, A., and Lord, C. (2003). "Social Communication Questionnaire: SCQ (W-381)". Los Angeles, CA: Western Psychological Services. Available online at: https://www.wpspublish.com/store/p/2954/scq-social-communication-questionnaire).

Sano, A., Picard, R. W., and Stickgold, R. (2014). Quantitative analysis of wrist electrodermal activity during sleep. *Int. J. Psychophysiol.* 94, 382–389. doi: 10.1016/j.ijpsycho.2014.09.011

Sargsyan, D., Jagannatha, S., Manyakov, N. V., Skalkin, A., Bangerter, A., Ness, S., et al. (In press). Feature selection with weighted importance index in an autism spectrum disorder study. *Stat. Biopharm. Res.* doi: 10.1080/19466315.2018.1537886

Sasson, N. J., Elison, J. T., Turner-Brown, L. M., Dichter, G. S., and Bodfish, J. W. (2011). Brief report: circumscribed attention in young children with autism. *J. Autism Dev. Dis.* 41, 242–247. doi: 10.1007/s10803-010-1038-3

Sasson, N. J., Turner-Brown, L. M., Holtzclaw, T. N., Lam, K. S., and Bodfish, J. W. (2008). Children with autism demonstrate circumscribed attention during passive viewing of complex social and nonsocial picture arrays. *Autism Res.* 1, 31–42. doi: 10.1002/aur.4

Scahill, L., Aman, M. G., Lecavalier, L., Halladay, A. K., Bishop, S. L., Bodfish, J. W., et al. (2015). Measuring repetitive behaviors as a treatment endpoint in youth with autism spectrum disorder. *Autism* 19, 38–52. doi: 10.1177/1362361313510069

Senju, A., Tojo, Y., Dairoku, H., and Hasegawa, T. (2004). Reflexive orienting in response to eye gaze and an arrow in children with and without autism. *J. Child. Psychol. Psychiatry* 45, 445–458. doi: 10.1111/j.1469-7610.2004.00236.x

Shic, F., Bradshaw, J., Klin, A., Scassellati, B., and Chawarska, K. (2011). Limited activity monitoring in toddlers with autism spectrum disorder. *Brain Res.* 1380, 246–254. doi: 10.1016/j.brainres.2010.11.074

Shic, F., Chen, G., Perlmutter, M., Gisin, E., Dowd, A., Prince, E., et al. (2014). "Components of limited activity monitoring in toddlers and children with ASD," in *International Meeting for Autism Research Atlanta* (Atlanta, GA).

Shou, G., Mosconi, M. W., Wang, J., Ethridge, L. E., Sweeney, J. A., and Ding, L. (2017). Electrophysiological signatures of atypical intrinsic brain connectivity networks in autism. *J. Neural Eng.* 14:046010. doi: 10.1088/1741-2552/aa6b6b

Souders, M. C., Mason, T. B., Valladares, O., Bucan, M., Levy, S. E., Mandell, D. S., et al. (2009). Sleep behaviors and sleep quality in children with autism spectrum disorders. *Sleep* 32, 1566–1578. doi: 10.1093/sleep/32.12.1566

Speer, L. L., Cook, A. E., McMahon, W. M., and Clark, E. (2007). Face processing in children with autism: effects of stimulus contents and type. *Autism* 11, 265–277. doi: 10.1177/1362361307076925

Sukhodolsky, D. G., Scahill, L., Gadow, K. D., Arnold, L. E., Aman, M. G., McDougle, C. J., et al. (2008). Parent-rated anxiety symptoms in children with pervasive developmental disorders: frequency and association with core autism symptoms and cognitive functioning. *J. Abnorm. Child. Psychol.* 36, 117–128. doi: 10.1007/s10802-007-9165-9

Tomasello, M., Carpenter, M., Call, J., Behne, T., and Moll, H. (2005). Understanding and sharing intentions: the origins of cultural cognition. *Behav. Brain Sci.* 28, 675–691. discussion: 691–735. doi: 10.1017/S0140525X05000129

Tseng, A., Bansal, R., Liu, J., Gerber, A. J., Goh, S., Posner, J., et al. (2014). Using the circumplex model of affect to study valence and arousal ratings of emotional faces by children and adults with autism spectrum disorders. *J. Autism Dev. Disord.* 44, 1332–1346. doi: 10.1007/s10803-013-1993-6

Umbricht, D., del Valle Rubido, M., Hollander, E., McCracken, J. T., Shic, F., Scahill, L., et al. (2017). A single dose, randomized, controlled proof-of-mechanism study of a novel vasopressin 1a receptor antagonist (RG7713) in high-functioning adults with autism spectrum disorder. *Neuropsychopharmacology* 42:1914. doi: 10.1038/npp.2016.232

Vaughan Van Hecke, A., Lebow, J., Bal, E., Lamb, D., Harden, E., Kramer, A., et al. (2009). Electroencephalogram and heart rate regulation to familiar and unfamiliar people in children with autism spectrum disorders. *Child. Dev.* 80, 1118–1133. doi: 10.1111/j.1467-8624.2009.01320.x

Wagner, J. B., Hirsch, S. B., Vogel-Farley, V. K., Redcay, E., and Nelson, C. A. (2013). Eye-tracking, autonomic, and electrophysiological correlates of emotional face processing in adolescents with autism spectrum disorder. *J. Autism Dev. Disord.* 43, 188–199. doi: 10.1007/s10803-012-1565-1

Wang, J., Barstein, J., Ethridge, L. E., Mosconi, M. W., Takarae, Y., and Sweeney, J. A. (2013). Resting state EEG abnormalities in autism spectrum disorders. *J. Neurodev. Disord.* 5:24. doi: 10.1186/1866-1955-5-24

Wang, Q., Campbell, D. J., Macari, S. L., Chawarska, K., and Shic, F. (2018). Operationalizing atypical gaze in toddlers with autism spectrum disorders: a cohesion-based approach. *Mol. Autism* 9:25. doi: 10.1186/s13229-018-0211-y

Webb, S. J., Bernier, R., Henderson, H. A., Johnson, M. H., Jones, E. J., Lerner, M. D., et al. (2015). Guidelines and best practices for electrophysiological data collection, analysis and reporting in autism. *J. Autism Dev. Disord.* 45, 425–443. doi: 10.1007/s10803-013-1916-6

Wetherby, A. M., Woods, J., Allen, L., Cleary, J., Dickinson, H., and Lord, C. (2004). Early indicators of autism spectrum disorders in the second year of life. *J. Autism Dev. Dis.* 34, 473–493. doi: 10.1007/s10803-004-2544-y

Wiggs, L., and Stores, G. (2004). Sleep patterns and sleep disorders in children with autistic spectrum disorders: insights using parent report and actigraphy. *Dev. Med. Child. Neurol.* 46, 372–380. doi: 10.1017/S0012162204000611

Woodard, C. R., Goodwin, M. S., Zelazo, P. R., Aube, D., Scrimgeour, M., Ostholthoff, T., et al. (2012). A comparison of autonomic, behavioral, and parent-report measures of sensory sensitivity in young children with autism. *Res. Autism Spectr. Disord.* 6, 1234–1246. doi: 10.1016/j.rasd.2012.03.012

Yirmiya, N., Kasari, C., Sigman, M., and Mundy, P. (1989). Facial expressions of affect in autistic, mentally retarded and normal children. *J. Child Psychol. Psychiatry* 30, 725–735. doi: 10.1111/j.1469-7610.1989.tb00785.x

Zarit, S. H., Reever, K. E., and Bach-Peterson, J. (1980). Relatives of the impaired elderly: correlates of feelings of burden. *Gerontologist* 20, 649–655. doi: 10.1093/geront/20.6.649

Conflict of Interest Statement: SN, AB, NM, MB, AS, SJ, MC and GP are employed by Janssen Research & Development, LLC and may hold company stock/stock options. DL was employed by Janssen Research & Development during the time of this study.

GD is on the Scientific Advisory Boards of Janssen Research & Development and Akili, Inc., a consultant to Roche, has received grant funding from Janssen Research & Development and PerkinElmer, is CEO of DASIO (Digital Approaches Improve Outcomes), Inc., and receives royalties from Guildford Press and Oxford University Press. MG has received research and consulting funding from Janssen Research & Development. JF has received research grant funding from the NIH, Alcobra Pharma, F. Hoffmann-La Roche, Ltd., Fulcrum Therapeutics, Janssen Research & Development, and SyneuRX International. RH is on the Scientific Advisory Boards of BioMarin Pharmaceutical Inc., Neuren Pharmaceuticals Limited, and Janssen Research & Development, and has research grant funding from Curemark, Roche, Shire, and Sunovion Pharmaceuticals, Inc. BL has received research grant funding from the NIH, is a consultant to Janssen Research & Development, and the Illinois Children's Healthcare Foundation, and is a board member of the Brain Research Foundation. FS has received research funding from Janssen Research & Development, and Roche. BK, RT have received research funding from Janssen Research & Development, and Roche.

The remaining authors declare that the research was conducted in the absence of any commercial or financial relationships that could be construed as a potential conflict of interest

frontiers in Neuroscience

REVIEW
published: 05 March 2019
doi: 10.3389/fnins.2019.00162

Experimental and Computational Methods for the Study of Cerebral Organoids: A Review

Daniele Poli[1], *Chiara Magliaro*[1] *and Arti Ahluwalia*[1,2]*

[1] Research Center E. Piaggio, University of Pisa, Pisa, Italy, [2] Department of Information Engineering, University of Pisa, Pisa, Italy

Cerebral (or brain) organoids derived from human cells have enormous potential as physiologically relevant downscaled *in vitro* models of the human brain. In fact, these stem cell-derived neural aggregates resemble the three-dimensional (3D) cytoarchitectural arrangement of the brain overcoming not only the unrealistic somatic flatness but also the planar neuritic outgrowth of the two-dimensional (2D) *in vitro* cultures. Despite the growing use of cerebral organoids in scientific research, a more critical evaluation of their reliability and reproducibility in terms of cellular diversity, mature traits, and neuronal dynamics is still required. Specifically, a quantitative framework for generating and investigating these *in vitro* models of the human brain is lacking. To this end, the aim of this review is to inspire new computational and technology driven ideas for methodological improvements and novel applications of brain organoids. After an overview of the organoid generation protocols described in the literature, we review the computational models employed to assess their formation, organization and resource uptake. The experimental approaches currently provided to structurally and functionally characterize brain organoid networks for studying single neuron morphology and their connections at cellular and sub-cellular resolution are also discussed. Well-established techniques based on current/voltage clamp, optogenetics, calcium imaging, and Micro-Electrode Arrays (MEAs) are proposed for monitoring intra- and extra-cellular responses underlying neuronal dynamics and functional connections. Finally, we consider critical aspects of the established procedures and the physiological limitations of these models, suggesting how a complement of engineering tools could improve the current approaches and their applications.

Keywords: brain, organoid, 3D culture, morphology, electrophysiology

OPEN ACCESS

Edited by:
Ioan Opris,
University of Miami, United States

Reviewed by:
Jennie Leach,
University of Maryland, Baltimore County, United States
Kim Drnec,
United States Army Research Laboratory, United States

***Correspondence:**
Arti Ahluwalia
arti.ahluwalia@unipi.it

Specialty section:
This article was submitted to Neural Technology, a section of the journal Frontiers in Neuroscience

Received: *06 November 2018*
Accepted: *12 February 2019*
Published: *05 March 2019*

Citation:
Poli D, Magliaro C and Ahluwalia A (2019) Experimental and Computational Methods for the Study of Cerebral Organoids: A Review. Front. Neurosci. 13:162. doi: 10.3389/fnins.2019.00162

INTRODUCTION

Studies in cellular neuroscience mainly focus on *in vivo* animal models (Marbacher et al., 2018), *ex vivo* brain slices (Brai et al., 2018), and *in vitro* two-dimensional (2D) cultures (Poli et al., 2018). However, these three different experimental conditions have some limitations. Specifically, *in vivo* (animal) models, ranging from worms to non-human primates, cannot infer human cognitive abilities at the cellular level (Premack, 2007) and often fail to translate into human relevant data or clinical trials (Tsilidis et al., 2013). Brain slices, on the other hand, are very sensitive to axotomy

(Humpel, 2015) and show artifacts induced by neuronal death (Dauguet et al., 2007), despite maintaining the native connections among cells. Finally, planar dissociated cultures allow the investigation of basic cellular and circuital mechanisms of neuronal networks but lack the *in vivo* microenvironment and architecture characterized by features such as neuritic outgrowth in all directions (Frega et al., 2014).

To overcome these drawbacks, recent advances in tissue engineering provide novel three-dimensional (3D) cerebral models derived from stem cells. Known as brain or cerebral organoids, these constructs mimic the 3D structure of the brain (Lancaster and Knoblich, 2014; Monzel et al., 2017; Quadrato et al., 2017) thanks to the self-organizing abilities of the stem cells they are derived from. Furthermore, human induced pluripotent stem cell (hiPSC)-derived organoids can be used to explore disease pathogenesis in a patient-oriented perspective, thus representing one of the most promising experimental models for developmental and neurodegenerative disorders (Lee et al., 2017). The scientific advances of this revolutionary technology, as well as its future prospects and limitations in modeling diseases, have been recently reviewed and discussed, exploring how these self-organized neuronal aggregates can mimic not only specific neurological and psychiatric disorders such as autism or schizophrenia (Amin and Paşca, 2018; Chuye et al., 2018; Paşca, 2018; Wang, 2018) but also the neurogenesis of congenital brain abnormalities such as microcephaly caused by the Zika virus infection during early pregnancy (Sutarjono, 2018).

Different methodological approaches, traditionally employed for characterizing brain slices and 3D *in vitro* cultures, have been applied to study brain organoids, and most investigations are geared toward assessing their reliability as novel and more accurate human brain models. In particular, advanced imaging techniques (Lancaster et al., 2013; Di Lullo and Kriegstein, 2017), delipidation protocols (Chung and Deisseroth, 2013) and novel image processing algorithms (Schmuck et al., 2017) have been proposed to observe the 3D structure of single neurons and their morphological connections at cellular and sub-cellular resolution. Well-established techniques based on current/voltage clamp (Li et al., 2017), optogenetics (Klapper et al., 2017), calcium imaging (Storm et al., 2017), and Micro-Electrode Arrays (MEAs) (Monzel et al., 2017) have been performed for monitoring intra- and extra-cellular responses underlying neuronal dynamics and functional or synaptic connections. Finally, computational models have been used to determine oxygen gradients within brain organoids (Berger et al., 2018).

However, despite the growing use of organoid technology in recent years (**Figure 1**), several challenges need to be addressed. In particular, a better understanding of their reproducibility in generating cellular diversity, producing mature traits and developing higher-order brain functions is still required (Quadrato et al., 2017). More in-depth knowledge and prediction of their cellular composition and distribution is also necessary. Crucially, brain organoids are often altered by non-viable centers probably due to limitations in oxygen and nutrient diffusion, thus affecting their physiological relevance and translational potential (Luo et al., 2016; Watanabe et al., 2017; Berger et al., 2018; Ogawa et al., 2018).

Neuroscientists are aware of the urgent need of improving brain organoids in terms of reproducibility and oxygen/nutrient supply as well as of fully characterizing their structural and functional features (i.e., mapping the structural and the functional connectome) for the assessment of model goodness through a quantitative comparison with their *in vivo* counterpart. In this context, we describe the state-of-art of the computational and experimental approaches recently applied to the cerebral organoids. The rationale is to inspire methodological improvements and novel applications of these brain organoids. Specifically, we first overview the organoid generation protocols commonly used in the literature (in "Brain Organoid Generation"). Then, we review the computational models employed to assess organoid formation, organization, and resource uptake (in "Computational Models"). In the sections on Structural Characterization and Integrated Electrophysiological Approaches, the experimental approaches currently provided to characterize the structure and function of cellular networks within brain organoids are discussed, focusing on methods for studying the 3D architectural of single neurons and their morphological and electrophysiological connections at cellular and subcellular resolution. Finally, in the Conclusion, we suggest how the potential of these imaging, computational and electrophysiological tools can be combined with bioprinting, fluidics and biomaterial engineering within an integrated experimental and theoretical framework so as to establish a quantitative, reproducible and accurate *in vitro* model of the human brain for a diverse range of applications.

BRAIN ORGANOID GENERATION

Brain organoids are different from classical 3D cultures of neurons, which are known as neurospheres, neural spheriods or neuro-aggregates. The latter are generated from differentiated neural cells or their progenitors. The cells are usually cultured in non-adherent plates and they cluster together, growing in suspension rather than on the base of the plate. On the other hand, brain organoids originate from (usually embryonic or pluripotent) stem cells which are cultured in conditions that promote differentiation and self-organization such that the cells spontaneously develop into various brain regions resembling the developing human brain. Hence, we can define an organoid as a mini-organ (or organ sub-region) which resembles the essential, albeit immature, structural features of its upscaled counterpart (**Figure 2**). Brain organoids come in different sizes, ranging from 1 to 3 mm in diameter (this includes the 3D matrix, see below). The initial cell number used to generate them varies from paper to paper, but is typically between 2,500 and 10,000 stem cells (Lancaster and Knoblich, 2014; Jo et al., 2016; Monzel et al., 2017; Quadrato et al., 2017) and is a factor which certainly conditions internal nutrient and oxygen gradients.

An established protocol for generating human brain organoids has been described by Lancaster et al. (2013) and Lancaster and Knoblich (2014) and shown in **Figure 3**. Briefly, starting from

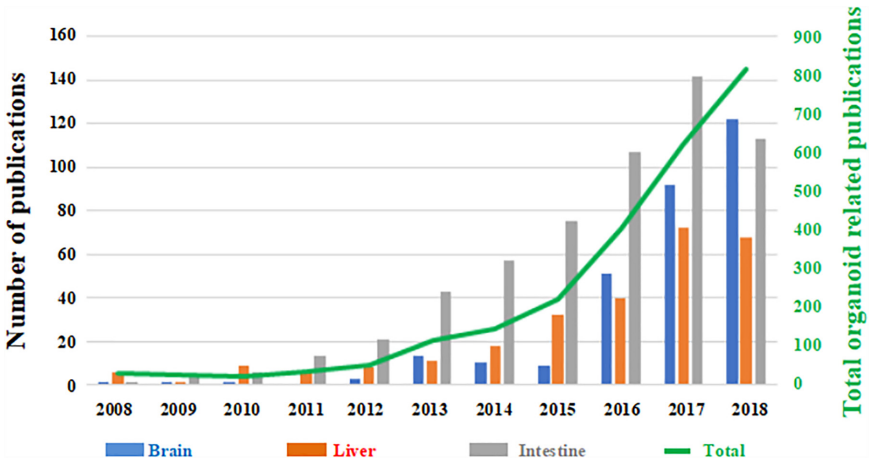

FIGURE 1 | Number of papers published on organoid technology since 2008. The number of papers focused on brain organoids (blue) are shown as a function the total number of published works based on this technology (green trend line, right hand secondary axis). Papers focused on liver (red) and intestinal (gray) organoids are shown for comparison. (Source: PubMed).

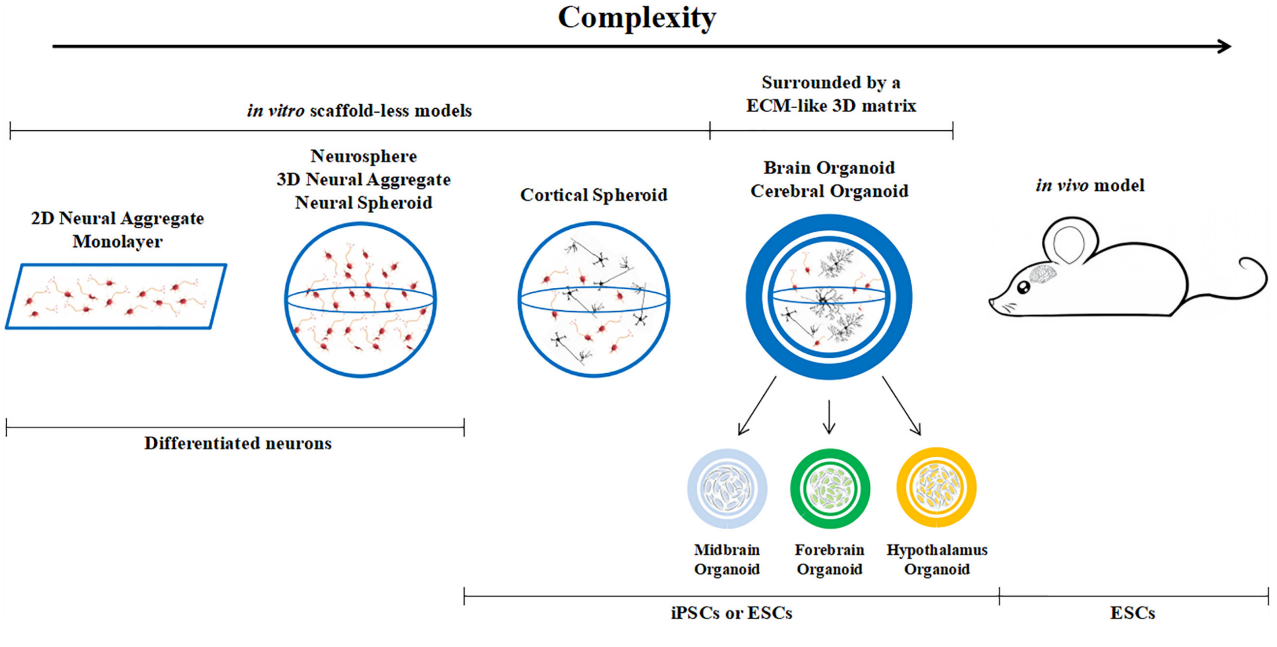

FIGURE 2 | Classification of brain models, from monolayers to *in vivo* animal models.

4500 iPSC, neuroectodermal tissues are generated from embryoid bodies (EBs) through feeding with NIM (commercial Neural Induction Media) and then maintained in droplets supported by a 3D matrix composed of Matrigel, a commercially available jelly-like extracellular matrix secreted by mouse sarcoma cells. At this stage they are fed with another media cocktail for maintenance. These droplets are transferred to a spinner flask in order to enhance nutrient absorption and allow rapid tissue development, forming cerebral organoids in 10 days and defined brain regions in 30 days.

The protocol developed by Lancaster and co-workers paved the way for several other studies. Most of them observed that brain organoids become necrotic in their core at later stages of culture and healthy neurons are found only along the perimeter (Luo et al., 2016; Watanabe et al., 2017; Ogawa et al., 2018). Recently, Quadrato et al. (2017) revised this culturing protocol and facilitated the establishment of mature synapses by extending the periods of cellular growth and development. Specifically, EBs were firstly derived from about 2500 dissociated hiPSCs and subsequently transferred to intermediate induction medium after 5 days in culture. Then, NIM was added and the EBs were embedded in Matrigel and further fed with cerebral differentiation medium (CDM). Finally, brain derived neurotrophic factor was added to the medium after 30 days.

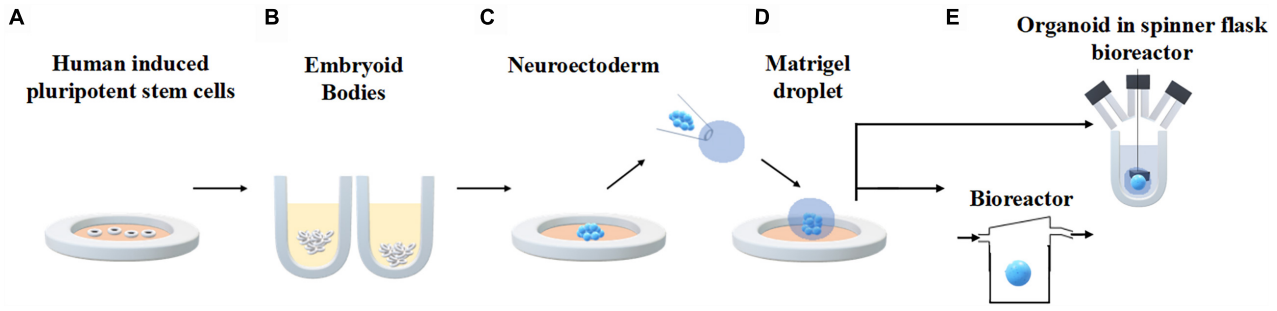

FIGURE 3 | Generation of human brain organoids. Human stem cells are seeded onto plates **(A)** in order to allow embryoid body formation **(B)**. Neuroectoderm is generated after neural induction **(C)**. The cells are embedded in Matrigel droplets **(D)** and transferred to a spinner flask or a fluidic bioreactor **(E)**.

The cerebral organoids obtained by performing these procedures could be cultured for up to 13 months. The expression of the H1F1-α marker demonstrated that brain organoids did not become hypoxic and levels of programmed cell death remain relatively low up to 9 months. In order to further improve the quality of brain organoids, Berger and co-workers focused on organoid culturing systems more than their generation protocols. In particular, by using fluidic devices, they not only observed a reduction of the necrotic core within organoids but also an improvement of neuronal differentiation and cellular vitality (Berger et al., 2018). The authors show that this is due to the increased flow-driven oxygen and nutrient turnover.

Although, a wide variety of chemical patterning factors have been used to drive the neuronal differentiation of specific brain sub-regions (Di Lullo and Kriegstein, 2017) such as hippocampus (Sakaguchi et al., 2015; Qian et al., 2016), midbrain (Jo et al., 2016; Monzel et al., 2017), or cerebellum (Muguruma et al., 2015), most of the literature focuses on multiple, but independent, individual brain region organoids. Using a somewhat different approach, Paşca et al. developed so-called human cortical spheroids from induced pluripotent stem cells (iPSCs) in the absence of a supporting extracellular matrix by plating the cells in non-adherent plates and supplying specific growth and patterning factors. Although, the spheroids lack the multiple brain regions and hence the organ-like quality of Lancaster's protocol, they contain both deep and superficial cortical neurons interspersed with quiescent astrocytes and the authors claim that they remain viable for over a year (Paşca et al., 2015).

Thanks to the possibility of generating different brain regions in a dish, it is reasonable to hypothesize that the next generation of organoids will be represented by more complex *in vitro* models characterized by co-culturing "building blocks" (i.e., different brain regions) describing distinct areas of the human brain (Bagley et al., 2017). This approach would allow the observation of complex interactions such as cell migration, chemiotaxis and axon growth among different developing brain regions and enable the investigation of epilepsy and other neurological diseases. Ideally, region-specific organoids could be functionally connected in a fluidic device such as a connected culture bioreactor system which allows different tissues to communicate through a shared medium (Yin et al., 2016; Ahluwalia, 2017).

However, all of these generation protocols suffer from the so-called "batch syndrome" (Kelava and Lancaster, 2016), meaning that they show significant variability not only among the organoids from different labs or from different patients but also between organoids from the same iPSC source (e.g., karyotype). These limitations make organoids unsuitable for higher-throughput applications requiring homogeneity from well to well, such as drug screening. Besides the intrinsic sensitivity of stem cells to environmental conditions (Di Nardo et al., 2011), one of the most well-established causes of the "batch syndrome" is due to the composition of the 3D matrix (hydrogels such as Matrigel or Geltrex) whose variability is induced by the tumor materials it is derived from as well as its purification process (Kleinman and Martin, 2005). Moreover, slight differences in the thickness of the Matrigel can result in large differences in oxygen, nutrient and growth or neurotropic factor gradients in the organoid, strongly conditioning cell differentiation. Finally, heterogeneous responses over time due to cells being interrogated at different times or at different passages may also contribute to variability.

Matrigel variability could be mitigated, for example, by substituting it with chemically defined homogeneous hydrogels. In particular, synthetic biomaterials with specifically-tailored compositions could be engineered to partially reduce the intrinsic variability in cell composition (Vazin and Schaffer, 2010). This would not only improve the repeatability from batch to batch but also the cellular coating and neuronal plating over recording devices. Bioprinting also offers a technological approach to improve the reproducibility between batches. Controlled pressure and volume droplet generators (Tirella et al., 2014) could be used to modulate and control the thickness of the 3D matrix and to determine the optimum trade-off between diffusion limitations and extracellular matrix cues as well as to control the 3D organization of different cell types (Zhuang et al., 2018). Further engineering strategies could be gainfully applied to modulate the micro-environment for harnessing and controlling stem cell differentiation. Moreover, hydrogel stiffness and physiochemical properties have been

already identified as key players in liver organoid formation and subsequently optimized (Takebe et al., 2013; Mattei et al., 2017). Although, assessed for stem cell technology and liver buds, the approaches can be translated and re-adapted for brain organoids to improve their reproducibility and internal core viability and to allow more control over their maturation and behavior.

COMPUTATIONAL MODELS

Organoid formation involves complex biological phenomena (e.g., stem cell differentiation into mature neurons, cell-cell contact and signaling, chemical diffusion, surface tension, and cell-substrate mechanical interactions), most of which are not well understood or easily observable (Dahl-Jensen and Grapin-Botton, 2017). Since it is well known that stem cells are highly sensitive to mechanical, biochemical and chemical stimuli (Di Nardo et al., 2011), *in silico* models provide a means to study and control single process dynamics, and thereby predict their influence on organoid growth and differentiation, providing guidance for optimizing experimental design. Moreover, in a patient-oriented perspective, computational modeling can be a powerful platform for virtual clinical trials (Karolak et al., 2018).

Unfortunately, little effort has been made in implementing models of organoid growth and differentiation, and even less for brain organoids. In particular, it has been recently demonstrated by Ahluwalia (2017), through oxygen consumption and diffusion modeling, that 3D spheroids or organoids can maintain allometric relationships between basal metabolic rate and construct mass (i.e., Kleiber's Law, widely considered a benchmark of physiological relevance in micro-scaled *in vitro* systems). One year later, using a carefully-judged combination of image processing tools and computational models of oxygen transport and consumption, Berger et al. (2018) estimated the critical oxygen concentration (0.04 mM) necessary for ensuring cell vitality. These studies can be used as a starting point for designing cell culture systems which guarantee the threshold oxygen concentration throughout a 3D volume without exposing the organoid to a high shear stress due to media flow and ensuring that they obey Kleiber's Law (Magliaro et al., 2019).

Using a different approach, in order to simulate the effects of cell proliferation, morphogenesis and tissue expansion occurring during organoid growth, Dahl-Jensen et al. provided a hybrid model between a cellular automata and a Douglas-Gunn diffusion scheme. Quantifying the similarity between the *in silico* and the *in vitro* outcomes, the same group demonstrated that the computational model can simulate the developing morphology of the organoid, suggesting that cell proliferation and a single inhibitory protein is enough to achieve organoid morphogenesis (Dahl-Jensen et al., 2016).

Organoids are a powerful tool for studying organogenesis. In this perspective, the evaluation of how cells move and distribute over time and arrange themselves (or spatio-temporal organization) to resemble the main architectural features of the brain allows the characterization of the mechanisms involved in brain formation such as proliferation, lineage specification and organ homeostasis. To this end, Buske et al. (2012) used computer simulations to evaluate the main structural and functional features of the organoid system as a function of the cell spatio-temporal organization. In particular they studied the possible interplay between stem and mature cells, and analyzed organoid formation in terms of cell proliferation, lineage specification and organ homeostasis (Buske et al., 2012). Comparing the results with those obtained in *in vitro* systems, they demonstrated the high sensitivity of the organoid to changes in its biomechanics, providing a framework for the selection of appropriate biomaterials for supporting organoid formation.

The combination of experimental procedures and computational models as proposed in the studies by Berger, Buske and Dahl-Jens and their respective co-workers offer several advantages for optimizing the design of more physiologically relevant *in vitro* models. Such models are also instrumental for understanding the complex mechanisms underlying organogenesis in a dish and wider collaborations between *in silico* and *in vitro* modelers should be encouraged. Finally, customized versions of the computational and theoretical frameworks established in Ahluwalia (2017) and Magliaro et al. (2019) on allometric scaling, Berger et al. (2018) on oxygen diffusion and consumption and Buske et al. (2012) on membrane biomechanics coupled with considerations on surface energy and work of cohesion, tensegrity mechanics and morphogen gradients (Dahl-Jensen et al., 2016) could be developed to predict, optimize and guide organoid formation and development.

STRUCTURAL CHARACTERIZATION FOR HIGH-FIDELITY MAPPING OF 3D NEURONAL STRUCTURES

Cerebral organoids resemble the main structural features of the human brain recapitulating its 3D cytoarchitectural arrangement. Characterizing the three-dimensional structural organization of the cells as well as neuronal shape, size, complexity and distribution and their physical/morphological cell-cell connections within organoids is important for establishing similarities with the human brain. Quantitative and precise morphometric measures [for instance descriptors of cell size and shape such as dendrite thickness, number of dendrites, fractal number and soma sphericity (Billeci et al., 2013)] are even more crucial considering the unprecedented opportunity given by hiPSCs to provide patient-specific organoids overcoming the typical "one size fits all" experimental approach. The "one size fits all" method evaluates the average response in groups rather than individual ones, thereby neglecting some important factors deriving from the genetic profiles of individuals. Brain organoids from patient-derived hiPSCs could be used for predicting alterations in dendritic and axonal arbor associated with neuro-pathological conditions (Lancaster et al., 2013; Lee et al., 2017; Li et al., 2017; Monzel et al., 2017; Quadrato et al., 2017; Zhuang et al., 2018). Moreover, assessing the ability of these organoids to model the intricacies of the human brain and its neurogenesis can be useful for inferring how uniquely human features are managed at the cellular level (Lancaster and Knoblich, 2014;

Di Lullo and Kriegstein, 2017; Lee et al., 2017; Quadrato et al., 2017). In this regard, a carefully-judged integration of advanced imaging techniques and image processing algorithms could enable high-fidelity mapping of the global neuronal organization within organoids and their morphological connections at cellular and sub-cellular scales.

Neuroanatomical features (e.g., neuron-glia connections, different cell types, and structural organization within the 3D construct) are generally extracted using optical methods such as confocal, multi-photon and light sheet microscopy, suitable for imaging within samples at cellular (sub-micrometric) resolution (Ntziachristos, 2010). Conversely, electron microscopy is commonly performed on thinner samples in order to detect the presence of structurally-defined synapses at a higher resolutions (Kelava and Lancaster, 2016; Li et al., 2017; Quadrato et al., 2017). The traditional approach for sample preparation is based on cryosections ranging from 14 to 30 μm thickness following fixation in 4% paraformaldehyde. Thicker samples may be used but are limited by the depth of penetration of light owing to optical scattering from lipids, which are present in significant amounts in the brain. Since almost all the optical imaging techniques quoted use fluorescence, the acquisition procedures are generally accompanied by fluorescent immunolabeling. Green Fluorescent Protein (GFP), as well as other biological fluorophores with different emission wavelengths can easily be integrated as genetic tags using CRISPR/Cas9 technology and are useful as markers of protein expression in transfected cells. The rationale is to reveal the presence of proteins characterizing specific cell populations (also known as molecular phenotyping) and to assess the differentiation of stem cells in mature neurons, astrocytes and oligodendrocites through the characteristic fluorescence signals of the tags (Quadrato et al., 2017; Matsui et al., 2018).

Organoid diameters range from 1 to 3 mm, as represented in **Figure 4**. However, as shown in the figure, none of the techniques mentioned have both the in-plane resolution and the depth of penetration necessary to reconstruct a high-fidelity structural connectivity map of cerebral organoids and quantitatively extract morphometrics classifying the different cell types involved (Lancaster et al., 2013; Monzel et al., 2017; Quadrato et al., 2017). Optical scattering occurs because the refractive index of lipid-rich brain tissue samples differ from that of the medium. In order to increase the depth of penetration, different optical clearing protocols have been developed in the last decade (Richardson and Lichtman, 2015). Basically tissue clearing involves exchanging the water in the sample with organic solvents, or aqueous solutions with the same refractive index as membrane lipids, such that the sample become essentially transparent. Therefore, these experimental procedures increase the depth of penetration of light and extend the depth range of optical microscopes. Clearing techniques such as CLARITY further allow permeability to both photons and macromolecules, providing sample transparency and molecular phenotyping compatibility (Chung and Deisseroth, 2013; Magliaro et al., 2016).

Although, they were originally developed for whole animal perfusion, clearing protocols can be adapted for use on vessel-free, unperfusable samples, such as brain organoids, obtaining unprecedented representations of their 3D cellular structure. For instance, Renner et al. identified internal connections between the cortical areas which appear isolated in 2D non-clarified sections using

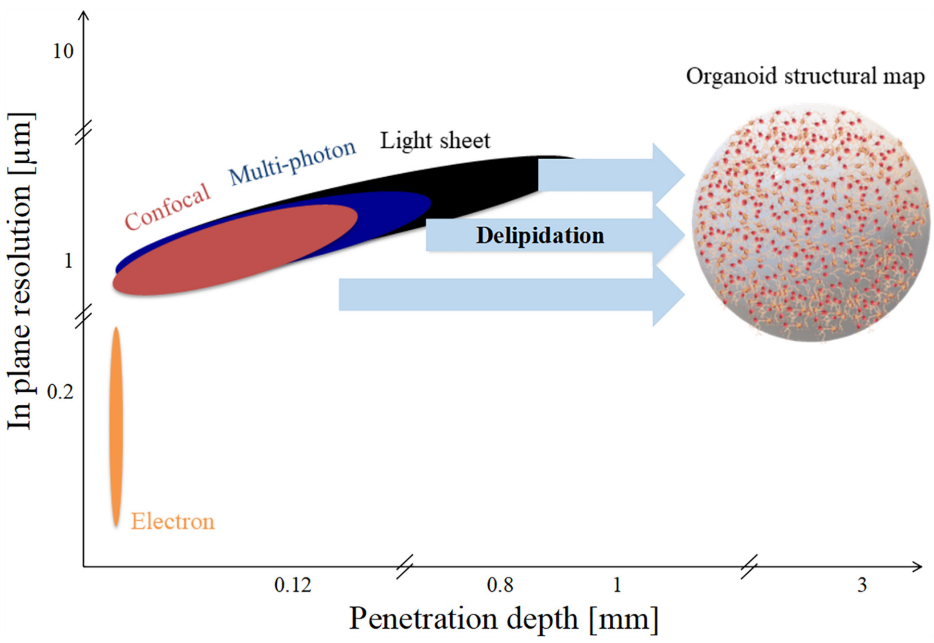

FIGURE 4 | Spatial limits of modern imaging techniques applied to brain organoids. Penetration depth and in-plane resolution of specific techniques such as confocal, multi-photon, and light sheet microscopy. Delipidation increases light penetration depth but not in-plane resolution.

the SWITCH clearing method and subsequent in-depth confocal imaging (Renner et al., 2017). However, clearing methodologies applied to organoid technology need further optimization: in fact, a rigorous workflow for establishing the best clearing practice as well as the optimization of the immunolabeling procedure for thick samples in terms of antibody concentration and staining times are necessary to avoid much of the trial and error usually affecting these methodologies. In this regard, Magliaro and co-workers demonstrated that an optimization of tissue transparency and loss of proteins due to the clearing process itself improves both signal-to-noise and contrast-to-noise ratio during image acquisition (Magliaro et al., 2016).

Despite the progress of imaging methods, the evaluation of the cellular and architectural similarities between human brain organoids and human brains (or *in vivo* animal models) are often qualitative and performed by visual inspection (Kelava and Lancaster, 2016). To the best of our knowledge, a quantitative assessment of the whole organoid micro-structure providing a detailed cell census, characterizing cell morphology and identifying cell-cell synaptic connections has not yet been performed. In particular, image processing methods are very rarely used to extract morphometric features, probably due to the lack of powerful computational algorithms and software for the automatic or semi-automatic segmentation of the neural structures (Meijering, 2010). **Table 1** reports some of the attempts so far to integrate microscopy techniques with the image processing tools or software usually used for analyzing brain organoids. Since these individual procedures are not enough to characterize the whole organoid structure, it is reasonable to assume that a rigorous work-flow combining experimental protocols and computational tools will be necessary to acquire cell morphometric parameters in the future (**Figure 5**). In particular, integration of optimized tissue clearing protocols and novel immunolabeling procedures will allow not only better-contrasted images but also efficient

TABLE 1 | Structural characterization of brain organoids using quantitative image processing: The state-of-art.

	Methods	Scope	Application and results	Reference
Sub-cellular level	Electron microscopy	Identification of sub-cellular structures	An 8 month old organoid was fixed, cut in 100 μm thick slices and acquired using backscatter electron imaging. The images were 3D rendered and manually segmented using the **VAST** lite tool, showing more axons than dendrites, appearing to preferentially run to the organoid surface.	Quadrato et al., 2017
	Confocal and multi-photon microscopy	Evaluation on cell maturation and morphology	Quantification and localization of direct contacts between the pre- and post-synaptic markers using **ImageJ.** A 3D surface reconstruction of confocal z-stacks performed with **Imaris (Bitplane)** showed an asymmetric distribution of dopaminergic neurons, unique features of the human mid-brain.	Monzel et al., 2017
Micro and macro-anatomical level			Organoids acquired with a confocal microscope were analyzed using **Fiji** to identify lobules staining positive for forebrain, midbrain and cerebellar/hindbrain markers and the total number of lobules were visible by DAPI staining.	Lancaster et al., 2013
			Integration of confocal microscopy analysis using **Matlab** and computational modeling for the identification of the critical oxygen concentration for cell vitality within organoids.	Berger et al., 2018
			Organoid sections imaged with confocal microscopy show neuronal layers and the formation of gaps between the organoid's interior that resemble the ventricular spaces, evaluated using **Nikon image processing software**	Yakoub and Sadek, 2018
	Light-sheet microscopy	Evaluation of topological organization of the cells	Quantification of the surface area, overall volume and fold density in control and PTEN-mutant Hoechst-stained organoids using the **Canny Edge Detection ImageJ plugin.**	Li et al., 2017

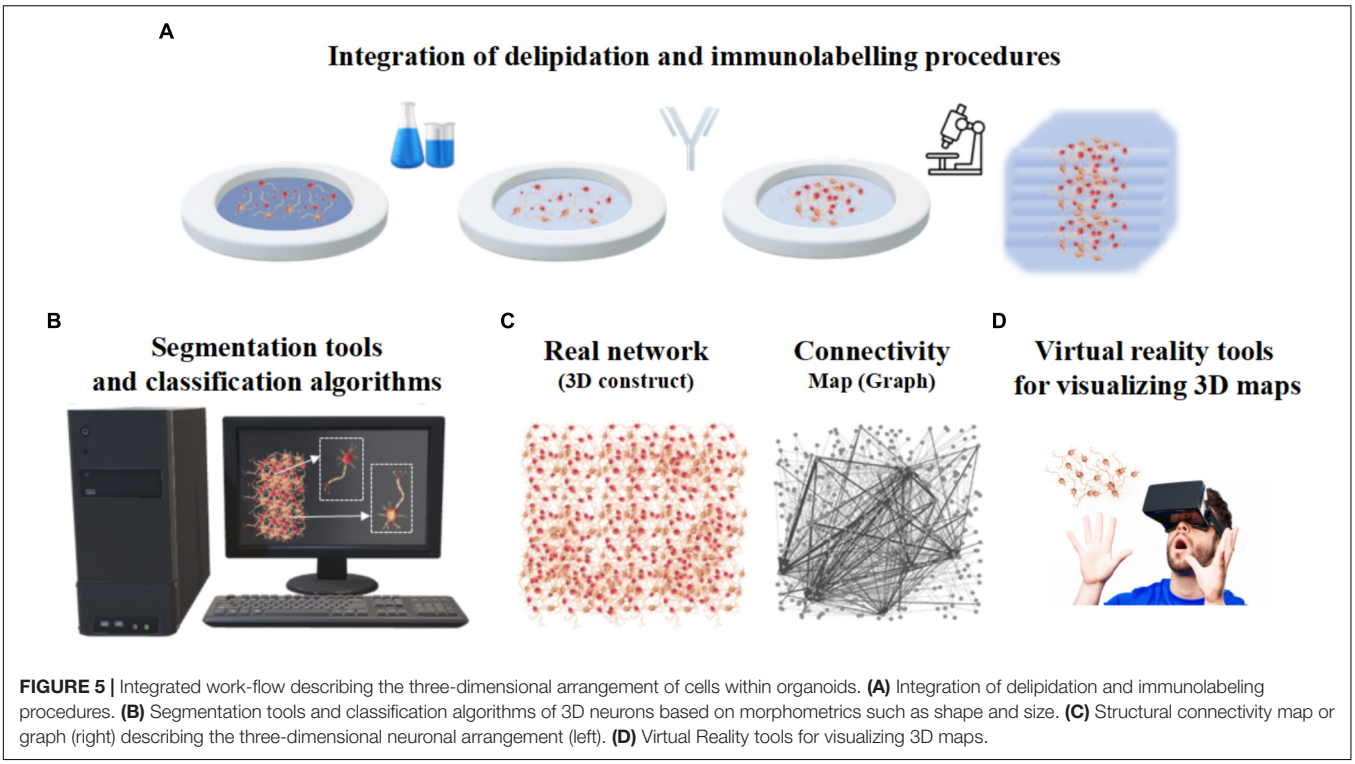

FIGURE 5 | Integrated work-flow describing the three-dimensional arrangement of cells within organoids. **(A)** Integration of delipidation and immunolabeling procedures. **(B)** Segmentation tools and classification algorithms of 3D neurons based on morphometrics such as shape and size. **(C)** Structural connectivity map or graph (right) describing the three-dimensional neuronal arrangement (left). **(D)** Virtual Reality tools for visualizing 3D maps.

and rapid thick sample staining (Magliaro et al., 2016; **Figure 5A**). Commercial Neurolucida (Glaser and Glaser, 1990) and freely available segmentation tools (Callara et al., 2018) may be used to extract morphometrics and quantitative shape-based neuron classification (**Figure 5B**), as well as high-fidelity structural maps (**Figure 5C**). The structural information, combined with the functional characteristics (detailed in the next section), are essential for digitalizing a computational graph of brain organoids. In the graph the nodes are the neurons and the links are the morphological or functional connections. Finally, thanks to virtual reality methods already used in neuroscience (Riddle et al., 2017; Usher et al., 2018), the visualization of 3D maps will be helpful for navigating through and interacting with the exact wiring of the neural circuits. This will be the first step towards elucidating organoid structural and functional organization (**Figure 5D**).

BRAIN ORGANOID FUNCTIONS PROVIDED BY INTEGRATED ELECTROPHYSIOLOGICAL APPROACHES

Human brain organoids can be also functionally characterized by applying specific experimental approaches able to discriminate different signal sources. The current/voltage-clamp (Li et al., 2017) and optogenetics (Klapper et al., 2017) can be used for monitoring individual cell activities, or calcium imaging for small cellular aggregations (Storm et al., 2017). Functional probing at the whole network scale can be performed in a non-invasive manner by coupling brain organoids to micro-electrode arrays (MEAs) (Monzel et al., 2017). The methodological aspects and recent applications of these approaches on brain organoids are summarized in **Table 2** and discussed in this section.

Briefly, current/voltage-clamp (**Figure 6A**) is commonly used to investigate individual cellular activity and provide mechanistic information on ion channels (Cummins et al., 2009). This technique, applied to brain organoids, allows the detection of emergent active networks producing complex synaptic events associated with postsynaptic neuronal spike firing (Paşca et al., 2015). Changes in resting membrane potentials (Hartfield et al., 2014), functionally active midbrain dopaminergic neurons (Jo et al., 2016), and cell maturation (Di Lullo and Kriegstein, 2017) also have been observed. These functional aspects, as well as the excitatory/inhibitory postsynaptic currents, the neuromelanin-like granules structurally similar to those isolated from human *substantia nigra* tissues and the inactivating inward/outward currents, support the reliability of cerebral organoids for modeling human brain (Paşca et al., 2015; Jo et al., 2016; Li et al., 2017). Furthermore, recent whole-cell voltage clamp recordings of individual neurons from air-liquid interface cerebral organoids show improved long-term survival of the cells distributed in three-dimensional space (Giandomenico et al., 2018).

As shown in Rajasethupathy et al. (2016), regional targeting capability without neuron-type specificity has been additionally provided by applying local electrical stimuli as well as rapidly changing magnetic fields to organoids. Conversely, optogenetic approaches (**Figure 6B**) based on light activation

TABLE 2 | Electrophysiological approaches adapted to functionally characterize brain organoids: The state-of-art.

	Methods	Scope	Application and results	Reference
Individual cells	Current/Voltage clamp	Membrane potential and neuronal firing. Mechanistic information on ion channels.	Changes in resting membrane potentials. Cell maturation. Emergent active network (Single spikes, Burst events). Excitatory postsynaptic currents (EPSCs) Dopaminergic (mDA) neurons functionally mature. Neural development and diseases investigation. Improved long-term neuronal survival.	Hartfield et al., 2014; Paşca et al., 2015; Li et al., 2017; Di Lullo and Kriegstein, 2017; Giandomenico et al., 2018
	Optogenetics	Excitation or inhibition of the neuronal activity at high temporal and spatial resolution. Cellular polarization through light activation of specific DNA-encoded light-sensitive ion channels (i.e., optogenes) or inhibitory pumps. Cell therapy.	Modulation in real time of electrophysiological and neurochemical properties of mesencephalic dopaminergic (mesDA) neurons. Cell-type specificity, Optogene expression triggered. Broad diversity of cellular responses.	Steinbeck et al., 2015; Rajasethupathy et al., 2016; Klapper et al., 2017; Quadrato et al., 2017
Small cellular aggregations	Calcium imaging	Characterization of the Ca^{2+} status and changes in fluorescence induced by the binding of the Ca^{2+} ions with genetically encoded calcium indicators or small molecules based on the aminopolyearbowlie acid BAPTA	Homogeneous fluorescence induced by calcium detection reagents such as Fluo-4 direct. Emergence of spontaneous and single cell tracings of calcium induced by glutamate and TTX application.	Lancaster et al., 2013
Network scale	Micro-electrode array (MEA)	Characterization of the extracellular electrophysiology. Acquisition of long-term spontaneous recordings and evoked responses induced by chemical or electrical stimulation at 60 or 120 up to 4,000 or 10,000 electrodes	Mono- and biphasic spikes closely in time. Firing frequency reduction induced by chemical perturbation (quinpirole treatment) on midbrain dopaminergic neurons (mDNs) Neuronal dynamics from spontaneous activity.	Monzel et al., 2017; Giandomenico et al., 2018

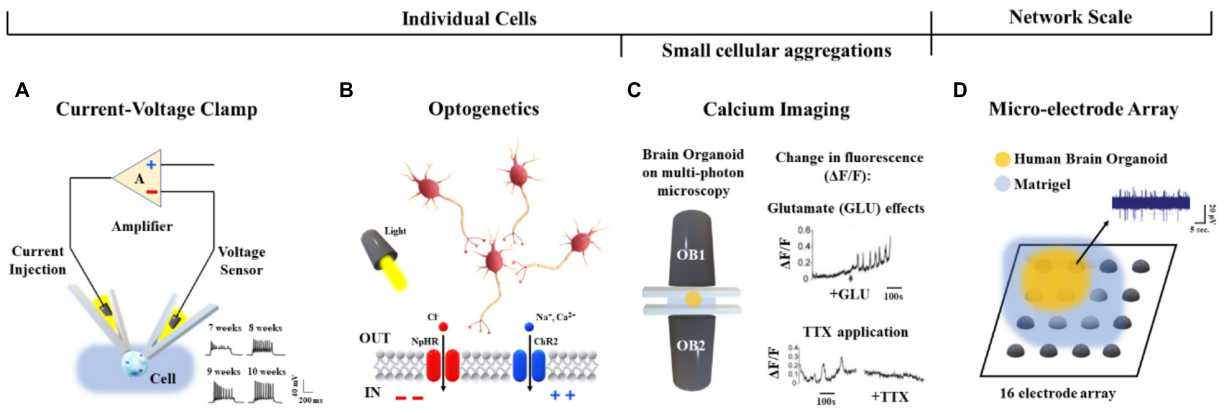

FIGURE 6 | Functional characterization approaches applied to human brain organoids. **(A)** Voltage/current clamp technique and representative recordings (bottom, right) from hiPSC-derived organoids after 7, 8, 9, and 10 weeks *in vitro* (Hartfield et al., 2014). **(B)** Cellular polarization changes can be achieved in a cell-type-specific manner via optogenetics by means of light activation of specific DNA-encoded light-sensitive ion channels (e.g., the channel rhodopsin ChR2 colored in blue) or inhibitory pumps (e.g., the halorhodopsin NpHR colored in red) (Rajasethupathy et al., 2016). **(C)** Calcium imaging based on multi-photon microscopy (left) and detected changes in fluorescence (ΔF/F) induced by Glutamate (top, right) and TTX (bottom, right) (Lancaster et al., 2013). **(D)** Representative midbrain organoid coupled to a 16-electrode array in a 48-well tissue culture plate and spontaneous activity from one active recording site.

of inhibitory pumps or specific DNA-encoded light-sensitive ion channels (i.e., optogenes; Deisseroth and Schnitzer, 2013) have been adapted to human brain organoids in order to target specific cell-types and establish a consolidated methodology for investigating cellular excitability at high temporal and spatial resolution (Klapper et al., 2017). In particular, the cellular polarization changes induced by the light stimulation of photoreceptor-like cells were shown to excite and inhibit neuronal activity within brain organoids, offering an opportunity for studying aspects of the regional complexity, cellular diversity and circuit functionality of the brain (Quadrato et al., 2017). Furthermore, light-modulated electrophysiological and neurochemical properties of mesencephalic dopaminergic neurons within human embryonic stem cell-derived organoids

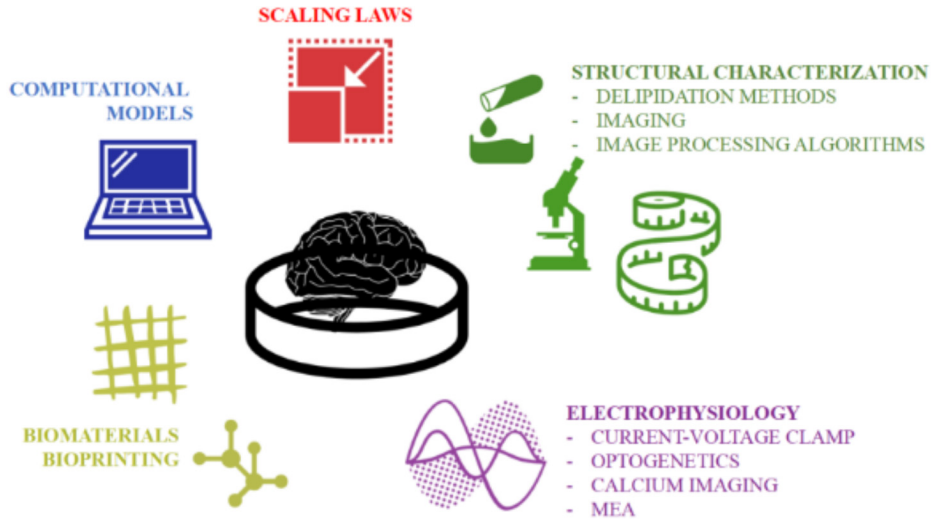

FIGURE 7 | The multidisciplinary tools toward establishing a quantitative and accurate *in vitro* model of the human brain. An integration of computational and experimental approaches would allow a rigorous structural and functional characterization of the neuronal networks within organoids and their validation as physiologically relevant downscaled *in vitro* models of the human brain.

also provide an important contribution in cell therapy driving real-time recovery from lesion-induced Parkinsonian motor deficits (Steinbeck et al., 2015).

Current/voltage-clamp and optogenetic methods can be used to investigate the neuronal dynamics involved at the single cell level. In order to functionally characterize neural aggregates, Calcium (Ca^{2+}) imaging has been applied to the human brain organoids (**Figure 6C**). Studies based on confocal or multi-photon microscopy (Grienberger and Konnerth, 2012) showed fluorescence changes induced by the binding of Ca^{2+} ions with genetically encoded calcium indicators or small molecules based on the aminopolycarboxylic acid BAPTA (Romoser et al., 1997). Calcium imaging based methods adapted to live human brain organoids were also reported by Lancaster et al. (2013).

Although, calcium imaging allows functional characterization of single neurons and small aggregates, this approach does not provide a more complex analysis of the dynamics involved at the whole network scale. Technologies such as MEAs may be used to acquire the electrophysiology from multiple recording sites, as well as to record cell responses evoked by chemical (Pancrazio et al., 2003) or electrical (Wagenaar et al., 2004) perturbations. In particular, MEAs simultaneously monitor long-term spontaneous recordings and responses induced by stimulation protocols using from 60 or 120 (Poli et al., 2018) up to 4,000 or 10,000 electrodes (Berdondini et al., 2009). Therefore, this technology allows high control of the system, supporting a direct reconstruction of the underlying functions and dynamics at the network scale (Poli et al., 2017). To the best of our knowledge, only a few reports describing the functional connectivity of brain organoids coupled to planar MEAs have been published. For example, Monzel et al. (2017) as well as Giandomenico et al. (2018) recently derived human midbrain organoids and plated them over an integrated MEA system for recording (**Table 2** and **Figure 6D**). In the future, cerebral organoids could be also coupled to three-dimensional MEAs (Musick et al., 2009; Yang et al., 2016) which better conform to their shape - for monitoring spontaneous or evoked neuronal signals from multiple layers.

Previous studies focusing on complex networks at the whole-brain scale of human neuroimaging (Bullmore and Sporns, 2009) and at a cellular scale in animal models (Maccione et al., 2012) suggest a strong interplay between the synaptic connections and neuronal morphology and the underlying electrophysiological dynamics. Therefore, a multi-disciplinary approach integrating these electrophysiological methods with morphological architectures obtained from structural characterization could be used to generate more realistic and refined functional networks coherent with and possibly superposed on the network structure (Ullo et al., 2014).

CONCLUSION

The development of stem cell-based organoids is one of the most fascinating and promising techniques for providing a physiologically relevant downscaled *in vitro* model of the human brain. However, since this technology is relatively young (Lancaster et al., 2013), the generation protocols and characterization procedures still need refinement. Firstly, the intrinsic stochasticity and sensitivity of the stem cells to their microenvironment contribute to the heterogeneity of organoids (i.e., the "batch-syndrome"). In addition the variability of the hydrogel matrix (i.e., Matrigel or Geltrex), a necessary feature of current brain organoid generation protocols, doubtless influences their reproducibility. Second, brain organoids (particularly those generated from $\geq$ 4,000 stem cells) often suffer from oxygen

and nutrient deprivation due to transport limitations (Berger et al., 2018). As a result, they are often reported to possess necrotic cores which likely affect not only their morphology but also their functional behavior. Therefore, a new reproducible and standardized production pipeline -preferably supported by computational and characterization tools- is deemed necessary to maintain self-organizing complexity and cell vitality. However, at present, bespoke computational tools supporting biologists in optimizing organoid generation and characterizing their structure and functions are still lacking. Efforts should be made to develop novel computational models and experimental procedures for better investigating the network dynamics as well as more complex cell-cell connections (e.g., synapses) and cell-microenvironment interactions (e.g., hypoxia). In this direction, we suggest an *ad hoc* work-flow overcoming the aforementioned limitations by combining the functional methodologies and imaging techniques illustrated in **Figure 7** for better assessing the ability of cerebral organoids to model specific pathological and developmental processes in the human brain. In order to support the realization of this integrated approach, we have described and discussed the well-established procedures used for generating organoids, as well as the current computational and experimental techniques used for simulating and measuring their structural and functional organization as they differentiate and mature. We hope that this review inspires new computational and technology driven ideas for methodological improvements and novel applications of brain organoids.

AUTHOR CONTRIBUTIONS

All authors contributed to the preparation and editing of the manuscript.

ACKNOWLEDGMENTS

CM was grateful to Fondazione Veronesi for her Post-Doctoral Fellowship 2018.

REFERENCES

Ahluwalia, A. (2017). Allometric scaling in-vitro. *Sci. Rep.* 7:42113. doi: 10.1038/srep42113

Amin, N. D., and Pașca, S. P. (2018). Building models of brain disorders with three-dimensional organoids. *Neuron* 100, 389–405. doi: 10.1016/j.neuron.2018.10.007

Bagley, J. A., Reumann, D., Bian, S., Lévi-Strauss, J., and Knoblich, J. A. (2017). Fused cerebral organoids model interactions between brain regions. *Nat. Methods* 14, 743–751. doi: 10.1038/nmeth.4304

Berdondini, L., Imfeld, K., Maccione, A., Tedesco, M., Neukom, S., Koudelka-Hep, M., et al. (2009). Active pixel sensor array for high spatio-temporal resolution electrophysiological recordings from single cell to large scale neuronal networks. *Lab Chip* 9, 2644–2651. doi: 10.1039/b907394a

Berger, E., Magliaro, C., Paczia, N., Monzel, A. S., Antony, P., Linster, C. L., et al. (2018). Millifluidic culture improves human midbrain organoid vitality and differentiation. *Lab Chip* 18, 3172–3183. doi: 10.1039/c8lc00206a

Billeci, L., Magliaro, C., Pioggia, G., and Ahluwalia, A. (2013). NEuronMOrphological analysis tool: open-source software for quantitative morphometrics. *Front. Neuroinformatics* 7:2. doi: 10.3389/fninf.2013.00002

Brai, E., Cogoni, A., and Greenfield, S. A. (2018). An Alternative approach to study primary events in neurodegeneration using ex vivo rat brain slices. *J. Vis. Exp.* 134:e57507. doi: 10.3791/57507

Bullmore, E., and Sporns, O. (2009). Complex brain networks: graph theoretical analysis of structural and functional systems. *Nat. Rev. Neurosci.* 10, 186–198. doi: 10.1038/nrn2575

Buske, P., Przybilla, J., Loeffler, M., Sachs, N., Sato, T., Clevers, H., et al. (2012). On the biomechanics of stem cell niche formation in the gut–modelling growing organoids. *FEBS J.* 279, 3475–3487. doi: 10.1111/j.1742-4658.2012.08646.x

Callara, A., Magliaro, C., Ahluwalia, A., and Vanello, N. (2018). Smart Region-Growing: a novel algorithm for the segmentation of 3D clarified confocal image stacks. *bioRxiv* [Preprint]. doi: 10.1101/287029

Chung, K., and Deisseroth, K. (2013). CLARITY for mapping the nervous system. *Nat. Methods* 10, 508–513. doi: 10.1038/nmeth.2481

Chuye, L. B., Dimitri, A., Desai, A., Handelmann, C., Bae, Y., Johari, P., et al. (2018). "Brain organoids: expanding our understanding of human development and disease bt - human neural stem cells: from generation to differentiation and application," in, ed. L. Buzanska (Cham: Springer International Publishing), 183–206 doi: 10.1007/978-3-319-93485-3_8

Cummins, T. R., Rush, A. M., Estacion, M., Dib-Hajj, S. D., and Waxman, S. G. (2009). Voltage-clamp and current-clamp recordings from mammalian DRG neurons. *Nat. Protoc.* 4, 1103–1112. doi: 10.1038/nprot.2009.91

Dahl-Jensen, S., and Grapin-Botton, A. (2017). The physics of organoids: a biophysical approach to understanding organogenesis. *Development* 144, 946–951. doi: 10.1242/dev.143693

Dahl-Jensen, S. B., Figueiredo-Larsen, M., Grapin-Botton, A., and Sneppen, K. (2016). Short-range growth inhibitory signals from the epithelium can drive non-stereotypic branching in the pancreas. *Phys. Biol.* 13:16007. doi: 10.1088/1478-3975/13/1/016007

Dauguet, J., Delzescaux, T., Condé, F., Mangin, J.-F., Ayache, N., Hantraye, P., et al. (2007). Three-dimensional reconstruction of stained histological slices and 3D non-linear registration with in-vivo MRI for whole baboon brain. *J. Neurosci. Methods* 164, 191–204. doi: 10.1016/j.jneumeth.2007.04.017

Deisseroth, K., and Schnitzer, M. J. (2013). Engineering approaches to illuminating brain structure and dynamics. *Neuron* 80, 568–577. doi: 10.1016/j.neuron.2013.10.032

Di Lullo, E., and Kriegstein, A. R. (2017). The use of brain organoids to investigate neural development and disease. *Nat. Rev. Neurosci.* 18, 573–584. doi: 10.1038/nrn.2017.107

Di Nardo, P., Minieri, M., and Ahluwalia, A. (2011). "Engineering the stem cell niche and the differentiative micro-and macroenvironment: technologies and tools for applying biochemical, physical and structural stimuli and their effects on stem cells," in *Stem Cell Engineering*, eds G. M. Artmann, et al. (Berlin: Springer), 41–59. doi: 10.1007/978-3-642-11865-4_2

Frega, M., Tedesco, M., Massobrio, P., Pesce, M., and Martinoia, S. (2014). Network dynamics of 3D engineered neuronal cultures: a new experimental model for in-vitro electrophysiology. *Sci. Rep.* 4:5489. doi: 10.1038/srep05489

Giandomenico, S. L., Mierau, S. B., Gibbons, G. M., Wenger, L. M. D., Masullo, L., Sit, T., et al. (2018). Cerebral organoids at the air-liquid interface generate diverse nerve tracts with functional output. *bioRxiv* [Preprint]. doi: 10.1101/353151

Glaser, J. R., and Glaser, E. M. (1990). Neuron imaging with Neurolucida—a PC-based system for image combining microscopy. *Comput. Med. Imaging Graph.* 14, 307–317. doi: 10.1016/0895-6111(90)90105-K

Grienberger, C., and Konnerth, A. (2012). Imaging calcium in neurons. *Neuron* 73, 862–885. doi: 10.1016/j.neuron.2012.02.011

Hartfield, E. M., Yamasaki-Mann, M., Ribeiro Fernandes, H. J., Vowles, J., James, W. S., Cowley, S. A., et al. (2014). Physiological characterisation of human iPS-derived dopaminergic neurons. *PLoS One* 9:e0087388. doi: 10.1371/journal.pone.0087388

Humpel, C. (2015). Organotypic brain slice cultures: a review. *Neuroscience* 305, 86–98. doi: 10.1016/j.neuroscience.2015.07.086

Jo, J., Xiao, Y., Sun, A. X., Cukuroglu, E., Tran, H.-D., Göke, J., et al. (2016). Midbrain-like organoids from human pluripotent stem cells contain functional dopaminergic and neuromelanin-producing neurons. *Cell Stem Cell* 19, 248–257. doi: 10.1016/j.stem.2016.07.005

Karolak, A., Markov, D. A., McCawley, L. J., and Rejniak, K. A. (2018). Towards personalized computational oncology: from spatial models of tumour spheroids, to organoids, to tissues. *J. R. Soc. Interface* 15:20170703. doi: 10.1098/rsif.2017.0703

Kelava, I., and Lancaster, M. A. (2016). Dishing out mini-brains: current progress and future prospects in brain organoid research. *Dev. Biol.* 420, 199–209. doi: 10.1016/j.ydbio.2016.06.037

Klapper, S. D., Sauter, E. J., Swiersy, A., Hyman, M. A. E., Bamann, C., Bamberg, E., et al. (2017). On-demand optogenetic activation of human stem-cell-derived neurons. *Sci. Rep.* 7:14450. doi: 10.1038/s41598-017-14827-6

Kleinman, H. K., and Martin, G. R. (2005). Matrigel: basement membrane matrix with biological activity. *Semin. Cancer Biol.* 15, 378–386. doi: 10.1016/j.semcancer.2005.05.004

Lancaster, M. A., and Knoblich, J. A. (2014). Organogenesis in a dish: modeling development and disease using organoid technologies. *Science* 345:1247125. doi: 10.1126/science.1247125

Lancaster, M. A., Renner, M., Martin, C.-A., Wenzel, D., Bicknell, L. S., Hurles, M. E., et al. (2013). Cerebral organoids model human brain development and microcephaly. *Nature* 501, 373–379. doi: 10.1038/nature12517

Lee, C.-T., Bendriem, R. M., Wu, W. W., and Shen, R.-F. (2017). 3D brain Organoids derived from pluripotent stem cells: promising experimental models for brain development and neurodegenerative disorders. *J. Biomed. Sci.* 24:59. doi: 10.1186/s12929-017-0362-8

Li, R., Sun, L., Fang, A., Li, P., Wu, Q., and Wang, X. (2017). Recapitulating cortical development with organoid culture in vitro and modeling abnormal spindle-like (ASPM related primary) microcephaly disease. *Protein Cell* 8, 823–833. doi: 10.1007/s13238-017-0479-2

Luo, C., Lancaster, M. A., Castanon, R., Nery, J. R., Knoblich, J. A., and Ecker, J. R. (2016). Cerebral organoids recapitulate epigenomic signatures of the human fetal brain. *Cell Rep.* 17, 3369–3384. doi: 10.1016/j.celrep.2016.12.001

Maccione, A., Garofalo, M., Nieus, T., Tedesco, M., Berdondini, L., and Martinoia, S. (2012). Multiscale functional connectivity estimation on low-density neuronal cultures recorded by high-density CMOS micro electrode arrays. *J. Neurosci. Methods* 207, 161–171. doi: 10.1016/j.jneumeth.2012.04.002

Magliaro, C., Callara, A. L., Mattei, G., Morcinelli, M., Viaggi, C., Vaglini, F., et al. (2016). Clarifying clarity: quantitative optimization of the diffusion based delipidation protocol for genetically labeled tissue. *Front. Neurosci.* 10:179. doi: 10.3389/fnins.2016.00179

Magliaro, C., Rinaldo, A., and Ahluwalia, A. (2019). Allometric scaling of physiologically-relevant organoids. *bioRxiv* [Preprint]. doi: 10.1101/559682

Marbacher, S., Grüter, B., Schöpf, S., Croci, D., Nevzati, E., D'Alonzo, D., et al. (2018). Systematic review of in vivo animal models of subarachnoid hemorrhage: species, standard parameters, and outcomes. *Transl. Stroke Res.* doi: 10.1007/s12975-018-0657-4 [Epub ahead of print].

Matsui, T. K., Matsubayashi, M., Sakaguchi, Y. M., Hayashi, R. K., Zheng, C., Sugie, K., et al. (2018). Six-month cultured cerebral organoids from human ES cells contain matured neural cells. *Neurosci. Lett.* 670, 75–82. doi: 10.1016/j.neulet.2018.01.040

Mattei, G., Magliaro, C., Giusti, S., Ramachandran, S. D., Heinz, S., Braspenning, J., et al. (2017). On the adhesion-cohesion balance and oxygen consumption characteristics of liver organoids. *PLoS One* 12:e0173206. doi: 10.1371/journal.pone.0173206

Meijering, E. (2010). Neuron tracing in perspective. *Cytometry Part A* 77, 693–704. doi: 10.1002/cyto.a.20895

Monzel, A. S., Smits, L. M., Hemmer, K., Hachi, S., Moreno, E. L., van Wuellen, T., et al. (2017). Derivation of human midbrain-specific organoids from neuroepithelial stem cells. *Stem Cell Rep.* 8, 1144–1154. doi: 10.1016/j.stemcr.2017.03.010

Muguruma, K., Nishiyama, A., Kawakami, H., Hashimoto, K., and Sasai, Y. (2015). Self-Organization of polarized cerebellar tissue in 3D culture of human pluripotent stem cells. *Cell Rep.* 10, 537–550. doi: 10.1016/j.celrep.2014.12.051

Musick, K., Khatami, D., and Wheeler, B. C. (2009). Three-dimensional micro-electrode array for recording dissociated neuronal cultures. *Lab Chip* 9, 2036–2042. doi: 10.1039/b820596e

Ntziachristos, V. (2010). Going deeper than microscopy: the optical imaging frontier in biology. *Nat. Methods* 7, 603–614. doi: 10.1038/nmeth.1483

Ogawa, J., Pao, G. M., Shokhirev, M. N., and Verma, I. M. (2018). Glioblastoma model using human cerebral organoids. *Cell Rep.* 23, 1220–1229. doi: 10.1016/j.celrep.2018.03.105

Pancrazio, J. J., Gray, S. A., Shubin, Y. S., Kulagina, N., Cuttino, D. S., Shaffer, K. M., et al. (2003). A portable microelectrode array recording system incorporating cultured neuronal networks for neurotoxin detection. *Biosens. Bioelectron.* 18, 1339–1347. doi: 10.1016/S0956-5663(03)00092-7

Paşca, A. M., Sloan, S. A., Clarke, L. E., Tian, Y., Makinson, C. D., Huber, N., et al. (2015). Functional cortical neurons and astrocytes from human pluripotent stem cells in 3D culture. *Nat. Methods* 12, 671–678. doi: 10.1038/nmeth.3415

Paşca, S. P. (2018). The rise of three-dimensional human brain cultures. *Nature* 553, 437–445. doi: 10.1038/nature25032

Poli, D., Thiagarajan, S., DeMarse, T. B., Wheeler, B. C., and Brewer, G. J. (2017). Sparse and specific coding during information transmission between co-cultured dentate gyrus and CA3 hippocampal networks. *Front. Neural Circuits* 11:13. doi: 10.3389/fncir.2017.00013

Poli, D., Wheeler, B. C., DeMarse, T. B., and Brewer, G. J. (2018). Pattern separation and completion of distinct axonal inputs transmitted via micro-tunnels between co-cultured hippocampal dentate, CA3, CA1 and entorhinal cortex networks. *J. Neural Eng.* 15:046009. doi: 10.1088/1741-2552/aabc20

Premack, D. (2007). Human and animal cognition: continuity and discontinuity. *Proc. Natl. Acad. Sci. U.S.A.* 104, 13861–13867. doi: 10.1073/pnas.0706147104

Qian, X., Nguyen, H. N., Song, M. M., Hadiono, C., Ogden, S. C., Hammack, C., et al. (2016). Brain-region-specific organoids using mini-bioreactors for modeling ZIKV exposure. *Cell* 165, 1238–1254. doi: 10.1016/j.cell.2016.04.032

Quadrato, G., Nguyen, T., Macosko, E. Z., Sherwood, J. L., Min Yang, S., Berger, D. R., et al. (2017). Cell diversity and network dynamics in photosensitive human brain organoids. *Nature* 545, 48–53. doi: 10.1038/nature22047

Rajasethupathy, P., Ferenczi, E., and Deisseroth, K. (2016). Targeting neural circuits. *Cell* 165, 524–534. doi: 10.1016/j.cell.2016.03.047

Renner, M., Lancaster, M. A., Bian, S., Choi, H., Ku, T., Peer, A., et al. (2017). Self-organized developmental patterning and differentiation in cerebral organoids. *EMBO J.* 36, 1316–1329. doi: 10.15252/embj.201694700

Richardson, D. S., and Lichtman, J. W. (2015). Clarifying tissue clearing. *Cell* 162, 246–257. doi: 10.1016/j.cell.2015.06.067

Riddle, S., Wasser, D., and McCarthy, M. (2017). Touching The human neuron: user-centric augmented reality viewing and interaction of in-vivo Cellular Confocal Laser Scanning Microscopy (CLSM) utilizing high resolution zStack data sets. *J. Biocommun.* 41, 22–31. doi: 10.5210/jbc.v41i1.7563

Romoser, V. A., Hinkle, P. M., and Persechini, A. (1997). Detection in living cells of Ca2+-dependent changes in the fluorescence emission of an indicator composed of two green fluorescent protein variants linked by a calmodulin-binding sequence A new class of fluorescent indicators. *J. Biol. Chem.* 272, 13270–13274. doi: 10.1074/jbc.272.20.13270

Sakaguchi, H., Kadoshima, T., Soen, M., Narii, N., Ishida, Y., Ohgushi, M., et al. (2015). Generation of functional hippocampal neurons from self-organizing human embryonic stem cell-derived dorsomedial telencephalic tissue. *Nat. Commun.* 6:8896. doi: 10.1038/ncomms9896

Schmuck, M. R., Temme, T., Dach, K., de Boer, D., Barenys, M., Bendt, F., et al. (2017). Omnisphero: a high-content image analysis (HCA) approach for phenotypic developmental neurotoxicity (DNT) screenings of organoid neurosphere cultures in vitro. *Arch. Toxicol.* 91, 2017–2028. doi: 10.1007/s00204-016-1852-2

Steinbeck, J. A., Choi, S. J., Mrejeru, A., Ganat, Y., Deisseroth, K., Sulzer, D., et al. (2015). Optogenetics enables functional analysis of human embryonic stem cell-derived grafts in a parkinson's disease model. *Nat. Biotechnol.* 33, 204–209. doi: 10.1038/nbt.3124

Storm, J. F., Boly, M., Casali, A. G., Massimini, M., Olcese, U., Pennartz, C. M. A., et al. (2017). Consciousness regained: disentangling mechanisms, brain systems, and behavioral responses. *J. Neurosci.* 37, 10882–10893. doi: 10.1523/JNEUROSCI.1838-17.2017

Sutarjono, B. (2018). Can we better understand how zika leads to microcephaly? A systematic review of the effects of the zika virus on human brain organoids. *J. Infect. Dis.* doi: 10.1093/infdis/jiy572 [Epub ahead of print].

Takebe, T., Sekine, K., Enomura, M., Koike, H., Kimura, M., Ogaeri, T., et al. (2013). Vascularized and functional human liver from an iPSC-derived organ bud transplant. *Nature* 499, 481–484. doi: 10.1038/nature12271

Tirella, A., Magliaro, C., Penta, M., Troncone, M., Pimentel, R., and Ahluwalia, A. (2014). Sphyga: a multiparameter open source tool for fabricating smart and tunable hydrogel microbeads. *Biofabrication* 6:025009. doi: 10.1088/1758-5082/6/2/025009

Tsilidis, K. K., Panagiotou, O. A., Sena, E. S., Aretouli, E., Evangelou, E., Howells, D. W., et al. (2013). Evaluation of excess significance bias in animal studies of neurological diseases. *PLoS Biol.* 11:e1001609. doi: 10.1371/journal.pbio.1001609

Ullo, S., Nieus, T. R., Sona, D., Maccione, A., Berdondini, L., and Murino, V. (2014). Functional connectivity estimation over large networks at cellular resolution based on electrophysiological recordings and structural prior. *Front. Neuroanat.* 8:137. doi: 10.3389/fnana.2014.00137

Usher, W., Klacansky, P., Federer, F., Bremer, P.-T., Knoll, A., Yarch, J., et al. (2018). A virtual reality visualization tool for neuron tracing. *IEEE Trans. Vis. Comput. Graph.* 24, 994–1003. doi: 10.1109/TVCG.2017.2744079

Vazin, T., and Schaffer, D. V. (2010). Engineering strategies to emulate the stem cell niche. *Trends Biotechnol.* 28, 117–124. doi: 10.1016/j.tibtech.2009.11.008

Wagenaar, D. A., Pine, J., and Potter, S. M. (2004). Effective parameters for stimulation of dissociated cultures using multi-electrode arrays. *J. Neurosci. Methods* 138, 27–37. doi: 10.1016/j.jneumeth.2004.03.005

Wang, H. (2018). Modeling neurological diseases with human brain organoids. *Front. Synaptic Neurosci.* 10:15. doi: 10.3389/fnsyn.2018.00015

Watanabe, M., Buth, J. E., Vishlaghi, N., de la Torre-Ubieta, L., Taxidis, J., Khakh, B. S., et al. (2017). Self-organized cerebral organoids with human-specific features predict effective drugs to combat zika virus infection. *Cell Rep.* 21, 517–532. doi: 10.1016/j.celrep.2017.09.047

Yakoub, A. M., and Sadek, M. (2018). Development and characterization of human cerebral organoids: an optimized protocol. *Cell Transplant.* 27, 393–406. doi: 10.1177/0963689717752946

Yang, H., Rahman, M. T., Du, D., Panat, R., and Lin, Y. (2016). 3-D printed adjustable microelectrode arrays for electrochemical sensing and biosensing. *Sensors Actuators B Chem.* 230, 600–606. doi: 10.1016/j.snb.2016.02.113

Yin, X., Mead, B. E., Safaee, H., Langer, R., Karp, J. M., and Levy, O. (2016). Engineering stem cell organoids. *Cell Stem Cell* 18, 25–38. doi: 10.1016/j.stem.2015.12.005

Zhuang, P., Sun, A. X., An, J., Chua, C. K., and Chew, S. Y. (2018). 3D neural tissue models: from spheroids to bioprinting. *Biomaterials* 154, 113–133. doi: 10.1016/j.biomaterials.2017.10.002

Conflict of Interest Statement: The authors declare that the research was conducted in the absence of any commercial or financial relationships that could be construed as a potential conflict of interest.

frontiers in Neuroscience

ORIGINAL RESEARCH
published: 24 April 2019
doi: 10.3389/fnins.2019.00387

Multimodal Evaluation of TMS - Induced Somatosensory Plasticity and Behavioral Recovery in Rats With Contusion Spinal Cord Injury

*Vijai S. Krishnan[1,2,3,4], Samuel S. Shin[3], Visar Belegu[5,6], Pablo Celnik[7], Mark Reimers[1,2], Kylie R. Smith[1,2] and Galit Pelled[1,2,3,4,8]**

[1] Department of Biomedical Engineering, Michigan State University, East Lansing, MI, United States, [2] The Institute for Quantitative Health Science and Engineering, Michigan State University, East Lansing, MI, United States, [3] F.M. Kirby Research Center for Functional Brain Imaging, Kennedy Krieger Institute, Baltimore, MD, United States, [4] Russell H. Morgan Department of Radiology and Radiological Science, Johns Hopkins University School of Medicine, Baltimore, MD, United States, [5] Department of Neurology and Pathology, Johns Hopkins University School of Medicine, Baltimore, MD, United States, [6] International Center for Spinal Cord Injury, Kennedy Krieger Institute, Baltimore, MD, United States, [7] Department of Physical Medicine and Rehabilitation, Johns Hopkins University School of Medicine, Baltimore, MD, United States, [8] Department of Radiology, Michigan State University, East Lansing, MI, United States

OPEN ACCESS

Edited by:
Laura Ballerini, Scuola Internazionale Superiore di Studi Avanzati (SISSA), Italy

Reviewed by:
Andrea Nistri, Scuola Internazionale Superiore di Studi Avanzati (SISSA), Italy
Maria Concepcion Serrano, Spanish National Research Council (CSIC), Spain

***Correspondence:**
Galit Pelled
pelledga@msu.edu

Specialty section:
This article was submitted to Neural Technology, a section of the journal Frontiers in Neuroscience

Received: *15 January 2019*
Accepted: *04 April 2019*
Published: *24 April 2019*

Citation:
Krishnan VS, Shin SS, Belegu V, Celnik P, Reimers M, Smith KR and Pelled G (2019) Multimodal Evaluation of TMS - Induced Somatosensory Plasticity and Behavioral Recovery in Rats With Contusion Spinal Cord Injury. Front. Neurosci. 13:387. doi: 10.3389/fnins.2019.00387

Introduction: Spinal cord injury (SCI) causes partial or complete damage to sensory and motor pathways and induces immediate changes in cortical function. Current rehabilitative strategies do not address this early alteration, therefore impacting the degree of neuroplasticity and subsequent recovery. The following study aims to test if a non-invasive brain stimulation technique such as repetitive transcranial magnetic stimulation (rTMS) is effective in promoting plasticity and rehabilitation, and can be used as an early intervention strategy in a rat model of SCI.

Methods: A contusion SCI was induced at segment T9 in adult rats. An rTMS coil was positioned over the brain to deliver high frequency stimulation. Behavior, motor and sensory functions were tested in three groups: SCI rats that received high-frequency (20 Hz) rTMS within 10 min post-injury (acute-TMS; n = 7); SCI rats that received TMS starting 2 weeks post-injury (chronic-TMS; n = 5), and SCI rats that received sham TMS (no-TMS, n = 5). Locomotion was evaluated by the Basso, Beattie, and Bresnahan (BBB) and gridwalk tests. Motor evoked potentials (MEP) were recorded from the forepaw across all groups to measure integrity of motor pathways. Functional MRI (fMRI) responses to contralateral tactile hindlimb stimulation were measured in an 11.7T horizontal bore small-animal scanner.

Results: The acute-TMS group demonstrated the fastest improvements in locomotor performance in both the BBB and gridwalk tests compared to chronic and no-TMS groups. MEP responses from forepaw showed significantly greater difference in the inter-peak latency between acute-TMS and no-TMS groups, suggesting increases in motor function. Finally, the acute-TMS group showed increased fMRI-evoked responses to hindlimb stimulation over the right and left hindlimb (LHL) primary somatosensory representations (S1), respectively; the chronic-TMS group showed moderate sensory

responses in comparison, and the no-TMS group exhibited the lowest sensory responses to both hindlimbs.

Conclusion: The results suggest that rTMS therapy beginning in the acute phase after SCI promotes neuroplasticity and is an effective rehabilitative approach in a rat model of SCI.

Keywords: transcranial magnetic stimulation, spinal cord injury, plasticity, behavior, functional magnetic resonance imaging

INTRODUCTION

Traumatic spinal cord injury (SCI) is a debilitating condition with a reported global incidence ranging from 10 to 80 million per population per year (Singh et al., 2014; Jazayeri et al., 2015). The changes in the cortex and the thalamus following SCI have been studied extensively (Bonatz et al., 2000; Aguilar et al., 2010; Ghosh et al., 2010, 2012). Deafferentation caused by SCI has been shown to induce short (days) and long-term (months) alterations in brain architecture and neuronal connections (Jain et al., 2008; Ghosh et al., 2010). However, it is still unclear how these changes translate into behavior and recovery.

Evidence from rodent models suggest that within minutes after SCI, decreases in spontaneous neuronal activity are observed in cortical areas that correspond to the injured limbs as well as cortical areas that normally process information from the non-injured limbs (Aguilar et al., 2010). Moreover, these decreases in spontaneous activity are correlated with poor recovery. Thus, an intervention to attenuate and reverse the injury-induced reduction in spontaneous cortical activity has the potential to accelerate post-SCI neurorehabilitation. Indeed, there are ongoing efforts to modulate the activity of the peripheral and central nervous system after SCI with the goal of enhancing recovery. A bulk of evidence demonstrates that peripheral nerve function is affected by SCI (Boland et al., 2010; Van De Meent et al., 2010) highlighting the importance of regulating peripheral nerve function during critical phases of SCI. For example, an intensive 6 week peripheral nerve stimulation regimen has been shown to prevent long term changes in axonal function post-SCI (Lee et al., 2015). Other non-pharmacological and non-invasive approaches such as spinal cord stimulation (functional electrical stimulation) (Martin et al., 2012) has been shown to improve recovery outcomes post-SCI. Functional electrical stimulation of central pattern generator mechanisms has been shown to improve responses in patients with complete or incomplete SCI (Harkema et al., 2011). Recent research has shown that the application of epidural electric stimulation (EES) improves spinal networks post-injury through the restoration of locomotion (Courtine et al., 2009; Formento et al., 2018). The future of neurorehabilitative strategies would involve using non-invasive treatments involving electrical stimulation.

In addition to assessing corticospinal transmission times, non-invasive brain stimulation technologies are additionally being used as therapies for a variety of neurological disorders and diseases (Schulz et al., 2013; Gunduz et al., 2017). A prominent FDA approved (O'Reardon et al., 2007), non-invasive technology shown to produce long lasting increases in cortical excitability is transcranial magnetic stimulation (TMS). TMS has been shown to induce neuronal excitation and plasticity beyond the stimulation period in several injury and disease conditions (Lefaucheur et al., 2014; Shin and Pelled, 2017), including in rodent models of brain injury (Lu et al., 2015; Shin et al., 2018). Reports in the past have demonstrated that applying TMS years after SCI has improved motor and sensory outcomes (Belci et al., 2004; Kuppuswamy et al., 2011). Another study showed that high-frequency repetitive TMS (rTMS) stimulation applied months after SCI improved motor function compared to the same treatment with sham stimulation (Benito et al., 2012).

This led us to test whether applying TMS over the cortex to enhance excitation, within days and weeks after the injury was sustained, could facilitate recovery in an animal model.

A contusion model of thoracic injury (T9) in adult rats shown to mimic similar pathological changes to human SCI (Metz et al., 2000a) was used. We tested if daily TMS sessions starting within minutes or weeks after the injury would accelerate neuroplasticity. MEP was used to test the effectiveness of TMS treatment by evaluating the changes in integrity of motor pathways (Curt et al., 1998; Nakamae et al., 2010). Weekly behavioral testing was conducted to assess gross behavior improvement. High-resolution functional MRI was used to detect cortical functional responses evoked by tactile limb stimulation (Pelled et al., 2006, 2009; Han et al., 2013; Li et al., 2014b; Lu et al., 2015) as a means to evaluate recovery of ascending spinal pathways.

Our results support the hypothesis that rescuing the hypoactive neuronal activity by TMS can accelerate post-SCI neuroplasticity.

MATERIALS AND METHODS

All animal procedures were conducted in accordance with the NIH *Guide for the Care and Use of Laboratory Animals* and approved by the Johns Hopkins University Animal Care and Use Committee.

Animals

17 male adult Sprague-Dawley rats (Harlan Laboratories) were provided with food and water *ad libitum* and housed in pairs (standard housing).

Spinal Cord Injury

An hour prior to surgery, rats were injected with buprenorphine (Buprenex; 0.05 mg/kg, s.c.). Animals were anesthetized using a Ketamine (75 mg/kg, i.p.) and Dexmedetomidine (0.25 mg/kg, i.p.) cocktail. An infinite horizon impactor was used to induce SCI. Displacement and velocity were tested to ensure instrument reliability (Scheff et al., 2003). A midline sagittal incision centered over the T9 vertebra was performed, and the muscles and connective tissue were separated to expose the spinal segments. Dorsal laminectomy of the T9 segment was followed. Afterward, adson forceps was used to clamp the spinal column, rostral and caudal to the laminectomy. The animal was transferred to the IH impactor and was centered with the exposed site immediately beneath the impactor. The impactor was lowered with a 4 mm tip above the exposed spinal cord segment. A 200 kdyne injury was used to impact the exposed segment, resulting in a severe contusion SCI (Cao et al., 2005; Anderson et al., 2009).

After the injury the muscle and fascia were sutured with a running 5–0 vicryl absorbable suture and the skin was closed using wound clips. Rats were given 10 ml of Ringers solution (i.p), 0.05 mL of gentamicin (i.m) and buprenorphine (Buprenex; 0.05 mg/kg, s.c.), and put in a 37°C incubator. Once in the incubator, Antisedan (1 mg/kg; i.m.) was administered to reverse the anesthesia. Water Gel pack and food pellets were provided at the bottom of the cage up to 72 h after SCI. Bladder expression was performed twice daily until the animals regained bladder control. Buprenorphine was administered twice a day for 48 h. Administration of 10 mL of Ringer's solution (i.p.) and 0.05 mL of gentamicin (i.m.) continued daily for 7 days. Wound clips were removed 7–10 days after injury. Animals showing lack of movement were not included in this study.

Transcranial Magnetic Stimulation

For TMS application, rats were anesthetized with 2% isoflurane and their heads secured using a stereotaxic frame. The TMS system (Magstim, Rapid2) was equipped with a figure eight, 25 mm custom rodent coil which was placed over the midline between bregma and lambda, covering both left and right sensorimotor cortices. The stimulus was delivered 3-times a week for 6 weeks using the following settings: 4 s cycles of 10 Hz stimuli, 26 s interval between cycles, and 7 cycles (total of 280 pulses per day, 1680 total stimuli). The length of this stimulation treatment was 10 min. Injured rats were divided into three groups: ***Acute-TMS Group*** **(*n* = 7)**, TMS delivered within 10 min following SCI and wound suturing; ***Chronic-TMS Group (n = 5)***, TMS beginning 2 weeks following SCI; ***No-TMS Group (n = 5)***. The TMS coil was placed exactly in the same position as in the experimental groups but no stimulation was applied. At the end of the procedure the animals were placed in a clean cage on a 37°C warming tray and monitored for return to normal activity.

Basso, Beattie, and Bresnahan (BBB) Locomotor Scale

In order to assess motor function post-SCI, rats were placed in an uninterrupted open field and allowed unrestricted movement. Rats were allowed to move freely and were scored by their ability to use their hindlimbs. A 21- point BBB locomotion scale was used based on the movement of joints, placement of paws and coordination of forepaw and hindlimbs (Basso et al., 1995).

Gridwalk Test

Motor behavior was assessed by performing the weekly gridwalk test. The gridwalk test was used to evaluate sensory motor coordination after SCI. In this test, the rats were examined in a long walkway consisting of irregularly spaced metal rungs over which the animals must travel in order to reach the end. The number of foot fall errors where the hindlimb of a test animal failed to grasp a bar and fell between the bars were recorded.

Electromyography

Motor evoked potentials (MEP) in response to TMS were recorded with needle electrodes inserted into both forepaws. The corticospinal excitability was measured in response to stimulatory TMS at 100% capacity for 10 single stimuli. Inter-peak latency responses to the first TMS stimulus in each rat forepaw were measured using Spike 2 software (CED, Cambridge, United Kingdom). Inter-peak latency was calculated as the difference in time between the two consecutive peaks of the MEP.

fMRI Acquisition and Data Analysis

Rats were anesthetized with dexmedetomidine (0.1 mg/kg/h, SC) which is known to preserve neurovascular coupling (Li et al., 2014a). Rats were then placed in an ultra-high field 11.7 Tesla/16 cm horizontal bore small-animal scanner (Bruker BioSpin, Rheinstetten, Germany). A 72-mm quadrature volume coil and a 15-mm-diameter surface coil were used to transmit and receive magnetic resonance signals, respectively.

Respiration rate, heart rate, rectal temperature, and partial pressure of oxygen were continuously monitored throughout fMRI measurements (Starr Life Sciences, Pennsylvania, United States). fMRI, gradient echo, echo planar imaging was used with a resolution of 150 × 150 × 1000 μm. Five 1 mm thick coronal slices covering the primary somatosensory cortex (S1) were acquired [effective echo time (TE), 11 ms; repetition time (TR), 1000 ms; bandwidth, 250 KHz; field of view (FOV), 1.92 × 1.92 cm; and matrix size, 128 × 128]. A T2-weighted RARE sequence was used to acquire high-resolution anatomical images (TE, 10 ms; TR, 5000 ms; bandwidth, 250 KHz; FOV, 1.92 × 1.92 cm; and matrix size, 256 × 256) corresponding to the fMRI measurements. Two needle electrodes were inserted into the left and right forepaws or hindlimbs to deliver electrical stimulation. Electrical stimulation (9 Hz, 0.3 mA, and 0.3 ms) was applied for two trains of 20 s with 40 s rest in between. Cross-correlation maps were cluster-size thresholded for an effective significance of $P < 0.05$ using Stimulate (University of Minnesota).

Statistical Analysis

Statistical analysis was performed using Graphpad Prism package (San Diego, CA, United States). For the BBB scores, gridwalk, and fMRI studies, we used one-way ANOVA with multiple comparisons (followed by sidak *post hoc* test) to verify differences

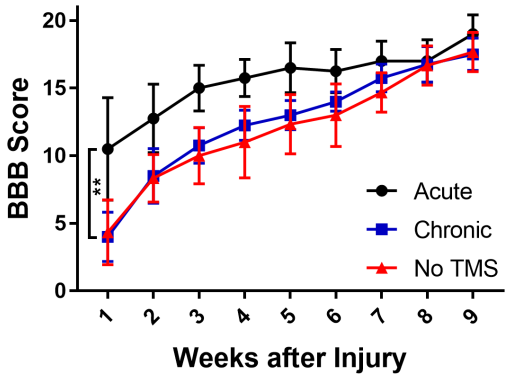

FIGURE 1 | Graph showing effects of TMS treatment on SCI rats assessed by BBB scores over 9 weeks. BBB scores were assessed on a 21-point score (21 being a normal motor function). The scores show that the acute-TMS group ($n = 4$) showed significant improvement in scores over chronic ($p = 0.004$, $n = 4$) and no-TMS ($p = 0.0015$, $n = 3$) groups. The chronic-TMS group did not show significant improvement over the no-TMS group. Statistical analysis was performed with one-way ANOVA involving multiple comparisons.

between groups. Linear regression analysis was also used for gridwalk test. MEP data were analyzed using student's *t*-test. Data are presented as means ± SEM. *P* value of <0.05 was considered significant for all the data analysis. *, **, and *** correspond to $p < 0.05$, $p < 0.01$, and $p < 0.001$.

RESULTS

BBB Locomotor Scale

Initial assessment of SCI motor recovery was done using the BBB scale which has been shown to be informative in evaluating post-SCI function in rats (Basso et al., 1995). The score (0–21) represents different combinations of movements and the associated degree of recovery where an increased score represents better functional motor recovery.

We compared the change in the mean score between the TMS-treated groups (acute and chronic) and no-TMS group (**Figure 1**). The BBB score for the acute-TMS group ($n = 4$) had the best improvement amongst the three groups with a mean initial score of 10.5 ± 3.8 in the first week and continuous improvement leading to a mean score of 19 ± 1.14 in week 9. The chronic TMS group ($n = 4$) and the no-TMS group ($n = 4$) had similar BBB scores with steady improvement throughout the study. By the end of the 9th week all groups reached similar scores. We compared scores over the period of 9 weeks and report that the acute-TMS group had overall significance ($p = 0.004$) with a mean score of 15.53 ± 0.84 vs the chronic-TMS group (12.5 ± 1.41). The mean overall BBB score was also significant ($p = 0.0015$) for acute (15.53 ± 0.84) vs no-TMS group (12 ± 1.39). The comparison between the chronic vs the no-TMS group did not yield any statistical significance. This result showed that early intervention using TMS resulted in a better locomotor recovery following SCI.

Gridwalk Test

Data in (**Figure 2A**) show the percent footfall errors for each individual animal from all three groups over a period of 9 weeks. The acute-TMS group had the lowest percent footfall errors compared to the chronic and no-TMS groups. Many recovery processes show a rapid initial recovery phase followed by gradual slowing and approach a stable long-term level (asymptote), although this asymptote may not be reached during the short time of the experiment. Such processes are often fitted by an exponential decay curve. We fitted an exponential curve (data figure not shown) to the mean missed steps data from each group and tested whether the asymptotes differed between groups. Exponential curve fit equation is ($y = a + be^{-t/\tau}$, where "a" is the asymptotic recovery value, and τ is the recovery time constant in weeks and a + b = 100%). The estimates for the asymptotes (long-term values) for the three groups are 1. Acute-TMS 7.0 +/− 2.8; 2. No-TMS 34.9 +/− 5.8; 3. Chronic-TMS 26.4 +/− 3.3. The *p*-values for the differences between groups are: $P < 0.005$ when comparing 1 vs 3 ($t = 4.48$ on 6 df) and when comparing 1 vs 2 ($t = 4.35$ on 6 df).

In addition, we compared the percent of foot fall errors between the groups (**Figure 2B**) using multiple-comparison ANOVA analysis. Consistent with BBB score analysis, the acute-TMS rats had the lowest footfall error rate through 9 weeks with mean percent error rate of 37.75 ± 11.38 (**Figure 2B**) during the first week which consistently improved to 20.21 ± 6.3 in week 5 and 11.77 ± 2.9 at week 9. The acute-TMS group showed a significantly lowered foot fall error rate compared to chronic TMS ($p = 0.0009$) and no-TMS group ($p = 0.0015$). We report that the chronic- TMS group did not show significant differences in the footfall error rate compared to the no-TMS group.

MEP Assessment

The MEP test is commonly used as a read-out of corticospinal excitability to probe the physiology of the motor cortex. Measuring MEPs provide quantification of this corticospinal excitability, which TMS is known to modulate (Bestmann and Krakauer, 2015). Our goal was to investigate whether TMS can improve motor activity in the limbs following SCI. This was assessed through changes in the late-latency MEPs in the limbs. Inter-peak latency to evaluate the motor pathway integrity was calculated as the difference in time between the two consecutive peaks of the MEP (**Figure 3A**). For statistical analysis, late latency parameters were compared between acute, chronic and non-TMS treatment groups using a Student's *t*-test. The inter-peak latencies for MEP calculated for both the right and left forelimbs were grouped together. Data graph (**Figure 3B**) show that the acute-TMS receiving rats have significantly longer inter-peak latencies (Mean ± SEM, 0.002908 ± 0.0009249, and $n = 4$) compared to no-TMS group (Mean ± SEM, 0.0009024 ± 0.000142, and $n = 7$). Though the chronic-TMS group had a longer inter-peak latency than the no-TMS group it did not show a significant difference.

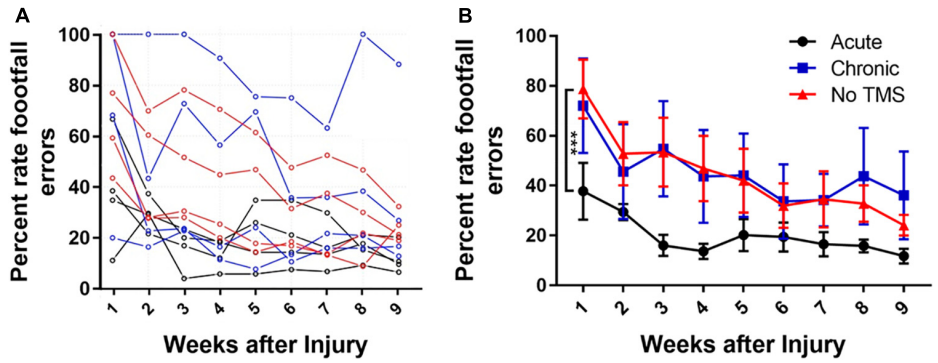

FIGURE 2 | (A) Line graph showing mean gridwalk scores measured in terms of percent footfall errors across a period of 9 weeks for each animal across all groups. The acute-TMS group had the lowest percent footfall errors compared to the chronic and no-TMS group. **(B)** One-way ANOVA with multiple comparison analyses show significant improvement in percentage of footfall errors measured in acute (n = 4) vs chronic (n = 4, p = 0.0009) and acute vs no-TMS groups (n = 3, p = 0.0015). No significant differences were found between the chronic vs no-TMS groups across 9 weeks.

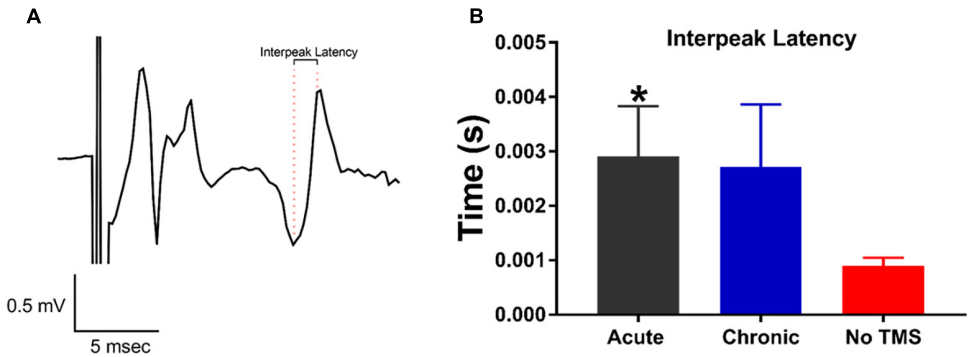

FIGURE 3 | MEP responses recorded from the forepaws evoked by transcranial magnetic stimulation (TMS) pulses. **(A)** Representative MEP trace showing the distance in time between consecutive maximal peaks defined as inter-peak latency. **(B)** Data summary show a significant increase in inter-peak latency in rats treated with acute-TMS vs the no-TMS group (p = 0.018, denoted by *). The chronic vs. no-TMS group did not show significant differences in inter-peak latencies.

TMS Treatment Enhances the Evoked fMRI Signal

High resolution fMRI was used to measure somatosensory responses in SCI animals after TMS treatment. Evoked blood-oxygenation-level-dependent (BOLD) fMRI in the primary somatosensory cortex was measured in response to contralateral hind limb and forepaw stimulation 10 weeks post-SCI.

Our results demonstrate that the acute-TMS group (n = 7) showed the greatest increase in sensory responses evoked by stimulation of right hindlimb (RHL) with 56.29 ± 7.61 activated pixels, and left hindlimb (LHL) with 52.29 ± 6.73 activated pixels (**Figure 4A**). The chronic-TMS group had an intermediate response in both limbs and the sham control group failed to evoke any cortical response. Data analysis (**Figure 4C**) of sensory responses showed significantly larger response in terms of activated pixels in the acute-TMS group: 56.29 ± 7.61 (RHL) and 52.29 ± 6.73 (LHL). The chronic-TMS showed 49.4 ± 10.45 (RHL) and 38.6 ± 2.69 (LHL) activated pixels exhibiting moderate response. The no-TMS group showed very few activated pixels in response to stimulation: 26.8 ± 2.41 (RHL) and 28.4 ± 4.02 (LHL). One way ANOVA revealed significant differences in the means between the groups (F(5,28) = 3.554, p = 0.01). We also used t-test to report that the acute-TMS group was significantly larger than the no-TMS group (p = 0.0043). The chronic group also show an improved response over the no-TMS group (p = 0.02).

We also measured somatosensory responses to forepaw stimulation (**Figure 4B**), as the T9 contusion should not have affected evoked forepaw response. Indeed, the extent of the fMRI responses to left and right forepaw stimulating was similar to values that were reported previously (Li et al., 2011, 2014a,b; Han et al., 2013). The fMRI results showed that injured rats receiving TMS therapy immediately after the injury demonstrated the most extensive cortical activity in the weeks following injury.

DISCUSSION

Non-invasive Brain Stimulation Improves Outlook in SCI

The aim of this study was to test whether applying TMS over the brain in minutes and weeks following SCI could

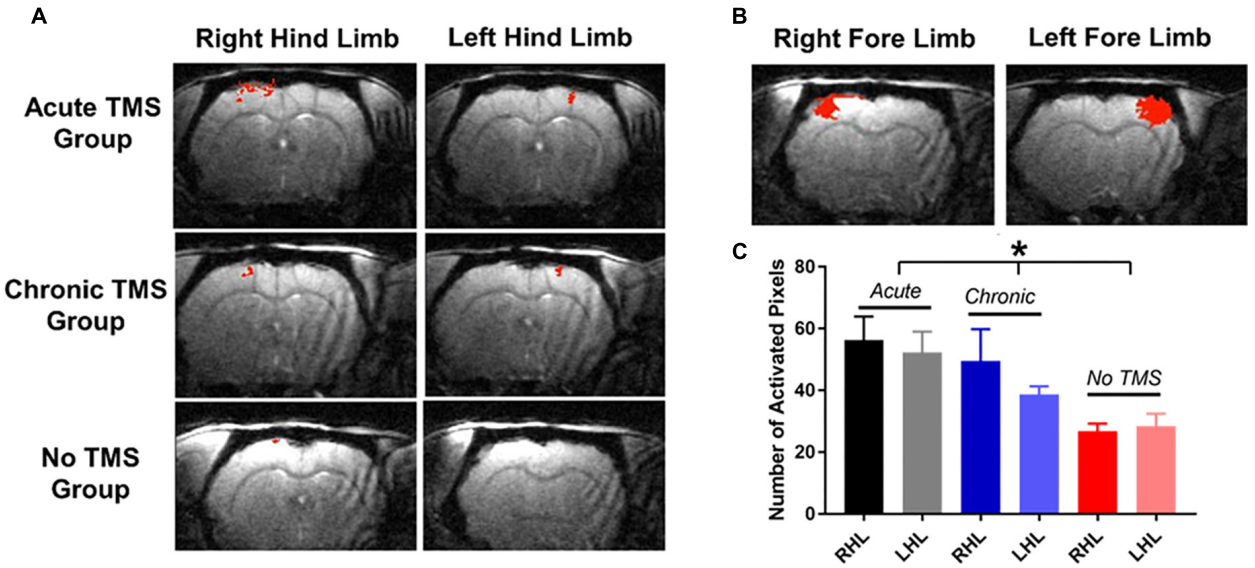

FIGURE 4 | (A) fMRI measurements: were obtained 10 weeks after SCI. Individual fMRI cross-correlation statistical maps demonstrate increases in fMRI responses (in red) to contralateral stimulation of hindlimbs in the acute-TMS (n = 7) and chronic-TMS (n = 5) treatment groups, but not in the no- TMS group (n = 5). **(B)** Show sensory responses to stimulation of forepaws. **(C)** Data plots shows that the acute-TMS group demonstrated the greatest sensory responses to right and left hindlimb (LHL) stimulation compared to chronic-TMS and no-TMS groups. Statistical significance was determined by one-way ANOVA [$F(5,28) = 3.554$, $p = 0.01$)].

facilitate recovery. In this study, rats subjected to SCI were assessed by behavior and physiological methods. Behavioral testing was evaluated by BBB score and gridwalk testing, and changes in corticospinal excitability was measured by MEP testing. Changes in cortical sensory information were evaluated using BOLD fMRI. TMS has been shown to be effective in facilitating recovery, enhancing neuroplasticity and alleviating pain in a number of neurological disorders and injuries (Lu et al., 2015; Shin et al., 2018) In addition, TMS has been shown to restore the transmission of corticospinal information and improve outcome in patients with SCI (Belci et al., 2004; Kumru et al., 2010).

There is a plethora of pharmacological and exercise therapy approaches in promoting brain plasticity after SCI. The use of 5-HT pharmacotherapy has been shown to promote cortical plasticity after SCI, especially in the improvement of behavioral outcome (Ganzer et al., 2013). Exercise interventions have also been shown to promote brain plasticity thereby aiding in the motor recovery in both the spinal cord and the brain. Animal studies involving exercise interventions have been shown to promote plasticity through the upregulation of various neurotrophic factors in the spinal cord (Liu et al., 2010; Keeler et al., 2012). In an animal model of traumatic brain injury we have recently demonstrated that combining enriched environment with TMS augment rehabilitation (Shin et al., 2018). Therefore, it is manifesting that a combination of therapies that target different physiological and neuroplasticity mechanisms might also be useful in facilitating recovery after SCI. A non-invasive method that changes cortical excitability thereby inducing plastic changes appears promising in the SCI arena (Gunduz et al., 2017).

Immediate Intervention Improves Recovery

One of the goals of this study was to determine the timeframe for effective intervention. It has been shown in rats that cortical reorganization after SCI occur in several temporal stages. Long term cortical expansion assessed by fMRI 1 to 3 months after injury (Endo et al., 2007) is preceded by early changes in reorganization that occur within a week after injury (Sydekum et al., 2014). Early expansion of cortical representations has been shown to be associated with decreases in spine density in the deafferented cortical areas in rats (Kim et al., 2006). It has also been shown that a complete thoracic SCI in anesthetized rats immediately changes state of cortical activity (Yagüe et al., 2014). In addition, changes in cortical representation after SCI occur within hours using electrophysiological techniques (Humanes-Valera et al., 2013). This highlights the use of an early intervention strategy to mediate changes in cortical function that might benefit functional outcome.

An important factor to be taken into consideration for the intervention is the time elapsed after injury. The optimal window of time for initiating therapy, to promote recovery following SCI may be varied. Although studies using TMS were performed in the chronic phase of SCI (Kumru et al., 2010, 2016), this is the first report to evaluate the long-term effects of an acute-TMS application.

We report that changes in sensory perception are accompanied by increases in the motor outputs induced by

acute TMS therapy. This is similar to previous research results that report that electrochemical neuromodulation restores motor activity in rodents with spinal cord contusion injury (Asboth et al., 2018). We also report that the beneficial effects of TMS in the acute group were seen earlier in the behavioral studies with all groups eventually catching up. Rapid improvement in the rehabilitation process is very impactful for human subjects, as this will reduce length of hospitalization, total cost of care, and minimize potential complications from a prolonged recovery process.

Multimodal Methods to Quantify Behavioral, Motor and Sensory Outcomes

There are several behavioral tests in animal model that have been shown to be useful to monitor and evaluate functional outcome after SCI. These include the BBB scale, gridwalk test (Metz et al., 2000b; Dijkstra et al., 2006) plantar test (Hargreaves et al., 1988), and tail flick test. Although these tests are used frequently, they are highly variable and often do not have the sensitivity to monitor subtle and long-term changes. For example, the gridwalk test was shown to have a high degree of variability, due to the number of footfall errors correlating poorly with the BBB scoring system in rats (McEwen and Springer, 2006). In our study, the gridwalk and BBB scoring correlated well in terms of locomotor recovery. The BBB locomotion assessment of rat's post-SCI, showed that the acute-TMS group recovered the fastest, with recovery plateauing by week 5. Additionally the acute-TMS group had a significantly better BBB score than the chronic and no-TMS group This is in agreement with previous evidence that show gradual recovery by week 5 (Nessler et al., 2006; Shinozaki et al., 2013). Gridwalk test results indicated that the acute-TMS group had the best scores with the fewest footfall errors compared to the chronic and no-TMS groups. We observed a trend of increased performance in BBB scoring and gridwalk test in the chronic-TMS group compared to no-TMS group although this trend did not reach significance. This suggests that TMS therapy could benefit if it starts at chronic stage after SCI injury (2 weeks post-SCI), but will be more effective if it begins in acute stages after the injury.

Previous studies have used MEP as a quantification method to assess recovery after SCI (Curt et al., 1998). In our study, the MEP test was performed to assess the extent of locomotor recovery post-TMS therapy. However, our results show that applying TMS to the sensorimotor cortex after SCI resulted in significantly longer inter-peak latency of MEPs. This may suggest a reorganization of motor pathways (Brum et al., 2016). As TMS is known to facilitate neuroplasticity, it is feasible that the applied TMS is facilitating reorganization of this corticospinal pathway as an adaptation to the global cortical silencing that occurs following SCI (Aguilar et al., 2010).

Various imaging techniques have been used successfully to monitor SCI changes. fMRI has been shown to be a useful tool in detecting changes in brain pathology after SCI (Wrigley et al., 2018) and brain connectivity, before and after SCI in mice (Matsubayashi et al., 2018). Furthermore, fMRI has been used to observe increased response to forepaw stimuli in the primary somatosensory region after thoracic SCI (Hofstetter et al., 2003). Here we used high-resolution fMRI obtained at ultra-high field of 11.7 T to monitor if TMS therapy induces post-injury neuroplasticity. We determined the optimal TMS therapy timing that lead to the greatest fMRI responses to limb stimulation. fMRI results from our study showed greater somatosensory response in the acute-TMS group followed by chronic with the no-TMS group showing very little signal. Our results show that fMRI is a sensitive method to report SCI neuroplasticity and report differences in cortical responses between the groups at 10 weeks post-injury while the behavioral tests suggested that, by the same time all the rats reached a similar level of behavioral performance.

Our study highlights the importance of utilizing a combination of methods that can assess behavioral performance, motor behavior, and sensory function in monitoring individuals post-SCI. Using fMRI as an additional tool alongside behavioral and electrophysiological methods provides a sensitive assessment of cortical function as well as a method to detect minute compensatory changes in response to brain activation.

We suggest that post-SCI TMS therapy should be further tested for its efficacy and safety. Subsequently, this non-invasive strategy could be readily translated to the clinic as an adjuvant to traditional rehabilitation strategies. One of the limitations of our study is the use of general anesthesia during TMS treatments electrophysiology, and fMRI measurements in the animal model, which may not mimic the human condition. However, the insights gained from this and similar animal model studies are valuable in developing and evaluating new therapies. Moreover, our results suggest that early intervention is key for recovery and might play a role in medical strategies and trauma care interventions.

ETHICS STATEMENT

All animal procedures were conducted in accordance with the NIH Guide for the Care and Use of Laboratory Animals and approved by the Johns Hopkins University Animal Care and Use Committee.

AUTHOR CONTRIBUTIONS

VK and GP designed all experiments and wrote the manuscript. VK, SS, and VB performed the experiments. GP, VK, SS, KS, PC, and MR analyzed the data. All authors read and approved the final manuscript.

FUNDING

This work was funded by NIH/NINDS R01NS072171 and R01NS079288 (GP).

ACKNOWLEDGMENTS

We thank Aline Thomas, Jineta Banerjee, and Anna Schwartz for technical assistance.

REFERENCES

Aguilar, J., Humanes-Valera, D., Alonso-Calvino, E., Yague, J. G., Moxon, K. A., Oliviero, A., et al. (2010). Spinal cord injury immediately changes the state of the brain. *J. Neurosci.* 30, 7528–7537. doi: 10.1523/JNEUROSCI.0379-10.2010

Anderson, K. D., Sharp, K. G., and Steward, O. (2009). Bilateral cervical contusion spinal cord injury in rats. *Exp. Neurol.* 220, 9–22. doi: 10.1016/j.expneurol.2009.06.012

Asboth, L., Friedli, L., Beauparlant, J., Martinez-Gonzalez, C., Anil, S., Rey, E., et al. (2018). Cortico-reticulo-spinal circuit reorganization enables functional recovery after severe spinal cord contusion. *Nat. Neurosci.* 21, 576–588. doi: 10.1038/s41593-018-0093-5

Basso, D. M., Beattie, M. S., and Bresnahan, J. C. (1995). A sensitive and reliable locomotor rating scale for open field testing in rats. *J. Neurotrauma* 12, 1–21. doi: 10.1089/neu.1995.12.1

Belci, M., Catley, M., Husain, M., Frankel, H., and Davey, N. (2004). Magnetic brain stimulation can improve clinical outcome in incomplete spinal cord injured patients. *Spinal Cord* 42:417. doi: 10.1038/sj.sc.3101613

Benito, J., Kumru, H., Murillo, N., Costa, U., Medina, J., Tormos, J., et al. (2012). Motor and gait improvement in patients with incomplete spinal cord injury induced by high-frequency repetitive transcranial magnetic stimulation. *Top. Spinal Cord Injury Rehabil.* 18, 106–112. doi: 10.1310/sci1802-106

Bestmann, S., and Krakauer, J. W. (2015). The uses and interpretations of the motor-evoked potential for understanding behaviour. *Exp. Brain Res.* 233, 679–689. doi: 10.1007/s00221-014-4183-7

Boland, R. A., Lin, C. S.-Y., Engel, S., and Kiernan, M. C. (2010). Adaptation of motor function after spinal cord injury: novel insights into spinal shock. *Brain* 134, 495–505. doi: 10.1093/brain/awq289

Bonatz, H., Röhrig, S., Mestres, P., Meyer, M., and Giehl, K. M. (2000). An axotomy model for the induction of death of rat and mouse corticospinal neurons in vivo. *J. Neurosci. Methods* 100, 105–115. doi: 10.1016/s0165-0270(00)00238-7

Brum, M., Cabib, C., and Valls-Solé, J. (2016). Clinical value of the assessment of changes in Mep duration with voluntary contraction. *Front. Neurosci.* 9:505. doi: 10.3389/fnins.2015.00505

Cao, Q., Zhang, Y. P., Iannotti, C., Devries, W. H., Xu, X.-M., Shields, C. B., et al. (2005). Functional and electrophysiological changes after graded traumatic spinal cord injury in adult rat. *Exp. Neurol.* 191, S3–S16.

Courtine, G., Gerasimenko, Y., Van Den Brand, R., Yew, A., Musienko, P., Zhong, H., et al. (2009). Transformation of nonfunctional spinal circuits into functional states after the loss of brain input. *Nat. Neurosci.* 12:1333. doi: 10.1038/nn.2401

Curt, A., Keck, M. E., and Dietz, V. (1998). Functional outcome following spinal cord injury: significance of motor-evoked potentials and ASIA scores. *Arch. Phys. Med. Rehabil.* 79, 81–86. doi: 10.1016/s0003-9993(98)90213-1

Dijkstra, S., Duis, S., Pans, I., Lankhorst, A., Hamers, F., Veldman, H., et al. (2006). Intraspinal administration of an antibody against CD81 enhances functional recovery and tissue sparing after experimental spinal cord injury. *Exp. Neurol.* 202, 57–66. doi: 10.1016/j.expneurol.2006.05.011

Endo, T., Spenger, C., Tominaga, T., Brene, S., and Olson, L. (2007). Cortical sensory map rearrangement after spinal cord injury: fMRI responses linked to Nogo signalling. *Brain* 130, 2951–2961. doi: 10.1093/brain/awm237

Formento, E., Minassian, K., Wagner, F., Mignardot, J. B., Le Goff-Mignardot, C. G., Rowald, A., et al. (2018). Electrical spinal cord stimulation must preserve proprioception to enable locomotion in humans with spinal cord injury. *Nat. Neurosci.* 21:1728. doi: 10.1038/s41593-018-0262-6

Ganzer, P. D., Moxon, K. A., Knudsen, E. B., and Shumsky, J. S. (2013). Serotonergic pharmacotherapy promotes cortical reorganization after spinal cord injury. *Exp. Neurol.* 241, 84–94. doi: 10.1016/j.expneurol.2012.12.004

Ghosh, A., Haiss, F., Sydekum, E., Schneider, R., Gullo, M., Wyss, M. T., et al. (2010). Rewiring of hindlimb corticospinal neurons after spinal cord injury. *Nat. Neurosci.* 13:97. doi: 10.1038/nn.2448

Ghosh, A., Peduzzi, S., Snyder, M., Schneider, R., Starkey, M., and Schwab, M. E. (2012). Heterogeneous spine loss in layer 5 cortical neurons after spinal cord injury. *Cereb Cortex* 22, 1309–1317. doi: 10.1093/cercor/bhr191

Gunduz, A., Rothwell, J., Vidal, J., and Kumru, H. (2017). Non-invasive brain stimulation to promote motor and functional recovery following spinal cord injury. *Neural Regen. Res.* 12:1933. doi: 10.4103/1673-5374.221143

Han, Y., Li, N., Zeiler, S. R., and Pelled, G. (2013). Peripheral nerve injury induces immediate increases in layer v neuronal activity. *Neurorehabil. Neural Repair* 27, 664–672. doi: 10.1177/1545968313484811

Hargreaves, K., Dubner, R., Brown, F., Flores, C., and Joris, J. (1988). A new and sensitive method for measuring thermal nociception in cutaneous hyperalgesia. *Pain* 32, 77–88. doi: 10.1016/0304-3959(88)90026-7

Harkema, S., Gerasimenko, Y., Hodes, J., Burdick, J., Angeli, C., Chen, Y., et al. (2011). Effect of epidural stimulation of the lumbosacral spinal cord on voluntary movement, standing, and assisted stepping after motor complete paraplegia: a case study. *Lancet* 377, 1938–1947. doi: 10.1016/S0140-6736(11)60547-3

Hofstetter, C. P., Schweinhardt, P., Klason, T., Olson, L., and Spenger, C. (2003). Numb rats walk–a behavioural and fMRI comparison of mild and moderate spinal cord injury. *Eur. J. Neurosci.* 18, 3061–3068. doi: 10.1111/j.1460-9568.2003.03062.x

Humanes-Valera, D., Aguilar, J., and Foffani, G. (2013). Reorganization of the intact somatosensory cortex immediately after spinal cord injury. *PLoS One* 8:e69655. doi: 10.1371/journal.pone.0069655

Jain, N., Qi, H.-X., Collins, C. E., and Kaas, J. H. (2008). Large-scale reorganization in the somatosensory cortex and thalamus after sensory loss in macaque monkeys. *J. Neurosci.* 28, 11042–11060. doi: 10.1523/jneurosci.2334-08.2008

Jazayeri, S. B., Beygi, S., Shokraneh, F., Hagen, E. M., and Rahimi-Movaghar, V. (2015). Incidence of traumatic spinal cord injury worldwide: a systematic review. *Eur. Spine J.* 24, 905–918. doi: 10.1007/s00586-014-3424-6

Keeler, B. E., Liu, G., Siegfried, R. N., Zhukareva, V., Murray, M., and Houlé, J. D. (2012). Acute and prolonged hindlimb exercise elicits different gene expression in motoneurons than sensory neurons after spinal cord injury. *Brain Res.* 1438, 8–21. doi: 10.1016/j.brainres.2011.12.015

Kim, B. G., Dai, H.-N., Mcatee, M., Vicini, S., and Bregman, B. S. (2006). Remodeling of synaptic structures in the motor cortex following spinal cord injury. *Exp. Neurol.* 198, 401–415. doi: 10.1016/j.expneurol.2005.12.010

Kumru, H., Benito-Penalva, J., Valls-Sole, J., Murillo, N., Tormos, J. M., Flores, C., et al. (2016). Placebo-controlled study of rTMS combined with Lokomat® gait training for treatment in subjects with motor incomplete spinal cord injury. *Exp. Brain Res.* 234, 3447–3455. doi: 10.1007/s00221-016-4739-9

Kumru, H., Murillo, N., Vidal Samso, J., Valls-Sole, J., Edwards, D., Pelayo, R., et al. (2010). Reduction of spasticity with repetitive transcranial magnetic stimulation in patients with spinal cord injury. *Neurorehabil. Neural Repair* 24, 435–441. doi: 10.1177/1545968309356095

Kuppuswamy, A., Balasubramaniam, A., Maksimovic, R., Mathias, C., Gall, A., Craggs, M., et al. (2011). Action of 5 Hz repetitive transcranial magnetic stimulation on sensory, motor and autonomic function in human spinal cord injury. *Clin. Neurophysiol.* 122, 2452–2461. doi: 10.1016/j.clinph.2011.04.022

Lee, M., Kiernan, M. C., Macefield, V. G., Lee, B. B., and Lin, C. S.-Y. (2015). Short-term peripheral nerve stimulation ameliorates axonal dysfunction after spinal cord injury. *J. Neurophysiol.* 113, 3209–3218. doi: 10.1152/jn.00839.2014

Lefaucheur, J.-P., André-Obadia, N., Antal, A., Ayache, S. S., Baeken, C., Benninger, D. H., et al. (2014). Evidence-based guidelines on the therapeutic use of repetitive transcranial magnetic stimulation (rTMS). *Clin. Neurophysiol.* 125, 2150–2206.

Li, N., Downey, J. E., Bar-Shir, A., Gilad, A. A., Walczak, P., Kim, H., et al. (2011). Optogenetic-guided cortical plasticity after nerve injury. *Proc. Natl. Acad. Sci.* 108, 8838–8843. doi: 10.1073/pnas.1100815108

Li, N., Van Zijl, P., Thakor, N., and Pelled, G. (2014a). Study of the spatial correlation between neuronal activity and BOLD fMRI responses evoked by sensory and channelrhodopsin-2 stimulation in the rat somatosensory cortex. *J. Mol. Neurosci.* 53, 553–561. doi: 10.1007/s12031-013-0221-3

Li, N., Yang, Y., Glover, D. P., Zhang, J., Saraswati, M., Robertson, C., et al. (2014b). Evidence for impaired plasticity after traumatic brain injury in the developing brain. *J. Neurotrauma* 31, 395–403. doi: 10.1089/neu.2013.3059

Liu, G., Keeler, B. E., Zhukareva, V., and Houlé, J. D. (2010). Cycling exercise affects the expression of apoptosis-associated microRNAs after spinal cord injury in rats. *Exp. Neurol.* 226, 200–206. doi: 10.1016/j.expneurol.2010.08.032

Lu, H., Kobilo, T., Robertson, C., Tong, S., Celnik, P., and Pelled, G. (2015). Transcranial magnetic stimulation facilitates neurorehabilitation after pediatric traumatic brain injury. *Sci. Rep.* 5:14769. doi: 10.1038/srep14769

Martin, R., Sadowsky, C., Obst, K., Meyer, B., and Mcdonald, J. (2012). Functional electrical stimulation in spinal cord injury: from theory to practice. *Top. Spinal Cord Injury Rehabil.* 18, 28–33. doi: 10.1310/sci1801-28

Matsubayashi, K., Nagoshi, N., Komaki, Y., Kojima, K., Shinozaki, M., Tsuji, O., et al. (2018). Assessing cortical plasticity after spinal cord injury by using resting-state functional magnetic resonance imaging in awake adult mice. *Sci. Rep.* 8:14406. doi: 10.1038/s41598-018-32766-8

McEwen, M. L., and Springer, J. E. (2006). Quantification of locomotor recovery following spinal cord contusion in adult rats. *J. Neurotrauma* 23, 1632–1653. doi: 10.1089/neu.2006.23.1632

Metz, G. A., Curt, A., Van De Meent, H., Klusman, I., Schwab, M. E., and Dietz, V. (2000a). Validation of the weight-drop contusion model in rats: a comparative study of human spinal cord injury. *J. Neurotrauma* 17, 1–17. doi: 10.1089/neu.2000.17.1

Metz, G. A., Merkler, D., Dietz, V., Schwab, M. E., and Fouad, K. (2000b). Efficient testing of motor function in spinal cord injured rats. *Brain Res.* 883, 165–177. doi: 10.1016/s0006-8993(00)02778-5

Nakamae, T., Tanaka, N., Nakanishi, K., Fujimoto, Y., Sasaki, H., Kamei, N., et al. (2010). Quantitative assessment of myelopathy patients using motor evoked potentials produced by transcranial magnetic stimulation. *Eur. Spine J.* 19, 685–690. doi: 10.1007/s00586-009-1246-8

Nessler, J. A., Leon, R. D. D., Sharp, K., Kwak, E., Minakata, K., and Reinkensmeyer, D. J. (2006). Robotic gait analysis of bipedal treadmill stepping by spinal contused rats: characterization of intrinsic recovery and comparison with Bbb. *J. Neurotrauma* 23, 882–896. doi: 10.1089/neu.2006.23.882

O'Reardon, J. P., Solvason, H. B., Janicak, P. G., Sampson, S., Isenberg, K. E., Nahas, Z., et al. (2007). Efficacy and safety of transcranial magnetic stimulation in the acute treatment of major depression: a multisite randomized controlled trial. *Biol. Psychiatry* 62, 1208–1216. doi: 10.1016/j.biopsych.2007.01.018

Pelled, G., Bergstrom, D. A., Tierney, P. L., Conroy, R. S., Chuang, K. H., Yu, D., et al. (2009). Ipsilateral cortical fmri responses after peripheral nerve damage in rats reflect increased interneuron activity. *Proc. Natl. Acad. Sci. U.S.A.* 106, 14114–14119. doi: 10.1073/pnas.0903153106

Pelled, G., Dodd, S. J., and Koretsky, A. P. (2006). Catheter confocal fluorescence imaging and functional magnetic resonance imaging of local and systems level recovery in the regenerating rodent sciatic nerve. *Neuroimage* 30, 847–856. doi: 10.1016/j.neuroimage.2005.10.027

Scheff, S. W., Rabchevsky, A. G., Fugaccia, I., Main, J. A., and Lumpp, J. E. Jr. (2003). Experimental modeling of spinal cord injury: characterization of a force-defined injury device. *J. Neurotrauma* 20, 179–193. doi: 10.1089/08977150360547099

Schulz, R., Gerloff, C., and Hummel, F. C. (2013). Non-invasive brain stimulation in neurological diseases. *Neuropharmacology* 64, 579–587. doi: 10.1016/j.neuropharm.2012.05.016

Shin, S. S., Krishnan, V., Stokes, W., Robertson, C., Celnik, P., Chen, Y., et al. (2018). Transcranial magnetic stimulation and environmental enrichment enhances cortical excitability and functional outcomes after traumatic brain injury. *Brain Stimul.* 11, 1306–1313. doi: 10.1016/j.brs.2018.07.050

Shin, S. S., and Pelled, G. (2017). Novel neuromodulation techniques to assess interhemispheric communication in neural injury and neurodegenerative diseases. *Front. Neural Circ.* 11:15. doi: 10.3389/fncir.2017.00015

Shinozaki, M., Yasuda, A., Nori, S., Saito, N., Toyama, Y., Okano, H., et al. (2013). Novel method for analyzing locomotor ability after spinal cord injury in rats. *Neurol. Med. Chir.* 53, 907–913. doi: 10.2176/nmc.tn2012-0223

Singh, A., Tetreault, L., Kalsi-Ryan, S., Nouri, A., and Fehlings, M. G. (2014). Global prevalence and incidence of traumatic spinal cord injury. *Clin. Epidemiol.* 6:309. doi: 10.2147/CLEP.S68889

Sydekum, E., Ghosh, A., Gullo, M., Baltes, C., Schwab, M., and Rudin, M. (2014). Rapid functional reorganization of the forelimb cortical representation after thoracic spinal cord injury in adult rats. *Neuroimage* 87, 72–79. doi: 10.1016/j.neuroimage.2013.10.045

Van De Meent, H., Hosman, A. J., Hendriks, J., Zwarts, M., Group, E.-S. S., and Schubert, M. (2010). Severe degeneration of peripheral motor axons after spinal cord injury: a European multicenter study in 345 patients. *Neurorehabil. Neural Repair* 24, 657–665. doi: 10.1177/1545968310368534

Wrigley, P. J., Siddall, P. J., and Gustin, S. M. (2018). New evidence for preserved somatosensory pathways in complete spinal cord injury: a fMRI study. *Hum. Brain Mapp.* 39, 588–598. doi: 10.1002/hbm.23868

Yagüe, J., Humanes-Valera, D., Aguilar, J., and Foffani, G. (2014). Functional reorganization of the forepaw cortical representation immediately after thoracic spinal cord hemisection in rats. *Exp. Neurol.* 257, 19–24. doi: 10.1016/j.expneurol.2014.03.015

Conflict of Interest Statement: The authors declare that the research was conducted in the absence of any commercial or financial relationships that could be construed as a potential conflict of interest.

frontiers in Neuroscience

ORIGINAL RESEARCH
published: 07 May 2019
doi: 10.3389/fnins.2019.00421

In vivo Two-Photon Imaging of Anesthesia-Specific Alterations in Microglial Surveillance and Photodamage-Directed Motility in Mouse Cortex

Weilun Sun[1†], Kunimichi Suzuki[2†], Dmytro Toptunov[3], Stoyan Stoyanov[1], Michisuke Yuzaki[2], Leonard Khiroug[3,4] and Alexander Dityatev[1,5,6*]*

[1] Molecular Neuroplasticity, German Center for Neurodegenerative Diseases (DZNE), Magdeburg, Germany, [2] Department of Neurophysiology, Keio University School of Medicine, Tokyo, Japan, [3] Neurotar Ltd., Helsinki, Finland, [4] HiLIFE/Neuroscience Center, University of Helsinki, Helsinki, Finland, [5] Medical Faculty, Otto-von-Guericke University, Magdeburg, Germany, [6] Center for Behavioral Brain Sciences, Magdeburg, Germany

OPEN ACCESS

Edited by:
Stephen Louis Macknik,
SUNY Downstate Medical Center,
United States

Reviewed by:
Marie-Eve Tremblay,
Laval University, Canada
Stefka Gyoneva,
Biogen Idec, United States

***Correspondence:**
Stoyan Stoyanov
stojanst@yahoo.com
Alexander Dityatev
alexander.dityatev@dzne.de

[†] These authors have contributed equally to this work

Specialty section:
This article was submitted to Neural Technology, a section of the journal Frontiers in Neuroscience

Received: 21 January 2019
Accepted: 12 April 2019
Published: 07 May 2019

Citation:
Sun W, Suzuki K, Toptunov D, Stoyanov S, Yuzaki M, Khiroug L and Dityatev A (2019) In vivo Two-Photon Imaging of Anesthesia-Specific Alterations in Microglial Surveillance and Photodamage-Directed Motility in Mouse Cortex. Front. Neurosci. 13:421. doi: 10.3389/fnins.2019.00421

Two-photon imaging of fluorescently labeled microglia *in vivo* provides a direct approach to measure motility of microglial processes as a readout of microglial function that is crucial in the context of neurodegenerative diseases, as well as to understand the neuroinflammatory response to implanted substrates and brain-computer interfaces. In this longitudinal study, we quantified surveilling and photodamage-directed microglial processes motility in both acute and chronic cranial window preparations and compared the motility under isoflurane and ketamine anesthesia to an awake condition in the same animal. The isoflurane anesthesia increased the length of surveilling microglial processes in both acute and chronic preparations, while ketamine increased the number of microglial branches in acute preparation only. In chronic (but not acute) preparation, the extension of microglial processes toward the laser-ablated microglial cell was faster under isoflurane (but not ketamine) anesthesia than in awake mice, indicating distinct effects of anesthetics and of preparation type. These data reveal potentiating effects of isoflurane on microglial response to damage, and provide a framework for comparison and optimal selection of experimental conditions for quantitative analysis of microglial function using two-photon microscopy *in vivo*.

Keywords: microglia, motility, two-photon imaging, anesthesia, isoflurane, ketamine

INTRODUCTION

Microglia are highly dynamic immune cells of the central nervous system which have a wide range of functions and play important roles in brain physiology and pathologies. Previous studies have shown microglia make contacts with the vasculature, neurons, and astrocytes (Nimmerjahn et al., 2005) and may promote dendritic spine formation (Parkhurst et al., 2013; Miyamoto et al., 2016). The homeostatic activity of microglia involves protecting the brain from a barrage of frequently

occurring small lesions, ranging from ruptured micro-capillaries to dying cells releasing toxic content into tightly controlled extracellular space (Kraft and Harry, 2011; Nayak et al., 2014). This protective function relies on at least two distinct types of motility of microglial processes: (i) surveilling motility, and (ii) damage-directed motility.

The surveilling, a.k.a. resting, motility refers to surveillance of the microglial cell's immediate environment, which enables timely detection of brain damage and pathogen infiltration (Hanisch and Kettenmann, 2007). This surveilling motility crucially depends on the membrane potential and requires the constitutive hyperpolarizing activity of a specific type of inwardly-rectifying potassium channel called TWIK-related Halothane-Inhibited K^+ channel, THIK-1 (Madry et al., 2018). Resting motility also underlies microglia-synapse interactions, during which microglial processes monitor synaptic function and modify the "wiring" of neuronal circuits by strengthening or eliminating individual synapses (Wake et al., 2009; Tremblay et al., 2010; Schafer et al., 2012). Noteworthy, microglial surveillance can be selective/directional in the sense that microglial cells monitor and interact with neurons during conditions of cerebral calcium reduction in the normal and diseased brain (Eyo et al., 2015).

The damage-directed motility manifests as an extension, or protrusion, of microglial processes toward a micro-lesion site (Davalos et al., 2005; Nimmerjahn et al., 2005; Haynes et al., 2006; Gyoneva et al., 2014). In contrast to surveillance, damage-directed motility of microglial processes does not require THIK-1 activity and hyperpolarized membrane potential but depends on activation of the metabotropic purinergic receptor P2Y12 by ATP released from the damaged cell(s) (Haynes et al., 2006). Other types of purinergic receptors, including P2Y6, are involved in the phagocytic activity of microglia at the site of damage (Hidetoshi et al., 2012). Microglial response to brain damage is also regulated by TAM (Tyro3, Axl, and Mer) receptors (Fourgeaud et al., 2016). These receptors play multiple functional roles as homeostatic regulators in adult tissues and organ systems that are subject to continuous challenge and renewal throughout life (Lemke, 2013) as well as in nervous system development and diseases (Pierce and Keating, 2014).

General anesthesia is commonly used during *in vivo* imaging, however, it may dramatically alter the function of brain cells, including microglia. Known effects of anesthetics range from suppressing neuronal firing and changing inter-cortical synchronization to altering the morphology of glial processes and affecting turnover rates of dendritic spines (Li et al., 2010; Huh and Cho, 2013; Pryazhnikov et al., 2018). Recently, Madry et al. (2018) have demonstrated that isoflurane and related gaseous anesthetics strongly suppressed the motility of microglial processes in acute brain slices. This suppression was mediated by anesthetics' blocking effect on THIK-1. The authors demonstrated that both types of motility, non-directional and damage-directed, were suppressed when isoflurane was applied either *in vivo* prior to slice preparation or *in situ* by direct exposure of slices.

Interestingly, suppression of microglial motility appears to be restricted to gaseous anesthetics, because injectable anesthetics such as urethane did not have such an effect (Madry et al., 2018). It remains unknown, however, whether another injectable anesthetic ketamine, which is widely used in mouse imaging experiments, also affects non-directional and/or damage-directed motility of microglial processes. Furthermore, since the motility-suppressing effect of isoflurane was observed *ex vivo* by imaging in brain slices, the question of whether this effect also occurs *in vivo* remains unanswered and must be addressed using microscopic analysis of the living brain. Besides anesthesia, other factors can affect the outcome of *in vivo* experiments, such as the interval between implantation of a cranial window and imaging (hours for acute preparation vs. weeks for chronic preparation).

Here, we set out to address these issues by using *in vivo* two-photon microscopy and directly compared the kinetics of both resting and damage-directed motility of microglial processes between awake and anesthetized states in acute and chronic preparations.

MATERIALS AND METHODS

Animals

Seven 3–4 month-old male CX3CR1-GFP heterozygous C57BL/6JCRL mice (B6.129P-Cx3cr1tm1Litt/J) (Jung et al., 2000) (Jackson Laboratory; Stock No.005582) bred at the DZNE (Magdeburg) animal facility were used in this study. Since we were comparing different conditions in the same animal, no randomization was performed. The mice were housed individually under a fixed 12-h light/dark cycle with food and water available *ad libitum*. All animals were treated in strict accordance with ethical animal research standards defined by the German law and approved by the Ethical Committee on Animal Health and Care of Saxony-Anhalt state, Germany (license number: 42502-2-1346).

Surgical Procedures

Surgeries were performed as described previously (Senkov et al., 2006; Holtmaat et al., 2009). Briefly, mice were sedated in a chamber with isoflurane (Baxter, Germany) prior to being stabilized in the stereotaxic apparatus (SR-6M, Narishige Scientific Instrument Lab, Japan). Under stereotaxic head fixation, isoflurane level was adjusted by using an isoflurane vaporizer (Matrx VIP 3000, Midmark, USA) to 4% for induction and 1.5–2% during surgery with 0.4 L/min O_2, while the depth of anesthesia was monitored by breathing rate. During surgery, mice were placed on a heating blanket connected to a temperature controller (ATC1000, World Precision Instruments, USA) with the temperature maintained at 37°C. An intraperitoneal (i.p.) injection of ketoprofen (5 mg/kg, body weight) was done before surgery to prevent inflammation and pain. In order to protect eyes from dehydration and irritation, ophthalmic ointment was applied. After shaving the hair and cleaning the scalp with 70% ethanol, a cutaneous incision was made and a flap of skin, $\sim$ 1 cm^2, covering the skull over both hemispheres was removed. Then the surface of the skull was cleaned with 10% povidone-iodine (Dynarex) and 3% hydrogen peroxide solution (Sigma-Aldrich, Germany).

A craniotomy (diameter ∼5 mm, centered over midline) was gently performed with a high-speed dental drill (Eickemeyer, Germany) over the cortical area between bregma and lambda. To prevent heat-induced damage of the underlying cortex, drilling was interrupted, and sterile saline was applied on the skull periodically. The craniotomy was then covered with a circular glass coverslip (6 mm diameter, Thermo Fisher Scientific, Germany) and fixed with cyano-acrylic glue (Roti Coll-1, CarlRoth, Germany). A custom-built 3D printed metal head-plate (i.materialize, Belgium) was then implanted on the exposed skull with glue and cemented with dental acrylic (Paladur, Heraeus Kulzer, Germany). After all procedures, mice were kept in a home cage with red-lamp warming for ∼30 min until they recovered from anesthesia.

Two-Photon *in vivo* Imaging

To address the differences of microglial morphology and dynamics between awake and anesthetized conditions, we performed the same imaging procedures in awake, isoflurane- and ketamine-anesthetized conditions, respectively. Because we were using the same animals for different conditions and the anesthesia method was too transparent, we could not perform blinding in this study. GFP-labeled microglial cells were imaged by a custom-built two-photon microscope (Thorlabs, USA) with a Ti: Sapphire pulsing laser (Chameleon, Coherent, USA) tuned to 850 nm. A 20 X water immersion lens (1.00 N.A.; Olympus, Japan) at a zoom of 1.0 was used to acquire 512 × 512 pixels images with a field-of-view of 393 × 393 μm throughout all imaging sessions. Imaging and two-photon laser ablation protocols were modified from previous studies (Davalos et al., 2005; Nimmerjahn et al., 2005) and time-plan of experiments is shown in **Figure 1A**. In order to avoid the effects of imaging under one condition on subsequent imaging under another condition, hemispheres were divided into quadrants and distinct quadrants were used in different imaging sessions (as shown in **Figure 1A**). For the first day after surgery, quadrants 1 and 3 were used for awake condition and isoflurane-anesthetized condition, respectively. Quadrants 2 and 4 were used for second awake condition and ketamine-anesthetized condition 2 days after surgery, respectively. 1&3 (anterior) and 2&4 (posterior) quadrants were counterbalanced between animals. For awake-condition (1 day after surgery), mice were head-fixed under the two-photon microscope using a Mobile HomeCage device (Neurotar, Finland) in which head-fixed animals could freely move a light cage around them. After 10 min habituation in the Mobile HomeCage, time-lapse imaging was performed for 33 min (100 frames, 20 s interval) by recording z-stacks (6 optical sections with a step size of 2 μm) around 100–150 μm below the pial surface to monitor microglial morphology and dynamics in the resting state. After acquiring images in the resting state, a single cell laser ablation was achieved by focusing a two-photon laser beam at a single microglia cell in the superficial layer of the cortex to induce a highly precise and reproducible local injury. The wavelength of the pulsed infrared laser was set to 780 nm and the power was ∼150–200 mW at the target. The laser beam was parked at the targeted cell by zooming in to an 18 × 18 μm field-of-view for ∼0.5 s to create a small highly localized photo-damage. The final injury area was determined by a relatively bright autofluorescent sphere (∼ 20 μm diameter) around the focal point. Immediately after the single cell laser ablation, the same imaging procedure as in the resting state was taken. Afterward, another laser ablation was performed at least 400 μm away from the first one. After imaging in awake mice, 2-h rest was given to each animal before we started the imaging session in the isoflurane-anesthetized condition. The same procedures of imaging as in awake-condition were applied in the other hemisphere, but the animal was head-fixed using a custom-made frame with a heating pad to keep body temperature constant, and anesthetized by 1.5% isoflurane during the imaging, which started 10 min after anesthesia induction, i.e., with the same interval as the habituation period in awake condition. On the next day (2 days after surgery), we repeated awake-condition imaging in another quadrant as described above. After 2-h rest, animals were intraperitoneally injected with ketamine (90 mg/kg body weight) and xylazine (18 mg/kg body weight) in 0.9% NaCl solution and placed in a head fixation frame in the same manner as used for imaging in isoflurane-anesthetized condition. During the imaging session, ketamine was added approximately every 35 min to maintain anesthesia between basal recording and after-damage recordings. The imaging procedure in ketamine-anesthetized condition was the same as for the other two conditions. All imaging sessions under different conditions were repeated at 4 months post-surgery, i.e., after the cranial window reached a chronic (steady-state) condition and the only difference was the interval between awake 1 and awake 2 imaging sessions, which was 7 days instead of 1 day (**Figure 1A**).

Analysis of Microglia Dynamics in Surveillance and Photodamage-Directed State

Before the quantitative analysis, the movement artifacts in obtained images (100 frames and 6 z-stacks) were neutralized using ImageJ software (Schindelin et al., 2012). Six sequential z-stacks of images were first subjected to the ImageJ plug-in StackReg/TurboReg with "rigid body" mode and the aligned z-stacks were maximally projected to a single image at every frame (Thévenaz et al., 1998). The projected images aligned along z-axis were then subjected to the same alignment processing along the time-axis (100 frames). Briefly, every 10 frames were averaged to improve the signal-to-noise ratio and compared between the first 10 frames (0–3 min) and the last 10 frames (30–33 min). Each microglia process was 2-dimensionally traced by the Fiji plug-in Simple Neurite Tracer (Longair et al., 2011). Tracing of microglial processes was done by an experimenter blind to the experimental conditions. The longest processes stemming from the microglial cell body were traced as the primary processes, and the arborized processes from each primary process were traced to include the secondary, but not tertiary or further, branches. We calculated the average length and number of primary processes per microglia, the average length of arborized primary processes per microglia, the average terminal number in the arborized primary processes, the total length of the primary

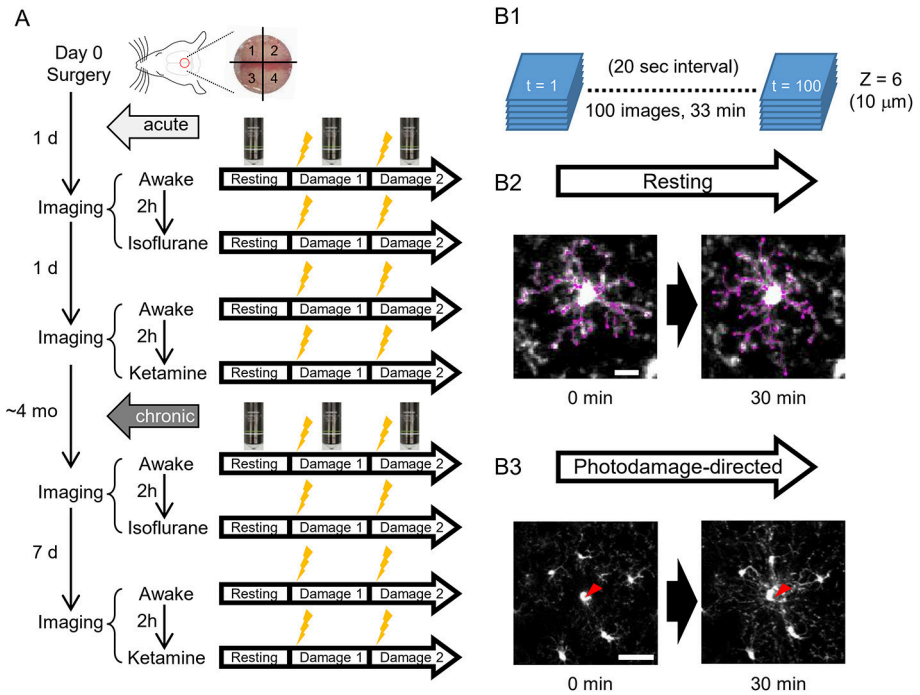

FIGURE 1 | A scheme of experiments. **(A)** Schedules of *in vivo* two-photon imaging of microglia in awake, isoflurane- and ketamine-anesthetized mice. For each condition, imaging is done in a resting and photodamage state. The same imaging protocols are applied acutely, i.e., 1–2 days after the surgery (5 animals), and/or in chronically implanted mice (around 4 months after the surgery, 4 animals). **(B)** Imaging examples in the resting and photodamage conditions. **(B1)** Z-stacks (6 images) are acquired at a 20 s interval for 33 min, generating 100 time frames. **(B2)** Two-dimensional tracing of microglia processes with 30 min interval in the resting state (scale bar, 10 μm). **(B3)** Analysis of microglia response to photodamage. A red arrowhead indicates the center of damage induced by the high-power laser stimulation (scale bar, 50 μm).

+ secondary (defined as "all") processes and the total numbers of the all processes per microglia. Each process was traced twice, with 30 min interval, and the changes were qualified as "Disappear," "Decrease," "No change," "Increase" and "Appear" with respect to each primary process, arborized process, and all processes. The parameters were measured and averaged from at least 3 microglial cells per animal. Our quantification method is similarly based on the manual tracing of processes and provides the terminal number that is comparable to the previously reported value by other researchers (on average, 18 vs. 20 in control conditions; Nimmerjahn et al., 2005). Although our measurements resulted in a shorter total length of processes than previously reported (226 vs. 400 μm; Nimmerjahn et al., 2005), probably due to differences in the imaging conditions and the criteria used for tracing of processes, we can compare the lengths of processes among different conditions within our study. The dynamics of microglial processes is similar for our and the previous work (same fractions of processes which were increased or decreased, resulting in constant total length), suggesting the validity of our measurements.

For the analysis of damage-directed response, the quantification of microglial process velocity was based on the intensity of microglia around damage spot, which is a method similar to Davalos et al. (2005) and rendered the comparable value (1.6 vs. 1.2 μm/min) in control conditions. In detail, as a method to calculate the velocity of damage-directed process motility, the center of each ROI was set to the microglial processes apparent attraction point. Using the Radial Profile Extended ImageJ plugin, the normalized intensity profiles for $R \leq 75$ μm for each time point were calculated. A set of these 100 radial profiles was converted into grayscale images and 3D height images using a custom-built R script. Microglial processes were readily visible as a distinct stripe on the 2D images and as a ridge on the 3D images. Using the 2D image, a line ROI was drawn along the path of the microglial processes and their projections onto time (Δt) and distance to the damage (ΔD) axes. *Velocity was measured as* $\Delta D/\Delta t$. Additionally, in order to get a better visualization of the events happening during the microglial activity, a stack was converted into a color-coded image, where each time point was coded with its own color (**Figure 5A**). Since the velocity of damage-directed process motility is a crucial parameter in such studies, we additionally applied another—more objective—method by using the Sholl analysis applied to the aligned z-projection images (100 frames) to measure the advance of microglia process toward the injury spot. The measurement was done from the time when the microglia process started to migrate toward the injury center to the time when the microglia reached the injury spot. To reduce the noise and background and specifically detect the dynamics of the microglia process, the

Gaussian filter ($\sigma = 0.5$) and background subtraction (10 px) was applied to every image and the bright signals of microglia soma and injury spot artifact were deleted by the masked images derived from Analyze Particles calculation (>50 px, default threshold, at the first frame). Then the process frontier was measured by detecting the peak intensity of microglia processes on the circumference at the distance from the injury spot. The auxiliary line was drawn to enhance the visible frontier in some images with a lower signal-to-noise ratio. The distance of peak intensity was plotted along the time and the regression curve was calculated as a linear line with the high correlation coefficient between the observed and predicted values ($R^2 > 0.9$). The slope was used as the calculated velocity (**Supplementary Figure 3A**). Finally, we defined the injury size as the size of the relatively bright autofluorescent sphere around the focal point immediately after laser ablation and the activation area was measured according to the radius of the apparent microglia process frontier starting to approach the center of the photodamage (**Supplementary Figure 4**). Statistical analysis was performed using XLSTAT (STATCON, Germany), as described in Results.

RESULTS

To analyze microglia functions *in vivo*, we implanted a glass-covered cranial window above the cortical region between bregma and lambda, including the retrosplenial cortex, which is one of the cortical areas critically involved in spatial navigation that is affected at early stages of Alzheimer's disease. Two-photon imaging was performed either in acute preparation, i.e., on the first and second days after the window implantation (5 mice), or in chronic preparation, i.e., 4 months after the implantation (3 of the 5 acutely imaged mice and 1 new mouse) (**Figure 1**). The effects of two commonly used anesthetics,

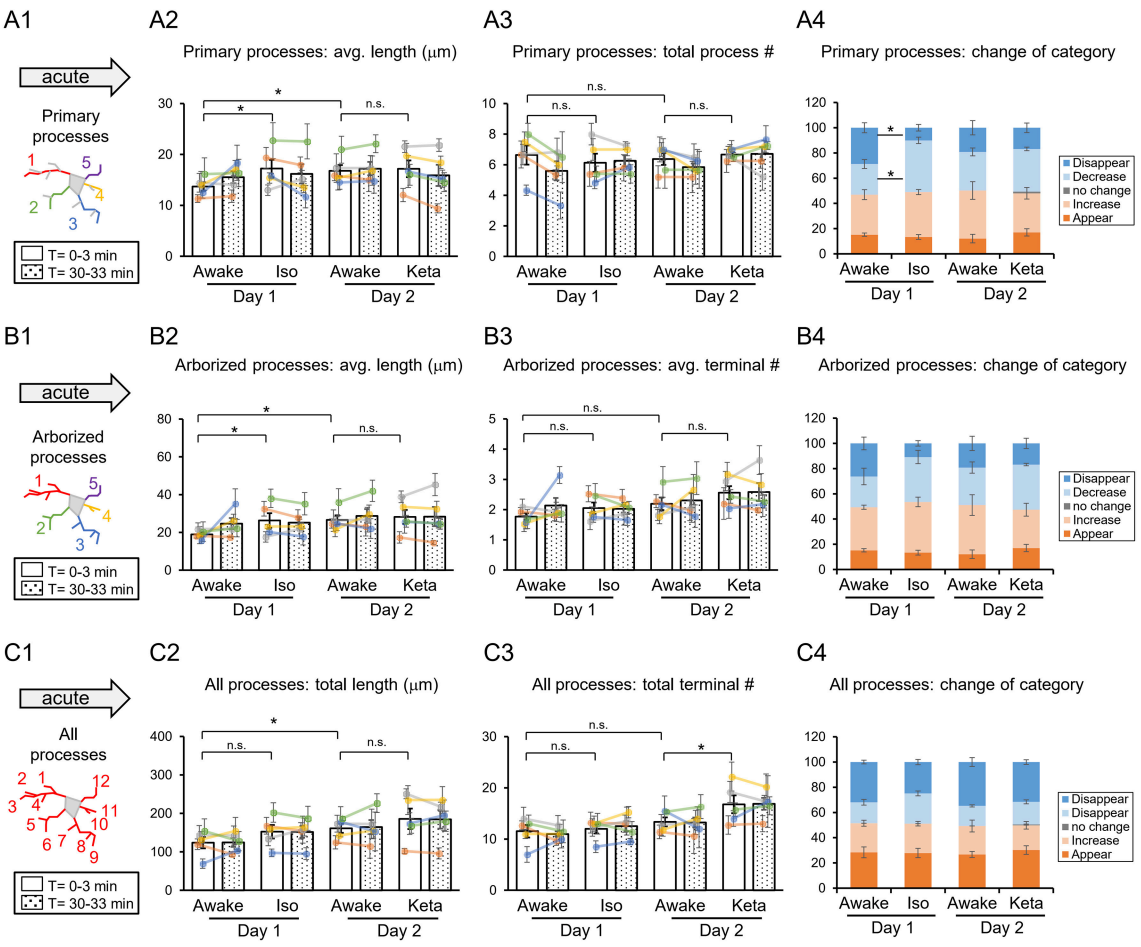

FIGURE 2 | Dynamics of microglial processes in awake, isoflurane (Iso)- and ketamine (Keta)-anesthetized mice in acute experiments (5 animals). Schematic drawing of microglial processes (represented in color-matching mode): primary processes **(A1)**, arborized processes **(B1)** and all processes **(C1)**. Quantification of the average or total length and the total terminal number per primary process **(A2,A3)**, arborized process **(B2,B3)** and all processes **(C2,C3)**. The dots show individual mean values ± SEMs per animal, the values from the same animal are connected by lines **(B2,B3,C2,C3)**. White and dotted bars show means ± SEMs for all animals at time = 0 and 30 min. Processes are categorized according to morphological changes, such as "Disappear," "Decrease," "No change," "Increase," or "Appear" **(A4,B4,C4)**. *$p < 0.05$, n.s., non-significant, one-way RM nested ANOVA, Newman-Keuls *post-hoc* test for A2–C2; Kruskal-Wallis test with Conover-Iman multiple comparison tests for A3–C3 and A4–C4.

isoflurane and ketamine, were analyzed. The longitudinal design allowed a within-animal comparison of microglial morphology and motility in awake vs. anesthetized conditions on the same day, with a 2-h interval between sessions. Each session included imaging of microglia at the resting state and after photodamage induced at two spatially separated sites by laser ablation of a single microglia cell (**Figure 1**), as the only unequivocally defined target in our experimental settings.

Analysis of Structure and Motility of Microglia at the Surveilling State

To characterize microglia at the surveilling state, we traced their processes and compared the length and number of primary microglial processes (the longest processes originating from the soma, without secondary, tertiary, etc. branches; **Figure 2A1**), as well as the length and number of terminals of arborized processes, i.e., including secondary but not tertiary or further branches (**Figure 2B1**). Then, we analyzed the total length and number of terminals of all processes per cell (**Figure 2C1**). The same cells were traced twice, at time 0 and in 30 min (white and dotted columns, respectively, in **Figures 2**, **3**) to quantify the cell motility. A representative movie of microglia at the surveilling state is shown in **Supplementary Material**.

In acute preparation, we found a difference between measurements done in awake and anesthetized conditions (using one-way repeated measures (RM) nested ANOVA for the length of processes and Kruskal-Wallis test for the number of processes and the change of the categories), with the type of anesthesia affecting the microglia processes in different ways (**Table 1**). During isoflurane anesthesia on day 1, microglial primary and secondary processes were significantly elongated compared to the awake condition. This was evident in terms of the average length of primary processes ($p = 0.038$; **Figure 2A2**) and the

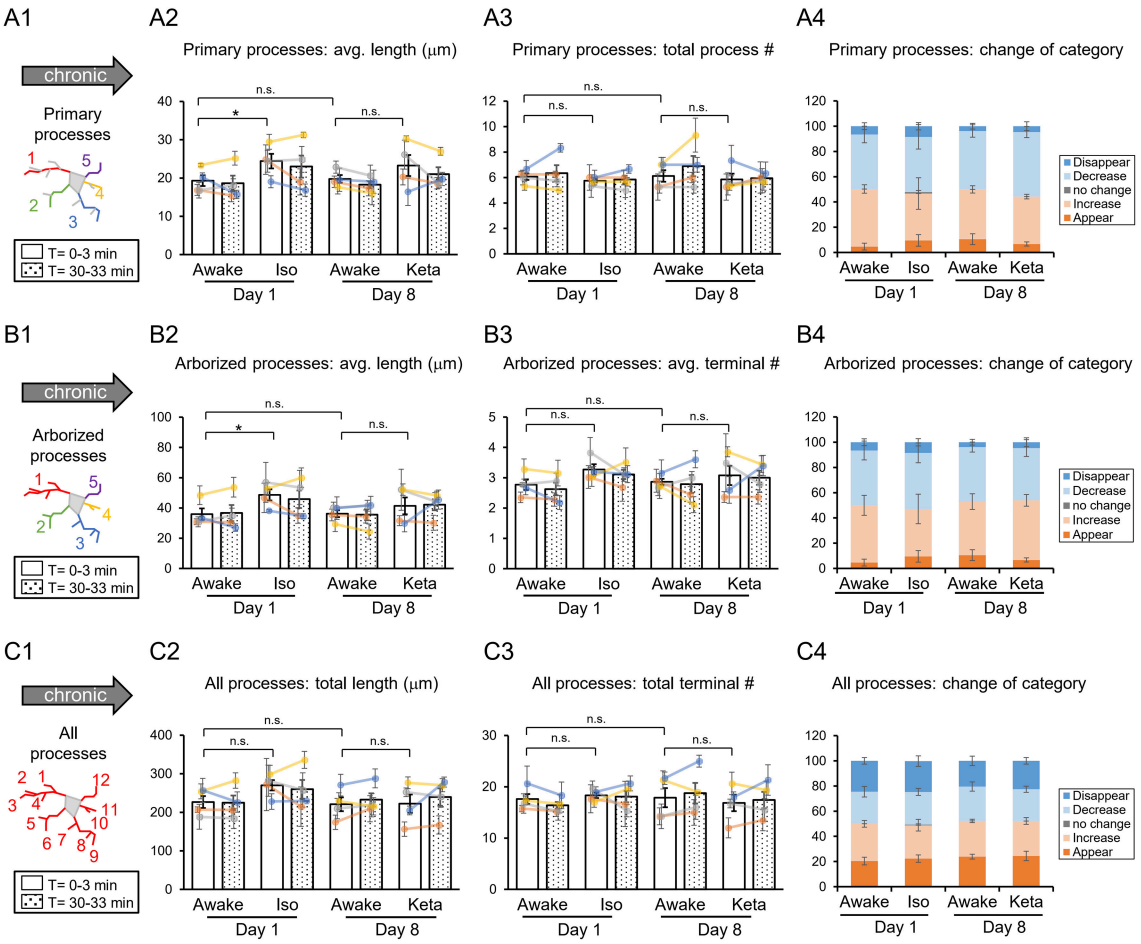

FIGURE 3 | Dynamics of microglial processes in awake, isoflurane (Iso)- and ketamine (Keta)-anesthetized mice in chronic experiments (4 animals). Schematic drawings of microglial processes to be analyzed (in colors): primary processes **(A1)**, arborized processes **(B1)**, and all processes **(C1)**. Quantification of average or total length and total terminal number of primary processes **(A2,A3)**, arborized processes **(B2,B3)** and all processes **(C2,C3)**. The dots show individual mean values ± SEMs per animal, the values from the same animal are connected by lines **(B2,B3,C2,C3)**. White and dotted bars show means ± SEMs for all animals at time = 0 and 30 min. Processes are categorized according to morphological changes, such as "Disappear," "Decrease," "No change," "Increase," or "Appear" **(A4,B4,C4)**. *$p < 0.05$, n.s., non-significant, one-way RM nested ANOVA, Newman-Keuls *post-hoc* test for A2–C2; Kruskal-Wallis test with Conover-Iman multiple comparison tests for A3–C3 and A4–C4.

TABLE 1 | Summary of results: "↑" and "↓" means a significant increase and decrease, respectively, $p < 0.05$.

Motility type		Acute cranial window		Chronic cranial window	
		Isoflurane	Ketamine	Isoflurane	Ketamine
Microglial surveilling	Length	↑		↑	
	Ramification		↑		
	Processes' disappearance	↓			
Damage- directed	Velocity			↑	
	Activation area				

average length of arborized processes ($p = 0.003$; **Figure 2B2**). A *post-hoc* pairwise comparison showed an increase in the average length of primary and arborized processes in the isoflurane group (17.2 ± 1.7 and 26.3 ± 3.9 μm, respectively) as compared to awake mice on day 1 (13.7 ± 0.8 and 18.9 ± 1.0 μm, respectively; **Figures 2A2,B2**). In contrast, during ketamine anesthesia on day 2, the average length of processes was unchanged but the number of total processes was increased compared to the awake condition (total number of terminals of all processes ($p < 0.001$; **Figure 2C3**). Specifically, ketamine increased the total terminal number of all processes (13.4 ± 0.9 vs. 16.8 ± 1.7; **Figure 2C3**). Additionally, a difference between awake mice imaged on days 1 and 2 was found in terms of process lengths (primary: 13.7 ± 0.8 and 16.8 ± 1.1 μm, respectively, **Figure 2A2**; arborized: 18.9 ± 1.0 and 26.6 ± 2.5 μm, respectively, **Figure 2B2**; all processes: 123.8 ± 14.7 and 161.1 ± 11.7 μm, respectively, **Figure 2C2**), suggesting that anesthetized condition, as well as imaging period, differentially affect the microglia processes in acute preparation.

When we followed microglia processes over a 30-min interval, we did not find any differences in the process length between awake and anesthetized conditions (**Supplementary Figure 1**). However, a closer inspection of process dynamics revealed that the isoflurane anesthesia affected the turnover of microglia processes, with fewer primary processes disappearing and more primary processes decreasing under isoflurane anesthesia than in awake mice on day 1, while the appearance and elongation of new processes were not affected (**Figures 2A4–C4**).

In chronic preparation, we again found a significant difference between the awake and isoflurane-anesthetized conditions in terms of the average length of primary processes ($p = 0.008$; **Figure 3A2**) and the average length of arborized processes ($p = 0.039$; **Figure 3B2**; one-way RM nested ANOVA). In line with acute experiments, we observed an increase in the length of primary and arborized processes in isoflurane-anesthetized (24.4 ± 2.1 and 48.6 ± 4.1 μm, respectively) vs. awake conditions (19.3 ± 1.6 and 35.9 ± 4.2 μm, respectively) in chronic experiments (**Figures 3A2,B2**). No difference in other structural parameters and motility was detected (**Figure 3**).

Analysis of acute vs. chronic preparation revealed the effect of an interaction between Condition and Preparation on the total length of all processes ($p = 0.017$; **Supplementary Table 2**). We observed an increase in the total length in chronic preparation (226.7 ± 17.2 μm) vs. acute preparation in the first awake condition (123.8 ± 14.7 μm; **Figure 4**), suggesting that in the chronic preparation microglia are more in the surveilling rather than activated state in contrast to the acute preparation. Statistical summary for comparisons of parameters at the resting state is displayed in **Supplementary Table 1**.

Analysis of Damage-Directed Microglia Response

To study the damage-directed microglia response, we induced photoablation of a single microglial cell. Laser irradiation of microglia soma resulted in a collapse of the microglia processes. The site of damage remained visible as a fluorescent spot to which other microglial cells extended their processes, forming a ring-like structure (**Figure 5A1**). A representative movie of microglial response to a photodamage is shown in **Supplementary Material**. Measuring the intensity of fluorescence as a function of distance to the damage center in the time series of 3D images (**Figures 5A1–3**), revealed a peak (at the position of the ring) that was approaching the damage site with a constant velocity. One-way RM nested ANOVA revealed a difference between four conditions in terms of velocity in both acute and chronic preparations ($p = 0.001$ and $p = 0.005$, respectively; **Figures 5B1**, **2**). In acute experiments, there was no effect of anesthetics, but there was a significant difference between days 1 and 2 under awake conditions (1.7 ± 0.4 and 2.5 ± 0.2 μm/min, respectively). In chronic experiments, the velocity was increased under isoflurane anesthesia (2.6 ± 0.4 μm/min) compared to awake condition (1.6 ± 0.1 μm/min) on day 1. Direct comparison between acute and chronic preparation revealed that a faster process velocity was seen in isoflurane condition in chronic than in acute preparations (**Figure 5C**), suggesting that the isoflurane differently affect microglia response in these experimental conditions. A slightly different method for measurements of velocity was based on the determination (for each frame) of the distance where the maximal fluorescence intensity was observed (**Supplementary Figures 3A1,A2**). Then a linear regression was used to determine the velocity (**Supplementary Figure 3A3**). Noteworthy, the linear regression provided an excellent fit to data ($R^2 > 0.9$) and the results obtained by this method (**Supplementary Figures 3B1–2, C1–2**) perfectly matched the outcome of the aforementioned analysis of velocity.

Additional analysis of damage-directed microglia behavior by measuring the cumulative intensity of microglial processes in the area surrounding the photodamage site revealed that at some sites there was a biphasic response: immediately after photodamage, microglia first moved away from the damage, i.e., was repelled from, and then attracted to the damage site (**Supplementary Figure 2**). Hence, as another measure of microglial activation, we estimated the maximal size of the area surrounded by microglia processes in a ring-like manner at the moment when the frontier of microglia processes starts to advance toward the damage site. There was large variability in this activation area in acute experiments ($p = 0.006$; **Supplementary Figure 4A**). On average, the profile of the mean activation area in all experimental groups mirrored that

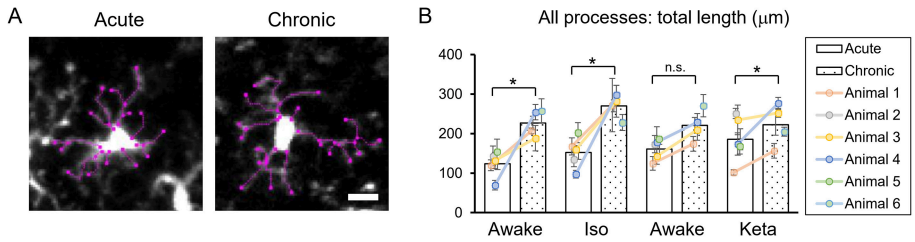

FIGURE 4 | Dynamics of microglial processes in acute vs. chronic preparations. **(A)** Representative images of microglia from acute and chronic preparations, respectively (scale bar, 10 μm). **(B)** Comparison of total length of all microglial process between acute and chronic preparation in all conditions. The dots show individual mean values ± SEMs per animal, the values from the same animal are connected by lines. White and dotted bars show means ± SEMs for all animals in acute and chronic preparations. *$p < 0.05$, n.s., non-significant, the Newman-Keuls *post-hoc* test.

of mean velocity (**Figure 5B**). Correlation analysis of velocity and activation area within individual experiments revealed a highly significant correlation between these parameters both in acute experiments (Spearman $r = -0.576$, $p = 0.00014$), and in chronic experiments (Spearman $r = -0.371$, $p = 0.043$), particularly under isoflurane anesthesia (Spearman $r = -0.526$, $p = 0.030$). To find out whether the velocity also depended on other parameters in photodamage experiments, we performed correlation analysis for the damage area, estimated as the fluorescent area at the site of laser irradiation, the number of microglia cells adjacent to the damage site and the mean distance between their somata and the damage site. There were no significant correlations between these parameters and velocity in acute and chronic experiments (**Supplementary Figure 4**). Statistical summary for comparisons of parameters in response to a photodamage is displayed in **Supplementary Table 3**.

Taken together, these data demonstrate that morphology and motility of microglia *in vivo* are strongly affected by such experimental conditions as the preparation type (acute vs. chronic preparation) and state of consciousness (awake vs. ketamine-anesthetized vs. isoflurane-anesthetized).

DISCUSSION

The main findings of this study are the significant effects of both the preparation type and the anesthetics on microglial morphology, motility, and response to damage. Notably, the potentiating effect of isoflurane on microglial motility that we observed using *in vivo* imaging is in sharp constant with the motility-suppressing effect of isoflurane observed previously using *ex vivo* and *in vitro* imaging (Madry et al., 2018), once again highlighting the need for caution when extrapolating the results of *ex vivo*/*in vitro* experiments to *in vivo* conditions. However, we acknowledge that the effect of anesthesia depends on the readout used for analysis.

In the chronic preparation, where the cranial window was implanted 4 months prior to imaging, isoflurane (but not ketamine) significantly increased the length of microglial processes and accelerated their damage-directed motility. These effects are consistent with the notion that isoflurane enhances the homeostatic microglial activity and reinforces the "resting-state" phenotype of microglia characterized by highly-ramified morphology and rapid reaction to microscale lesions. Ketamine anesthesia had no effect on the parameters quantified in this study (**Table 1**), suggesting that this injectable anesthetic may be more suitable than gaseous ones (such as isoflurane) for chronic microglia imaging.

In acute preparation, isoflurane also induced significant elongation of microglial processes like in chronic preparation; however, isoflurane did not accelerate damage-directed microglial motility (**Table 1**). It seems plausible to suggest that in the acute preparation the strong effects of post-surgical inflammation on microglial motility and morphology may have masked the effect of isoflurane on damage-directed motility. Ketamine significantly increased microglial ramification under acute conditions, in contrast to chronic conditions where ketamine had no effect (**Table 1**). These findings indicate that putative post-surgical inflammation occurring during the first days after acute window implantation can have a dramatic effect on microglial motility and morphology, comparable to or even more prominent than the effects of anesthesia.

Interestingly, certain time-dependent changes observed in the acute preparation apparently resulted in a variety of alterations in microglial morphology and dynamics. Indeed, compared to post-surgical day 1, on day 2 the microglial processes were significantly elongated (**Figures 2A2–C2**), the damage-directed motility was significantly accelerated (**Figure 5B1**), and the activation area surrounding the damaged site was reduced (**Supplementary Figure 3B2**). While elucidation of the mechanisms underlying the observed time-dependent changes will require further studies, these changes are most likely related to a gradual onset of post-surgical inflammation.

Our findings, therefore, highlight the need for caution in interpreting data obtained with acute cranial windows (i.e., windows freshly prepared on the same day or 1–2 days prior to imaging). In sharp contrast to acute preparation, in chronic cranial windows, none of the quantified microglial parameters changed significantly between first and second imaging sessions (**Figures 3A3–C3**, **Figure 5B2**, and **Supplementary Figure 3C**). This is consistent with a relative stability of microglial morpho-functional parameters in chronic preparation, and is also in line with the conclusion of a previous study (Dorand et al., 2014) that a resting period of at least 1–3 weeks is preferable before collecting experimental data on microglia in order to

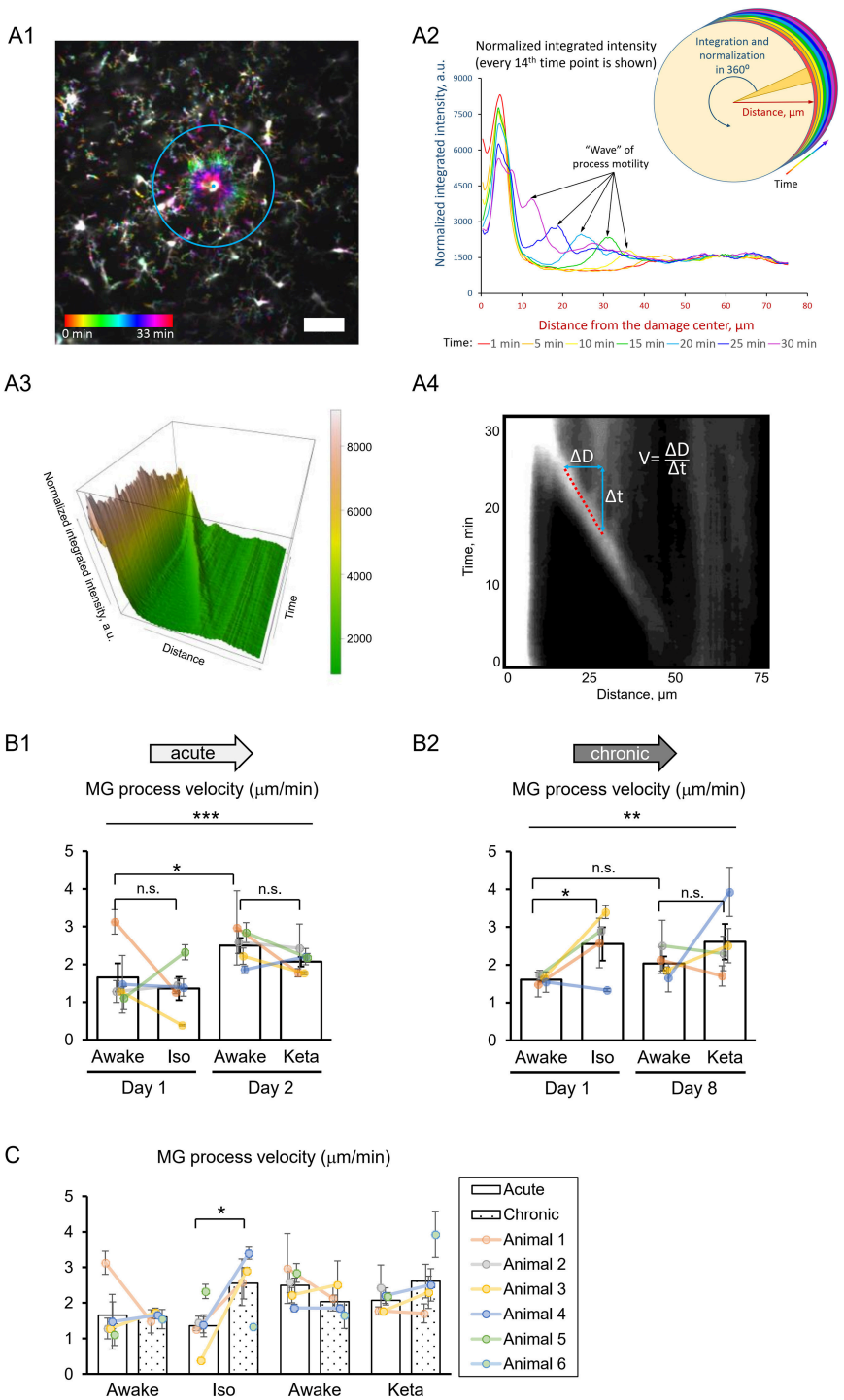

FIGURE 5 | 3D analysis of the photodamage-directed response of microglia. **(A1)** In order to get a better visualization of the events happening during the microglia activity, a time stack is converted into a color-coded image using a standard Fiji (ImageJ) function, where each time point is coded with its own color (scale bar, 50 µm). **(A2)** Sholl-analysis of fluorescence intensity as a function of distance from the damage site with colors matching those in **(A1)**. **(A3)** The three-dimensional plot to show the advance of microglial processes to the damage site. **(A4)** The same data as in **(A3)** are shown as a gray-coded image, with a line used to calculate the velocity. B. Quantification of microglial process velocity in acute **(B1)** and chronic **(B2)** experiments. **(C)** Comparison of microglial process velocity between acute and chronic experiments. The dots show individual mean values ± SEMs per animal, the values from the same animal are connected by lines (**B1,B2,C**). Bars show means ± SEMs values for all animals. *$p < 0.05$, **$p < 0.01$, ***$p < 0.001$, n.s., non-significant, the Newman-Keuls *post-hoc* test, 5 animals for acute and 4 animals for chronic experiments.

minimize local and systemic host responses toward potential damage resulting from the surgical procedure. As a valuable alternative preparation, a thinned-skull window has been widely used for imaging microglia *in vivo*, both for acute experiments (Wake et al., 2009; Liu et al., 2010) and chronic experiments (after implanting a coverslip on top of the thinned bone: Marker et al., 2010; Yang et al., 2010). This type of preparation is believed to minimize the inflammatory background unavoidable in cranial window preparations. However, the thinned-skull approach has limitations for deep imaging studies, and studies requiring a large visual field or direct access to brain parenchyma for drug or virus delivery. Therefore, our results outline optimal conditions for acute and chronic imaging in applications that may benefit from cranial window preparation due to a necessity to perform deep high-resolution imaging, for instance of interaction between microglia processes and presynaptic boutons or postsynaptic spines, or reproducible, stereotypical induction of the laser injury with a fixed set of parameters.

An alternative explanation for significant alterations in microglia dynamics observed on day 2 in acute preparation is that the effect of isoflurane administered on day 1 did not subside completely by the time when the same animal was re-imaged in awake conditions (day 2). A recent study has demonstrated that isoflurane anesthesia promoted phosphorylation of TrkB receptors in several brain regions (Antila et al., 2017). Although the phosphorylation *per se* was transient and subsided in 15 min (Antila et al., 2017), the downstream effects of TrkB phosphorylation may be much more long-lasting, as reported for clinical effects of isoflurane (Langer et al., 1985, 1995; Weeks et al., 2013). With the present design of the experiment, we intended to avoid possible long-lasting effects of ketamine anesthesia done on day 1 on subsequent imaging on day 2. However, we acknowledge that this approach imposes some limitations in the interpretation of our data due to the possible effect of previous exposures to anesthesia and/or laser injuries may affect the readout on the subsequent imaging day.

There are multiple mechanisms by which anesthetics (both volatile and injectable) could affect microglial dynamics. One of ketamine's best-characterized mechanisms of action is via inhibition of NMDA-type glutamate receptors, which are also expressed by microglial cells (Kaindl et al., 2008; Murugan et al., 2013). Furthermore, ketamine can exert its action via other receptors and/or signaling pathways, including brain-derived neurotrophic factor, which is considered to be a key player in ketamine's antidepressant action (Björkholm and Monteggia, 2016) as well as TLR3, NO and HCN1 (Mei et al., 2011; Sleigh et al., 2014). Considering ketamine's well-documented potentiating effect on dendritic spine formation rate (Li et al., 2010; Phoumthipphavong et al., 2016; Pryazhnikov et al., 2018), and the role of activated microglia in spine elimination under pathological conditions (Bisht et al., 2016, 2018), it is reasonable to hypothesize that ketamine's spine-promoting effect may, at least in part, be due to ketamine suppressing microglial activation. Indeed, our results demonstrate that, at least in acute preparation, ketamine increased ramification of microglial processes. The fact that this effect was not seen in chronic conditions suggests that the influence of ketamine on microglia is enhanced by a global stressor (i.e., surgery), while local damage did not result in a detectable influence of ketamine.

Like ketamine, isoflurane has been reported to affect microglia via several distinct mechanisms, involving modulation of NMDA receptors (which are inhibited by isoflurane, albeit less potently than by ketamine) as well as the TLR4/NF-kB pathway and GABAA receptors (Brosnan, 2011; Xiang et al., 2014; Sun et al., 2015). Changes in microglia behavior under isoflurane anesthesia are noteworthy in the context of the isoflurane-induced elevation in TrkB signaling (Antila et al., 2017) that might reflect the microglial release of BDNF or matrix metalloproteinases converting pro-BDNF to mature BDNF. In a recent study (Szalay et al., 2016), longitudinal two-photon imaging was performed in isoflurane-anesthetized mice to demonstrate a protective role of microglia in a model of stroke. While the authors argue that the low-level isoflurane (0.8–1.1%) used during imaging should not influence the observed detrimental effect of microglia removal on neuronal activity, it is noteworthy that a slightly higher level of isoflurane (1.5%) used during imaging in the current study, did have a significant effect on microglial process morphology, in both acute and chronic preparations (see **Table 1**).

In conclusion, considering the reproducibility and quality of data obtained with two-photon imaging of microglia in awake mice with a chronically implanted transcranial window, we recommend this approach for the studies of microglia morphology and function *in vivo* in adult animals. Obviously, this approach allows to avoid the confounding effects of anesthetics and transient inflammation induced by window implantation. Because we did not detect any differences between awake and ketamine-anesthetized mice with a chronically implanted transcranial window, the ketamine anesthesia could be a useful alternative to awake imaging, at least for analysis of parameters quantified in the present studies. However, other experimental factors, such as mouse genotype or global experimental stressors, may interact with chronic inflammation and ketamine in a yet unknown fashion and unpredictably bias the outcome; thus, microscopic imaging experiments in awake mice still should be preferred. Apart from the Mobile Home Cage used in the current study, alternative methods have been employed for imaging of head-fixed awake mice (Rangroo Thrane et al., 2012; Akiyoshi et al., 2018). If a laboratory is not equipped with a head-fixation device that allows awake imaging, then ketamine anesthesia could be preferable to isoflurane.

ETHICS STATEMENT

All animals were treated in strict accordance with ethical animal research standards defined by the German law and approved by the Ethical Committee on Animal Health and Care of Saxony-Anhalt state, Germany (license number: 4250 2-2-1346).

AUTHOR CONTRIBUTIONS

AD and LK initiated the study, SS and WS generated a detailed plan of experiments. SS, AD, LK, and MY supervised the research. WS performed imaging experiments, KS, DT, and AD analyzed the data. AD, LK, WS, and KS wrote the first draft. All authors edited the manuscript.

FUNDING

WS has been supported by the State Scholarship Fund of the China Scholarship Council (grant number 201406170032 to WS). The project has been supported by JSPS KAKENHI (15H05772 and 16H06461 to MY, 26860148 and 14J07587 to KS) and the federal state Saxony-Anhalt and the European Structural and Investment Funds (ESF, 2014-2020), project number ZS/2016/08/80645 (to AD). The authors gratefully acknowledge support from the Young Glia collaboration program (to WS, SS, and KS).

ACKNOWLEDGMENTS

The authors thank Dr. Janelle Pakan and Ms. Carla Cangalaya for comments to the manuscript.

SUPPLEMENTARY MATERIAL

The Supplementary Material for this article can be found online at: https://www.frontiersin.org/articles/10.3389/fnins.2019.00421/full#supplementary-material

Supplementary Video 1 | Representative movie of microglia at the surveilling state.

Supplementary Video 2 | Representative movie of microglial response to a photodamage.

REFERENCES

Akiyoshi, R., Wake, H., Kato, D., Horiuchi, H., Ono, R., Ikegami, A., et al. (2018). Microglia enhance synapse activity to promote local network synchronization. *eNeuro* 5:ENEURO.0088-18.2018. doi: 10.1523/ENEURO.0088-18.2018

Antila, H., Ryazantseva, M., Popova, D., Sipilä, P., Guirado, R., Kohtala, S., et al. (2017). Isoflurane produces antidepressant effects and induces TrkB signaling in rodents. *Sci. Rep.* 7:7811. doi: 10.1038/s41598-017-08166-9

Bisht, K., Sharma, K., and Tremblay, M. È. (2018). Chronic stress as a risk factor for Alzheimer's disease: roles of microglia-mediated synaptic remodeling, inflammation, and oxidative stress. *Neurobiol. Stress* 9, 9–21. doi: 10.1016/j.ynstr.2018.05.003

Bisht, K., Sharma, K. P., Lecours, C., Gabriela Sánchez, M., El Hajj, H., Milior, G., et al. (2016). Dark microglia: a new phenotype predominantly associated with pathological states. *Glia* 64, 826–839. doi: 10.1002/glia.22966

Björkholm, C., and Monteggia, L. M. (2016). BDNF - a key transducer of antidepressant effects. *Neuropharmacology* 102, 72–79. doi: 10.1016/j.neuropharm.2015.10.034

Brosnan, R. J. (2011). GABA(A) receptor antagonism increases NMDA receptor inhibition by isoflurane at a minimum alveolar concentration. *Vet. Anaesth. Analgesia* 38, 231–239. doi: 10.1111/j.1467-2995.2011.00605.x

Davalos, D., Grutzendler, J., Yang, G., Kim, J. V., Zuo, Y., Jung, S., et al. (2005). ATP mediates rapid microglial response to local brain injury *in vivo*. *Nat. Neurosci.* 8:752. doi: 10.1038/nn1472

Dorand, R. D., Barkauskas, D. S., Evans, T. A., Petrosiute, A., and Huang, A. Y. (2014). Comparison of intravital thinned skull and cranial window approaches to study CNS immunobiology in the mouse cortex. *Intravital* 3:e29728. doi: 10.4161/intv.29728

Eyo, U. B., Gu, N., De, S., Dong, H., Richardson, J. R., and Wu, L.-J. (2015). Modulation of microglial process convergence toward neuronal dendrites by extracellular calcium. *J. Neurosci.* 35, 2417–2422. doi: 10.1523/JNEUROSCI.3279-14.2015

Fourgeaud, L., Través, P. G., Tufail, Y., Leal-Bailey, H., Lew, E. D., Burrola, P. G., et al. (2016). TAM receptors regulate multiple features of microglial physiology. *Nature* 532, 240. doi: 10.1038/nature17630

Gyoneva, S., Davalos, D., Biswas, D., Swanger, S. A., Garnier-Amblard, E., Loth, F., et al. (2014). Systemic inflammation regulates microglial responses to tissue damage *in vivo*. *Glia* 62, 1345–1360. doi: 10.1002/glia.22686

Hanisch, U. K., and Kettenmann, H. (2007). Microglia: active sensor and versatile effector cells in the normal and pathologic brain. *Nat. Neurosci.* 10:1387–1394. doi: 10.1038/nn1997

Haynes, S. E., Hollopeter, G., Yang, G., Kurpius, D., Dailey, M. E., Gan, W.-B., et al. (2006). The P2Y12 receptor regulates microglial activation by extracellular nucleotides. *Nat. Neurosci.* 9, 1512–1519. doi: 10.1038/nn1805

Hidetoshi, T. S., Makoto, T., and Inoue, K. (2012). P2Y receptors in microglia and neuroinflammation. *Wiley Int. Rev.* 1, 493–501. doi: 10.1002/wmts.46

Holtmaat, A., Bonhoeffer, T., Chow, D. K., Chuckowree, J., De Paola, V., Hofer, S. B., et al. (2009). Long-term, high-resolution imaging in the mouse neocortex through a chronic cranial window. *Nat. Protocols* 4, 1128–1144. doi: 10.1038/nprot.2009.89

Huh, Y., and Cho, J. (2013). Urethane anesthesia depresses activities of thalamocortical neurons and alters its response to nociception in terms of dual firing modes. *Front. Behav. Neurosci.* 7:141. doi: 10.3389/fnbeh.2013.00141

Jung, S., Aliberti, J., Graemmel, P., Sunshine, M. J., Kreutzberg, G. W., Sher, A., et al. (2000). Analysis of fractalkine receptor CX3CR1 function by targeted deletion and green fluorescent protein reporter gene insertion. *Molecul. Cell. Biol.* 20:4106. doi: 10.1128/MCB.20.11.4106-4114.2000

Kaindl, A. M., Koppelstaetter, A., Nebrich, G., Stuwe, J., Sifringer, M., Zabel, C., et al. (2008). Brief Alteration of NMDA or GABAA receptor-mediated neurotransmission has long term effects on the developing cerebral cortex. *Molecul. Cell Proteom.* 7, 2293–2310. doi: 10.1074/mcp.M800030-MCP200

Kraft, A. D., and Harry, G. J. (2011). Features of microglia and neuroinflammation relevant to environmental exposure and neurotoxicity. *Int. J. Environ. Res. Public Health* 8, 2980–3018. doi: 10.3390/ijerph8072980

Langer, G., Karazman, R., Neumark, J., Saletu, B., Schönbeck, G., Grünberger, J., et al. (1995). Isoflurane narcotherapy in depressive patients refractory to conventional antidepressant drug treatment. *Neuropsychobiology* 31, 182–194. doi: 10.1159/000119190

Langer, G., Neumark, J., Koinig, G., Graf, M., and Schönbeck, G. (1985). Rapid psychotherapeutic effects of anesthesia with isoflurane (ES Narcotherapy) in treatment-refractory depressed patients. *Neuropsychobiology* 14, 118–120. doi: 10.1159/000118216

Lemke, G. (2013). Biology of the TAM receptors. *Cold Spring Harb. Perpect. Biol.* 5:a009076–a009076 doi: 10.1101/cshperspect.a009076

Li, N., Lee, B., Liu, R. J., Banasr, M., Dwyer, J. M., Iwata, M., et al. (2010). mTOR-dependent synapse formation underlies the rapid antidepressant effects of NMDA antagonists. *Science* 329, 959–964. doi: 10.1126/science.1190287

Liu, Z., Condello, C., Schain, A., Harb, R., and Grutzendler, J. (2010). CX3CR1 in microglia regulates brain amyloid deposition through selective protofibrillar amyloid-β phagocytosis. *J. Neurosci.* 30, 17091–17101. doi: 10.1523/JNEUROSCI.4403-10.2010

Longair, M. H., Baker, D. A., and Armstrong, J. D. (2011). Simple neurite tracer: open source software for reconstruction, visualization and analysis of neuronal processes. *Bioinformatics* 27, 2453–2454. doi: 10.1093/bioinformatics/btr390

Madry, C., Kyrargyri, V., Arancibia-Cárcamo, I. L., Jolivet, R., Kohsaka, S., Bryan, R. M., et al. (2018). Microglial ramification, surveillance, and interleukin-1β; release are regulated by the two-pore domain K+ channel THIK-1. *Neuron* 97:e296. doi: 10.1016/j.neuron.2017.12.002

Marker, D. F., Tremblay, M. E., Lu, S. M., Majewska, A. K., and Gelbard, H. A. (2010). A thin-skull window technique for chronic two-photon *in vivo* imaging of murine microglia in models of neuroinflammation. *J. Visual. Exp.* 43:2059. doi: 10.3791/2059

Mei, X. P., Zhou, Y., Wang, W., Tang, J., Wang, W., Zhang, H., et al. (2011). Ketamine depresses toll-like receptor 3 signaling in spinal microglia in a rat model of neuropathic pain. *Neurosignals* 19, 44–53. doi: 10.1159/000324293

Miyamoto, A., Wake, H., Ishikawa, A. W., Eto, K., Shibata, K., Murakoshi, H., et al. (2016). Microglia contact induces synapse formation in developing somatosensory cortex. *Nat. Commun.* 7:12540. doi: 10.1038/ncomms12540

Murugan, M., Ling, E. A., and Kaur, C. (2013). Glutamate receptors in microglia. *CNS Neurol. Disord. Drug Targets* 12, 773–784. doi: 10.2174/18715273113126660174

Nayak, D., Roth, T. L., and McGavern, D. B. (2014). Microglia development and function. *Ann. Rev. Immunol.* 32, 367–402. doi: 10.1146/annurev-immunol-032713-120240

Nimmerjahn, A., Kirchhoff, F., and Helmchen, F. (2005). Resting microglial cells are highly dynamic surveillants of brain parenchyma *in vivo*. *Science* 308, 1314–1318. doi: 10.1126/science.1110647

Parkhurst, C. N., Yang, G., Ninan, I., Savas, J. N., Yates, J. R. III, Lafaille, J. J., et al. (2013). Microglia promote learning-dependent synapse formation through brain-derived neurotrophic factor. *Cell* 155, 1596–1609. doi: 10.1016/j.cell.2013.11.030

Phoumthipphavong, V., Barthas, F., Hassett, S., and Kwan, A. C. (2016). Longitudinal effects of ketamine on dendritic architecture *in vivo* in the mouse medial frontal cortex. *eNeuro* 3:ENEURO.0133-0115.2016. doi: 10.1523/ENEURO.0133-15.2016

Pierce, A. M., and Keating, A. K. (2014). TAM receptor tyrosine kinases: expression, disease and oncogenesis in the central nervous system. *Brain Res.* 1542, 206–220. doi: 10.1016/j.brainres.2013.10.049

Pryazhnikov, E., Mugantseva, E., Casarotto, P., Kolikova, J., Fred, S. M., Toptunov, D., et al. (2018). Longitudinal two-photon imaging in somatosensory cortex of behaving mice reveals dendritic spine formation enhancement by subchronic administration of low-dose ketamine. *Sci. Rep.* 8:6464. doi: 10.1038/s41598-018-24933-8

Rangroo Thrane, V., Thrane, A. S., Chanag, J., Alleluia, V., Nagelhus, E. A., and Nedergaard, M. (2012). Real-time analysis of microglial activation and motility in hepatic and hyperammonemic encephalopathy. *Neuroscience* 220, 247–255. doi: 10.1016/j.neuroscience.2012.06.022

Schafer, D. P., Lehrman, E. K., Kautzman, A. G., Koyama, R., Mardinly, A. R., Yamasaki, R., et al. (2012). Microglia sculpt postnatal neural circuits in an activity and complement-dependent manner. *Neuron* 74, 691–705. doi: 10.1016/j.neuron.2012.03.026

Schindelin, J., Arganda-Carreras, I., Frise, E., Kaynig, V., Longair, M., Pietzsch, T., et al. (2012). Fiji: an open-source platform for biological-image analysis. *Nat. Methods* 9, 676–682 doi: 10.1038/nmeth.2019

Senkov, O., Sun, M., Weinhold, B., Gerardy-Schahn, R., Schachner, M., and Dityatev, A. (2006). Polysialylated neural cell adhesion molecule is involved in induction of long-term potentiation andmemory acquisition and consolidation in a fear-conditioning paradigm. *J. Neurosci.* 26:10888–109898. doi: 10.1523/JNEUROSCI.0878-06.2006

Sleigh, J., Harvey, M., Voss, L., and Denny, B. (2014). Ketamine - more mechanisms of action than just NMDA blockade. *Trends Anaesth. Crit. Care* 4, 76–81. doi: 10.1016/j.tacc.2014.03.002

Sun, M., Deng, B., Zhao, X., Gao, C., Yang, L., Zhao, H., et al. (2015). Isoflurane preconditioning provides neuroprotection against stroke by regulating the expression of the TLR4 signalling pathway to alleviate microglial activation. *Sci. Rep.* 5:11445. doi: 10.1038/srep11445

Szalay, G., Martinecz, B., Lénárt, N., Környei, Z., Orsolits, B., Judák, L., et al. (2016). Microglia protect against brain injury and their selective elimination dysregulates neuronal network activity after stroke. *Nat. Commun.* 7:11499. doi: 10.1038/ncomms11499

Thévenaz, P., Ruttimann, U. E., and Unser, M. (1998). A pyramid approach to subpixel registration based on intensity. *IEEE Transac. Image Proces.* 7, 27–41. doi: 10.1109/83.650848

Tremblay, M. È., Lowery, R. L., and Majewska, A. K. (2010). Microglial interactions with synapses are modulated by visual experience. *PLOS Biol.* 8:e1000527. doi: 10.1371/journal.pbio.1000527

Wake, H., Moorhouse, A. J., Jinno, S., Kohsaka, S., and Nabekura, J. (2009). Resting microglia directly monitor the functional state of synapses *in vivo* and determine the fate of ischemic terminals. *J. Neurosci.* 29, 3974–3980. doi: 10.1523/JNEUROSCI.4363-08.2009

Weeks, H. R. III, Tadler, S. C., Smith, K. W., Iacob, E., Saccoman, M., White, A. T., et al. (2013). Antidepressant and neurocognitive effects of isoflurane anesthesia versus electroconvulsive therapy in refractory depression. *PLoS ONE* 8:e69809. doi: 10.1371/journal.pone.0069809

Xiang, H. F., Cao, D. H., Yang, Y. Q., Wang, H. Q., Zhu, L. J., Ruan, B. H., et al. (2014). Isoflurane protects against injury caused by deprivation of oxygen and glucose in microglia through regulation of the toll-like receptor 4 pathway. *J. Molecul. Neurosci.* 54, 664–670. doi: 10.1007/s12031-014-0373-9

Yang, G., Pan, F., Parkhurst, C. N., Grutzendler, J., and Gan, W. B. (2010). Thinned-skull cranial window technique for long-term imaging of the cortex in live mice. *Nat. Protocols* 5, 201–208. doi: 10.1038/nprot.2009.222

Conflict of Interest Statement: LK is a co-founder and CSO of Neurotar Ltd that produces the Mobile HomeCage devices; DT is an employee of Neurotar Ltd.

The remaining authors declare that the research was conducted in the absence of any commercial or financial relationships that could be construed as a potential conflict of interest.

frontiers in Neuroscience

ORIGINAL RESEARCH
published: 08 May 2019
doi: 10.3389/fnins.2019.00432

A Biohybrid Setup for Coupling Biological and Neuromorphic Neural Networks

Hanna Keren[1,2,3], Johannes Partzsch[3], Shimon Marom[1,2] and Christian G. Mayr[3]*

[1] Department of Physiology, Biophysics and Systems Biology, Ruth and Bruce Rappaport Faculty of Medicine, Technion – Israel Institute of Technology, Haifa, Israel, [2] Network Biology Research Laboratory, Faculty of Electrical Engineering, Technion – Israel Institute of Technology, Haifa, Israel, [3] Institute of Circuits and Systems, Faculty of Electrical and Computer Engineering, School of Engineering Sciences, Dresden University of Technology, Dresden, Germany

Developing technologies for coupling neural activity and artificial neural components, is key for advancing neural interfaces and neuroprosthetics. We present a biohybrid experimental setting, where the activity of a biological neural network is coupled to a biomimetic hardware network. The implementation of the hardware network (denoted NeuroSoC) exhibits complex dynamics with a multiplicity of time-scales, emulating 2880 neurons and 12.7 M synapses, designed on a VLSI chip. This network is coupled to a neural network *in vitro*, where the activities of both the biological and the hardware networks can be recorded, processed, and integrated bidirectionally in real-time. This experimental setup enables an adjustable and well-monitored coupling, while providing access to key functional features of neural networks. We demonstrate the feasibility to functionally couple the two networks and to implement control circuits to modify the biohybrid activity. Overall, we provide an experimental model for neuromorphic-neural interfaces, hopefully to advance the capability to interface with neural activity, and with its irregularities in pathology.

Keywords: neural engineering, brain-machine interfacing, neural networks, neuromorphic networks, neural coupling

OPEN ACCESS

Edited by:
Michele Giugliano, University of Antwerp, Belgium

Reviewed by:
Alexandre Schmid, École Polytechnique Fédérale de Lausanne, Switzerland
Guo-Qiang Bi, University of Science and Technology of China, China

****Correspondence:***
Hanna Keren
hanna.keren@nih.gov

Specialty section:
This article was submitted to Neural Technology, a section of the journal Frontiers in Neuroscience

Received: *14 December 2018*
Accepted: *15 April 2019*
Published: *08 May 2019*

Citation:
Keren H, Partzsch J, Marom S and Mayr CG (2019) A Biohybrid Setup for Coupling Biological and Neuromorphic Neural Networks. Front. Neurosci. 13:432. doi: 10.3389/fnins.2019.00432

INTRODUCTION

Developing interfaces between brain activity and electrical circuits could bring new perspectives for basic research and medical applications, as therapeutic brain stimulation or neuroprosthetics. The development of such interfaces involves multiple challenges and expertise, spanning the fields of neurobiology, electrophysiology, bioengineering, computational neuroscience, and neuromorphic electrical engineering. Among the challenges are the different organizational levels of the neural systems involved, from *in vitro* to the whole brain; the different methodologies for stimulating and recording neural activity; various signal processing tools for detecting neural activity; biomimetic designs in hardware; and a variety of neural networks modeling approaches (Broccard et al., 2017; Chiolerio et al., 2017). The attempts which have been made to implement such interfaces show great promise (O'Doherty et al., 2011; Capogrosso et al., 2016; Joucla et al., 2016), and therefore, immense efforts are invested in tackling this challenge.

For example, novel neurotherapeutic devices [see Greenwald et al. (2016) for review], use neural stimulation to help with epilepsy (Vagus Nerve Stimulation Study Group, 1995; Fisher and Velasco, 2014), chronic pain (Kumar et al., 2007), and rehabilitation following spinal cord injury (Harkema et al., 2011; Angeli et al., 2014). Other studies use bidirectional stimulation to develop motoric feedback interfaces (O'Doherty et al., 2011; Vato et al., 2012), or to reinstate the input

output relations of brain regions (Berger et al., 2012). These methods often modify the stimulation parameters based on response biomarkers, at the time of initiation of the procedure or in real-time. However, it is yet unclear whether impacts of such therapeutic stimulation paradigms are also reflected indirectly in other downstream modular networks.

Here we present the outcome of a consortium under the European Union Seventh Framework Program (CORONET), targeted at developing a biohybrid interface between biological and artificial neural networks. We describe the designed setup and show how it can integrate the activities of neural networks *in vitro* with biomimetic hardware networks.

The hardware components are a CMOS-based VLSI, denoted the NeuroSoC system. These components may be integrated, functionally and physically, with neural systems. The overall NeuroSoC system, is built of nine individual NeuroSoCs and a support system realized on a commercial Field Programmable Gate Array (FPGA). This design allows routing of action potentials and communicating with both a host PC and the neural biological network. The NeuroSoC implements biophysical short-term dynamics and a large network size (320 neurons and up to 1.4 million presynaptic spike inputs per chip), for a realistic counterpart to the biological network. Output spikes of the neuron influence both its spike frequency adaptation (SFA) as well as its downstream presynaptic short-term plasticity (STP). The biological neural network is connected in a closed-loop to the NeuroSoC system via Ethernet, where the host PC is running a Matlab Simulink program which enables real-time configuration, monitoring and control of the experiment, with a sub-milliseconds delay.

We couple the hardware network to a biological network, comprises a large-scale, random network of cortical neurons *in vitro*. These networks develop from a culture of dissociated neurons, which form functional connections via synapses. It has been shown that such networks maintain properties of cortical networks *in vivo*, such as the cell type distribution and the response dynamics (Marom and Shahaf, 2002). When embedded on Micro-Electrode Arrays (MEAs), this experimental setup enables stimulation and recording from tens to hundreds of neurons simultaneously, at high spatio-temporal resolution (Gross et al., 1977, 1993; Jimbo et al., 1998; Massobrio et al., 2015). Therefore, it has been a very useful experimental model for neural connectivity, cellular and synaptic physiology, learning and synchronization (Shahaf and Marom, 2001; Chiappalone et al., 2008; Shahaf et al., 2008; Gal et al., 2010; Le Feber et al., 2010; Wallach et al., 2011; Kaufman et al., 2014; Keren and Marom, 2014, 2016; Reinartz et al., 2014; Haroush and Marom, 2015).

The coupling is configured by feeding the output of the 60 MEA channels, following spike detection, to a predefined subset of all 2880 neurons of the NeuroSoC network. The connection is made via Ethernet and the host PC enables the configuration, live experiment monitoring and control. The strength of recurrent and background connections is finely balanced for the hardware network to experience short population spikes.

Such neural networks *in vitro* have been already integrated with electronic devices, in order to record and stimulate activity (Wagenaar et al., 2005; Bontorin et al., 2007; Rolston et al., 2010; Keren and Marom, 2014). Moreover, progress in very-large-scale integration (VLSI) has advanced the design of complex integrated circuits and system-on-chip (SoC) devices (Greenwald et al., 2016). Bidirectional neural interfaces have become a focus for investigation, where stimulation and PID control parameters are explored (Liu et al., 2017), and advancements are also made in the coupling to *in vitro* networks (Chou et al., 2015).

Here we describe an advanced hybridization setup – where the integrated hardware device is an artificial neural network demonstrating complex architecture and response dynamics, and the coupling is with short, millisecond range, processing, and stimulation delays.

We first present the feasibility to functionally couple the biomimetic hardware network with an *in vitro* neural network. Then, we demonstrate the tightness of the coupling by implementing a closed-loop control circuit – where the hardware network activity is modified via an indirect stimulation, which is provided to the biological network. We show also that modifying the activity of the biological network, affects functional properties of the hardware NeuroSoC network. These examples raise questions regarding possible impacts of local stimulation on other networks in modular constructs. Whether such long-range effects of stimulation are a desirable target or not, they are important to study when developing neural control interfaces.

RESULTS

For coupling the *in vitro* networks with the biomimetic network, it was configured on all 2880 neurons of the NeuroSoC system (**Figure 3A**). Specifically, we can obtain bursting behavior as observed in cultured networks (Shahaf and Marom, 2001) (see **Figure 3B** for obtainable behavior range). We use the bursting behavior seen in graph 2 of **Figure 3B** as viable counterpart to the *in vitro* network.

The feasibility to couple the hardware network with the biological culture, is demonstrated first by showing a congruent synchronization between the two networks, when transferring all biological spiking activity in real-time as inputs to the hardware network. We show that due to the tight coupling, it is also feasible to implement a control circuit which reads the activity of one network while providing stimulation to the other (hence, considers the two as a unified compartment). This design creates a bidirectional interaction between the networks – while the hardware network receives as inputs the spiking activity from the biological network, also the biological activity is stimulated in an intensity which represents the activity level of the hardware network (as illustrated in **Figure 4A**). The circuit is comprised of the following steps: Sampling the activity of the hardware by a subset of 60 neurons, similarly, to the recording of the culture activity; This activity is then sent to a PI controller algorithm, which calculates the appropriate stimulation amplitude to be applied next; This stimulation is provided to the biological network. The transmission of data packets from culture to hardware and back spans the order of 1 ms. The control parameter is the probability of a network synchronization event to occur following a stimulation. This

measure reflects the general activity level, as evoked activity is dominating the network under such stimulation frequency. The control target value of probability was of a sin shape (inset of **Figure 4B**). Both networks followed this target [see also Wallach et al. (2011) and Keren and Marom (2014) for further technical details of the control algorithm]. The control efficiently modified the activity level of both networks to the target pattern, while eliminating the typical random fluctuations (even though in fact no direct stimulation is provided to the hardware network. See **Figure 4C**).

Next, we explore how alterations in activity levels in the biological network are reflected in the hardware network. Under this design, the biological network activity level is controlled to maintain two different activity levels, each for more than an hour, while being coupled to the hardware network. This is shown in **Figure 5A** by three such coupling experiments. Due to the coupling, both the biological and the hardware networks are, similarly, changing between high and low activity levels (**Figure 5A**, depicted blue and black, respectively). To modify the activity level of the biological network, a similar control algorithm is used to calculate the stimulation amplitude required to either increase or decrease the activity level (**Figure 5B**). The hardware network activity, however, is not exposed directly to stimulation, hence, any changes are evoked by the activity of the biological network (**Figure 5C**). Nevertheless, the hardware network activity is being efficiently controlled indirectly via stimulating the biological network.

Moreover, while the activity level of both networks is being congruently modified, we find that additional characteristics are affected as well on both sides. Propagation becomes faster during high activity level. Propagation speed in this context is derived from propagation delays, calculated as the inter-spike-intervals during the recruitment rate of an evoked synchronization. **Figure 6A** demonstrates that this effect on propagation times, occurs congruently in both networks of the biohybrid. Congruently, synchronization latencies are also altered during high activity level, becoming shorter (inset to **Figure 6A**). We also find that network synchronization duration is altered between high and low activity levels, in a similar direction in both biological and hardware networks. From a spatial perspective, we find that maintaining the activity level at a higher or lower level, results in an exploitation of different propagation paths across the biological network (**Figure 6B**, left, a pair-wise similarity matrix, between all response recruitment orders. Note two distinguished groups of responses). This is reflected to some extent in the hardware network as well (**Figure 6B**, right panel). Of all features, it seems that propagation paths are more affected by the intensity of stimulation, as this feature is mainly altered in the biological network which received the stimulation intensity directly. Therefore, this result suggests that while it can be possible to modify propagation paths using stimulation intensity, it might not be as efficiently modified in another downstream network.

All the described examples for coupling experiments (each comprised of three experiments), were set to a connectivity strength of 20%, but were then replicated with a connectivity of 10% without affecting the results.

DISCUSSION

We present a setup for coupling a biological neural network with a neuromorphic hardware network. This experimental setting enables to design a real-time functional communication between neural networks, which is well-monitored from one hand while allowing access to complex features of neural networks from the other.

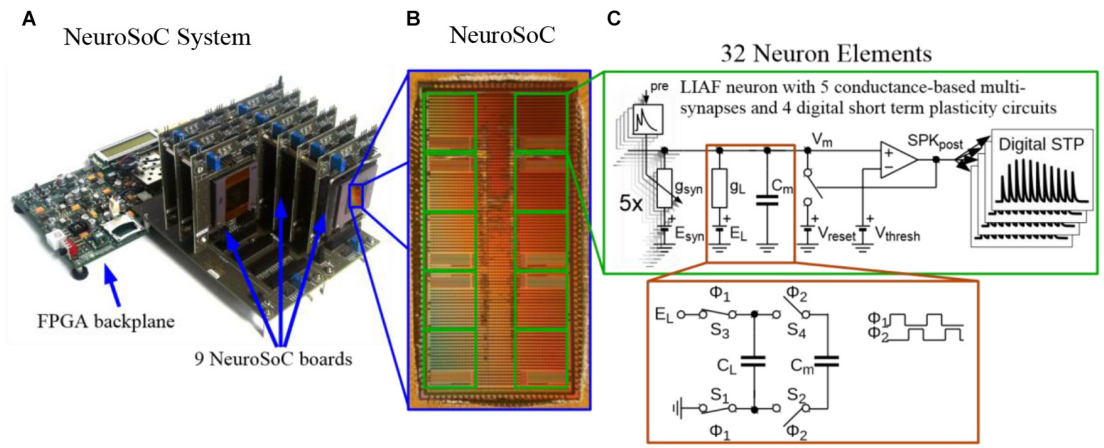

FIGURE 1 | The Neuromorphic System-on-Chip (NeuroSoC) **(A)** The overall NeuroSoC system, with nine individual NeuroSoCs in combined operation; a support system realized on a commercial Field Programmable Gate Array (FPGA) supplies action potential routing and configuration between the individual NeuroSoC chips; Also, the FPGA backplane enables communication to the host PC and the neural culture. **(B)** The NeuroSoC implements biophysical short-term dynamics and a big network size (320 neurons and up to 1.4 million presynaptic spike inputs per chip) for a realistic counterpart to the neural culture. **(C)** Circuit of one of the 10 neuron groups contained on the NeuroSoC, each with 32 neurons realized in switched capacitor technique (see red insert), each with five types of conductance based synaptic input.

The bidirectional coupling between the networks is implemented by: transferring in real-time the biological spiking activity as inputs to the hardware nodes; modifying the stimulation input provided to the biological network according to the hardware activity. Here, the biological spiking parameters being transferred to the hardware are spike time and electrode identity. The hardware activity is affecting the stimulation of the biological network, by changing its stimulation amplitude. However, this setup allows simple modification of this experimental design and the characteristics of the coupling. For example, the feedback from the hardware to the biological network can be implemented using other stimulation parameters, as stimulation frequency, the spatial pattern of stimulation, etc.

There are various possibilities for implementing such interfaces, which are being currently investigated. These designs can include an *in vivo* or an *in vitro* biological network, can use intracellular or extracellular recording electrodes, can be implemented in a hardware or a software level, can use discrete components or integrated circuits (IC), and digital or analog data processing (Reger et al., 2000; Jung et al., 2001; Masson et al., 2002; Carmena et al., 2003; Nowotny et al., 2003; Oprisan et al., 2004; Whittington et al., 2005; Potter et al., 2006; Bontorin et al., 2007; Novellino et al., 2007). Here, the hardware NeuroSoC network is a SC circuit, which exhibits significantly more robust and reproducible behavior than conventional subthreshold neuromorphic circuits. Even though SC circuits have been typically used with simple membrane leakage current and synaptic transmission (Vogelstein et al., 2007; Folowosele et al., 2009), we implement a more biologically realistic model with conductance-based synapse types and spike-frequency adaptation (Noack et al., 2014, 2015).

We show that using this implementation we can generate a similar pattern and dynamics of activity in the two networks. Such tight coupling between the networks is achieved also under sparse connectivity (tested as low as 10% of connection probability). Moreover, during this coupling, various activity features are also altered congruently between the coupled networks. In both networks, propagation of evoked synchronies is faster when activity is pushed to higher levels by a closed-loop control stimulation. This potentially reflects increased excitatory resources when activity is pushed to higher rates (Haroush and Marom, 2015). Both networks also show shorter latencies to synchronization during higher activity rates. This might suggest that even though the stimulation altering the activity rate is local, it has the potential to alter activity features also of other sparsely connected networks. This is an example of how this experimental design can be relevant to questions of impacts of stimulation on neural functional properties, when embedded in a modular organization (for evidence of such impacts in single networks, see Jimbo et al., 1998, 1999; Madhavan et al., 2006; Chao et al., 2007; Chiappalone et al., 2008; Vajda et al., 2008; Bologna et al., 2010; Le Feber et al., 2010; Keren and Marom, 2014). Interestingly, changes in stimulation amplitude and in response probability, did not affect consistently the network response amplitude. This could be related to more heterogenous neural latencies under higher stimulation amplitudes (Keren and Marom, 2014):

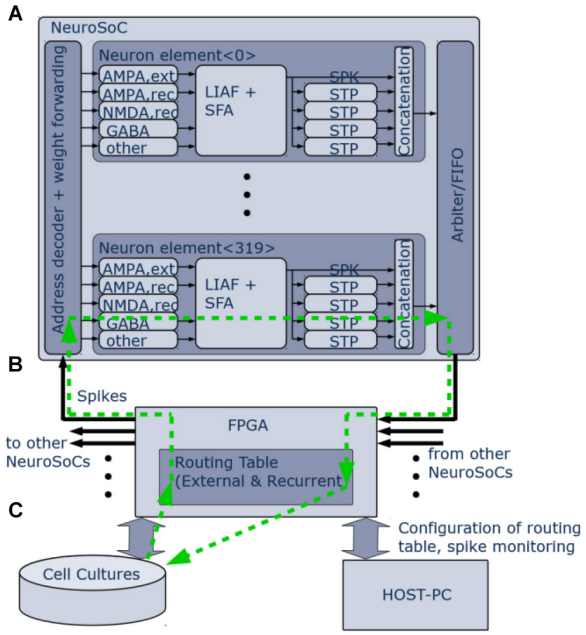

FIGURE 2 | Logical organization of the NeuroSoC system. **(A)** Single NeuroSoC and its processing elements with sample spike processing chain illustrated in the green, dashed line. A spike enters via the address decoder and gets transmitted to the respective multi-synapse; this in turn generates a conductance change (excitatory or inhibitory) on the SC-neuron. Output spikes of the neuron influence its spike frequency adaptation (SFA) as well as its downstream presynaptic short-term plasticity (STP). The spike address plus its four STP values are concatenated into a pulse packet and sent off-chip. **(B)** The FPGA backplane contains playback memory for background stimulation and the routing table between the NeuroSoCs; as well, it enables communication with the neural culture setup and the controlling host PC. **(C)** Neural cultures are connected in a closed loop to the NeuroSoC system via Ethernet; the host PC enables configuration, live experiment monitoring and control.

if neurons reach their firing peak at different times, there would not be a consistent change in the overall synchrony amplitude. This suggests that the changes in hardware response probability are not elicited by differences in the overall biological network response, but by individual neurons properties during the recruitment time. The biological network is being controlled by the intensity of stimulation which causes faster/more spread direct responses, and the hardware network is then, respectively, controlled by these individual responses properties (propagation delays, firing rate and individual neurons latency changes).

Overall, we present an experimental setup for studying neural-neuromorphic coupling dynamics and impacts of stimulation on such modular constructs. This setup enables to integrate the activities of an *in vitro* MEA setup with a hardware network, in real-time, with a short time delay. Specifically, such experimental setup provides the feasibility to explore many important questions, from signal propagation in modular constructs, functional transference between networks, impacts of the density of modular connections, local versus global stimulation effects to external intervention in activity of modular constructs. Hopefully,

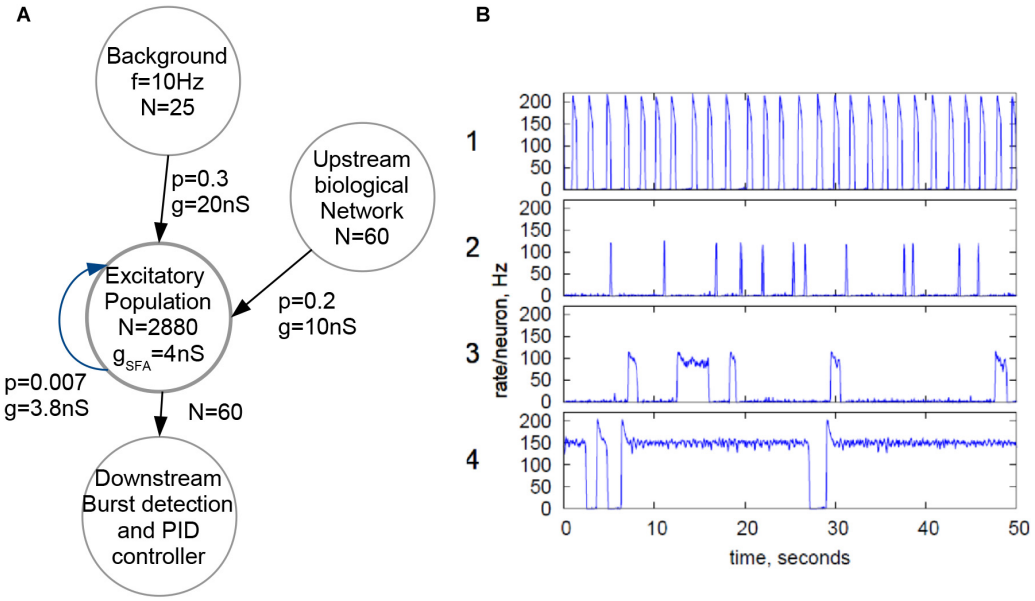

FIGURE 3 | Configuration of the NeuroSoC system. **(A)** Hardware network structure, with background stimulus provided by the FPGA and a single excitatory population configured with all 2880 neurons available; spike activity from the culture is added as additional synapses into a fraction of the excitatory network. Each circle denotes a population of neurons/spike sources (e.g., the Poisson background provided by the FPGA at the top). N denotes the number of neurons/spike sources in said population, with the arrows indicating linkages and synapse direction; p is the connection probability between each pair of pre- and postsynaptic neuron of the two populations and g the conductance of the synapse. **(B)** Four sample population behaviors (population average firing rate, normalized to single neuron); the parameters of the excitatory network and the background stimulus can be configured for a range of behaviors; for similarity with the neural culture behavior, behavior type 2 was chosen, resulting in the parameters given in **A**.

the efficient experimental access to these questions, would enable to expose significant considerations for developing brain-neuromorphic interfaces.

MATERIALS AND METHODS

Hardware System

While we do not give a fully detailed description of the hardware circuits, we do describe to some extent the hardware part of the system in the following section. A more detailed overview of our Neuromorphic System-on-Chip (NeuroSoC, **Figure 1B**) can be found in Noack et al. (2014). As the NeuroSoC should only replicate short-term dynamics, it omits the usual synaptic matrix with its long-term plasticity computation (Qiao et al., 2015). Thus, instead of the conventional neuromorphic chip layout with presynaptic adaptation at the input, a synaptic matrix and postsynaptic neurons, the NeuroSoC can be thought of as a collection of neuron building blocks, the neuron elements (see right half of **Figure 1**, respectively, **Figure 2A** for an organizational overview). The neuron elements are grouped in 10 groups of each 32 neuron elements (for a total of 320 neuron elements per chip). Overall, the system in **Figure 1A** contains 9 NeuroSoCs with 2880 neurons, 14400 conductance-based multi-synapses (equivalent to 12.7 M synapses) and 11520 presynaptic STP circuits. Analog biasing voltages for neurons and synapses (e.g., synaptic reversal potentials, membrane resting potentials, etc.) are generated via digital-analog converters on chip.

Figure 2 gives an organizational overview of the hardware system. The incoming synapses are conductance-based. Five individually configurable multi-synapses per neuron allow to model five separate synapse characteristics of either AMPA, NMDA, or GABA type. One inhibitory conductance is triggered by the neuron itself and thus acts as spike-frequency-adaptation. The output of the neuron feeds into four digital short-term adaptation modules. Each of these can be configured individually and thus provide the neuron with different types of synaptic adaptation for its downstream connections. All pulses are routed via an FPGA (**Figure 2B**) that also handles the routing in between the nine NeuroSoC chips that make up the system. Routing was designed to allow for arbitrary network topologies. Each of the four STP outputs of every neuron has 3.4 k routing entries in the FPGA routing table, which can either target individual multi-synapses of neurons inside the system or addresses outside, the latter being used for communication with other devices such as the neural cultures setup. Each routing entry includes a 6-bit synaptic weight, which is sent to the NeuroSoC together with the adaptation state of the source STP circuit. Both values are multiplied on-chip giving the resulting synaptic efficacy value to be added to the target multi-synapse. The NeuroSoC receives the incoming FPGA pulses via an address decoder, while an arbiter handles conflicts between outgoing pulses. The FPGA also handles the host communication and control (**Figure 2C**). The green arrows illustrate a sample spike

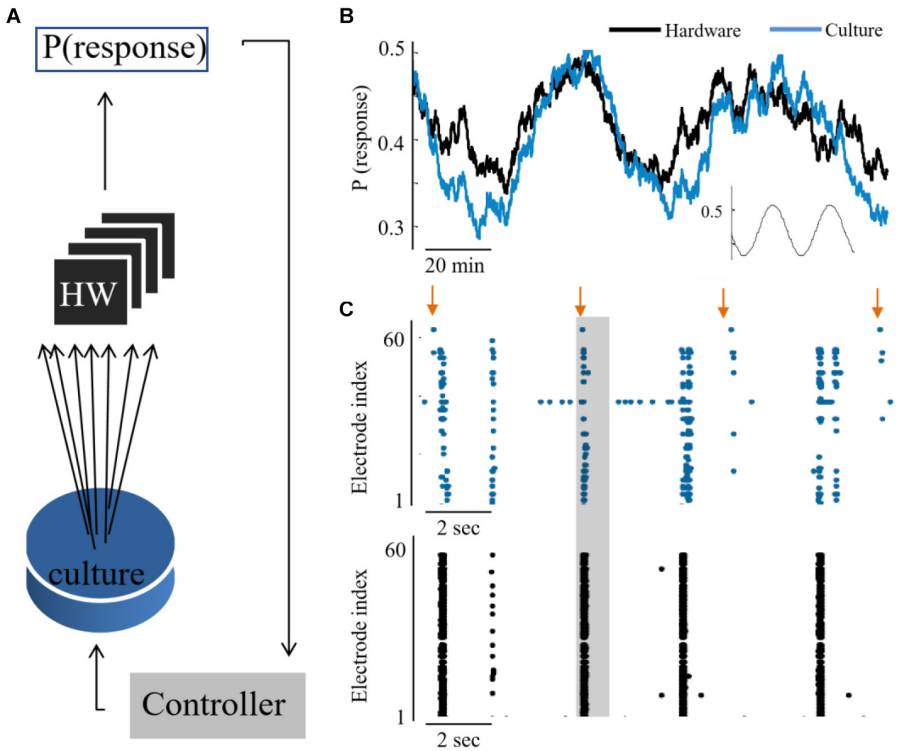

FIGURE 4 | Hybrid coupling and control circuits. **(A)** Scheme of the coupling and control between the culture and neuromorphic device: a PI controller receives the activity of the hardware network, calculates the required stimulation amplitude to reach a predefined activity level in hardware, but then this stimulation is applied to the biological network. **(B)** The output of synchronization probability of an example experiment, where a culture and hardware networks are coupled (see methods for the control algorithm). **(C)** Extracts of aligned activity as recorded in the biological network (blue) and hardware (black). Each point depicts a single spike detected in one of the electrodes (indexed in the vertical axis). Arrows depict stimulation times and shaded regions depict the time window for detection of an evoked burst (10–800 ms after stimulation).

path from/to the culture. The Ethernet-based interface to the neural cultures is also implemented on the FPGA (George et al., 2015). For simplicity, the clock for the SC circuits is supplied by the FPGA but could in principle also be generated on chip (Eisenreich et al., 2009).

Hardware Components

The neurons and synapses on the NeuroSoC are carried out in the Switched Capacitor (SC) circuit technique. This means that conductances are determined by the switching frequency in connection with the capacitance (see **Figure 1C**). This reliance on frequencies and capacitance ratios, instead of process-dependent transistor parameters, lets the NeuroSoC exhibit very robust and reproducible behavior, ideal for biological experiments. A specialized switching circuit has been used to reach the necessary timescales in the order of 1 s (Mayr et al., 2016), which are otherwise hard to obtain in semiconductor circuits due to leakage currents (Roy et al., 2003). **Figure 1C** shows the analog circuits comprising the neuron element. In essence, this is a differential SC realization of a Leaky Integrate-and-Fire neuron with spike-frequency-adaptation and conductance-based multi-synapses at the input. The NMDA synapses constitute a special case as they exhibit a non-linear dependence on the membrane voltage plus a saturation. We have approximated this by an analog computation along a piecewise linear curve (Noack et al., 2014). The biological realism we aimed for in our SC circuits compares favorably with the literature, i.e., SC circuits were previously only used for simple membrane leakage current generation and synaptic transmission (Vogelstein et al., 2007; Folowosele et al., 2009; Noack et al., 2015).

When modeling the synaptic conductance in SC technique, a fixed frequency would result in a fixed conductance. Therefore, a digital circuit generates an exponentially-decaying frequency to emulate an instantaneous-onset, exponentially-decaying synaptic conductance. Each of the five synaptic conductances is implemented as a multi-synapse, meaning that multiple synaptic connections are modeled by overlaying them linearly on the same synaptic circuit. Hence the instantaneous increase will be re-triggered for each synaptic input on that conductance type and subsequent exponential decay performed on the accumulated value. Due to its widely configurable behavior range, we employ a model of presynaptic STP in the NeuroSoC (Markram et al., 1998). A fully digital translation of the model is used, as it was comparable in power and area to an SC implementation and offered superior programmability and repeatability. It transmits its 6-bit adaptation state off-chip for further routing in the FPGA. This state is used at the input of the next NeuroSoC

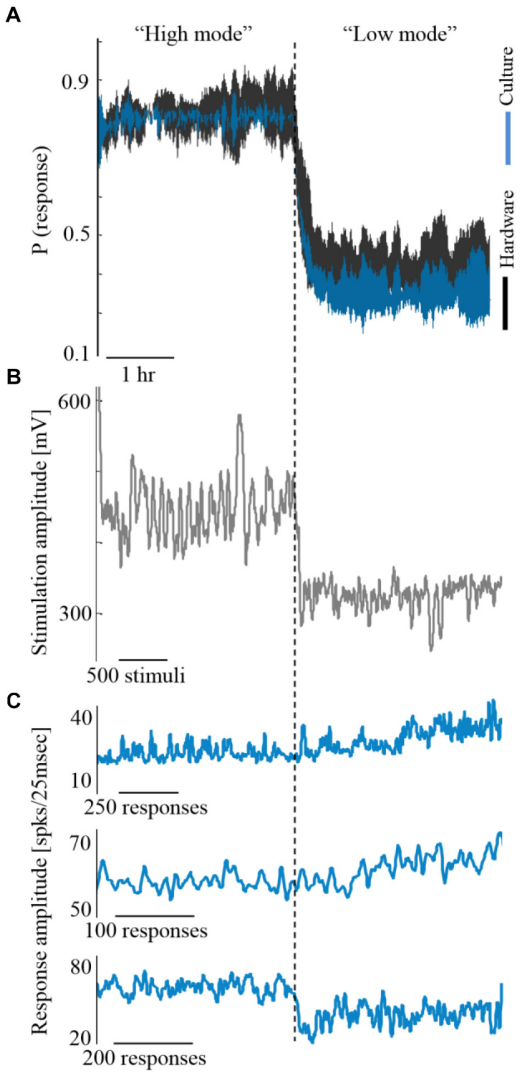

FIGURE 5 | Coupling during different activity levels. **(A)** Three experiments exemplifying coupling while the biological network is controlled to high and low activity levels (blue). Trace margins are standard deviation values across the three cultures. Hardware network activity is depicted black. **(B)** The stimulation amplitudes required for controlling one of the biological networks, as computed by the control algorithm. Higher stimulation amplitudes are required for maintaining higher activity level (shown for one of the cultures, although all three experiments showed a similar trend). **(C)** The evoked synchronization sizes of the three cultures show no consistent relation to the activity level, hence this is not the feature that modifies the hardware network activity.

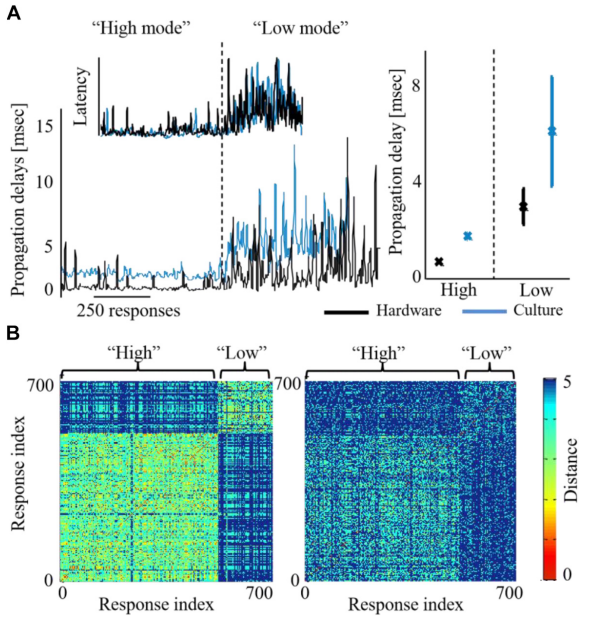

FIGURE 6 | Activity features modified across both biohybrid networks. **(A)** Propagation delays of synchronizations, under either high or low activity leve l (blue depicts the biological network and black the hardware one). Inset shows the respective alteration of synchronization latency, calculated as the time from stimulation to the synchronization peak. Right panel: average latency values across three coupling experiments, error bars show standard deviation ($p < 0.05$ in a t-test between the activity levels for both biological and hardware networks). **(B)** Synchronization recruitment order in the biological (left) and the hardware (right) networks, during high and low activity levels, of a single coupling experiment. Pair-wise difference between propagation paths are presented (calculated with the Levenshtein distance metric), for the first five responding electrodes, across all evoked bursts consecutively [see Shahaf et al. (2008) for details]. The distance between order vectors of evoked burst i and j is color coded in pixel (i,j) between red (0, identical order) and blue (5, no identity in order). Different propagation paths between the high and the low activity levels, would result in a non-homogenous image with two visible squares (where the within-level comparison square has a warmer shade, i.e., lower differences).

as a dynamic synaptic weight value. In the same spirit as the multi-synapses, we did not implement a specific presynaptic adaptation circuit per single synapse configured in the system. Instead, four different realizations of the STP circuit driven by the same neuron provide for differently-configured flavors of presynaptic adaptation to postsynaptic neurons. That is, one STP channel could be configured for facilitation, one for depression, one for combined facilitation and depression (Noack et al., 2011) and each postsynaptic neuron can be configured in the FPGA routing table to receive one of those flavors. Please note that the multi-synapses do not implement long term plasticity, as this is usually a monosynaptic process, i.e., it would need individually realized synapses. This was intentionally omitted as we are only replicating short-term effects of the biological network. Due to the corresponding savings in silicon area, this in turn allowed us to realize more neurons per chip and it also allowed potentially very densely connected networks via the multi-input synapses. However, we could still implement long-term plasticity on the permanent weights via a plasticity processor on the FPGA similar to Friedmann et al. (2013) and George et al. (2015), as the FPGA has access to the weights as well as to, e.g., the pre- and postsynaptic spike trains.

Biomimetic Network

Figure 3A shows the topology employed for the biohybrid experiment on the NeuroSoC system. At its center, all 2880 neurons of the system (distributed across the nine

NeuroSoCs) are configured as an excitatory recurrent network with SFA. This network size approximately resembles the number of neurons present in the region of the MEA. For parametrization of the network, we use a theory-guided approach (Giulioni et al., 2012; Partzsch et al., 2019), employing mean-field theory. While smaller neuromorphic systems have been employed for a mean-field approach (Giulioni et al., 2012), the underlying diffusion approximation asks for synaptic fan-in being significantly smaller than the network size, which is a second motivation for fully utilizing the hardware system. In turn, recurrent connection probability was set to a low value of 0.007, i.e., on average a single neuron is recurrently connected to 20 other neurons. Feeding into this network is a background stimulus of 25 Poisson spike sources at 10 Hz, with each spike source connected to the recurrent network with $p = 0.3$ and a maximum synaptic conductance of $g = 20$ nS. Also feeding into this network is the output of the spike detection operating on the 60 MEA channels, i.e., 60 channels of biological spikes. Aided by the good statistical adherence of our implementation to the model behavior, we can configure the recurrent network for a wide range of dynamical regimes, guided by mean-field theory (Giulioni et al., 2012; Partzsch et al., 2019), see **Figure 3B**. For the hybrid experiments in this paper, the SFA strength, strength of recurrent connections and the background are finely balanced for the network to experience short population spikes, as shown in behavior 2 of **Figure 3B**. Parameters of this configuration are given in **Figure 3A**. In this setting, the network can have spontaneous population spikes driven by the background stimulus as well as evoked spikes driven by the input from the neural cultures.

Cell Preparation

Cortical neurons were obtained from newborn rats (Sprague-Dawley) within 24 h after birth using mechanical and enzymatic procedures described in earlier studies (Marom and Shahaf, 2002). Rats were anesthetized by CO_2 inhalation according to protocols approved by the Technion's ethics committee. The neurons were plated directly onto a substrate-integrated multi electrode array and allowed to develop into functionally and structurally mature networks over a period of 2–3 weeks. The number of plated neurons was of the order of 450,000, covering an area of about 380 mm^2. The preparations were bathed in MEM supplemented with heat-inactivated horse serum (5%), glutamine (0.5 mM), glucose (20 mM), and gentamycin (10 μg/ml), and maintained in an atmosphere of 37°C, 5% CO_2 and 95% air, also during electrophysiological recording.

Electrophysiology

An array of Ti/Au extracellular electrodes, 30 μm in diameter, spaced 500 μm from each other and located in the center, was used (MultiChannelSystems, Reutlingen, Germany). A commercial amplifier (MEA-1060-inv-BC, MCS, Reutlingen, Germany) with frequency limits of 150–3,000 Hz and a gain of ×1024 was obtaining data. Data was digitized using data acquisition board (PD2-MF-64-3M/12H, UEI, Walpole, MA, United States). Each channel was sampled at a frequency of 16 kHz. The sampling rate was defined to allow multiple samples of the extracellular action potential, especially during the most rapid voltage change phase. In an intracellular action potential, the steepest voltage change lasts for about 200 μs, during the depolarization. Therefore, the highest frequencies during an extra cellular action potential are in this frequency range (Gydikov and Trayanova, 1986; Mitra, 2007). The insulation layer (silicon nitride) was pre-treated with polyethyleneimine (Sigma, 0.01% in 0.1 M Borate buffer solution). Data acquired was analyzed using Matlab (Mathworks, Natick, MA, United States). Specifically, Simulink was used to process, analyze and transfer data on-line. Voltage stimulation was applied in a monophasic 200 μs square pulse 100–1000 mV, through extracellular electrodes, using a dedicated stimulus generator (MCS, Reutlingen, Germany). We based the choice of these parameters on previous works which focused on studying these aspects. These stimulation parameters were shown to generate efficiently action potentials in single neurons, for long time scales.

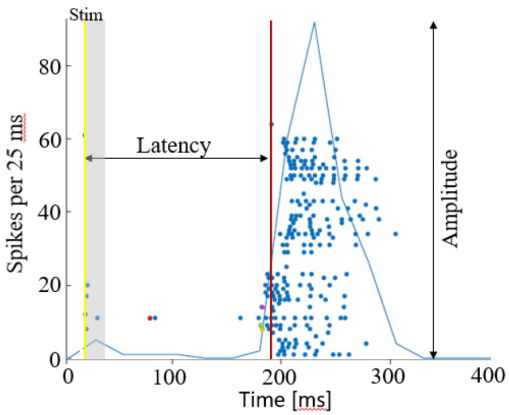

FIGURE 7 | Network synchronization parameters. A raster plot of a single network burst, where each dot depicts an action potential by the time and electrode index. The latency is calculated as the time from stimulation time (yellow line), to the synchronization detection (red line). The amplitude of synchronization is the maximal sum of action potentials, in 25 ms. Action potentials occurring within the first 15 ms after stimulation are excluded from the propagation path analysis, assuming these are caused by direct excitation from the stimulation current. The propagation path is then identified by the order of responding electrodes, in this case it the first 4 are electrodes 11 (red), 9 (green), 8 (yellow), 14 (purple). The propagation speed/delay, would be in this case the time interval between these first spikes occurring in each of the electrodes.

Analyses

Action potentials were detected by threshold crossing which is defined separately for each of the recording channels at the beginning of an experiment (6 × standard deviation of a 2 s voltage trace). A refractory period of 6 ms was considered. The detected activity in the electrodes can originate from one to two neurons. Nonetheless, it has been shown that using this spike detection method maintains the functional phenomena observed when using spike sorting (Eytan and Marom, 2006; Shahaf et al., 2008). Therefore, we found that for the purpose of this study it is sufficient if activity is comprised of 1–2

different neurons, which we consider here as an activation unit. Spike sorting could be added to the algorithm if individual spike shape properties are studied, for example. Detection of network bursts (i.e., synchronization events) was performed on-line by threshold crossing of the summed action potentials, binned to 25 ms. Exact threshold was determined according to 25% of the active electrodes, typically 20 action potentials. See **Figure 7** below for illustration of a network synchronization parameters: each dot indicates a single action potential, described by its time stamp (*x*-axis) and the recording electrode index (*y*-axis). The solid blue line represents the sum of action potentials. The figure indicates the electrical stimulation time (yellow vertical line), the burst detection time (red vertical line), latency from stimulation to occurrence of synchronization, the amplitude of synchronization event and the propagation order.

PI Algorithm

A *Proportional-Integral-Derivative (PID)* controller was realized on the xPC target system (Levine, 1996). The input to the controller is the error signal,

$$e_n = P^*_n - \breve{P}_n \quad (1)$$

where P^*_n and $\breve{P}_n$ are the desired and estimated response probabilities at the *n*th stimulus, respectively. The output of the controller is generally composed of four components,

$$A_n = A_{baseline} + g_P e_n + g_P e_n + g_I \sum_{i=1}^{n} e_i + g_D(e_n - e_{n-1}) \quad (2)$$

where g_P, g_I, and g_D are the proportional, integral, and derivative gain parameters, respectively (typically g_P is 1, 400 mV; $g_P e_n + g_I$ is 0.2, 80 mV; and g_D is 0), and $A_{baseline}$ is the baseline amplitude bias (set to the amplitude which evokes the desired response probability in an open loop stimulation prior to the experiment). In this setup the stimulation amplitude range is between 100 and 1150 mV. Reaching the limit of this stimulation amplitude range, results in a saturation of the input signal to a constant uncontrolled signal, while the integrative error value steadily increases. Hence, for maintaining the control, stimulation within this range is required.

On-Line Estimation of Network Response Probability

The control algorithm uses a reduced binary response characteristic, representing the occurrence of a synchronized network response. Let s_i be an indicator function, so that $s_i = 1$ if the network generated a network burst within a predefined interval after the *i*th stimulus and $s_i = 0$ otherwise. The time interval for detecting an evoked synchronization event following a stimulation was set to 10–800 s. This interval was chosen according to previous studies which validated this time as the optimal for separating evoked synchronization from a spontaneous one (Gigante et al., 2015; Bauermeister et al., 2018). We denote as $\breve{P}_n$ the estimated probability, calculated at time $t > t_n$, based on the set of responses $\{s_1, s_2, \ldots, s_n\}$ to stimuli given at times $\{t_1, t_2, \ldots, t_n\}$. A weighted average was realized by using the recursive formula,

$$\tilde{P}_n = (1 - e^{-\frac{t_n - t_{n-1}}{\tau}}) \cdot s_n + e^{-\frac{t_n - t_{n-1}}{\tau}} \cdot \tilde{P}_{n-1} \quad (3)$$

the estimation time-constant, τ, was typically set to 250 s.

ETHICS STATEMENT

This study was carried out in accordance with protocols approved by the Technion's ethics committee.

AUTHOR CONTRIBUTIONS

HK and SM set up the *in vitro* component of the biohybrid. JP and CM set up the hardware component of the biohybrid. HK led the biohybrid measurements and data analysis, with JP and CM contributing. All authors contributed to the writing of the manuscript and approved it for publication.

REFERENCES

Angeli, C. A., Edgerton, V. R., Gerasimenko, Y. P., and Harkema, S. J. (2014). Altering spinal cord excitability enables voluntary movements after chronic complete paralysis in humans. *Brain* 137, 1394–1409. doi: 10.1093/brain/awu038

Bauermeister, C., Hanna, K., and Jochen, B. (2018). Broadly heterogeneous network topology begets order-based representation by privileged neurons. arXiv:1802.10131 [Preprint].

Berger, T. W., Song, D., Chan, R. H. M., Marmarelis, V. Z., LaCoss, J., Wills, J., et al. (2012). A hippocampal cognitive prosthesis: multi-input, multi-output nonlinear modeling and VLSI implementation. *IEEE Trans. Neural Syst. Rehabil. Eng.* 20, 198–211. doi: 10.1109/TNSRE.2012.2189133

Bologna, L. L., Nieus, T., Tedesco, M., Chiappalone, M., Benfenati, F., and Martinoia, S. (2010). Low frequency stimulation enhances burst activity in cortical cultures during development. *Neuroscience* 165, 692–704. doi: 10.1016/j.neuroscience.2009.11.018

Bontorin, G., Renaud, S., Garenne, A., Alvado, L., Le Masson, G., and Tomas, J. (2007). "A real-time closed-loop setup for hybrid neural networks, medicine and biology society (EMBC 2007)," in *Proceedings of the 29th Annual International conference of the IEEE Engineering*, (Piscataway, NJ: IEEE), 3004–3007.

Broccard, F. D., Joshi, S., Wang, J., and Cauwenberghs, G. (2017). Neuromorphic neural interfaces: from neurophysiological inspiration to biohybrid coupling with nervous systems. *J. Neural Eng.* 14:041002. doi: 10.1088/1741-2552/aa67a9

Capogrosso, M., Milekovic, T., Borton, D., Wagner, F., Moraud, E. M., Mignardot, J. B., et al. (2016). A brain-spine interface alleviating gait deficits after spinal cord injury in primates. *Nature* 539, 284–288. doi: 10.1038/nature20118

Carmena, J. M., Lebedev, M. A., Crist, R. E., O'Doherty, J. E., Santucci, D. M., Dimitrov, D. F., et al. (2003). Learning to control a brain-machine interface for reaching and grasping by primates. *PLoS Biol.* 1:e42. doi: 10.1371/journal.pbio.0000042

Chao, Z. C., Bakkum, D. J., and Potter, S. M. (2007). Region-specific network plasticity in simulated and living cortical networks: comparison of the center of activity trajectory (CAT) with other statistics. *J. Neural Eng.* 4, 294–308. doi: 10.1088/17412560/4/3/015

Chiappalone, M., Massobrio, P., and Martinoia, S. (2008). Network plasticity in cortical assemblies. *Eur. J. Neurosci.* 28, 221–237. doi: 10.1111/j.1460-9568.2008.06259.x

Chiolerio, A., Chiappalone, M., Ariano, P., and Bocchini, S. (2017). Coupling resistive switching devices with neurons: state of the art and perspectives. *Front. Neurosci.* 11:70. doi: 10.3389/fnins.2017.00070

Chou, Z., Lim, J., Brown, S., Keller, M., Bugbee, J., Broccard, F. D., et al. (2015). "Bidirectional neural interface: closed-loop feedback control for hybrid neural systems," in *Proceedings of the 37th Annual International Conference of the IEEE Engineering in Medicine and Biology Society (EMBC)*, (Piscataway, NJ: IEEE).

Eisenreich, H., Mayr, C., Henker, S., Wickert, M., and Schüffny, R. (2009). A novel ADPLL design using successive approximation frequency control. *Elsevier Microelectron. J.* 40, 1613–1622. doi: 10.1016/j.mejo.2008.12.005

Eytan, D., and Marom, S. (2006). Dynamics and effective topology underlying synchronization in networks of cortical neurons. *J. Neurosci.* 26, 8465–8476. doi: 10.1523/jneurosci.1627-06.2006

Fisher, R. S., and Velasco, A. L. (2014). Electrical brain stimulation for epilepsy. *Nat. Rev. Neurol.* 10, 261–270. doi: 10.1038/nrneurol.2014.59

Folowosele, F., Etienne-Cummings, R., and Hamilton, T. J. (2009). "A CMOS switched capacitor implementation of the Mihalas-Niebur neuron," in *Proceedings of the 2009 IEEE Biomedical Circuits and Systems Conference*, (Piscataway, NJ: IEEE), 105–108.

Friedmann, S., Frémaux, N., Schemmel, J., Gerstner, W., and Meier, K. (2013). Reward-based learning under hardware constraints—using a RISC processor embedded in a neuromorphic substrate. *Front. Neurosci.* 7:160. doi: 10.3389/fnins.2013.00160

Gal, A., Eytan, D., Wallach, A., Sandler, M., Schiller, J., and Marom, S. (2010). Dynamics of excitability over extended timescales in cultured cortical neurons. *J. Neurosci.* 30, 16332–16342. doi: 10.1523/JNEUROSCI.4859-10.2010

George, R., Mayr, C., Indiveri, G., and Vassanelli, S. (2015). "Event-based softcore processor in a biohybrid setup applied to structural plasticity," in *2015 International Conference on Event-Based Control, Communication, and Signal Processing (EBCCSP)*, (Piscataway, NJ: IEEE), 1–4.

Gigante, G., Deco, G., Marom, S., and Del Giudice, P. (2015). Network events on multiple space and time scales in cultured neural networks and in a stochastic rate model. *PLoS Comput. Biol.* 11:e1004547. doi: 10.1371/journal.pcbi.1004547

Giulioni, M., Camilleri, P., Mattia, M., Dante, V., Braun, J., and Del Giudice, P. (2012). Robust working memory in an asynchronously spiking neural network realized with neuromorphic VLSI. *Front. Neurosci.* 5:149. doi: 10.3389/fnins.2011.00149

Greenwald, E., Masters, M. R., and Thakor, N. V. (2016). Implantable neurotechnologies: bidirectional neural interfaces—applications and VLSI circuit implementations. *Med. Biol. Eng. Comput.* 54, 19–22. doi: 10.1007/s11517-016-1452-6

Gross, G. W., Rhoades, B. K., Reust, D. L., and Schwalm, F. U. (1993). Stimulation of monolayer networks in culture through thin-film indium-tin oxide recording electrodes. *J. Neurosci. Methods* 50, 131–143. doi: 10.1016/0165-0270(93)90001-8

Gross, G. W., Rieske, E., Kreutzberg, G. W., and Meyer, A. (1977). A new fixed-array multielectrode system designed for long-term monitoring of extracellular single unit neuronal activity in vitro. *Neurosci. Lett.* 6, 101–105. doi: 10.1016/0304-3940(77)90003-9

Gydikov, A. A., and Trayanova, N. A. (1986). Extracellular potentials of single active muscle fibres: effects of finite fibre length. *Biol. Cybern.* 53, 363–372.

Harkema, S., Gerasimenko, Y., Hodes, J., Burdick, J., Angeli, C., Chen, Y., et al. (2011). Effect of epidural stimulation of the lumbosacral spinal cord on voluntary movement, standing, and assisted stepping after motor complete paraplegia: a case study. *Lancet* 377, 1938–1947. doi: 10.1016/S0140-6736(11)60547-3

Haroush, N., and Marom, S. (2015). Slow dynamics in features of synchronized neural network responses. *Front. Comput. Neurosci.* 9:40. doi: 10.3389/fncom.2015.00040

Jimbo, Y., Robinson, H. P., and Kawana, A. (1998). Strengthening of synchronized activity by tetanic stimulation in cortical cultures: application of planar electrode arrays. *IEEE Trans. Biomed. Eng.* 45, 1297–1304.

Jimbo, Y., Tateno, T., and Robinson, H. P. (1999). Simultaneous induction of pathway-specific potentiation and depression in networks of cortical neurons. *Biophys. J.* 76, 670–678.

Joucla, S., Ambroise, M., Levi, T., Lafon, T., Chauvet, P., Saïghi, S., et al. (2016). Generation of locomotor-like activity in the isolated rat spinal cord using intraspinal electrical microstimulation driven by a digital neuromorphic CPG. *Front. Neurosci.* 10:7. doi: 10.3389/fnins.2016.00067

Jung, R., Brauer, E. J., and Abbas, J. J. (2001). Real-time interaction between a neuromorphic electronic circuit and the spinal cord. *IEEE Trans. Neural Syst. Rehabil. Eng.* 9, 319–326.

Kaufman, M., Reinartz, S., and Ziv, N. E. (2014). Adaptation to prolonged neuromodulation in cortical cultures: an invariable return to network synchrony. *BMC Biol.* 12:83. doi: 10.1186/s12915-014-0083-3

Keren, H., and Marom, S. (2014). Controlling neural network responsiveness: tradeoffs and constraints. *Front. Neuroeng.* 7:11. doi: 10.3389/fneng.2014.00011

Keren, H., and Marom, S. (2016). Long-range synchrony and emergence of neural reentry. *Sci. Rep.* 6:36837. doi: 10.1038/srep36837

Kumar, K., Taylor, R. S., Jacques, L., Eldabe, S., Meglio, M., Molet, J., et al. (2007). Spinal cord stimulation versus conventional medical management for neuropathic pain: a multicentre randomised controlled trial in patients with failed back surgery syndrome. *Pain* 132, 179–188.

Le Feber, J., Stegenga, J., and Rutten, W. L. C. (2010). The effect of slow electrical stimuli to achieve learning in cultured networks of rat cortical neurons. *PLoS One* 5:e8871. doi: 10.1371/journal.pone.0008871

Levine, W. S. (1996). *The Control Handbook*. Boca Raton, FL: CRC Press.

Liu, X., Zhang, M., Richardson, A. G., Lucas, T. H., and Van der Spiegel, J. (2017). Design of a closed-loop, bidirectional brain machine interface system with energy efficient neural feature extraction and PID control. *IEEE Trans. Biomed. Circ. Syst.* 11, 729–742. doi: 10.1109/TBCAS.2016.2622738

Madhavan, R., Chao, Z. C., Wagenaar, D. A., Bakkum, D. J., and Potter, S. M. (2006). Multi-site stimulation quiets network-wide spontaneous bursts and enhances functional plasticity in cultured cortical networks. *Conf. Proc. IEEE Eng. Med. Biol. Soc.* 1, 1593–1596. doi: 10.1109/IEMBS.2006.260571

Markram, H., Wang, Y., and Tsodyks, M. (1998). Differential signaling via the same axon of neocortical pyramidal neurons. *Proc. Natl. Acad. Sci. U.S.A.* 95, 5323–5328.

Marom, S., and Shahaf, G. (2002). Development, learning and memory in large random networks of cortical neurons: lessons beyond anatomy. *Q. Rev. Biophys.* 35, 63–87.

Massobrio, P., Tessadori, J., Chiappalone, M., and Ghirardi, M. (2015). In vitro studies of neuronal networks and synaptic plasticity in invertebrates and in mammals using multielectrode arrays. *Neural Plast.* 2015:196195. doi: 10.1155/2015/196195

Masson, G. L., Renaud, S., Debay, D., and Bal, T. (2002). Feedback inhibition controls spike transfer in hybrid thalamic circuits. *Nature* 417, 854–858.

Mayr, C., Partzsch, J., Noack, M., Haenzsche, S., Scholze, S., Hopepner, S., et al. (2016). A biological real time neuromorphic system in 28nm CMOS using low leakage switched capacitor circuits. *IEEE Trans. Biomed. Circ. Syst.* 10, 243–254. doi: 10.1109/TBCAS.2014.2379294

Mitra, P. (2007). *Observed Brain Dynamics*. Oxford: Oxford University Press.

Vagus Nerve Stimulation Study Group (1995). A randomized controlled trial of chronic vagus nerve stimulation for treatment of medically intractable seizures. *Neurology* 45, 224–230.

Noack, M., Krause, M., Mayr, C., Partzsch, J., and Schuffny, R. (2014). "VLSI implementation of a conductance-based multi-synapse using switched-capacitor circuits," in *Proceedings of the 2014 IEEE International Symposium on Circuits and Systems (ISCAS)*, (Piscataway, NJ: IEEE), 850–853.

Noack, M., Mayr, C., Partzsch, J., and Schüffny, R. (2011). "Synapse dynamics in CMOS derived from a model of neurotransmitter release," in *Proceedings of the 20th European Conference on Circuit Theory and Design (ECCTD)*, (Piscataway, NJ: IEEE), 198–201.

Noack, M., Partzsch, J., Mayr, C., Hänzsche, S., Scholze, S., Höppner, S., et al. (2015). Switched capacitor realization of presynaptic short-term-plasticity and stop-learning synapses in 28 nm CMOS. *Front. Neurosci.* 9:10. doi: 10.3389/fnins.2015.00010

Novellino, A., Angelo, P. D., Cozzi, L., Chiappalone, M., Sanguineti, V., and Martinoia, S. (2007). Connecting neurons to a mobile robot: an in vitro bidirectional neural interface. *Comput. Intell. Neurosci.* 2007:2. doi: 10.1155/2007/12725

Nowotny, T., Zhigulin, V. P., Selverston, A. I., Abarbanel, H. D. I., and Rabinovich, M. I. (2003). Enhancement of synchronization in a hybrid neural circuit by spike-timing dependent plasticity. *Neurosci. J.* 23, 9776–9785.

O'Doherty, J. E., Lebedev, M. A., Ifft, P. J., Zhuang, K. Z., Shokur, S., Bleuler, H., et al. (2011). Active tactile exploration using a brain-machine-brain interface. *Nature* 479, 228–231. doi: 10.1038/nature10489

Oprisan, S. A., Prinz, A. A., and Canavier, C. C. (2004). Phase resetting and phase locking in hybrid circuits of one model and one biological neuron. *Biophys. J.* 87, 2283–2298.

Partzsch, J., Mayr, C., Giulioni, M., Noack, M., Hänzsche, S., Scholze, S., et al. (2019). Mean field approach for configuring population dynamics on a biohybrid neuromorphic system. arXiv:1904.10389 [Preprint].

Potter, S., Wagenaar, D., and DeMarse, T. (2006). "Closing the loop: stimulation feedback systems for embodied MEA cultures," in *Advances in Network Electrophysiology*, eds M. Taketani and M. Baudry (Boston, MA: Springer).

Qiao, N., Mostafa, H., Corradi, F., Osswald, M., Stefanini, F., Sumislawska, D., et al. (2015). A recon_gurable on-line learning spiking neuromorphic processor comprising 256 neurons and 128K synapses. *Front. Neurosci.* 9:141. doi: 10.3389/fnins.2015.00141

Reger, B. D., Fleming, K. M., Sanguineti, V., Alford, S., and Mussa- Ivaldi, F. A. (2000). Connecting brains to robots: the development of a hybrid system for the study of learning in neural tissues. *Artif. Life* 6, 307–324.

Reinartz, S., Biro, I., Gal, A., Giugliano, M., and Marom, S. (2014). Synaptic dynamics contribute to long-term single neuron response fluctuations. *Front. Neural Circ.* 8:71. doi: 10.3389/fncir.2014.00071

Rolston, J. D., Gross, R. E., and Potter, S. M. (2010). Closed-loop, open-source electrophysiology'. *Front. Neurosci.* 4:31. doi: 10.3389/fnins.2010.00031

Roy, K., Mukhopadhyay, S., and Mahmoodi-Meimand, H. (2003). "Leakage current mechanisms and leakage reduction techniques in deep-submicrometer CMOS circuits," in *Proceedings of the IEEE*, Vol. 91, (Piscataway, NJ: IEEE), 305–327.

Shahaf, G., Eytan, D., Gal, A., Kermany, E., Lyakhov, V., Zrenner, C., et al. (2008). Order based representation in random networks of cortical neurons. *PLoS Comput. Biol.* 4:e1000228. doi: 10.1371/journal.pcbi.1000228

Shahaf, G., and Marom, S. (2001). Learning in networks of cortical neurons. *J. Neurosci.* 21, 8782–8788. doi: 10.1523/JNEUROSCI.21-22-08782.2001

Vajda, I., van Pelt, J., Wolters, P., Chiappalone, M., Martinoia, S., van Someren, E., et al. (2008). Low-frequency stimulation induces stable transitions in stereotypical activity in cortical networks. *Biophys. J.* 94, 5028–5039. doi: 10.1529/biophysj.107.112730

Vato, A., Semprini, M., Maggiolini, E., Szymanski, F. D., Fadiga, L., Panzeri, S., et al. (2012). Shaping the dynamics of a bidirectional neural interface. *PLoS Comput. Biol.* 8:e1002578. doi: 10.1371/journal.pcbi.1002578

Vogelstein, R. J., Mallik, U., Vogelstein, J. T., and Cauwenberghs, G. (2007). "Dynamically reconfigurable silicon array of spiking neurons with conductance-based synapses," in *Proceedings of the IEEE Transactions on Neural Networks*, Vol. 18, (Piscataway, NJ: IEEE), 253–265.

Wagenaar, D. A., Madhavan, R., Pine, J., and Potter, S. M. (2005). Controlling bursting in cortical cultures with closed-loop multi-electrode stimulation. *J. Neurosci.* 25, 680–688. doi: 10.1523/JNEUROSCI.4209-04.2005

Wallach, A., Eytan, D., Gal, A., Zrenner, C., and Marom, S. (2011). Neuronal response clamp. *Front. Neuroeng.* 4:3. doi: 10.3389/fneng.2011.00003

Whittington, R. H., Giovangrandi, L., and Kovacs, G. T. A. (2005). A closed loop electrical stimulation system for cardiac cell cultures. *IEEE Trans. Biomed. Eng.* 52, 1261–1270.

Conflict of Interest Statement: The authors declare that the research was conducted in the absence of any commercial or financial relationships that could be construed as a potential conflict of interest.

frontiers in Neuroscience

ORIGINAL RESEARCH
published: 21 May 2019
doi: 10.3389/fnins.2019.00464

In vivo Recording Quality of Mechanically Decoupled Floating Versus Skull-Fixed Silicon-Based Neural Probes

Laetitia Chauvière[1†‡], Frederick Pothof[2‡], Kai S. Gansel[1], Johanna Klon-Lipok[1], Arno A. A. Aarts[3], Tobias Holzhammer[3], Oliver Paul[2,4], Wolf J. Singer[1,5,6] and Patrick Ruther[2,4]*

[1] Max Planck Institute for Brain Research, Frankfurt am Main, Germany, [2] Department of Microsystems Engineering (IMTEK), University of Freiburg, Freiburg im Breisgau, Germany, [3] ATLAS Neuroengineering bvba, Leuven, Belgium, [4] BrainLinks-BrainTools Cluster of Excellence, University of Freiburg, Freiburg im Breisgau, Germany, [5] Ernst Strüngmann Institute for Neuroscience in Cooperation with Max Planck Society, Frankfurt am Main, Germany, [6] Frankfurt Institute for Advanced Studies, Frankfurt am Main, Germany

OPEN ACCESS

Edited by:
Arti Ahluwalia, University of Pisa, Italy

Reviewed by:
Antonino Casile, Istituto Italiano di Tecnologia, Italy
Daniele Poli, University of Pisa, Italy

***Correspondence:**
Patrick Ruther
ruther@imtek.de

[†]**Present address:**
Laetitia Chauvière, Institut de Psychiatrie et Neurosciences de Paris (IPNP), INSERM U1266, Paris, France

[‡]*These authors have contributed equally to this work*

Specialty section:
This article was submitted to Neural Technology, a section of the journal Frontiers in Neuroscience

Received: *10 December 2018*
Accepted: *24 April 2019*
Published: *21 May 2019*

Citation:
Chauvière L, Pothof F, Gansel KS, Klon-Lipok J, Aarts AAA, Holzhammer T, Paul O, Singer WJ and Ruther P (2019) In vivo Recording Quality of Mechanically Decoupled Floating Versus Skull-Fixed Silicon-Based Neural Probes. Front. Neurosci. 13:464. doi: 10.3389/fnins.2019.00464

Throughout the past decade, silicon-based neural probes have become a driving force in neural engineering. Such probes comprise sophisticated, integrated CMOS electronics which provide a large number of recording sites along slender probe shanks. Using such neural probes in a chronic setting often requires them to be mechanically anchored with respect to the skull. However, any relative motion between brain and implant causes recording instabilities and tissue responses such as glial scarring, thereby shielding recordable neurons from the recording sites integrated on the probe and thus decreasing the signal quality. In the current work, we present a comparison of results obtained using mechanically fixed and floating silicon neural probes chronically implanted into the cortex of a non-human primate. We demonstrate that the neural signal quality estimated by the quality of the spiking and local field potential (LFP) recordings over time is initially superior for the floating probe compared to the fixed device. Nonetheless, the skull-fixed probe also allowed long-term recording of multi-unit activity (MUA) and low frequency signals over several months, especially once pulsations of the brain were properly controlled.

Keywords: silicon-based neural probes, floating probes, fixed probes, *in vivo* recording, non-human primates, visual cortex

INTRODUCTION

Chronically stable, extracellular recording of cortical activity is mandatory for brain-computer interfaces used to accurately and reliably control a robotic arm (Velliste et al., 2008; Hochberg et al., 2012). Long-term stable recordings are further required in any neuroscientific study analyzing brain activity at the neuronal level to gain a better understanding of brain dysfunction. Technical tools applied in this context include microwires, i.e., singles wires (Nicolelis et al., 2003) or tetrodes (Gray et al., 1995), flexible, polymer-based probes (Liu et al., 2015; Luan et al., 2017) as well as a variety of silicon-based micro-electrode arrays (Wise et al., 2008; Normann and Fernandez, 2016). While wire electrodes and tetrodes are widely established tools in neuroscientific laboratories which

can easily be integrated in multi-channel micro-drives (Lewis et al., 2016), each implanted probe comprises either one or four recording sites only. In contrast, neural probes based on polymeric or silicon substrates comprise a large number of recording sites arranged along slender probe shafts. So far, the number of recording sites of polymer-based probes is limited, however, by the minimally achievable dimensions of metal leads running along the probe shafts. Recent technical developments in case of silicon-based probe arrays (Blanche et al., 2005; Scholvin et al., 2016; Barz et al., 2017) apply sophisticated CMOS-based circuitry integrated directly in the probe shanks (Seidl et al., 2011; Fiáth et al., 2016; Raducanu et al., 2017; De Dorigo et al., 2018; Herbawi et al., 2018). With up to 1600 electrodes along a 10-mm-long probe shaft (Herbawi et al., 2018), a pronounced increase in the number of recording sites is achieved in comparison to any other recording technology.

In view of the long-term recording stability of cortical implants a variety of probe parameters promoting a low tissue response are discussed controversially (Polikov et al., 2005; Karumbaiah et al., 2013; Prodanov and Delbeke, 2016; Salatino et al., 2017). While some studies state that the cross-sectional area, a given surface coating (Rousche et al., 2001), or the tip geometry (Edell et al., 1992) are the main factors influencing the cortical foreign-body response, others negate the importance of these probe characteristics in decreasing the signal quality of neural implants (Szarowski et al., 2003). The mismatch in mechanical properties, i.e., elastic modulus (Nguyen et al., 2014) and material density (Lind et al., 2013), of cortical tissue and neural probe materials was further rated as a possible factor influencing glial scarring and inflammation eventually reducing the long-term recording stability. Responding to the demand for high-density recordings with a large number of simultaneously addressable electrode sites (Dimitriadis et al., 2018) would call for polymer-based probes. Here, the mismatch in mechanical properties of probe material and cortical tissue is minimized (Lacour et al., 2016; Lecomte et al., 2018) resulting in an inherently reduced probe stiffness (Harris et al., 2011). The probe performance is further improved by providing a high level of mechanical decoupling, i.e., by using flexible interconnecting wires (Markwardt et al., 2013).

A histological study by Biran et al. (2007) compared the tissue response caused by silicon-based skull-fixed neural probes and probes floating with the brain. The study clearly indicates a higher immune response from tissue near skull-fixed probes compared to floating implants. It seems further to be widely accepted that mechanical forces acting on neural implants cause a stronger glial response than freely floating devices. Thus, more recent work studying cortical tissue reactions caused by brain implants use by default floating devices (Chestek et al., 2011; Woolley et al., 2013; Ersen et al., 2015). These requirements impose, however, tough constraints on future neural probes that are not easy to fulfill. As an example, advanced CMOS-based probe arrays, as developed by the European project *NeuroSeeker* (Raducanu et al., 2017; Dimitriadis et al., 2018), call for electrically shielded equipment and mechanically stable leads used for the high-frequency data transfer between the probe carrying a large number of recording sites and the external instrumentation. A floating application in a chronic setting would be highly beneficial for *in vivo* recordings from freely behaving animals. However, due to the probe design with a slender probe shaft and a larger probe base, a floating use of this implant is prohibited by the mechanical probe stability. Further, it has been unclear so far whether glial reactions in tissue of non-human primates (NHP) are directly comparable to those in rodents and to which extent glial scarring will prevent the recording of single-unit activity (SUA) from the brain. Recently it has been shown that skull-fixed approaches can be used to record SUA for more than 100 days in mice (Okun et al., 2016) and up to several weeks in a monkey (Lanzilotto et al., 2016).

To find a suitable trade-off between technological requirements of high-frequency circuitry and biological demands regarding glial response, we fabricated a system allowing to directly compare the electrical recording quality of a floating silicon-based neural probe with a skull-fixed device. Both probes consist of the exact same materials and have the same geometry. We implanted and recorded signals over the course of 65 days. Based on the recorded data, we draw a first conclusion regarding the electrical signal quality of the recordings from a NHP (*Macaca fascicularis*).

MATERIALS AND METHODS

In order to use both types of probes in close proximity to each other within the same brain area, we fabricated a custom-designed recording chamber to host the floating and skull-fixed neural probes. The silicon-based probes are identical in design; both are 8 mm long and comprise 16 platinum-coated recording sites (diameter 35 μm). They are implanted within a few millimeters of each other.

Recording Chamber

Figure 1A shows a schematic of the custom-designed recording chamber. It is based on a commercially available chamber from Gray Matter Research, Bozeman, MT, United States (Gray et al., 2007). The hollow titanium (Ti) cylinder of the chamber with an inner diameter of 12.7 mm is inserted into a circular craniotomy, lowered until it touches the dura mater and fixed to the skull using bone screws and cement. In order to seal the brain surface, a silastic membrane is spun over a sleeve (**Figure 1A-left**) and lowered to the dura mater using the inner thread of the chamber. In this way, a tight sealing of the brain with respect to the environment is assured. The floating and skull-fixed recording probes will be inserted into the cortical tissue through this silastic membrane and the dura mater. The membrane successfully prevents infections of the brain over a long period of time and blocks body fluids from reaching the electrical connectors inside the recording chamber.

In its upper section, the chamber base (**Figure 1A**) is equipped with a thread used to fix a mounting ring made of Ti. The mounting ring comprises 16 smaller threaded holes evenly distributed along the perimeter and located on a 20-mm-diameter circle (**Figure 1A-right**). As indicated in **Figure 1A-left**, this ring is additionally secured with a second layer of bone cement prohibiting its removal due to excessive torque forces

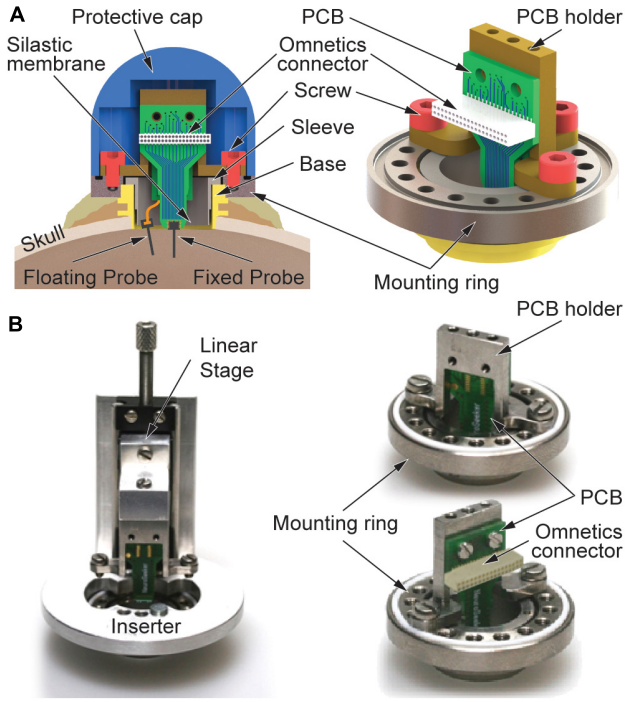

FIGURE 1 | Recording device comprising floating and skull-fixed silicon-based probe arrays. **(A)** Schematic of the recording chamber with mounting frame, PCB holder, and a protective cap. Floating and fixed probes are interfaced with the recording system using an Omnetics connector on the joint PCB. **(B)** Optical images of the mounting frame with (left) inserter used to lower the skull-fixed probe into the brain tissue and (right) fixed PCB holder seen from different perspectives.

possibly exerted by the freely behaving monkey. As shown in **Figure 1B**, all custom-designed parts of the novel chamber concept are attached to this mounting ring using screws, i.e., either a linear stage (left) which is temporarily applied during implantation of the skull-fixed neural probe or a holder made of Ti (right) carrying a printed circuit board (PCB) to which the skull-fixed probe is attached. In combination with the 16 threads of the mounting ring, the fact that the probe position on the holder is 1.75 mm off-center provides the possibility to choose different positions of the skull-fixed probe inside the recording chamber. This offers an increased flexibility during probe implantation, enabling to avoid the penetration of larger, visible blood vessels on the brain surface. The entire chamber including its base and mounting ring, together with the PCB holder and respective probe interfaces are mechanically protected by a dome-shaped Ti cap fixed to the mounting ring by four screws.

Silicon-Based Neural Probes

The silicon (Si) probes used in this study comprise an 8-mm-long probe shaft (width 140 μm, thickness 50 μm) and carry 16 platinum recording sites. These are equidistantly distributed at a pitch of 250 μm over a length of 3.75 mm of the distal shaft section. The probe shaft terminates in a pointy tip which facilitates probe insertion through both the silastic membrane and the dura mater. While the skull-fixed probe is adhesively attached and wire bonded to a PCB mechanically secured on the holder of the recording chamber, we interface the floating probe via a 10-μm-thin polyimide cable with a length of 30 mm (Kisban et al., 2009). The mechanical properties of the cable material, i.e., low elastic modulus, and the geometrical cable dimensions are beneficial in view of minimizing forces caused by brain movements. The flexible cable is connected to the PCB of the skull-fixed probe using a zero-insertion-force (ZIF) connector soldered to the rear of the PCB. Both probes are interfaced to the external instrumentation using a strip connector (NPD series, Omnetics Connector Corp., Minneapolis, MN, United States). The probe fabrication using microsystem technologies has been described in detail elsewhere (Herwik et al., 2011).

Implantation

For implantation of the recording chamber, a trepanation fitting to the diameter of the chamber base is cut into the skull of the monkey at the desired position. Bone screws are in addition implanted into the skull close to the chamber. They are used to fix the chamber base to the skull using acrylic bone cement. The brain surface with intact dura mater is sealed using the silastic membrane mechanically fixed using the Ti sleeve. The skull-bone cement interface is allowed to mechanically strengthen in a subsequent healing period of 3 weeks before the probes are implanted through the silastic membrane and the dura mater. In this period, the chamber is closed by a flat cap from Gray Matter Research, effectively sealing the chamber.

Using a vacuum inserter, the floating probe is inserted under microscope control into the targeted brain area, as previously described in Bonini et al. (2014). If needed, the inserter provides the possibility to retract and reposition the floating probe at a different position within the chamber. The skull-fixed probe assembled on a PCB is slowly lowered into the cerebral cortex using the inserter temporarily fixed on the mounting ring, as shown in **Figure 1B-left**. The inserter comprises a manually operated linear stage. The PCB holder together with the probe-carrying PCB are connected to this linear stage using screws. Before lowering the PCB-mounted probe into the cortical tissue, the floating probe is electrically connected to the PCB using the ZIF connector on the PCB rear. As in the case of the floating probe implantation, lowering the PCB-mounted probe using the linear stage causes the silastic membrane and the dura mater to be penetrated. The penetration of both layers is facilitated by the beveled probe tip. Maximal implantation depth is reached once the PCB holder is in contact with the mounting ring. At this point, the PCB holder is fixed to the ring using three screws, followed by the removal of the inserter, as depicted in **Figure 1B-right** with front and rear views of the holder. The electrophysiological recordings start the next day, once the animal has fully recovered from anesthesia.

The study was conducted with one adult macaque (*Macaca fascicularis*) following the guidelines of the European Community for the care and use of laboratory animals (European Union Directive 86/609/EEC) with approval by the appropriate local committee on animal welfare (Regierungspräsidium

Hessen, Darmstadt, Germany). During the recordings of this study, the monkey was exclusively in the awake state while receiving rewards for fixating his eyes on a fixation spot at the center of a monitor screen [cf. methods section of Chauvière and Singer (2019)].

Electrophysiology and Data Analysis

The electrophysiological recordings of the study were performed using a recording system from Tucker Davis Technologies (RZ2 Z-series processor, Tucker Davis Technologies, Alachua, FL, United States). We sampled broadband activity at 25 kHz which was band-pass filtered between 1 and 300 Hz for local field potentials (LFPs) and between 300 and 3000 Hz for multi-unit activity (MUA). The recorded data were stored offline, and sessions were concatenated before sorting the recorded spiking activity in all the sessions at once using a custom-made spike sorter based on a dynamic template matching algorithm. Statistics have been performed using the ANOVA test, with further *post hoc* testing using Dunnett's test.

Spike Sorting Analysis

Offline spike sorting was performed using a dynamic template matching method implemented in a custom software package ("Smart Spike Sorter"). Initially, up to twelve different clusters were automatically defined by an artificial neural network based on the adaptive resonance theory (Carpenter and Grossberg, 1987). Various cluster properties like auto-correlations of spike times and recording stabilities of spike waveforms were monitored and considered in conjunction with the shape of the waveforms to guide decisions about which clusters to merge or delete. Only clusters visibly separated in 3D principal component space were assigned to single units. Accuracy of spike assignment was validated by objective measurements of cluster separation provided by the J3 and Pseudo-F statistics. Based on these criteria, only well-isolated putative single units were considered for further analysis.

Behavioral Paradigm and Passive Viewing Task

As described in **Figure 2A**, in this study the monkey had to perform a passive viewing task. The task consists of pressing and releasing a lever in response to the color change of a light dot shown at the center of a monitor screen. In order to initiate a trial, the monkey was trained to press the lever. This is followed by the appearance of the green fixation spot at the center of the monitor screen. The monkey has to keep fixation and the lever pressed until the point changes color (e.g., from green to red). If the monkey has kept fixation and released the lever within a short interval after the color change it gets a reward (a drop of water or juice). An error signal (i.e., a sound) is presented in case the monkey does not press the lever, does not maintain it pressed, does not fixate the color spot or releases the lever too late or too early. In these cases, the monkey does not get a reward. Eye movements were recorded with an infra-red eye tracker (Thomas Recording, Giessen, Germany) to assure that the monkey maintained fixation within a 0.5° window of visual angle.

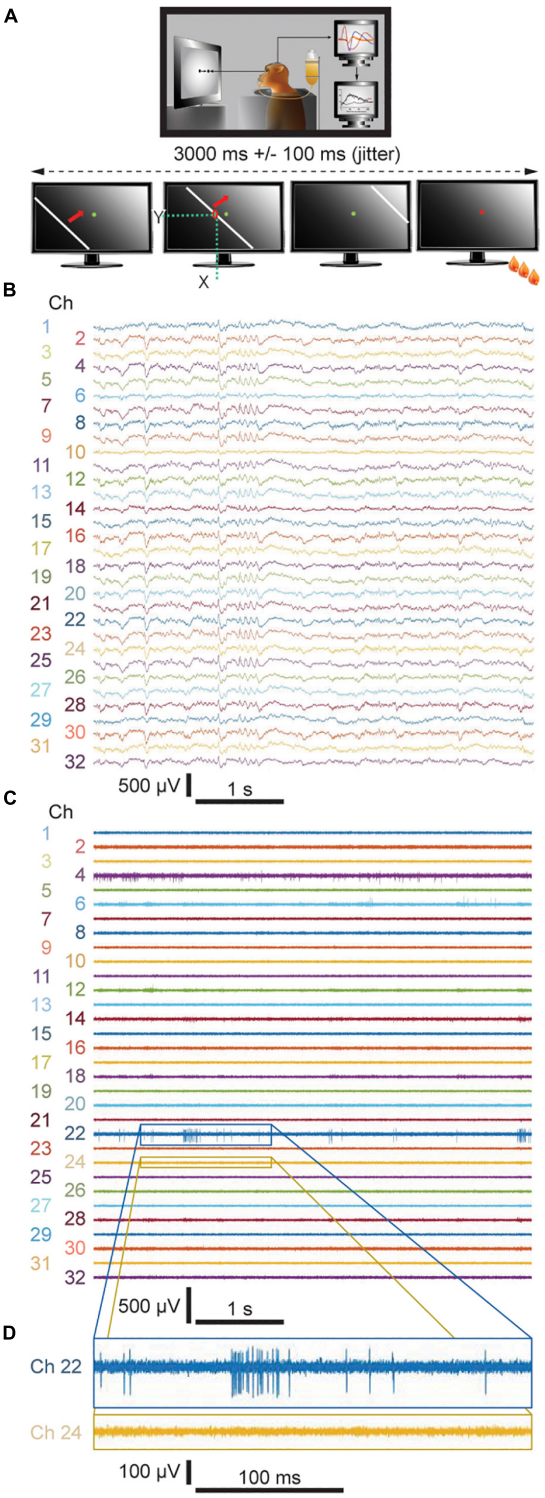

FIGURE 2 | (A) Visual task applied during the recording sessions. **(B)** Representative 5-sec-long traces of LFP signals downsampled to 1525.9 Hz from both the fixed and floating probes recorded during Week 8. **(C)** Representative 5-sec-long traces of unit activity from both the fixed and floating probes bandpass filtered between 300 and 3000 Hz and **(D)** 500-ms-long enlarged views of two representative channels. **(B,C)** even numbers: floating probe; odd numbers: skull-fixed probe.

If the monkey broke fixation before the fixation spot changed color the trial was aborted.

During the viewing task, a white bar with 16 different, predefined orientations evenly distributed over 360°, travels across the monitor screen within 3 s with an added jitter of 100 ms (**Figure 2A**, lower schematics). Spike amplitude above a given threshold, i.e., 3 times the standard deviation from the noise level, was recorded at each channel for each position of the bar. The 16 directions are randomly repeated 10 times per recording session and responses to the same stimulus were averaged. The receptive fields were determined for each channel by adding the number of spikes on the respective channel at the moment when the bar passes by an individual pixel (x and y positions) on the monitor screen (**Figure 2A**). For each channel of the probe, the boundaries of the receptive fields correspond to the location of the bar where it starts to induce increased discharges.

RESULTS

Comparison of Neuronal Activity Between the Two Types of Silicon-Based Neural Probes

Over the course of 8 weeks, neuronal activity was recorded within the primary visual cortex of one awake behaving monkey. We applied one floating and one skull-fixed silicon-based neural probe implanted within the same recording chamber, while the monkey was performing a simple passive viewing task (**Figure 2A**; cf. Methods section for a detailed description of the behavioral paradigm). We then compared the neuronal activity from both types of probes and found that LFPs could be recorded from both probe types already 1 day after probe implantation (**Figure 2B** where exemplary signals are from recordings during Week 8). In the raw signal traces, a difference between floating and fixed probe cannot be discerned (floating probe, even numbers; fixed probe, odd numbers). The LFP signals were stable throughout the entire observation period (cf. **Supplementary Figure S1** for similarity measures between LFP signals recorded by means of both types of probes and **Supplementary Table S1** for their quantification).

Spiking Activity

Comparing MUA between the floating and skull-fixed probe, we found that 3 days post-implantation, MUA was identifiable from the floating probe (**Figure 2C**, even numbers), providing reliably mappable receptive fields for Week 2 and Week 5 (**Figure 3A**).

Retesting the animal at regular time intervals revealed that the floating and the skull-fixed probes both reliably recorded MUA activity from varying cell populations over the first five sessions (**Figures 3B,C** for the floating probe, **Figures 3E,F** for the skull-fixed probe). However, some differences were noted: while in the third session, i.e., 13 days after probe implantation, the floating probe yielded higher spike counts, those from the fixed probe remained unchanged. For both probes, however, MUA activity decreased over the last (sixth) session (ca. 8 weeks after implantation). Comparing the spike counts (or rate) obtained from the fixed and the floating probe, respectively, we found that the former represented ∼98.2, 55.1, 24.9, 66.1, 51.6, and 0.1% of the latter during the recording sessions 3, 7, 13, 35, 49, and 56 days after implantation, respectively. The receptive fields were mappable for both probes (**Figures 3A,D**), but spikes varied in amplitude for the different recording sites, sometimes barely exceeding the noise level at some of the recording sites (**Figure 2**). Overall, however, the variability between recording channels of the same electrode exceeded the variability among the two probes.

Unit Activity

For each of the recording channels, spikes were sorted on concatenated recording sessions and split into putative single units according to their waveforms using a dynamic template matching algorithm allowing for slow drifts in spike amplitude of a single unit. We isolated 2 to 8 units per recording site, with an average of 4 units per site for the floating probe and of 5–6 units for the skull-fixed probe (see details in **Figure 4**). We analyzed in further detail a total of 19 units for the floating probe and 33 units for the fixed probe which displayed overall more units per recording site. For this in-detail analysis, a total of 52 units over a period of 8 weeks following probe insertion were thus considered. We studied the temporal stability of the units across different recording sessions, displayed in **Figure 5**. For each unit and session we analyzed the spike rate and spike count (**Figure 4**), the spike amplitude (**Figures 6A,D**), the spike width (**Figures 6B,E**), and the inter-spike interval coefficient of variation (ISI CV, **Figures 6C,F**) for the floating probe (**Figures 4A**, **6A–C**) and the skull-fixed probe (**Figures 4B**, **6D–F**). **Table 1** summarizes the statistical results for the comparisons of the sessions (ANOVA).

Spike Amplitude and Spike Width

Overall, the measured peak-to-peak spike amplitudes varied between 40 and 150 μV. For the fixed probe, the amplitude remained rather stable over the recording sessions, except for the last session when the amplitude clearly dropped (**Figure 6D** and **Table 1**). For recordings with the floating probe, a slight but steady increase of the average spike amplitude could be detected over the entire course of the recording sessions (**Figure 6A** and **Table 1**). The interquartile range is, however, strongly increased for the sixth recording session. The individual spike widths were quite stable along the whole recording period (53 days) for both the floating and the fixed probe ($p > 0.05$ for both probes; see **Table 1** and **Figures 6B,E**).

Stability of Spiking Activity Over Recording Sessions

To illustrate the stability of spiking activity over recording sessions for both probe types, examples of units displaying stable waveforms and spike widths with stable (Channel 7 of the fixed probe, Channel 20 of the floating probe) or varying spike amplitudes (Channel 2 of the floating probe, Channel 17 of the fixed probe) along different recording sessions are

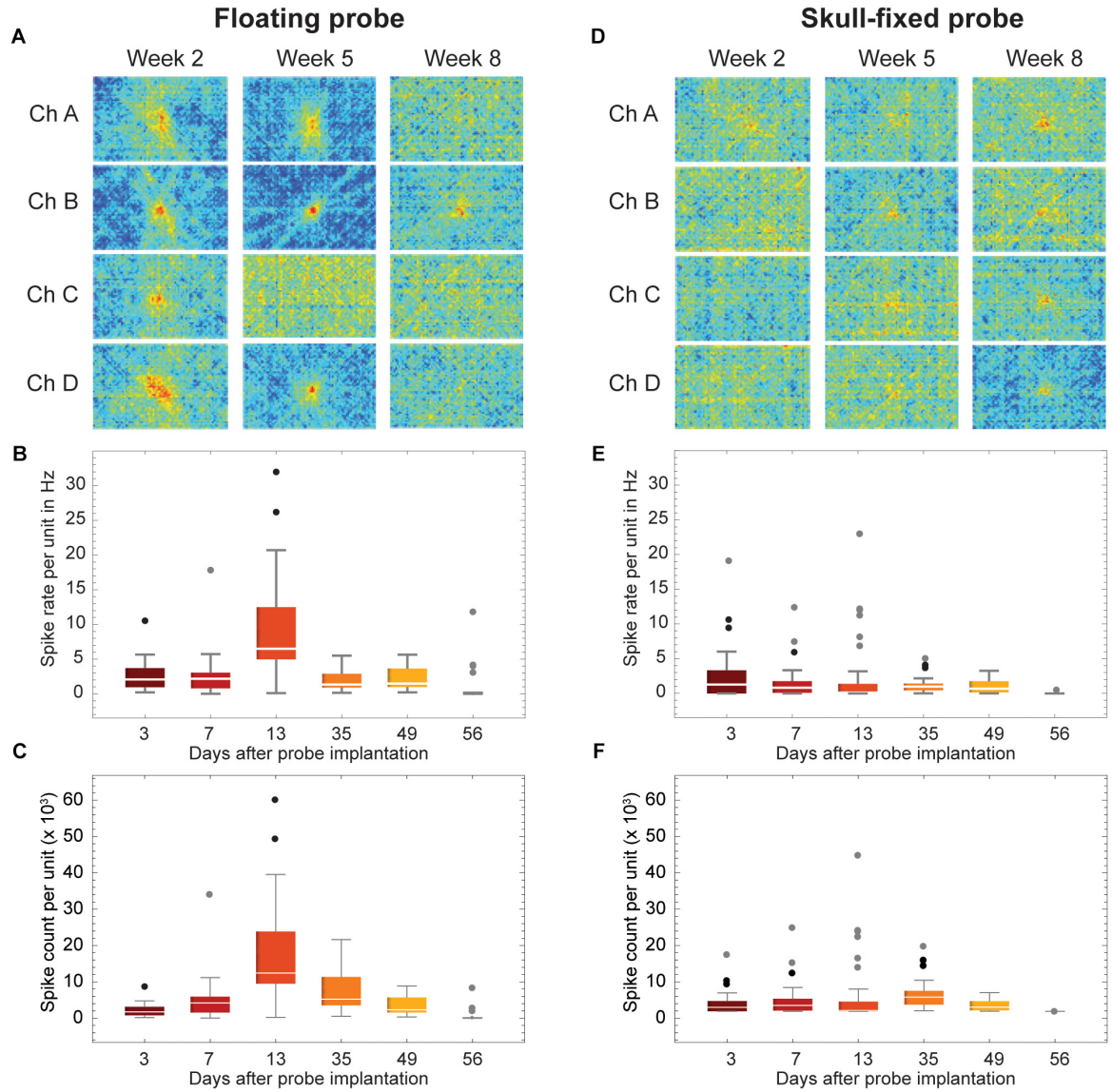

FIGURE 3 | Recordings stability across weeks of recordings. **(A,D)** Examples of visual response stability, i.e., receptive fields, across weeks of recordings (2 weeks, 5 weeks, and 8 weeks post-insertion of the probes). **(B,E)** Spike rate and **(C,F)** spike count of all units for selected recording sessions. Data is grouped for **(A–C)** floating and **(D–F)** skull-fixed neural probes (black circles: outlier, outside 1.5× interquartile range; gray circles: far outlier, outside 3× interquartile range).

shown in **Figure 5**. Altogether, these results showed that the quality of the recorded signals was good and fairly stable over 8 weeks following probe insertion for both types of probes. However, in the last session (8 weeks post-implantation) recording quality had decreased as indicated by the drop in MUA activity.

Coefficient of Variation and Inter-Spike Interval

Finally, the ISI CV was close to one in most instances (**Figures 6C,F**), showing a significant excursion only for recordings with the fixed probe during the third session (**Figure 6F**), indicating less regular firing at a constant overall firing rate.

DISCUSSION

Stability of Recordings With Chronic Laminar Probes

In the present study we assessed the stability of long-term recordings from chronically implanted silicon-based laminar probes. Stability criteria were the ability to record spiking activity (MUA), the drift in the shape of action potentials analyzed after spike sorting and application of template matching procedures and the signal-to-noise ratio of LFPs. In agreement with previous publications we found that LFP recordings were stable over the whole analysis period (Andersen et al., 2004; Flint et al., 2013; Hall et al., 2014) but recordings of spiking activity exhibited

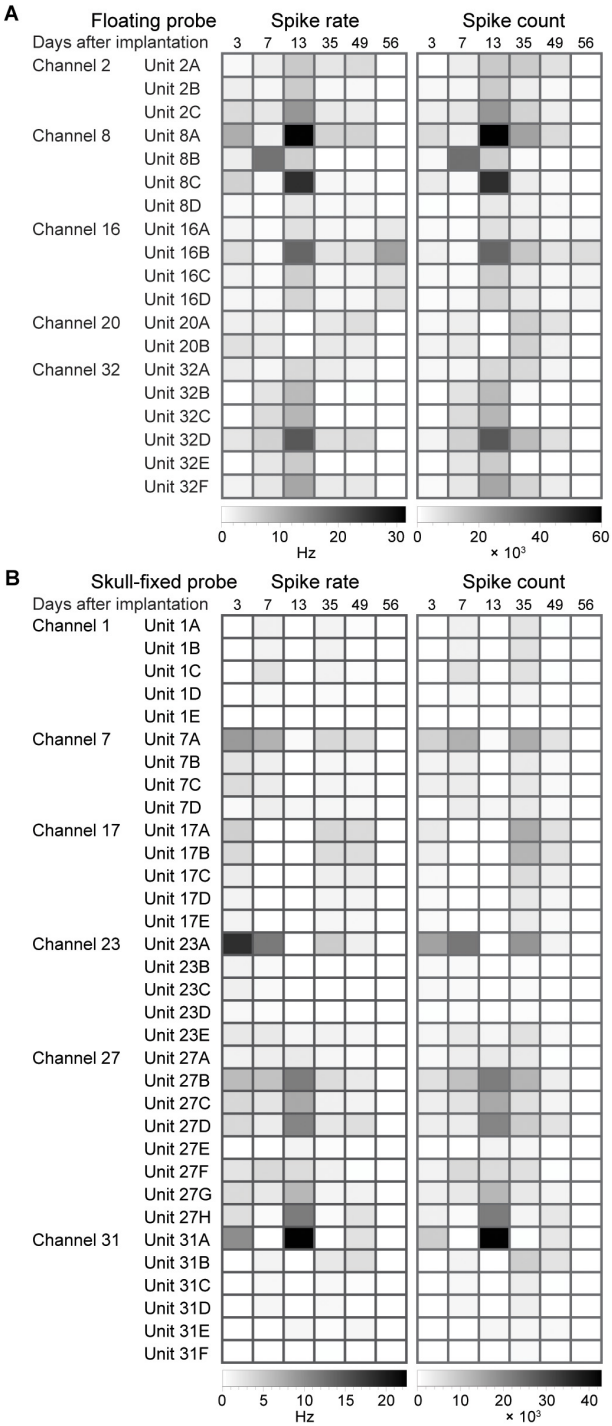

FIGURE 4 | Evolution of spike statistics across units and over weeks of recordings. Spike rate and spike count for **(A)** floating and **(B)** skull-fixed probes for different channels and units sorted on the specific channel.

both short and long-term variability. The probability to pick up well isolatable unit discharges changed from session to session for individual recording channels of both probes and spike shape analysis suggested changes in the relative position of recording sites and contributing neurons. This is expected since the brain can move substantially due to changes of intracranial pressure caused by respiration, coughing, heart beat and changes in posture, and as a consequence of rapid head movements. In addition to these short-term and mostly reversible changes in recording conditions we observed a gradual deterioration of the ability to record MUA responses that became manifest 8 weeks after implantation.

Comparison of Recording Stability Between Floating and Fixed Silicon-Based Laminar Probes

The comparison between the recording performances of a floating and a skull-fixed silicon-based neural probe, inserted in the same custom-made chamber, demonstrated that both implantation types are suitable to obtain long-term stable recordings of LFP and MUA from the primary visual cortex of awake behaving monkeys. The floating probe yielded slightly more stable recordings with better signal-to-noise ratios right after implantation and during the first weeks. The likely and anticipated reason for the higher recording performance variability of the skull-fixed probe is movements of the brain relative to the fixed probe. Such movements can account for the transient loss of spiking activity from individual recording sites and changing composition of neurons contributing to the recorded MUA. In addition, it is likely that the mechanical irritation caused by the movement induced glial reactions that may have further reduced recording performance (Ward et al., 2009). However, the differences between the floating and the fixed probe diminished with time because the recordings from the fixed electrode became more stable and at the end of the recording period, signal-to-noise ratios had decreased for both probes at some recording sites. This gradual degradation is expected and likely results from glial proliferation and chemical processes deteriorating the interface between the electrodes and the nervous tissue. We cannot differentiate between the two processes but apparently they had affected both probes, similarly. However, we anticipate that the yield of the skull-fixed probe can be increased substantially, in particular over long durations, if mounted on a microdrive permitting further adjustments – an option not available for floating probes (see below).

Spike Sorting

If spikes have similar waveform but are recorded from different sites with single electrodes, it must be assumed that they come from different neurons. However, spikes with similar waveforms recorded in the same session from the same electrode are likely to originate from the same cell, in particular if there are indications for a refractory time in the interval distribution. The recording horizon of a single electrode typically includes only up to twenty neurons in cortical layer V and fifty neurons in layer IV, the majority of cells tend to be most of the time silent and numerous cells with small spikes escape sorting. Thus, chances that more than one neuron contributes to a collection of identical spikes are reasonably low. Whether spikes with similar waveforms recorded

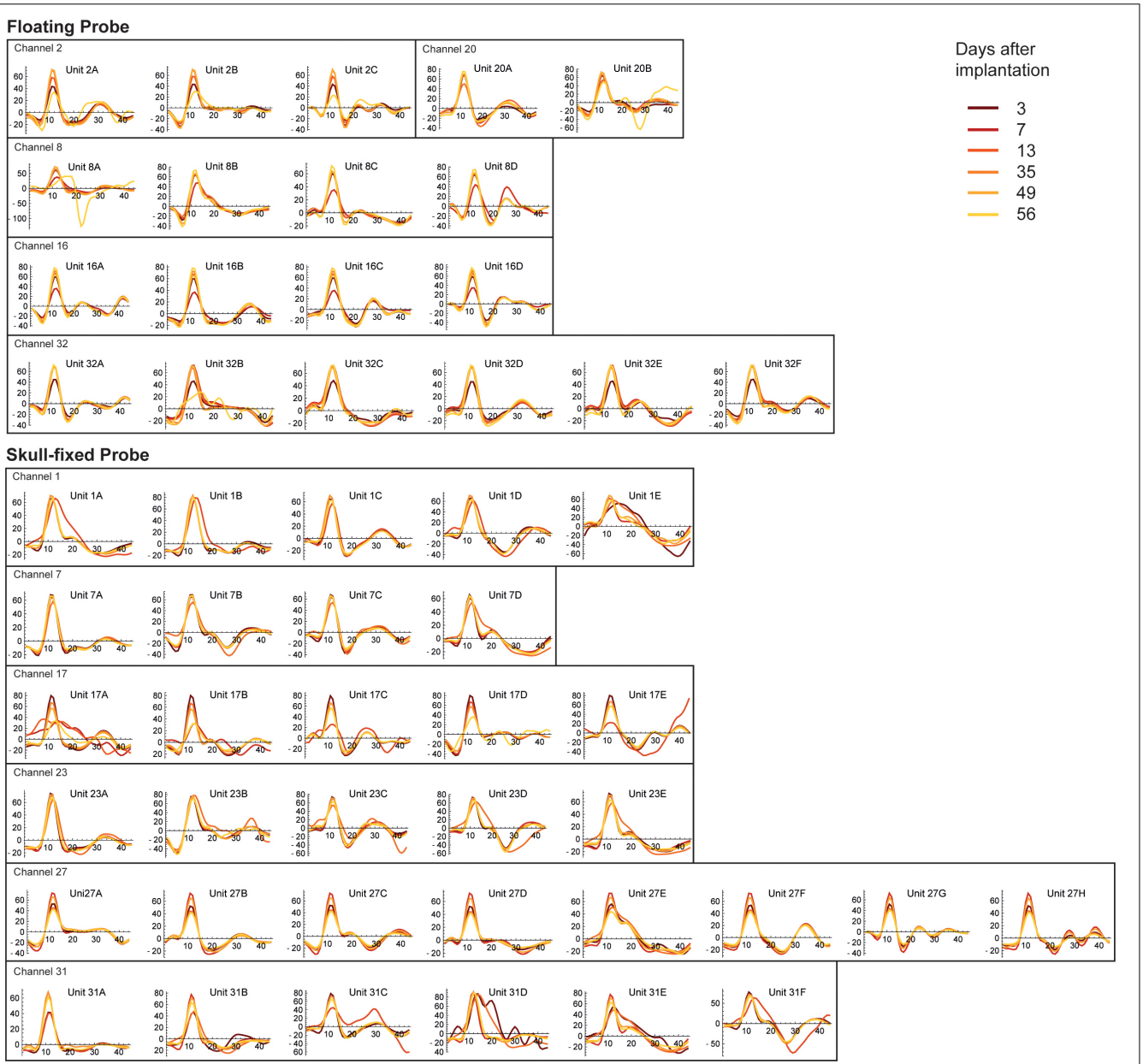

FIGURE 5 | Stability of spike waveforms across units, recording sites, and recording sessions. The *y*-axis displays spike amplitude (in μV), the *x* axis displays time, expressed in samples. As the sampling frequency of our recording system was 24414 Hz, one sample corresponds to 40.96 μs (therefore 44 samples correspond to ∼1.8 ms). Note units displaying stable waveforms and spike widths with stable (Channel 7 of the fixed probe, Channel 20 of the floating probe) or varying spike amplitudes (Channel 2 of the floating probe and Channel 17 of the fixed probe) along different recording sessions.

from the same channel but in different sessions are from the same cell is impossible to decide when recordings are discontinuous as in the present experiment. Thus, we ignore for how long individual cells can be followed.

Firing Rates

The spontaneous firing rates of the sampled neurons were low as is characteristic for cortical neurons. They increase to variable extents with light stimulation. However, the increase depends critically on the type of neurons and the match between stimulus configuration and receptive field structure. In the present experiments no attempts were made to optimize this match. For the determination of basic receptive field properties (position, orientation preference, and direction preference) we used simple grating stimuli and light bars, whose orientation and direction of drift were varied systematically. Thus, it is conceivable that we failed to optimally drive some of the recorded cells. However, we had no indications for pathological discharge patterns such as sustained high frequency discharges or high frequency bursts.

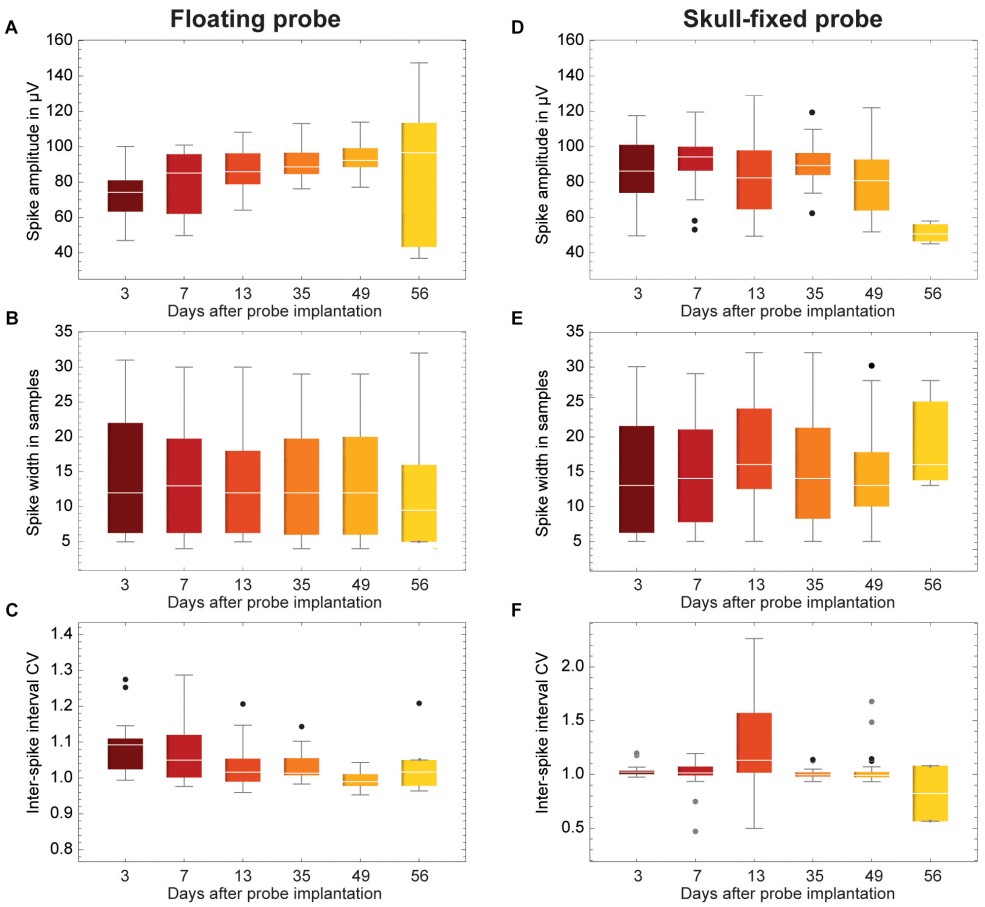

FIGURE 6 | Evolution of spike statistics across units and over weeks of recordings. **(A,D)** Spike amplitude; **(B,E)** Spike width; and **(C,F)** Coefficient of variation of inter-spike interval (ISI CV). Data is grouped for **(A–C)** floating and **(D–F)** skull-fixed neural probes (black circles, outlier, outside 1.5× interquartile range; gray circles, far outlier, outside 3× interquartile range).

Potential Explanations for Recording Stability Variations

The gradual increase in recording stability observed for the fixed probe is probably due to several processes that reduced relative movements between the brain and the probe. Insertion of probes is inevitably associated with dimpling of brain tissue due to compression, and the gradual re-expansion of tissue that may last several days leads to relative motion and unstable recordings. The floating probe is less exposed to this effect as it moves with the brain. Another factor for a protracted increase in stability is improved sealing. After craniotomies the exposed dura mater tends to proliferate. This has the dual effect that the leakage of cerebrospinal fluid through the hole caused by the penetrating probe gets sealed and that the stiffness of the dura increases. Both factors reduce movements of the brain and thereby enhance recording stability. Again, the floating probe is less likely to benefit from these proliferative processes which likely account for the time-dependent decrease of the differences in performance between the two probes (Santhanam et al., 2007). As expected from numerous previous studies we observed neither a time-dependent change in the ability to record LFPs, nor did we see differences between the two probes. LFPs reflect the activity of large populations of neurons, and hence are little influenced by small movements nor by changes in the micro-environment of the neural probe (Andersen et al., 2004; Flint et al., 2013; Hall et al., 2014).

The fact that spikes get smaller across sessions probably results from a deterioration of the interface between the electrode and the tissue (glial reactions, oxidation of the electrode, etc.). That spikes become wider could mean that electrodes become less sensitive and pick up only cells with large dipoles and these tend to be large pyramids with broad spikes.

Numerous studies have shown that long-term recordings can be obtained with skull-fixed, chronically implanted microwires, or matrix electrodes in rodents (Karumbaiah et al., 2013; Kozai et al., 2015), NHP (Jackson and Fetz, 2007; Tolias et al., 2007; Hall et al., 2014; McMahon et al., 2014) and human subjects (Serruya et al., 2002). However, in cases where the electrodes could not be moved once implanted, there was always a gradual degradation of the ability to record spiking activity. Most likely this is not due to a general deterioration of the electrodes because small movements of the electrode can often reinstall

TABLE 1 | Summary of ANOVA statistics together with Dunnett's *post hoc* tests for spike rate per unit, spike amplitude, spike width and ISI CV comparing recording sessions for both types of probes.

		DF[1]	Sum of Sq	Mean Sq	F Ratio	*p* Value
Spike rate (per unit and per session)						
Floating probe						
	Model	5	977.776	195.555	10.965	1.499×10^{-8}
	Error	108	1926.16	17.835		
	Total	113	2903.93			
Post tests	Dunnett: session 3 significant					
Fixed probe						
	Model	5	146.58	29.316	3.673	3.384×10^{-3}
	Error	192	1532.48	7.982		
	Total	197	1679.06			
Post tests	Dunnett: session 6 significant					
Spike amplitude (per session)						
Floating probe						
	Model	5	5707.25	1141.45	4.017	2.321×10^{-3}
	Error	99	28129.5	284.136		
	Total	104	33836.8			
Post tests	Dunnett: sessions 3, 4, 5 significant					
Fixed probe						
	Model	5	6961.07	1392.21	4.978	3.020×10^{-4}
	Error	150	41955	279.7		
	Total	155	48916.1			
Post tests	Dunnett: session 6 significant					
Spike width (per session)						
Floating probe						
	Model	5	24.430	4.886	0.068	0.997
	Error	99	7089.53	71.611		
	Total	104	7113.96			
Post tests	Dunnett: no session significant					
Fixed probe						
	Model	5	242.815	48.563	0.828	0.532
	Error	150	8798.33	58.656		
	Total	155	9041.15			
Post tests	Dunnett: no session significant					
ISI coefficient of variation						
Floating probe						
	Model	5	0.131	0.026	2.185	0.062
	Error	95	1.139	0.012		
	Total	100	1.270			
Post tests	Dunnett: session 5 significant					
Fixed probe						
	Model	5	8.159	1.632	6.755	1.097×10^{-5}
	Error	144	34.782	0.242		
	Total	149	42.941			
Post tests	Dunnett: session 3 significant					

[1] *DF: degrees of freedom.*

satisfactory recording conditions (cf. method section of Gray et al. (2007). Thus, the likely reason for degradation are changes in the micro-environment in the immediate vicinity of the electrode tips or the hot spots in case of silicon probes. Such adjustments are routinely performed in rodent experiments with chronically implanted hyperdrives that allow continuous advancement of micro-wire electrodes (tetrodes) and permit good recordings over months. Similarly, successful long-term recordings have been reported in NHPs implanted with the multi-electrode drive from Gray Matter Research, that permits continuous depth adjustments of 32 independently controlled glass-coated platinum-iridium or tungsten microelectrodes. We work with Gray Matter Research drives and can obtain MUA activity from the large majority of electrodes even 4 years after implantation (personal observation). In our experience, small movements of the electrodes (∼50 μm up or down) suffice to recuperate MUA recordings.

Conclusion

In conclusion, our results suggest a slight advantage in recording stability of floating over fixed probes in early phases after chronic implantation but this advantage levels off after several weeks. Therefore, a number of arguments lead us to suggest to not pursue the floating solution any further, but to rather invest in the perfection of chronic implantation of head fixed high-density laminar probes in NHPs. A major disadvantage of floating probes is that they cannot be adjusted after insertion which limits the possibility to optimize the number of hot spots recording MUA responses. Another problem is their connection with the plug in the chamber. Already with our 16-channel probes, these connections required the development of special highly flexible ribbon cables. When the number of hot spots is scaled up to several hundreds, this solution becomes obsolete because the cables become too rigid. The alternative to realize connections via a PCB is equally incompatible with a floating solution.

Future Directions of Research

In the light of this evidence the results obtained in the present study with laminar probes are promising and suggest the following strategy for the chronic implantation of high-density laminar probes. We suggest opting for a skull-fixed configuration and the use of a PCB for connections as described in this study. Leaving the dura mater intact and assuring a hermetic seal of the intracranial space with an additional silastic membrane proved sufficient to prevent loss of cerebrospinal fluid and infections. However, this approach required beveling of the tip of the laminar probe in order to permit penetration of the two barriers. To overcome the initial instability of recording performance and to minimize tissue irritation by movement-related friction it is imperative to further reduce brain movement. In a pilot experiment, we have therefore begun to test a viable and simple solution for the reduction of pulsations. We enlarged the base plate of the inserter, brought it in direct contact with the silastic membrane and advanced the electrode through a small hole in the baseplate. This effectively reduced brain pulsation and assured stable recordings right from the beginning. Furthermore, we suggest to miniaturize the inserter so that it can remain in the chamber and permit repeated adjustment of the probe position. In this case the probe can be moved up and down without further surgical intervention. In this way the distance of the hot spots relative to active neurons can be optimized and neuronal responses recovered over very long periods of time. In addition, the probe can be retracted once laminar recordings have been completed, the inserter can be removed

together with the electrode and replaced by other devices that permit insertion of electrode arrays covering larger regions. All these manipulations can be executed without breaking the seal between the chamber and intracranial space and without surgery. This should permit long-term recordings with changing electrode configurations and will substantially enhance the wealth and quality of data obtainable from a single animal. As NHP can learn to perform a great variety of tasks and usually cooperate over many years, numerous different paradigms can be investigated in the same animal following a single surgical intervention for the implantation of the recording chamber.

We are currently investigating these options further and hope to be able to report about the results in the near future. If successful, this approach would pave the way for the chronic implantation of various electrode configurations, including high density laminar probes and would substantially scale up the amount of data obtainable per animal, thereby complying with two of the three R's (reduce, refine, and replace) which are mandatory for the protection of experimental animals.

AUTHOR CONTRIBUTIONS

PR and WS developed the concept and design of the study. LC was involved in the feasibility of the study in monkeys, organized the database, analyzed the LFP data, and performed spike-sorting. KG performed the statistical analysis on spike-sorted data. JK-L performed the *in vivo* recordings. FP realized the modified recording chamber and designed the probe interfaces. AA, TH, and OP participated in the technical aspects of the probe design. LC wrote the first draft of the manuscript. LC, FP, PR, and WS wrote sections of the manuscript. All authors contributed to manuscript revision, read and approved the submitted version.

FUNDING

We gratefully acknowledge funding from the European Union's Seventh Framework Program (FP7/2007-2013) under grant agreement no. 600925 (NeuroSeeker). The article processing charge was funded by the German Research Foundation (DFG) and the University of Freiburg in the funding programme Open Access Publishing.

ACKNOWLEDGMENTS

This work has also been previously assigned for presentation at the 8th International IEEE EMBS Conference On Neural Engineering (NER'17) on May, 2018.

SUPPLEMENTARY MATERIAL

The Supplementary Material for this article can be found online at: https://www.frontiersin.org/articles/10.3389/fnins.2019.00464/full#supplementary-material

REFERENCES

Andersen, R. A., Musallam, S., and Pesaran, B. (2004). Selecting the signals for a brain–machine interface. *Curr. Opin. Neurobiol.* 14, 720–726. doi: 10.1016/j.conb.2004.10.005

Barz, F., Livi, A., Lanzilotto, M., Maranesi, M., Bonini, L., Paul, O., et al. (2017). Versatile, modular 3D microelectrode arrays for neuronal ensemble recordings: from design to fabrication, assembly, and functional validation in non-human primates. *J. Neural Eng.* 14:036010. doi: 10.1088/1741-2552/aa5a90

Biran, R., Martin, D. C., and Tresco, P. A. (2007). The brain tissue response to implanted silicon microelectrode arrays is increased when the device is tethered to the skull. *J. Biomed. Mater. Res. A* 82, 169–178. doi: 10.1002/jbm.a.31138

Blanche, T. J., Spacek, M. A., Hetke, J. F., and Swindale, N. V. (2005). Polytrodes: high-density silicon electrode arrays for large-scale multiunit recording. *J. Neurophysiol.* 93, 2987–3000.

Bonini, L., Maranesi, M., Livi, A., Bruni, S., Fogassi, L., Holzhammer, T., et al. (2014). Application of floating silicon-based linear multielectrode arrays for acute recording of single neuron activity in awake behaving monkeys. *Biomed. Eng.* 59, 273–281. doi: 10.1515/bmt-2012-0099

Carpenter, G. A., and Grossberg, S. (1987). Discovering order in chaos - stable self-organization of neural recognition codes. *Ann. N. Y. Acad. Sci.* 504, 33–51. doi: 10.1111/j.1749-6632.1987.tb48724.x

Chauvière, L., and Singer, W. (2019). Neurofeedback training of gamma oscillations in monkey primary visual cortex. *Cereb. Cortex* doi: 10.1093/cercor/bhz013 [Epub ahead of print].

Chestek, C. A., Gilja, V., Nuyujukian, P., Foster, J. D., Fan, J. M., Kaufman, M. T., et al. (2011). Long-term stability of neural prosthetic control signals from silicon cortical arrays in rhesus macaque motor cortex. *J. Neural Eng.* 8:045005. doi: 10.1088/1741-2560/8/4/045005

De Dorigo, D., Moranz, C., Graf, H., Marx, M., Wendler, D., Shui, B., et al. (2018). Fully immersible subcortical neural probes with modular architecture and a delta-sigma ADC integrated under each electrode for parallel readout of 144 recording sites. *IEEE J. Solid-State Circuits* 53, 3111–3125. doi: 10.1109/JSSC.2018.2873180

Dimitriadis, G., Neto, J. P., Aarts, A., Alexandru, A., Ballini, M., Battaglia, F., et al. (2018). Why not record from every channel with a CMOS scanning probe? *bioRxiv* 275818. doi: 10.1101/275818

Edell, D. J., Vo Toi, V. V., McNeil, V. M., and Clark, L. D. (1992). Factors influencing the biocompatibility of insertable silicon microshafts in cerebral cortex. *IEEE Trans. Biomed. Eng.* 39, 635–643. doi: 10.1109/10.141202

Ersen, A., Elkabes, S., Freedman, D. S., and Sahin, M. (2015).). Chronic tissue response to untethered microelectrode implants in the rat brain and spinal cord. *J. Neural Eng.* 12:16019. doi: 10.1088/1741-2560/12/1/016019

Fiáth, R., Beregszászi, P., Horváth, D., Wittner, L., Aarts, A. A. A., Ruther, P., et al. (2016). Large-scale recording of thalamocortical circuits: in vivo electrophysiology with the two-dimensional electronic depth control silicon probe. *J. Neurophysiol.* 116, 2312–2330. doi: 10.1152/jn.00318.2016

Flint, R. D., Wright, Z. A., Scheid, M. R., and Slutzky, M. W. (2013). Long term, stable brain machine interface performance using local field potentials and multiunit spikes. *J. Neural Eng.* 10:056005. doi: 10.1088/1741-2560/10/5/056005

Gray, C., Maldonado, P., Wilson, M., and McNaughton, B. (1995). Tetrodes markedly improve the reliability and yield of multiple single-unit isolation from multi-unit recordings in cat striate cortex. *J. Neurosci. Methods* 63, 43–54. doi: 10.1016/0165-0270(95)00085-2

Gray, C. M., Goodell, B., and Lear, A. (2007). Multichannel micromanipulator and chamber system for recording multineuronal activity in alert, non-human primates. *J. Neurophysiol.* 98, 527–536. doi: 10.1152/jn.00259.2007

Hall, T. M., Nazarpour, K., and Jackson, A. (2014). Real-time estimation and biofeedback of single-neuron firing rates using local field potentials. *Nat. Commun.* 5:5462. doi: 10.1038/ncomms6462

Harris, J. P., Capadona, J. R., Miller, R. H., and Healy, B. C. (2011). Mechanically adaptive intracortical implants improve the proximity of neuronal cell bodies. *J. Neural Eng.* 8:066011. doi: 10.1088/1741-2560/8/6/066011

Herbawi, A. S., Christ, O., Kiessner, L., Mottaghi, S., Hofmann, U. G., Paul, O., et al. (2018). CMOS neural probe with 1600 close-packed recording Sites and 32 analog output channels. *J. Microelectromechan. Syst.* 27, 1023–1034. doi: 10.1109/JMEMS.2018.2872619

Herwik, S., Paul, O., and Ruther, P. (2011). ultrathin silicon chips of arbitrary shape by etching before grinding. *Microelectromech. Syst. J.* 20, 791–793. doi: 10.1109/JMEMS.2011.2148159

Hochberg, L. R., Bacher, D., Jarosiewicz, B., Masse, N. Y., Simeral, J. D., Vogel, J., et al. (2012). Reach and grasp by people with tetraplegia using a neurally controlled robotic arm. *Nature* 485, 372–375. doi: 10.1038/nature11076

Jackson, A., and Fetz, E. E. (2007). Compact movable microwire array for long-term chronic unit recording in cerebral cortex of primates. *J. Neurophysiol.* 98, 3109–3118. doi: 10.1152/jn.00569.2007

Karumbaiah, L., Saxena, T., Carlson, D., Patil, K., Patkar, R., Gaupp, E. A., et al. (2013). Relationship between intracortical electrode design and chronic recording function. *Biomaterials* 34, 8061–8074. doi: 10.1016/j.biomaterials.2013.07.016

Kisban, S., Kenntner, J., Janssen, P., Metzen, R. V., Herwik, S., Bartsch, U., et al. (2009). "A novel assembly method for silicon-based neural devices," in *Proceedings of the IFMBE*, eds O. Doessel and W. C. Schlegel (Berlin: Springer), 107–110.

Kozai, T. D. Y., Du, Z., Gugel, Z. V., Smith, M. A., Chase, S. M., Bodily, L. M., et al. (2015). Comprehensive chronic laminar single-unit, multi-unit, and local field potential recording performance with planar single shank electrode arrays. *J. Neurosci. Methods* 242, 15–40. doi: 10.1016/j.jneumeth.2014.12.010

Lacour, S. P., Courtine, G., and Guck, J. (2016). Materials and technologies for soft implantable neuroprostheses. *Nat. Rev. Mater.* 1, 16063–16064. doi: 10.1038/natrevmats.2016.63

Lanzilotto, M., Livi, A., Maranesi, M., Gerbella, M., Barz, F., Ruther, P., et al. (2016). Extending the cortical grasping network: pre-supplementary motor neuron activity during vision and grasping of objects. *Cereb. Cortex* 26, 4435–4449. doi: 10.1093/cercor/bhw315

Lecomte, A., Descamps, E., and Bergaud, C. (2018). A review on mechanical considerations for chronically-implanted neural probes. *J. Neural Eng.* 15:031001. doi: 10.1088/1741-2552/aa8b4f

Lewis, C. M., Bosman, C. A., Brunet, N. M., Lima, B., Roberts, M. J., Womelsdorf, T., et al. (2016). Two frequency bands contain the most stimulus-related information in visual cortex. *bioRxiv* 3, doi: 10.1101/049718

Lind, G., Linsmeier, C. E., and Schouenborg, J. (2013). The density difference between tissue and neural probes is a key factor for glial scarring. *Sci. Rep.* 3:2942. doi: 10.1038/srep02942

Liu, J., Fu, T.-M., Cheng, Z., Hong, G., Zhou, T., Jin, L., et al. (2015). Syringe-injectable electronics. *Nat. Nanotechnol.* 10, 629–636. doi: 10.1038/nnano.2015.115

Luan, L., Wei, X., Zhao, Z., Siegel, J. J., Potnis, O., Tuppen, C. A., et al. (2017). Ultraflexible nanoelectronic probes form reliable, glial scar–free neural integration. *Sci. Adv.* 3:e1601966. doi: 10.1126/sciadv.1601966

Markwardt, N. T., Stokol, J., and Rennaker, R. L. II (2013). Sub-meninges implantation reduces immune response to neural implants. *J. Neurosci. Methods* 14, 119–125. doi: 10.1016/j.jneumeth.2013.01.020

McMahon, D. B. T., Bondar, I. V., Afuwape, O. A. T., Ide, D. C., and Leopold, D. A. (2014). One month in the life of a neuron: longitudinal single-unit electrophysiology in the monkey visual system. *J. Neurophysiol.* 112, 1748–1762. doi: 10.1152/jn.00052.2014

Nguyen, J. K., Park, D. J., Skousen, J. L., Hess-dunning, A. E., Tyler, D. J., and Rowan, S. J. (2014). Mechanically-compliant intracortical implants reduce the neuroin fl ammatory response. *J. Neural Eng.* 11:056014. doi: 10.1088/1741-2560/11/5/056014

Nicolelis, M. A. L., Dimitrov, D., Carmena, J. M., Crist, R., Lehew, G., Kralik, J. D., et al. (2003). Chronic, multisite, multielectrode recordings in macaque monkeys. *PNAS* 100, 11041–11046. doi: 10.1073/pnas.1934665100

Normann, R. A., and Fernandez, E. (2016). Clinical applications of penetrating neural interfaces and utah electrode array technologies. *J. Neural Eng.* 13:061003. doi: 10.1088/1741-2560/13/6/061003

Okun, M., Lak, A., Carandini, M., and Harris, K. D. (2016). Long term recordings with immobile silicon probes in the mouse cortex. *PLoS One* 11:e0151180. doi: 10.1371/journal.pone.0151180

Polikov, V. S., Tresco, P. A., and Reichert, W. M. (2005). Response of brain tissue to chronically implanted neural electrodes. *J. Neurosci. Methods* 148, 1–18. doi: 10.1016/j.jneumeth.2005.08.015

Prodanov, D., and Delbeke, J. (2016). Mechanical and biological interactions of implants with the brain and their impact on implant design. *Front. Neurosci.* 10:11. doi: 10.3389/fnins.2016.00011

Raducanu, B. C., Yazicioglu, R. F., Lopez, C. M., Ballini, M., Putzeys, J., Wang, S., et al. (2017). Time multiplexed active neural probe with 1356 parallel recording sites. *Sensors* 17:E2388. doi: 10.3390/s17102388

Rousche, P. J., Pellinen, D. S., Pivin, D. P., Williams, J. C., Vetter, R. J., and Kipke, D. R. (2001). Flexible polyimide-based intracortical electrode arrays with bioactive capability. *Biomed. Eng. IEEE Trans.* 48, 361–371. doi: 10.1109/10.914800

Salatino, J. W., Ludwig, K. A., Kozai, T. D. Y., Purcell, E. K., Lansing, E., Clinic, M., et al. (2017). Glial responses to implanted electrodes in the brain. *Nat. Biomed. Eng.* 1, 862–877. doi: 10.1038/s41551-017-0154-1.Glial

Santhanam, G., Linderman, M. D., Gilja, V., Afshar, A., Ryu, S. I., Meng, T. H., et al. (2007). HermesB: a continuous neural recording system for freely behaving primates. *IEEE Trans. Biomed. Eng.* 54, 2037–2050. doi: 10.1109/TBME.2007.895753

Scholvin, J., Kinney, J. P., Bernstein, J. G., Moore-Kochlacs, C., Kopell, N., Fonstad, C. G., et al. (2016). Close-packed silicon microelectrodes for scalable spatially oversampled neural recording. *IEEE Trans. Biomed. Eng.* 63, 120–130. doi: 10.1109/TBME.2015.2406113

Seidl, K., Herwik, S., Torfs, T., Neves, H. P., Paul, O., and Ruther, P. (2011). CMOS-based high-density silicon microprobe arrays for electronic depth control in intracortical neural recording. *J. Microelectromech. Syst.* 20, 1439–1448. doi: 10.1109/JMEMS.2011.2167661

Serruya, M. D., Hatsopoulos, N. G., Paninski, L., Fellows, M. R., and Donoghue, J. P. (2002). Brain-machine interface: instant neural control of a movement signal. *Nature* 416, 141–142. doi: 10.1038/416141a

Szarowski, D. H., Andersen, M. D., Retterer, S., Spence, A. J., and Isaacson, M. (2003). Brain responses to micro-machined silicon devices. *Brain Res.* 983, 23–35. doi: 10.1016/S0006-8993(03)03023-3

Tolias, A. S., Ecker, A. S., Siapas, A. G., Hoenselaar, A., Keliris, G. A., and Logothetis, N. K. (2007). Recording chronically from the same neurons in awake, behaving primates. *J. Neurophysiol.* 98, 3780–3790. doi: 10.1152/jn.00260.2007

Velliste, M., Perel, S., Spalding, M. C., Whitford, A. S., and Schwartz, A. B. (2008). Cortical control of a prosthetic arm for self-feeding. *Nature* 453, 1098–1101. doi: 10.1038/nature06996

Ward, M. P., Rajdev, P., Ellison, C., and Irazoqui, P. P. (2009). Toward a comparison of microelectrodes for acute and chronic recordings. *Brain Res.* 1282, 183–200. doi: 10.1016/j.brainres.2009.05.052

Wise, K. D., Sodagar, A. M., Yao, Y., Gulari, M. N., Perlin, G. E., and Najafi, K. (2008). Microelectrodes, microelectronics, and implantable neural microsystems. *Proc. IEEE* 96, 1184–1202. doi: 10.1109/JPROC.2008.922564

Woolley, A. J., Desai, H. A., and Otto, K. J. (2013). Chronic intracortical microelectrode arrays induce non-uniform, depth-related tissue responses. *J. Neural Eng.* 10:26007. doi: 10.1088/1741-2560/10/2/026007

Conflict of Interest Statement: TH, AA, OP, and PR are co-founders of ATLAS Neuroengineering bvba, Leuven, Belgium. TH and AA are CTO and CEO of ATLAS, respectively.

The remaining authors declare that the research was conducted in the absence of any commercial or financial relationships that could be construed as a potential conflict of interest.

frontiers in Neuroscience

ORIGINAL RESEARCH
published: 20 August 2019
doi: 10.3389/fnins.2019.00820

Low-Frequency Pulsed Magnetic Field Improves Depression-Like Behaviors and Cognitive Impairments in Depressive Rats Mainly via Modulating Synaptic Function

Jiajia Yang[1†], Ling Wang[1†], Faqi Wang[2], Xiaoxuan Tang[1], Peng Zhou[1], Rong Liang[1], Chenguang Zheng[1] and Dong Ming[1,2*]*

[1] Laboratory of Neural Engineering and Rehabilitation, Department of Biomedical Engineering, College of Precision Instruments and Optoelectronics Engineering, Tianjin University, Tianjin, China, [2] Tianjin International Joint Research Center for Neural Engineering, Academy of Medical Engineering and Translational Medicine, Tianjin University, Tianjin, China

Transcranial magnetic stimulation (TMS) has shown great promise as a medical treatment of depression. The effectiveness of TMS treatment at high frequency has been well investigated; however, low-frequency TMS in depression treatment has rarely been investigated in depression-induced cognitive deficits. Herein, this study was carried out to assess the possible modulatory role of low-frequency pulsed magnetic field (LFPMF) on reversing cognitive impairment in a model of depression induced by chronic unpredictable stress (CUS). Wistar rats were randomly allocated into four groups as follows: a control group (CON), a control applied with LFPMF (CON + LFPMF), a CUS group, and a CUS treated with LFPMF (CUS + LFPMF) group. During 8 weeks of CUS, compared to those in the CON group, animals not only gained less weight but also exhibited anhedonia, anxiety, and cognitive decline in behavioral tests. After 2-week treatment of LFPMF, a 20 mT, 1 Hz magnetic stimulation, it reversed the impairment of spatial cognition as well as hippocampal synaptic function including long-term potentiation and related protein expression. Thus, LFPMF has shown effectively improvements on depressant behavior and cognitive dysfunction in CUS rats, possibly via regulating synaptic function.

Keywords: depression, low-frequency pulsed magnetic field, cognition function, synaptic plasticity, neuronal oscillation

OPEN ACCESS

Edited by:
Alexander Dityatev, German Center for Neurodegenerative Diseases (DZNE), Germany

Reviewed by:
Brent Winslow, Design Interactive, United States
Vishnu Suppiramaniam, Auburn University, United States

***Correspondence:**
Chenguang Zheng
cgzheng@tju.edu.cn
Dong Ming
richardming@tju.edu.cn

[†] These authors have contributed equally to this work

Specialty section:
This article was submitted to Neural Technology, a section of the journal Frontiers in Neuroscience

Received: *28 February 2019*
Accepted: *23 July 2019*
Published: *20 August 2019*

Citation:
Yang J, Wang L, Wang F, Tang X, Zhou P, Liang R, Zheng C and Ming D (2019) Low-Frequency Pulsed Magnetic Field Improves Depression-Like Behaviors and Cognitive Impairments in Depressive Rats Mainly via Modulating Synaptic Function. Front. Neurosci. 13:820. doi: 10.3389/fnins.2019.00820

INTRODUCTION

Depression is a major neuropsychological disorder and has the third-largest disease burden, with around 350 million patients suffering from it globally as of 2012 (Smith, 2014). It is a chronic disease and exhibits a wide variety of symptoms, such as depressive mood, sluggish ideation, and suicidal ideation (Pazini et al., 2016). Depressive disorder may lead to burden of patients, their families, and society. Besides emotional problems, recently researchers have frequently observed depressed

patients with cognitive impairment (Lam et al., 2014; Rock et al., 2014; Trivedi and Greer, 2014). Furthermore, one third to half of depressed patients who are in remission are still suffering from the cognitive deficits (Rosenblat et al., 2016). Although understanding of the pathophysiology of depression is still rudimentary due to its complex etiology. Previous findings suggest that neuronal activity, neural plasticity, oxidative stress, and cortisol levels contribute to the pathogenesis of depression (Neylan et al., 2001; Bremner et al., 2004; Hassouna et al., 2016). Among them, neural plasticity and oxidative stress also have great impact on cognition. And many antidepressants are beneficial to cognitive function in depression, such as vortioxetine and duloxetine (McIntyre and Lee, 2016). Cognitive dysfunction refers to significant and persistent functional impairment, which has attracted increased attention in the treatment of depression.

Transcranial magnetic stimulation (TMS), as a non-invasive brain stimulation technique, modulates brain activity via electromagnetic pulses discharged through a coil placed over the subject's head (Myczkowski et al., 2018). This technology has been used for the treatment of many neurological and psychiatric disorders (Sachdev et al., 2002). Furthermore, repetitive transcranial magnetic stimulation (rTMS) has been approved by the United States FDA for medication-resistant depression (O'Reardon et al., 2010). At present, the majority of studies have focused on the effects of high-frequency TMS (>1 Hz) on depression (Lage et al., 2016), at which the cognition is indeed improved in depressive patients (Galletly et al., 2016; Myczkowski et al., 2018). However, the potential mechanism has not been clarified yet.

Recently, Huang et al. (2017) reported that low-frequency rTMS (1 Hz) treatment alleviated the deficits of AD-related cognitive function and synaptic plasticity. These results caused concerns about the role of low-frequency ($\leq$1 Hz) magnetic fields on brain function. According to previous investigations, low-frequency pulsed magnetic field (LFPMF) could regulate synaptic functions and cortical excitability (Chauviere et al., 2009; Guosheng et al., 2014; Senkowski and Gallinat, 2015), which suggested that LFPMF may play a particular role on the neuromodulation of brain. Furthermore, according to a conductance-based neuron model, LFPMF could modulate neuronal activities, such as changing spike times and further modulating spiking rhythms (Guosheng et al., 2014). Because rhythmic or repetitive neural activity of neuronal ensembles, also called as neural oscillation, has been demonstrated to be closely associated with the cognitive functions (Winson, 1978; Chauviere et al., 2009; Ehrlichman et al., 2009; Senkowski and Gallinat, 2015), LFPMF may have the potential to be applied to reduce depression-induced cognition impairment.

Herein, in the present study we recorded local field potential (LFP) and excitatory postsynaptic potential (EPSP) in hippocampal CA1 and CA3 regions to explore the alternation of synaptic plasticity and neural oscillations. Meanwhile, western blot assay was performed for measuring synaptic-associated protein alternations to explore the potential synaptic mechanism. Overall, we indicate LFPMF (1 Hz) can ameliorate depression-like behaviors and cognitive impairment in a model of depression induced by chronic unpredictable stress (CUS), as well as the potential mechanisms.

MATERIALS AND METHODS

Animals

Thirty-six adult male Wistar rats were purchased from the Laboratory Animal Center, Academy of Military Medical Science of People's Liberation Army, and they were allowed to habituate for 1 week. Unless otherwise specified, animals were kept under a 12-h light-dark cycle and allowed *ad libitum* access to food and water. They were randomly divided into control group (n = 16) and model group (n = 20). The rats of the model group received the CUS procedure for 8 weeks, while control group rats were with standard housing. Unfortunately, one control group rat died of fighting and one of the model group died during the CUS procedure. After 8 weeks, rats of the model group were randomly divided into LFPMF (CUS + LFPMF, n = 10) or standard housing (CUS, n = 9). Control group rats were randomized into two groups, CON (n = 8, standard housing) and CON + LFPMF (n = 7, LFPMF). All experiments were performed in accordance with the Animal Management Rules of the Ministry of Health of the People's Republic of China. All animal experiments were approved by the Animal Research Ethics Committee, School of Medicine, Nankai University. The experimental schedules are depicted in **Figure 1**.

CUS Procedure

To induce chronic stress in rats from the model group, we used a previously validated CUS protocol with some modifications (Willner et al., 1987, 1992; Zhang et al., 2018). Rats were subjected to various and repeated unpredictable stressors for a period of 8 weeks. Stressors were from the following list: ice–water swim (4°C ± 2 for 5 min), reversal of dark/light cycle, white noise (60 min), hot-water swim (40°C ± 2 for 5 min), clamping tail (1 min), tilt cages (45° tilt), and food and water deprivation. Each rat received one stressor per day. In order to achieve unpredictability, the stressors were applied in a different sequence each week to avoid any habituation. At the same time, control rats did not receive any stressors and were housed in normal conditions.

LFPMF Stimulation Procedure

During treatment, the round coil was placed on the head of awake animal at an approximately 5 mm distance from the skin. Each animal received 1 Hz pulsed trains at 20 mT magnetic field intensity, which were conducted during one LFPMF session in 14 days, 1 h per day. The rats were in the restraint device throughout their individual treatments.

Behavioral Experiment

Sucrose preference test (SPT): prior to the SPT, all rats were trained to habituate 2% sucrose water by placing a bottle of normal water and a bottle of sucrose solution with them for 2 days. Afterward, they were deprived of food and water for 23 h. Then animals were exposed to one bottle of tap water and one

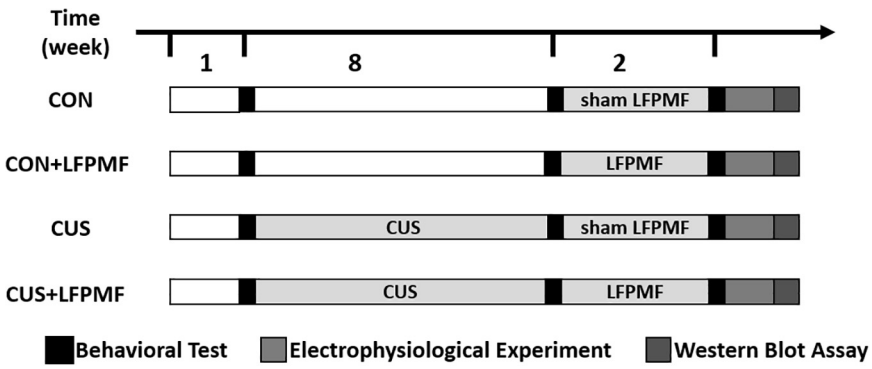

FIGURE 1 | Experimental protocol.

bottle of 2% sucrose solution for 1 h. The sucrose preference index (SPI) is defined as the ratio of the sucrose consumption to the total amount of solution consumed (Yi-Huan et al., 2015). The test was performed before and after CUS procedure.

Anxiolytic activity was measured in the elevated plus-maze (EPM) test. In this test, rats were placed in a standard EPM sized maze. Animals were allowed to freely explore the maze for 5 min, and the total number of arm entries and the percentage of entries into and the proportion of time spent in the open arms were assessed (Hu et al., 2016). The test was performed after LFPMF or sham stimulation.

Morris water maze (MWM) was performed as described previously with some changes (Wang et al., 2017b). The whole task comprised four consecutive stages: acquisition training, probe trial, reversal training, and reversal probe trial. Training trials (days 1–4) consisted of eight sessions (two sessions per day, 7 h apart), each with four trials. One trial ended when the rat located the hidden platform. Rats were allowed to swim for a maximum of 60 s for each trial. At 24 h after the last training session, the rats were tested in the probe trial in which the platform was removed. In reversal phases, the platform was moved to the opposite quadrant. The test was performed after LFPMF or sham stimulation. All behaviors were carried out with the experimenter blind to the treatment groups.

Electrophysiological Experiment

Animals were anaesthetized with urethane with a dosage of 4 ml/kg prior to placement in a stereotaxic frame. A monopolar extracellular stainless steel recording electrode was implanted into hippocampal CA1 region (2.5 mm lateral and 3.5 mm posterior to Bregma; depth from dura, 2.0–2.5 mm), while a concentric bipolar stainless steel electrode was placed into the Schaffer collaterals region (3.5 mm lateral and 4.2 mm posterior to Bregma; depth from dura, 2.5–3.0 mm). LFP signals were sampled simultaneously in both CA1 and Schaffer collaterals at a 1-kHz sample frequency. Before the long-term potentiation (LTP) induction, the test stimuli were delivered to CA1 region every minute to evoke a response of 70% of its maximum (range 0.3–0.5 mA). Afterward, theta burst stimulation (TBS) consisting of 30 bursts (12 pulses) of high-frequency stimulation (200 Hz) was used to induce LTP. The electrophysiological data were measured in Clampfit 10.0 (Molecular Devices, CA). More details were illustrated in the previous papers (Xu et al., 2015; Zheng and Zhang, 2015).

LFP Analysis

All the LFP data processing was conducted offline using custom routines in MATLAB (MathWorks). In our paper, several mathematical methods were used to conduct hippocampal neurodynamic analysis, including power spectrum, sample entropy (SampEn), phase locking value (PLV), and modulation index (MI) of theta-gamma cross frequency coupling between CA1 and CA3 regions. The details were described in previous studies (Xu et al., 2015; Zheng and Zhang, 2015).

Western Blot Assay

After electrophysiological experiment, the rats were sacrificed immediately and the following protocols reported previously with minor modification were conducted (Wang et al., 2017a; Yang et al., 2017). The hippocampus was removed at 0°C and homogenized in RIPA buffer which contained 1% PMSF (Solarbio, China). Lysates were then centrifuged at 12,000 rpm at 4°C for 20 min, and the supernatants were collected. Protein concentration was determined using the BCA Protein assay kit (Solarbio, China). After that, equal amounts of protein (40 ug/lane) for each sample were loaded and run on an 8–15% SDS-PAGE gel, which were transferred to 0.44 um polyvinylidene difluoride (PVDF) membrane (Millipore Corporation) at 4°C (BIO-RAD, United States). The PVDF membrane was blocked in Tris-buffered saline with Tween-20 (TBST) containing 5% skimmed milk for 1 h at room temperature. Next, the membranes were incubated with primary antibody overnight at 4°C (anti-SYP 1:10000, anti-PSD95, anti-NMDAR2B 1:2000, Genetex). After washing thrice with TBST, the PVDF membranes were subsequently incubated with secondary antibody (anti-mouse IgG HRP conjugate, anti-rabbit IgG HRP conjugate, 1:2000, Genetex) for 1 h at room temperature. Finally, a computerized chemiluminescent imaging system (Tanon Science & Technology, China) was employed to identify the protein band intensities.

Statistical Analysis

Statistical analysis was carried out with SPSS 11.0. Results are expressed as the mean ± SEM. The data of weight, MWM and fEPSP slop were analyzed using three-way repeated measures ANOVA, with treatment × model as the between-subjects factor and measurement session as the within-subjects factor. All other data were evaluated by a two-way ANOVA with treatment × model as the between-subjects factor, followed by Bonferroni test as *post hoc* analysis for further examination of group differences. Significance level was set at $p < 0.05$.

RESULTS

Representations of Anxiety-Related Behaviors

During the behavioral experiments, there were some accidents causing loss of data for some rats. Specifically, after the SPI test, two bottles of two CUS + LFPMF rats were found to be leaking. And during the EPM test, one rat in CON group and one in CON + LFPMF group always fell down from the elevated plus-maze. So during the analysis of behavioral data, there were CON (n = 7), CON + LFPMF (n = 6), CUS (n = 9), and CUS + LFPMF (n = 7).

The effect of chronic stress on body weight is shown in **Figure 2A**. After 8 weeks, animal weight was significantly decreased in model group compared to the control group [main effect of CUS model: $F(1,25) = 17.337$, $p < 0.001$, repeated measures ANOVA]. However, the CUS rats' weights were not increased after LFPMF treatment [main effect of treatment: $F(1,25) = 0.021$, $p = 0.886$, no CUS model × treatment interaction: $F(1,25) = 0.035$, $p = 0.853$, repeated measures ANOVA]. The results showed that after the CUS procedure, the SPI of the control group was significantly higher than that of the model group [**Figure 2B**, main effect of CUS model: $F(1,25) = 108.153$, $p < 0.001$, main effect of treatment: $F(1,25) = 0.008$, $p = 0.929$, no CUS model × treatment interaction: $F(1,25) = 0.009$, $p = 0.925$, two-way ANOVA], suggesting that CUS model rats behaved in anhedonia similarly as depressive patients. Analogously, in EPM compared to the control group, CUS-exposed rats exhibited anxiety behaviors as a decrease in the number percentage of entries into open arms [**Figure 2C**, main effect of CUS model: $F(1,25) = 12.966$, $p = 0.001$, main effect of treatment: $F(1,25) = 1.628$, $p = 0.214$, CUS model × treatment interaction: $F(1,25) = 9.087$, $p = 0.006$, two-way ANOVA] rather than the percentage of residence time in open arms [**Figure 2D**, main effect of CUS model: $F(1,25) = 0.651$, $p = 0.427$, main effect of treatment: $F(1,25) = 0.141$, $p = 0.711$, no CUS model × treatment interaction: $F(1,25) = 1.369$, $p = 0.253$, two-way ANOVA].

LFPMF Prevents CUS-Induced Spatial Learning and Memory Deficits

Learning occurred in all groups as the escape latencies progressively became shorter over the training period [**Figure 3A**, main effect of time: $F(7,175) = 66.327$, $p < 0.001$; **Figure 3D**, main effect of time: $F(3,75) = 52.087$, $p < 0.001$, repeated measures ANOVA]. The rats with LFPMF treatment took less time to find the hidden platform than other groups in acquisition trainings of MWM test [main effect of treatment: $F(1, 25) = 3.055$, $p = 0.093$, main effect of CUS model: $F(1, 25) = 0.043$, $p = 0.838$, CUS model × treatment interaction: $F(1,25) = 6.741$, $p = 0.016$, repeated measures ANOVA]. Notably, this impairment could not be attributed to alterations of sensorimotor functions since the swimming speed remained unchanged among these groups (**Figures 3B,E**). After training, in the probe trial the rats showed robust spatial memory with a strong preference for the target quadrant [**Figure 3C**, main effect of treatment: $F(1, 25) = 2.702$, $p = 0.113$, main effect of CUS model: $F(1, 25) = 1.185$, $p = 0.287$, no CUS model × treatment interaction: $F(1,25) = 1.503$, $p = 0.232$, two-way ANOVA], as well as in the reversal probe trial [**Figure 3F**, main effect of treatment: $F(1, 25) = 7.695$, $p = 0.010$, main effect of CUS model: $F(1, 25) = 2.714$, $p = 0.112$, no CUS model × treatment interaction: $F(1,25) = 3.922$, $p = 0.059$, two-way ANOVA]. The results showed that LFPMF treatment impacted the reversal memory of rats. Besides the statistical results, **Figure 3G** shows representative training swim tracks in acquisition and reversal stages.

The Effects of LFPMF on Synaptic Plasticity in Hippocampus

In the electrophysiological experiment, the induction of LTP did not succeed in all rats. There were CON (n = 4), CON + LFPMF (n = 4), CUS (n = 7), CUS + LFPMF (n = 4). EPSPs were evoked by a range of stimuli from Schaffer collaterals to CA1. To quantify these responses, measurements were taken from the slope of EPSPs. The slopes of I/O curves from Schaffer to CA1 in CON + LFPMF, CUS or CUS + LFPMF were similar to CON rats [**Figure 4A**, main effect of time: $F(7, 98) = 82.655$, $p < 0.001$, main effect of treatment: $F(1, 14) = 0.004$, $p = 0.950$, main effect of CUS model: $F(1, 14) = 0.347$, $p = 0.565$, no CUS model × treatment interaction: $F(1,14) = 0.429$, $p = 0.523$, repeated measures ANOVA]. After TBS, LTP in CON + LFPMF and CUS + LFPMF rats was sustained at the same level as CON rats for the duration of the recordings [**Figure 4B**, main effect of time: $F(29, 406) = 50.596$, $p < 0.001$, main effect of treatment: $F(1, 14) = 1.414$, $p = 0.254$, repeated measures ANOVA]. In contrast, potentiation significantly declined in CUS model rats by 60 min after LTP induction [**Figure 4B**, main effect of CUS model: $F(1, 14) = 13.005$, $p = 0.003$, no CUS model × treatment interaction: $F(1,14) = 4.527$, $p = 0.052$, repeated measures ANOVA]. The synapses also showed two forms of brief potentiation: post-tetanic potentiation (PTP), which lasts for 5–10 min, and short-term potentiation (STP), which lasted rather longer, around 30 min (Hannay et al., 1993). Following the brief potentiation, the LTP was generated and lasted for an hour or longer (Colino et al., 1992). Therefore, the slopes of different stages were analyzed to evaluate the differences among the four groups. As shown in **Figure 4C**, there were significant differences in the three phases [PTP: main effect of treatment: $F(1, 14) = 1.778$, $p = 0.204$, main effect of CUS model: $F(1, 14) = 8.176$, $p = 0.013$, no CUS model × treatment

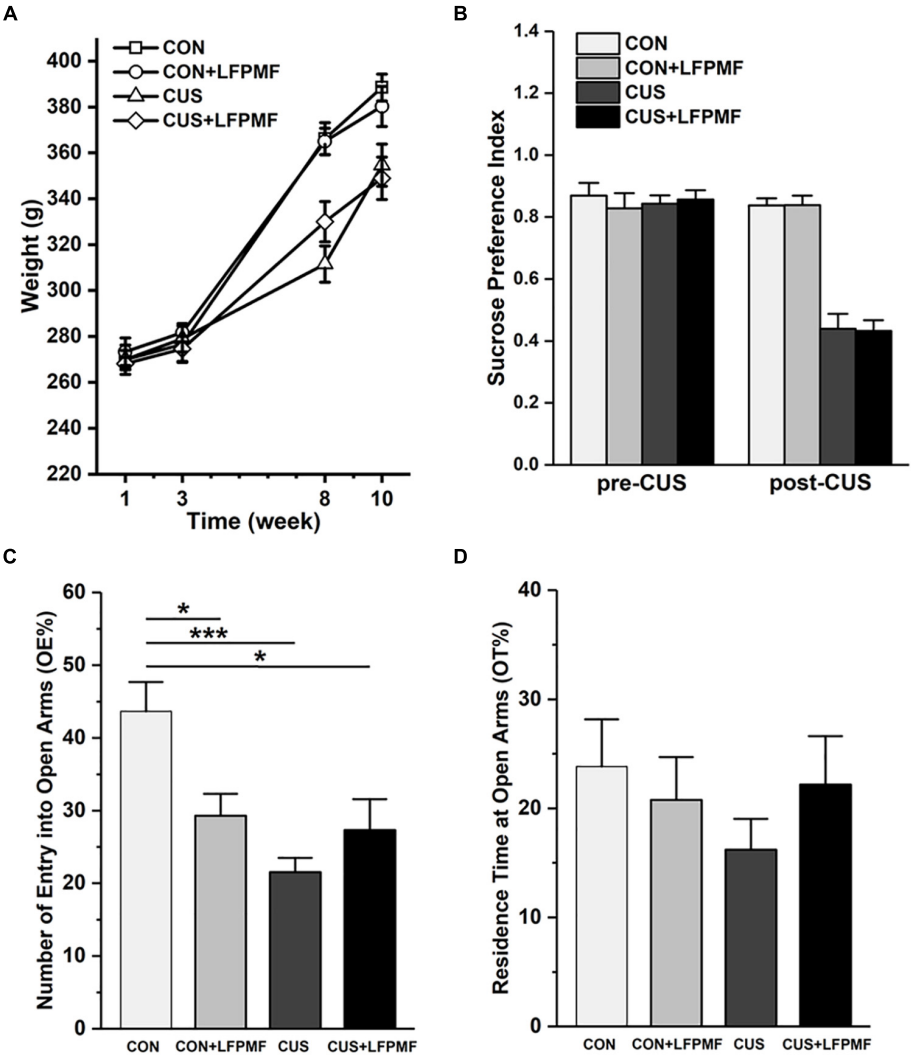

FIGURE 2 | Effects of LFPMF and CUS on depressive- and anxiety-like behavior. **(A)** Mean weight. **(B)** Mean sucrose preference index. **(C)** Mean number of entries into open arms. **(D)** Mean residence time at open arms. *$p < 0.05$, ***$p < 0.001$.

interaction: $F(1,14) = 2.947$, $p = 0.108$; STP: main effect of treatment: $F(1, 14) = 1.856$, $p = 0.195$, main effect of CUS model: $F(1, 14) = 11.575$, $p = 0.004$, no CUS model × treatment interaction: $F(1,14) = 3.638$, $p = 0.077$; LTP: main effect of treatment: $F(1, 14) = 0.460$, $p = 0.509$, main effect of CUS model: $F(1, 14) = 14.245$, $p = 0.002$, CUS model × treatment interaction: $F(1,14) = 5.715$, $p = 0.031$, two-way ANOVA].

The Effects of LFPMF on Neural Oscillation in the Hippocampus

Signals of LFP in Schaffer collaterals and CA1 were collected simultaneously. Represented LFP power spectra are shown in **Figures 5A,B**. The grand average is illustrated in **Figures 5C,D**, which includes the data of CA1 and CA3 as well as various frequency bands containing delta (1–4 Hz), theta (4–8 Hz), alpha (8–15 Hz), beta (15–30 Hz), and gamma (30–50 Hz). There were significant differences of power density at delta and theta rhythms both in CA1 [**Figure 5C**, delta rhythm, main effect of treatment: $F(1, 14) = 16.733$, $p = 0.001$, main effect of CUS model: $F(1, 14) = 0.553$, $p = 0.469$, CUS model × treatment interaction: $F(1,14) = 13.426$, $p = 0.003$; theta rhythm, main effect of treatment: $F(1, 14) = 10.143$, $p = 0.007$, main effect of CUS model: $F(1, 14) = 0.435$, $p = 0.520$, CUS model × treatment interaction: $F(1,14) = 27.414$, $p < 0.001$, two-way ANOVA] and CA3 regions [**Figure 5D**, main effect of treatment: $F(1, 14) = 18.105$, $p = 0.001$, main effect of CUS model: $F(1, 14) = 1.192$, $p = 0.293$, CUS model × treatment interaction: $F(1,14) = 18.912$, $p = 0.001$; theta rhythm, main effect of treatment: $F(1, 14) = 9.181$, $p = 0.009$, main effect of CUS model: $F(1, 14) = 0.145$, $p = 0.709$, CUS model × treatment interaction: $F(1,14) = 22.760$, $p < 0.001$, two-way ANOVA]. The pattern of field neural activity in depression rats was slightly changed by LFPMF.

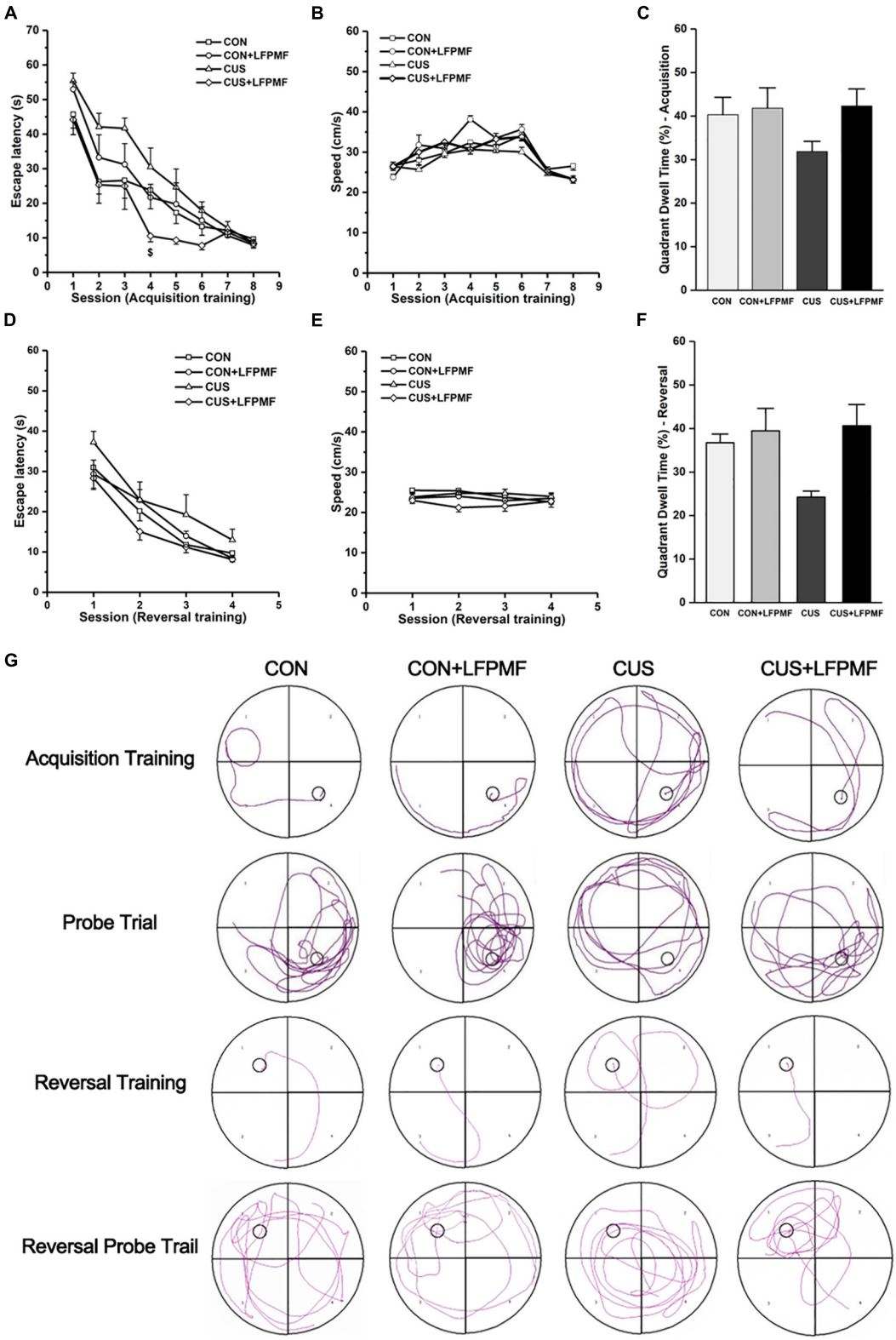

FIGURE 3 | Effects of LFPMF on the improvement of spatial cognition. **(A,D)** Mean escape latency was calculated for each session in acquisition training and reversal training. **(B,E)** Mean swimming speed in acquisition training and reversal training. **(C,F)** Mean percentage of time spend in target quadrant in probe trial and reversal probe trial. **(G)** Representative swim tracks. $^{\$}$CUS vs. CUS + LFPMF, $p < 0.05$.

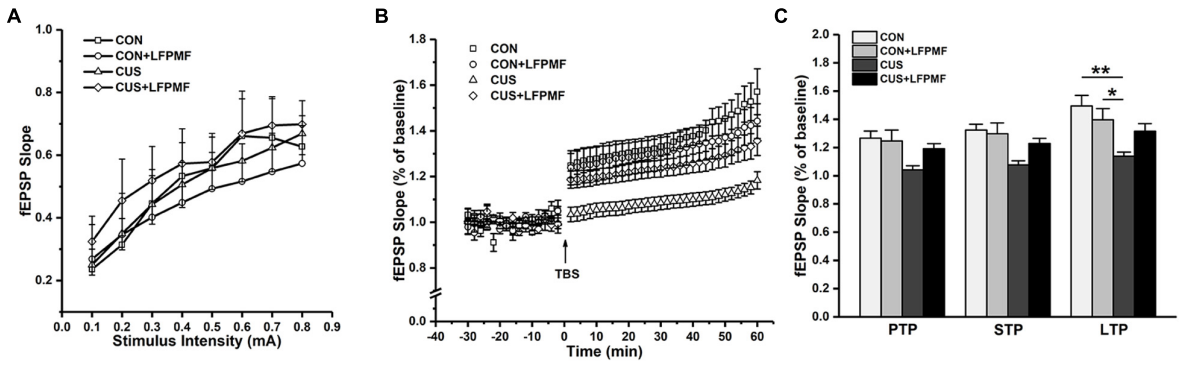

FIGURE 4 | Basal synaptic transmission and synaptic plasticity recorded from Schaffer collaterals to CA1 region. **(A)** I/O curves: slopes of EPSPs were plotted against stimuli ranging from 0.1 to 0.8 mA. **(B)** The time coursing of normalized EPSPs slopes in LTP stage. **(C)** Histogram shows the average changes in EPSPs slopes in PTP, STP, and LTP. *$p < 0.05$, **$p < 0.01$.

Sample entropy (SampEn) of LFP is presented in **Figure 5E**. The analysis demonstrated that SampEn values were not significantly changed among the four groups in either CA1 [main effect of treatment: $F(1, 14) = 0.952$, $p = 0.346$, main effect of CUS model: $F(1, 14) = 1.842$, $p = 0.196$, no CUS model × treatment interaction: $F(1,14) = 0.170$, $p = 0.687$, two-way ANOVA] or CA3 [main effect of treatment: $F(1, 14) = 1.019$, $p = 0.330$, main effect of CUS model: $F(1, 14) = 0.481$, $p = 0.499$, no CUS model × treatment interaction: $F(1,14) = 0.047$, $p = 0.831$, two-way ANOVA]. However, both in CA1 and CA3 regions, the SampEn of model groups was slightly higher than control groups.

Although the differences were not significant, a trend of decrease occurred in the CUS group of the PLV on theta [**Figure 5F**, main effect of treatment: $F(1, 14) = 0.385$, $p = 0.545$, main effect of CUS model: $F(1, 14) = 0.024$, $p = 0.880$, no CUS model × treatment interaction: $F(1,14) = 0.708$, $p = 0.414$, two-way ANOVA] and alpha [main effect of treatment: $F(1, 14) = 0.007$, $p = 0.934$, main effect of CUS model: $F(1, 14) = 1.115$, $p = 0.309$, no CUS model × treatment interaction: $F(1,14) = 0.996$, $p = 0.335$, two-way ANOVA] rhythms. Additionally, it can be seen that there was a visible theta-gamma PAC in CON and LFPMF groups [**Figure 5G**, main effect of treatment: $F(1, 14) = 4.664$, $p = 0.049$, main effect of CUS model: $F(1, 14) = 0.460$, $p = 0.508$, no CUS model × treatment interaction: $F(1,14) = 0.192$, $p = 0.668$, two-way ANOVA]. Additionally, **Figure 5H** shows the mean modulation indices in all groups.

Effects of LFPMF on the Expression of Related Synaptic Proteins

Our data so far demonstrated that CUS disrupted the LTP of the Schaffer-CA1 pathway. Synaptic and extrasynaptic N-methyl-D-aspartic acid receptor (NMDAR) proteins play different roles in regulating synaptic plasticity. We therefore measured the levels of synaptic-related proteins including synaptophysin (SYP), postsynaptic density protein 95 (PSD95), and NMDAR 2B (NR2B). The protein content of SYP (∼43 kDa) in the brain of CUS rats was lower than other rats [**Figure 6A**, main effect of treatment: $F(1, 120) = 0.003$, $p = 0.958$, main effect of CUS model: $F(1, 120) = 2.007$, $p = 0.159$, no CUS model × treatment interaction: $F(1,120) = 1.671$, $p = 0.199$, two-way ANOVA], although the differences were not significant. Significant differences were present in the relative expression of PSD95 (∼80 kDa) [**Figure 6B**, main effect of treatment: $F(1, 132) = 2.255$, $p = 0.136$, main effect of CUS model: $F(1, 132) = 34.865$, $p < 0.001$, CUS model × treatment interaction: $F(1,132) = 10.312$, $p = 0.002$, two-way ANOVA] and NR2B (∼166 kDa) [**Figure 6C**, main effect of treatment: $F(1, 80) = 0.623$, $p = 0.432$, main effect of CUS model: $F(1, 80) = 11.907$, $p = 0.001$, CUS model × treatment interaction: $F(1,80) = 4.989$, $p = 0.028$, two-way ANOVA]. *Post hoc* analysis revealed that LFPMF in the CUS rats caused a significant increase in hippocampal PSD95 and NR2B levels, while LFPMF had no distinct effect on CON rats.

DISCUSSION

Transcranial magnetic stimulation was introduced as a diagnostic method in 1985 (Barker et al., 1985), and recently it has been well established in neurology. Given that stimulation in different parameters leads to different outcomes, here, in the present study, we demonstrated that LFPMF (1 Hz, 20 mT) relieved the impaired spatial cognition induced by CUS. The potential mechanisms were correlated with the alternation of hippocampal synaptic efficacy and neural oscillation. These results indicated that a feasible and effective TMS protocol at low frequency has the potential to treat cognitive impairment in depression.

Chronic unpredictable stress as a well-validated paradigm has been used to induce a depression-like syndrome with some degree of cognitive deficit (Bondi et al., 2008; Logan et al., 2015), which was selected in this study. Compared to control groups, the CUS model animals showed typical depression symptoms in a SPT. It is noticeable, however, compared with the CON group, that the other three groups had anxiety symptoms observed in EPM. Nevertheless, in EPM the differences of the percentages of residence time in open arms among groups were not significant. This may be due to the sample size and differences within groups.

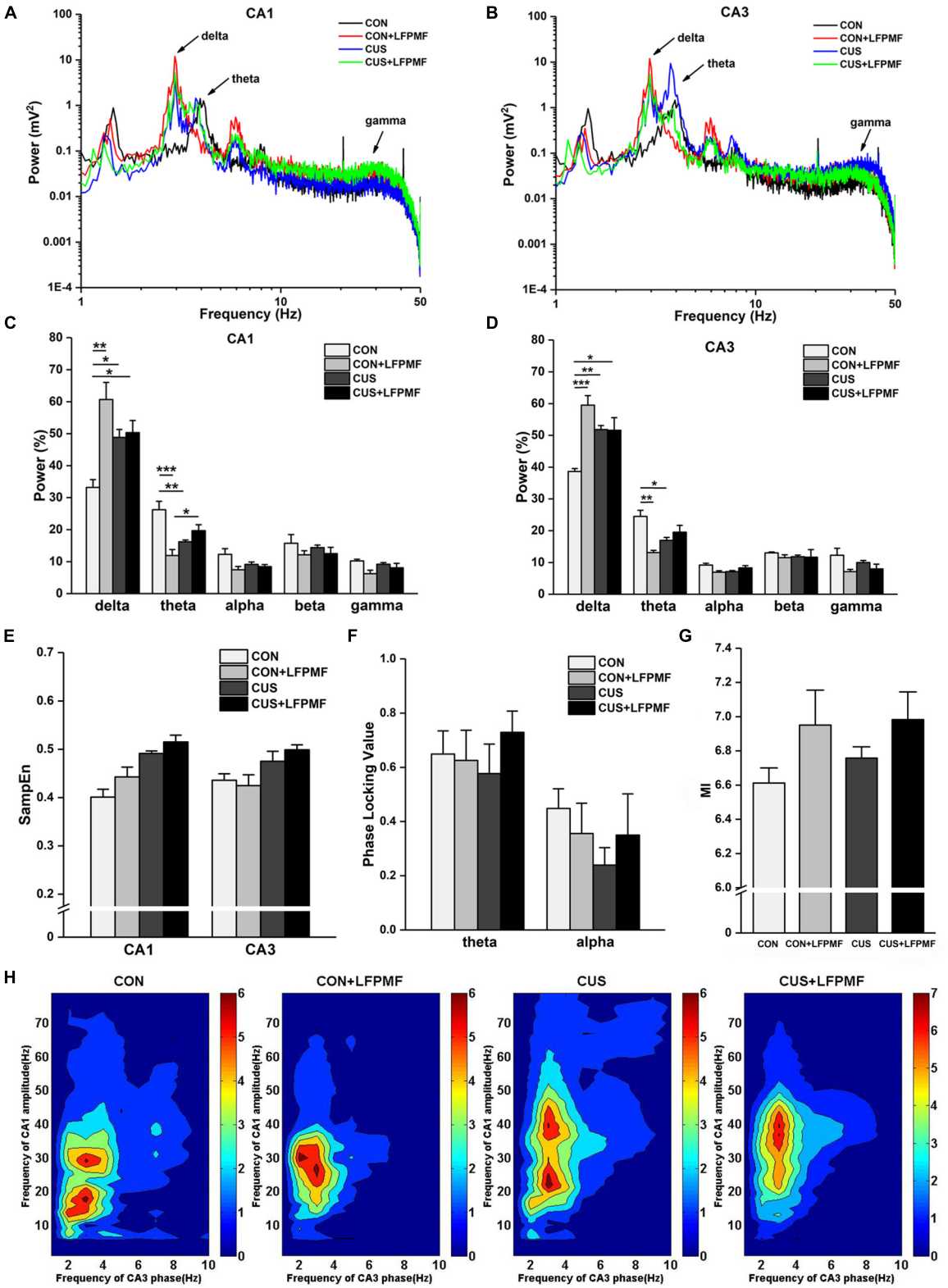

FIGURE 5 | Changes of power within various frequency bands and neural oscillation in hippocampus. **(A,B)** Representative traces of CA1 and CA3 LFPs in CON, CON + LFPMF, CUS, and CUS + LFPMF groups. **(C)** The group data of the power of various rhythms in both CA1 and **(D)** CA3 regions. **(E)** Non-linear sample entropy (SampEn) of LFP in CA1 and CA3 regions. **(F)** Averaged Schaffer-CA1 PLV at the theta rhythm and alpha rhythm. **(G)** Statistical MI data of phase-amplitude coupling between theta and gamma rhythms in the hippocampal Schaffer-CA1 pathway. **(H)** Mean PAC-MI measurement (Z-scored) of hippocampus in four groups. $^{*}p < 0.05$, $^{**}p < 0.01$, $^{***}p < 0.001$.

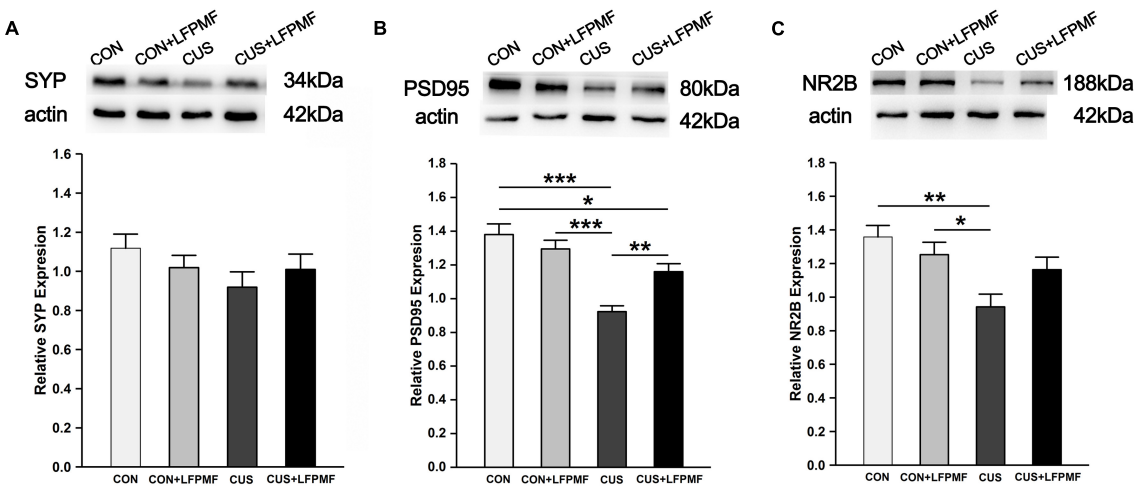

FIGURE 6 | Effects of LFPMF on the expression of synaptic-related proteins in hippocampus. Representative immunoreactive bands of SYP **(A)**, PSD95 **(B)**, NR2B **(C)**, and β-actin (upper) and quantitative analysis of the optical density ratio of SYP/β-actin **(A)**, PSD95/β-actin **(B)**, and NMDAR2B/β-actin **(C)**. $^{*}p < 0.05$, $^{**}p < 0.01$, $^{***}p < 0.001$.

As expected, the stress rats (CUS treated) also showed abnormal memory function which have been shown in MWM.

In order to assess the protective effect of LFPMF on cognition, MWM was set out to perform the training and probe trials. In the training trial, spatial learning is assessed across repeated trials, while in the probe trial reference memory was determined by preference for the platform area when the platform was absent. The reversal phase can reveal whether animals can extinguish their initial learning and memory of the platform's position and acquire a direct path to the new goal position. This method was used to evaluate the flexibility of learning and self-regulation (Vorhees and Williams, 2005). Most people with depression cannot regulate emotions very well, thus they are likely to be sustained in negative emotion (Ehring et al., 2010; Joormann and Vanderlind, 2014). Animal studies found that the impairment of reversal learning and behavioral flexibility was related to the disruption of LTD (Mills et al., 2014). Furthermore, reversal learning has been shown to involve disparate brain functional connectivity, including prefrontal connectivity and functional connectivity between the hippocampus and cingulate cortex (de Bruin et al., 1994; Shah et al., 2018). In this study, the results revealed that LFPMF could improve the spatial memory ability of rats, while they reacted quickly to the change of the platform's position. Therefore, our results implied that LFPMF as an effective and non-invasive brain stimulation method might improve cognition impairments induced by CUS.

The spatial cognition is strongly correlated with hippocampal synaptic plasticity and synaptic proteins. Furthermore, there is mounting evidence that damage to the hippocampus can produce inflexible and maladaptive behavior in humans (Henke et al., 1999; Mumby et al., 2002; Rubin et al., 2014) in areas such as memory, navigation, exploration, establishing and maintaining social bonds, etc. In different hippocampal subfields, the CA1 region is crucial for behavioral cognition, especially for spatial cognition, while the CA3 region is important for memory retention (Noble et al., 2014; Shang et al., 2016). The synaptic connection from CA3 Schaffer collaterals to CA1 pyramidal neurons belongs to the trisynaptic circuit of the hippocampus, which plays an important role in learning and memorizing (Scullin and Partridge, 2012). Hence, we measured multiform synaptic plasticity of the CA3-CA1 pathway, including long-term and short-term plasticity (Ohno et al., 2011). As mentioned before, LTP could last for an hour or longer (Colino et al., 1992). In our control group, the slope of fEPSPs was higher over time after TBS, which is consistent with some published articles (Petit-Pedrol et al., 2018; Wang et al., 2019). Previous studies have shown that depression impairs LTP, which may be a direct manifestation of abnormal neural plasticity (Shang et al., 2016; Wang et al., 2017b; Yang et al., 2017). In particular, the idea that LTP in the hippocampus supports associative memory formation has been widely accepted and has only rarely been questioned (Bannerman et al., 2014). As for short-term plasticity, it has been experimentally characterized in hippocampal neurons and considered to be one candidate mechanism for short-term memory (Erickson et al., 2010; Wang et al., 2017b; Tian et al., 2018). In the present study, both long-term and short-term plasticity of the CA3-CA1 pathway in CUS was ameliorated by LFPMF, in line with behavioral manifestations of MWM. As is widely known, hippocampal synaptic proteins are critical for synaptic plasticity (Fox et al., 2010; Counts et al., 2014; Shang et al., 2016; Han et al., 2018). It has been found that NMDAR plays an important role in the induction of LTP (Barkus et al., 2010). Thus, as one of the NMDAR subunits, NR2B is also believed to be closely related to synaptic plasticity and cognitive function (Barkus et al., 2010; Fox et al., 2010). There are other synaptic proteins which are also related to synaptic function, such as SYP and PSD95. The former is an essential membrane protein in synaptic vesicle, while PSD95 protein is present in the core part of the postsynapse (Counts et al., 2014; Shang et al., 2016; Han et al., 2018). In this study, the semiquantitative changes

(**Figure 6**) implied that the damage of CUS in depression may be mainly relevant to a postsynaptic mechanism rather than presynaptic. Crucially, after LFPMF, the damage could be alleviated, which implied that the target of LFPMF may be postsynaptic specific. In short, the up-regulation of synaptic plasticity and postsynaptic protein expression in the hippocampus may be the mechanisms of LFPMF on depression.

Apart from synaptic function, neural oscillation is also closely associated with cognition. The central problem for cognitive neuroscience is to describe how cognitive processes arise from brain processes. Informed by modern functional imaging techniques such as PET and fMRI, previous research has made an impressive beginning on this task. But cognitive processes are not static; they are dynamic (Ward, 2003). Rhythms with different frequencies in neural oscillation are related to various brain processes. Memory processes are most closely related to theta and gamma rhythms (Ward, 2003; Xu et al., 2015, 2016; Zheng and Zhang, 2015). Although the pathway from the ventral hippocampus to the medial prefrontal cortex (mPFC) is thought to play a significant role in emotional memory processing, the hippocampal CA3-CA1 pathway is recognized to be closely linked with spatial cognition (Montgomery and Buzsáki, 2007; Li et al., 2013; Wu et al., 2013; Kojima et al., 2016). Thus, neural oscillation of the CA1 and CA3 regions in the hippocampus was analyzed in this study. Moreover, the previous study (Wang et al., 2011) found that LFPMF (1 Hz) could increase the energy of low frequency bands (1–40 Hz) of human brain, especially the band of 1–3 Hz, which is called "resonance effects." Our animal experiments were consistent with the previous findings. LFPMF had a strong effect in CON rats, especially on delta and theta activities. The power of delta rhythm in CON rats was significantly lower than other groups, and we speculate that this could be induced by CUS treatment and 1 Hz magnetic stimulation, which could exert an effect on neuronal rhythmic activity of rats, especially on low-frequency rhythm. In some investigations, delta activity was significantly increased in animals of the Katz model, a depression model similar to CUS (Sarbadhikari et al., 1996). In our previous research, furthermore, it was found that LFPMF significantly improved the undesirable changes of the identical-frequency synchronization and theta-gamma phase-amplitude coupling in CUS rats' hippocampi (Wang et al., 2018). With a few exceptions, in this paper LFPMF made an increasing tendency in the phase synchronization and the phase-amplitude coupling of the CUS group, but there was no significant difference. The cause may be that the number of animals used in neural oscillation analysis was not enough. On the other hand, there may also be other parameters that are affected which were not measured. In short, these results suggest that the regulation of neural oscillation in the hippocampus may be the potential mechanism of LFPMF, which needs further research in the future.

So far, we have tried to reveal the potential mechanisms of LFPMF from two aspects, synaptic function and neural oscillation, which have been proved to be closely related. For example, it has been found that theta phase coupling was positively correlated with synaptic plasticity in the vCA1–mPFC pathway in depression rats (Zheng and Zhang, 2015). In addition, Xu et al. (2013) reported that CA3-CA1 synaptic plasticity was positively correlated with the unidirectional indices from CA3 to CA1 in melamine-treated rats. This study showed that low-frequency magnetic stimulation can modulate synaptic function of CUS-induced depressive rats. The parameters we used in neural oscillation presented the effect of LFPMF in control rats rather than CUS model rats. Thus, other methods of neural oscillation analysis need further investigation, as well as the relationship between synaptic function and neural oscillation.

Overall, our study demonstrated that LFPMF could ameliorate the deficits of cognitive and synaptic functions through up-regulating the expression of related proteins in CUS rats, suggesting that LFPMF may serve as an effective treatment of cognition impairment caused by depression or other diseases. In the future, the molecular mechanisms underlying the beneficial effects of LFPMF and its remarkable effects on mood need to be further investigated.

DATA AVAILABILITY

Publicly available datasets were analyzed in this study. This data can be found here: https://doi.org/10.5281/zenodo.3261843.

ETHICS STATEMENT

This study was carried out in accordance with the recommendations of Animal Management Rules of the Ministry of Health of the People's Republic of China. The protocol was approved by the Animal Research Ethics Committee, School of Medicine, Nankai University.

AUTHOR CONTRIBUTIONS

JY and DM conceived and designed the manuscript. JY and LW drafted the manuscript. LW, FW, and RL performed the behavioral and electrophysiological experiments. LW and XT performed the western blot assay. PZ provided the technical support on magnetic stimulation. CZ contributed to the data analysis. All authors read and approved the final version of the manuscript.

FUNDING

This study was supported by grants from the National Natural Science Foundation of China (81871517, 31800889, and 81870847), the National Key R&D Program of China (2017YFB1300302), and the Tianjin Municipal Natural Science Foundation (17JCQNJC10500).

ACKNOWLEDGMENTS

The authors are grateful to Professors Zhuo Yang and Tao Zhang from the Nankai University for providing technical assistance.

REFERENCES

Bannerman, D. M., Sprengel, R., Sanderson, D. J., McHugh, S. B., Rawlins, J. N., Monyer, H., et al. (2014). Hippocampal synaptic plasticity, spatial memory and anxiety. *Nat. Rev. Neurosci.* 15, 181–192.

Barker, A. T., Jalinous, R., and Freeston, I. L. (1985). Non-invasive magnetic stimulation of human motor cortex. *Lancet* 325, 1106–1107. doi: 10.1016/s0140-6736(85)92413-4

Barkus, C., McHugh, S. B., Sprengel, R., Seeburg, P. H., Rawlins, J. N., and Bannerman, D. M. (2010). Hippocampal NMDA receptors and anxiety: at the interface between cognition and emotion. *Eur. J. Pharmacol.* 626, 49–56. doi: 10.1016/j.ejphar.2009.10.014

Bondi, C. O., Rodriguez, G., Gould, G. G., Frazer, A., and Morilak, D. A. (2008). Chronic unpredictable stress induces a cognitive deficit and anxiety-like behavior in rats that is prevented by chronic antidepressant drug treatment. *Neuropsychopharmacology* 33, 320–321.

Bremner, J. D., Vythilingam, M., Vermetten, E., Vaccarino, V., and Charney, D. S. (2004). Deficits in hippocampal and anterior cingulate functioning during verbal declarative memory encoding in midlife major depression. *Am. J. Psychiatry* 161, 637–645. doi: 10.1176/appi.ajp.161.4.637

Chauviere, L., Rafrafi, N. B. C., Bartolomei, F., Esclapez, M., and Bernard, C. (2009). Early deficits in spatial memory and theta rhythm in experimental temporal lobe epilepsy. *J. Neurosci.* 29, 5402–5410. doi: 10.1523/JNEUROSCI.4699-08.2009

Colino, A., Huang, Y. Y., and Malenka, R. C. (1992). Characterization of the integration time for the stabilization of long-term potentiation in area CA1 of the hippocampus. *J. Neurosci.* 12, 180–187. doi: 10.1523/jneurosci.12-01-00180.1992

Counts, S. E., Alldred, M. J., Che, S., Ginsberg, S. D., and Mufson, E. J. (2014). Synaptic gene dysregulation within hippocampal CA1 pyramidal neurons in mild cognitive impairment. *Neuropharmacology* 79, 172–179. doi: 10.1016/j.neuropharm.2013.10.018

de Bruin, J. P., Sanchez-Santed, F., Heinsbroek, R. P., Donker, A., and Postmes, P. (1994). A behavioural analysis of rats with damage to the medial prefrontal cortex using the morris water maze: evidence for behavioural flexibility, but not for impaired spatial navigation. *Brain Res.* 652, 323–333. doi: 10.1016/0006-8993(94)90243-7

Ehring, T., Tuschen-Caffier, B., Schnülle, J., Fischer, S., and Gross, J. J. (2010). Emotion regulation and vulnerability to depression: spontaneous versus instructed use of emotion suppression and reappraisal. *Emotion* 10, 563–572. doi: 10.1037/a0019010

Ehrlichman, R. S., Gandal, M. J., Maxwell, C. R., Lazarewicz, M. T., Finkel, L. H., Contreras, D., et al. (2009). N-methyl-d-aspartic acid receptor antagonist-induced frequency oscillations in mice recreate pattern of electrophysiological deficits in schizophrenia. *Neuroscience* 158, 705–712. doi: 10.1016/j.neuroscience.2008.10.031

Erickson, M. A., Maramara, L. A., and Lisman, J. (2010). A single brief burst induces GluR1-dependent associative short-term potentiation: a potential mechanism for short-term memory. *J. Cogn. Neurosci.* 22, 2530–2540. doi: 10.1162/jocn.2009.21375

Fox, C. J., Russell, K. I., Wang, Y. T., and Christie, B. R. (2010). Contribution of NR2A and NR2B NMDA subunits to bidirectional synaptic plasticity in the hippocampus in vivo. *Hippocampus* 16, 907–915. doi: 10.1002/hipo.20230

Galletly, C., Gill, S., Rigby, A., Carnell, B. L., and Clarke, P. (2016). Assessing the effects of repetitive transcranial magnetic stimulation on cognition in major depressive disorder using computerized cognitive testing. *J. ECT* 32:1. doi: 10.1097/YCT.0000000000000308

Guosheng, Y. I., Jiang, W., Xile, W. E. I., Bin, D., Kai-Ming, T., Wai-Lok, C., et al. (2014). Effects of extremely low-frequency magnetic fields on the response of a conductance-based neuron model. *Int. J. Neural Syst.* 24, 527–584. doi: 10.1142/S0129065714500075

Han, M., Bae, J. S., Shin, C. Y., Ban, J. J., Quan, Q. L., Lee, D. H., et al. (2018). UV irradiation through skin or eye reduces hippocampal neurogenesis and synaptic protein expression. *Photodermatol. Photoimmunol. Photomed.* 34, 276–278. doi: 10.1111/exd.12687

Hannay, T., Larkman, A., Stratford, K., and Jack, J. (1993). A common rule governs the synaptic locus of both short-term and long-term potentiation. *Curr. Biol.* 3, 832–841. doi: 10.1016/0960-9822(93)90217-c

Hassouna, I., Ott, C., Wüstefeld, L., Offen, N., Neher, R. A., Mitkovski, M., et al. (2016). Revisiting adult neurogenesis and the role of erythropoietin for neuronal and oligodendroglial differentiation in the hippocampus. *Mol. Psychiatry* 21:1752. doi: 10.1038/mp.2015.212

Henke, K., Weber, B., Kneifel, S., Wieser, H. G., and Buck, A. (1999). Human hippocampus associates information in memory. *Proc. Natl. Acad. Sci. U.S.A.* 96, 5884–5889. doi: 10.1073/pnas.96.10.5884

Hu, M., Zou, W., Wang, C. Y., Chen, X., Zeng, H. Y., Zhang, P., et al. (2016). Hydrogen sulfide protects against chronic unpredictable mild stress-induced oxidative stress in hippocampus by upregulation of BDNF-TrkB pathway. *Oxid. Med. Cell. Longev.* 2016:2153745. doi: 10.1155/2016/2153745

Huang, Y. J., Lane, H. Y., and Lin, C. H. (2017). New treatment strategies of depression: based on mechanisms related to neuroplasticity. *Neural Plast.* 2017:4605971. doi: 10.1155/2017/4605971

Joormann, J., and Vanderlind, W. M. (2014). Emotion regulation in depression: the role of biased cognition and reduced cognitive control. *Clin. Psychol. Sci.* 2, 402–421. doi: 10.1177/2167702614536163

Kojima, N., Yasuda, H., Hanamura, K., Ishizuka, Y., Sekino, Y., and Shirao, T. (2016). Drebrin a regulates hippocampal LTP and hippocampus-dependent fear learning in adult mice. *Neuroscience* 324, 218–226. doi: 10.1016/j.neuroscience.2016.03.015

Lage, C., Wiles, K., Shergill, S. S., and Tracy, D. K. (2016). A systematic review of the effects of low-frequency repetitive transcranial magnetic stimulation on cognition. *J. Neural. Transm.* 123, 1479–1490. doi: 10.1007/s00702-016-1592-8

Lam, R. W., Kennedy, S. H., McIntyre, R. S., and Khullar, A. (2014). Cognitive dysfunction in major depressive disorder: effects on psychosocial functioning and implications for treatment. *Can. J. Psychiatry* 59, 649–654. doi: 10.1177/070674371405901206

Li, S., Jin, M., Zhang, D., Yang, T., Koeglsperger, T., Fu, H., et al. (2013). Environmental novelty activates β2-adrenergic signaling to prevent the impairment of hippocampal LTP by Aβ oligomers. *Neuron* 77:929. doi: 10.1016/j.neuron.2012.12.040

Logan, R. W., Edgar, N., Gillman, A. G., Hoffman, D., Zhu, X., and McClung, C. A. (2015). Chronic stress induces brain region-specific alterations of molecular rhythms that correlate with depression-like behavior in mice. *Biol. Psychiatry* 78, 249–258. doi: 10.1016/j.biopsych.2015.01.011

McIntyre, R. S., and Lee, Y. (2016). Cognition in major depressive disorder: a 'Systemically Important Functional Index'(SIFI). *Curr. Opin. Psychiatry* 29, 48–55. doi: 10.1097/yco.0000000000000221

Mills, F., Bartlett, T. E., Dissing-Olesen, L., Wisniewska, M. B., Kuznicki, J., Macvicar, B. A., et al. (2014). Cognitive flexibility and long-term depression (LTD) are impaired following β-catenin stabilization in vivo. *Proc. Natl. Acad. Sci. U.S.A.* 111, 8631–8636. doi: 10.1073/pnas.1404670111

Montgomery, S. M., and Buzsáki, G. (2007). Gamma oscillations dynamically couple hippocampal CA3 and CA1 regions during memory task performance. *Proc. Natl. Acad. Sci. U.S.A.* 104, 14495–14500. doi: 10.1073/pnas.0701826104

Mumby, D. G., Gaskin, S., Glenn, M. J., Schramek, T. E., and Lehmann, H. (2002). Hippocampal damage and exploratory preferences in rats: memory for objects, places, and contexts. *Learn. Mem.* 9, 49–57. doi: 10.1101/lm.41302

Myczkowski, M. L., Fernandes, A., Moreno, M., Valiengo, L., Lafer, B., Moreno, R. A., et al. (2018). Cognitive outcomes of TMS treatment in bipolar depression: safety data from a randomized controlled trial. *J. Affect. Disord.* 235:20. doi: 10.1016/j.jad.2018.04.022

Neylan, T. C., Canick, J. D., Hall, S. E., Reus, V. I., Sapolsky, R. M., and Wolkowitz, O. M. (2001). Cortisol levels predict cognitive impairment induced by electroconvulsive therapy. *Biol. Psychiatry* 50, 331–336. doi: 10.1016/s0006-3223(01)01119-2

Noble, E. E., Mavanji, V., Little, M. R., Billington, C. J., Kotz, C. M., and Wang, C. (2014). Exercise reduces diet-induced cognitive decline and increases hippocampal brain-derived neurotrophic factor in CA3 neurons. *Neurobiol. Learn. Mem.* 114, 40–50. doi: 10.1016/j.nlm.2014.04.006

Ohno, T., Hasegawa, T., Tsuruoka, T., Terabe, K., Gimzewski, J. K., and Aono, M. (2011). Short-term plasticity and long-term potentiation mimicked in single inorganic synapses. *Nat. Mater.* 10, 591–595. doi: 10.1038/nmat3054

O'Reardon, J. P., Solvason, H. B., Janicak, P. G., Sampson, S., Isenberg, K. E., Nahas, Z., et al. (2010). Efficacy and safety of transcranial magnetic stimulation in the acute treatment of major depression: a multisite randomized controlled trial. *Biol. Psychiatry* 62, 1208–1216. doi: 10.1016/j.biopsych.2007.01.018

Pazini, F. L., Cunha, M. P., Rosa, J. M., Colla, A. R., Lieberknecht, V., Oliveira, Á, et al. (2016). Creatine, similar to ketamine, counteracts depressive-like behavior induced by corticosterone via PI3K/Akt/mTOR pathway. *Mol. Neurobiol.* 53, 6818–6834. doi: 10.1007/s12035-015-9580-9

Petit-Pedrol, M., Sell, J., Planagumà, J., Mannara, F., Radosevic, M., Haselmann, H., et al. (2018). LGI1 antibodies alter Kv1. 1 and AMPA receptors changing synaptic excitability, plasticity and memory. *Brain* 141, 3144–3159. doi: 10.1093/brain/awy253

Rock, P. L., Roiser, J. P., Riedel, W. J., and Blackwell, A. D. (2014). Cognitive impairment in depression: a systematic review and meta-analysis. *Psychol. Med.* 44, 2029–2040. doi: 10.1017/S0033291713002535

Rosenblat, J. D., Kakar, R., and McIntyre, R. S. (2016). The cognitive effects of antidepressants in major depressive disorder: a systematic review and meta-analysis of randomized clinical trials. *Int. J. Neuropsychopharmacol.* 19:yv082.

Rubin, R. D., Watson, P. D., Duff, M. C., and Cohen, N. J. (2014). The role of the hippocampus in flexible cognition and social behavior. *Front. Hum. Neurosci.* 8:742. doi: 10.3389/fnhum.2014.00742

Sachdev, P. S., McBride, R., Loo, C., Mitchell, P. M., Malhi, G. S., and Croker, V. (2002). Effects of different frequencies of transcranial magnetic stimulation (TMS) on the forced swim test model of depression in rats. *Biol. Psychiatry* 51, 474–479. doi: 10.1016/s0006-3223(01)01298-7

Sarbadhikari, S. N., Dey, S., and Ray, A. K. (1996). Chronic exercise alters EEG power spectra in an animal model of depression. *Indian J. Physiol. Pharmacol.* 40, 47–57.

Scullin, C. S., and Partridge, L. D. (2012). Modulation by pregnenolone sulfate of filtering properties in the hippocampal trisynaptic circuit. *Hippocampus* 22, 2184–2198. doi: 10.1002/hipo.22038

Senkowski, D., and Gallinat, J. (2015). Dysfunctional prefrontal gamma-band oscillations reflect working memory and other cognitive deficits in schizophrenia. *Biol. Psychiatry* 77, 1010–1019. doi: 10.1016/j.biopsych.2015.02.034

Shah, D., Verhoye, M., Van der Linden, A., and D'Hooge, R. (2018). Acquisition of spatial search strategies and reversal learning in the morris water maze depend on disparate brain functional connectivity in mice. *Cereb. Cortex.* doi: 10.1093/cercor/bhy329

Shang, Y., Wang, X., Shang, X., Zhang, H., Liu, Z., Yin, T., et al. (2016). Repetitive transcranial magnetic stimulation effectively facilitates spatial cognition and synaptic plasticity associated with increasing the levels of BDNF and synaptic proteins in Wistar rats. *Neurobiol. Learn. Mem.* 134, 369–378. doi: 10.1016/j.nlm.2016.08.016

Smith, K. (2014). Mental health: a world of depression. *Nature* 515:181.

Tian, Y., Yang, C., Cui, Y., Su, F., Wang, Y., Wang, Y., et al. (2018). An excitatory neural assembly encodes short-term memory in the prefrontal cortex. *Cell Rep.* 22, 1734–1744. doi: 10.1016/j.celrep.2018.01.050

Trivedi, M. H., and Greer, T. L. (2014). Cognitive dysfunction in unipolar depression: implications for treatment. *J. Affect. Disord.* 15, 19–27. doi: 10.1016/j.jad.2013.09.012

Vorhees, C. V., and Williams, M. T. (2005). Morris water maze: procedures for assessing spatial and related forms of learning and memory. *Nat. Protoc.* 1, 848–858. doi: 10.1038/nprot.2006.116

Wang, L., Wang, F., Liu, S., Yang, X., Yang, J., and Ming, D. (2017a). VEGF attenuates 2-VO induced cognitive impairment and neuronal injury associated with the activation of PI3K/Akt and Notch1 pathway. *Exp. Gerontol.* 102, 93–100. doi: 10.1016/j.exger.2017.12.010

Wang, L., Wang, J., Wang, F., Liu, C., Yang, X., Yang, J., et al. (2017b). VEGF-mediated cognitive and synaptic improvement in chronic cerebral hypoperfusion rats involves autophagy process. *Neuromolecular Med.* 19, 423–435. doi: 10.1007/s12017-017-8458-6

Wang, L., Yang, J., Wang, F., Zhou, P., Wang, K., and Ming, D. (2018). "Modulation of low-frequency pulsed magnetic field on hippocampal neural oscillation in depression rats"," in *Proceedings of the 2018 40th Annual International Conference of the IEEE Engineering in Medicine and Biology Society (EMBC)*, (Piscataway, NJ: IEEE).

Wang, X. M., Fang, C., Hong-Qiang, Y. U., and Peng, Z. (2011). Resonance effects on human brain based on magnetic stimulation of extremely low frequency. *J. Tianjin University* 44, 823–828.

Wang, Z. T., Lu, M. H., Zhang, Y., Ji, W. L., Lei, L., Wang, W., et al. (2019). Disrupted-in-schizophrenia-1 protects synaptic plasticity in a transgenic mouse model of Alzheimer's disease as a mitophagy receptor. *Aging Cell* 18:e12860. doi: 10.1111/acel.12860

Ward, L. M. (2003). Synchronous neural oscillations and cognitive processes. *Trends Cogn. Sci.* 7, 553–559. doi: 10.1016/j.tics.2003.10.012

Willner, P., Muscat, R., and Papp, M. (1992). Chronic mild stress-induced anhedonia: a realistic animal model of depression. *Neurosci. Biobehav. Rev.* 16, 525–534. doi: 10.1016/s0149-7634(05)80194-0

Willner, P., Towell, A., Sampson, D., Sophokleous, S., and Muscat, R. J. P. (1987). Reduction of sucrose preference by chronic unpredictable mild stress, and its restoration by a tricyclic antidepressant. *Psychopharmacology* 93, 358–364.

Winson, J. (1978). Loss of hippocampal theta rhythm results in spatial memory deficit in the rat. *Science* 201, 160–163. doi: 10.1126/science.663646

Wu, P. Y., Huang, Y. Y., Chen, C. C., Hsu, T. T., Lin, Y. C., Weng, J. Y., et al. (2013). Acid-sensing ion channel-1a is not required for normal hippocampal LTP and spatial memory. *J. Neurosci.* 33, 1828–1832. doi: 10.1523/JNEUROSCI.4132-12.2013

Xu, X., An, L., Mi, X., and Zhang, T. (2013). Impairment of cognitive function and synaptic plasticity associated with alteration of information flow in theta and gamma oscillations in melamine-treated rats. *PLoS One* 8:e77796. doi: 10.1371/journal.pone.0077796

Xu, X., Liu, C., Li, Z., and Tao, Z. (2015). Effects of hydrogen sulfide on modulation of theta–gamma coupling in hippocampus in vascular dementia rats. *Brain Topogr.* 28, 879–894. doi: 10.1007/s10548-015-0430-x

Xu, X., Zheng, C., An, L., Wang, R., and Zhang, T. (2016). Effects of dopamine and serotonin systems on modulating neural oscillations in hippocampus-prefrontal cortex pathway in rats. *Brain Topogr.* 29, 539–551. doi: 10.1007/s10548-016-0485-3

Yang, J., Yang, Y., Wang, L., Yang, C., Wang, F., Guo, J., et al. (2017). Gastrin-releasing peptide facilitates glutamatergic transmission in the hippocampus and effectively prevents vascular dementia induced cognitive and synaptic plasticity deficits. *Exp. Neurol.* 287(Pt. 1), 75–83. doi: 10.1016/j.expneurol.2016.08.008

Yi-Huan, C., Rui-Guo, Z., Fen, X., Hua-Ning, W., Yun-Chun, C., Guang-Tao, H., et al. (2015). Quetiapine and repetitive transcranial magnetic stimulation ameliorate depression-like behaviors and up-regulate the proliferation of hippocampal-derived neural stem cells in a rat model of depression: the involvement of the BDNF/ERK signal pathway. *Pharmacol. Biochem. Behav.* 136, 39–46. doi: 10.1016/j.pbb.2015.07.005

Zhang, Y., Du, L., Bai, Y., Han, B., He, C., Gong, L., et al. (2018). CircDYM ameliorates depressive-like behavior by targeting miR-9 to regulate microglial activation via HSP90 ubiquitination. *Mol. Psychiatry* doi: 10.1038/s41380-018-0285-0 [Epub ahead of print].

Zheng, C., and Zhang, T. (2015). Synaptic plasticity related neural oscillations on hippocampus-prefrontal cortex pathway in depression. *Neuroscience* 292, 170–180. doi: 10.1016/j.neuroscience.2015.01.071

Conflict of Interest Statement: The authors declare that the research was conducted in the absence of any commercial or financial relationships that could be construed as a potential conflict of interest.

frontiers in Neuroscience

MINI REVIEW
published: 18 February 2020
doi: 10.3389/fnins.2020.00036

New Vision for Visual Prostheses

Alexander Farnum[1,2] *and Galit Pelled*[1,2,3]*

[1] Department of Biomedical Engineering, College of Engineering, Michigan State University, East Lansing, MI, United States,
[2] Institute for Quantitative Health Science and Engineering, Michigan State University, East Lansing, MI, United States,
[3] Department of Radiology, College of Human Medicine, Michigan State University, East Lansing, MI, United States

Developments of new strategies to restore vision and improving on current strategies by harnessing new advancements in material and electrical sciences, and biological and genetic-based technologies are of upmost health priorities around the world. Federal and private entities are spending billions of dollars on visual prosthetics technologies. This review describes the most current and state-of-the-art bioengineering technologies to restore vision. This includes a thorough description of traditional electrode-based visual prosthetics that have improved substantially since early prototypes. Recent advances in molecular and synthetic biology have transformed vision-assisted technologies; For example, optogenetic technologies that introduce light-responsive proteins offer excellent resolution but cortical applications are restricted by fiber implantation and tissue damage. Other stimulation modalities, such as magnetic fields, have been explored to achieve non-invasive neuromodulation. Miniature magnetic coils are currently being developed to activate select groups of neurons. Magnetically-responsive nanoparticles or exogenous proteins can significantly enhance the coupling between external electromagnetic devices and any neurons affiliated with these modifications. The need to minimize cytotoxic effects for nanoparticle-based therapies will likely restrict the number of usable materials. Nevertheless, advances in identifying and utilizing proteins that respond to magnetic fields may lead to non-invasive, cell-specific stimulation and may overcome many of the limitations that currently exist with other methods. Finally, sensory substitution systems also serve as viable visual prostheses by converting visual input to auditory and somatosensory stimuli. This review also discusses major challenges in the field and offers bioengineering strategies to overcome those.

Keywords: vision, bioengineering, visual prostheses, neuromodulation, magnetic stimulation, cortical implant

OPEN ACCESS

Edited by:
Yael Hanein,
Tel Aviv University, Israel

Reviewed by:
Serge Picaud,
INSERM U968 Institut de la Vision, France
Anja Kunze,
Montana State University, United States

***Correspondence:**
Galit Pelled
pelledga@msu.edu

Specialty section:
This article was submitted to Neural Technology, a section of the journal Frontiers in Neuroscience

Received: *14 November 2019*
Accepted: *13 January 2020*
Published: *18 February 2020*

Citation:
Farnum A and Pelled G (2020) New Vision for Visual Prostheses. Front. Neurosci. 14:36. doi: 10.3389/fnins.2020.00036

INTRODUCTION

The development of bioelectrical interfaces in the 18th century enthralled scientists looking for strategies to treat brain pathologies and restore vision. Revolutionary experiments by LeRoy (1755) and Volta in 1800 (Volta and Banks, 1800) succeeded in demonstrating that electrical stimulation of the eye could produce spots of light, or phosphenes, in one's visual field.

Since then, advancements in neuroimaging, electrophysiology hardware, and surgical equipment have spurred ground-breaking research uncovering intricacies of visual pathways and possible therapeutic targets. Visual prostheses allowing for the restoration of basic abilities promoting object discrimination (Stingl et al., 2013) and simple mobility (Humayun et al., 2012), are now viable therapeutic considerations for visually impaired and blind individuals. A few retinal-based prosthetic devices have already been approved for commercial use in

Europe (Humayun et al., 2012; Hornig et al., 2017), one of which is also approved in the United States (Luo and Da Cruz, 2016).

This review describes state-of-the-art electrode-based visual prostheses technologies, and the ongoing development of cutting-edge biological- and genetic-based technologies to restore visual function including nanoparticles, optogenetics, magnetic manipulation and sensory substitution systems. These methods have the capability of artificially encoding sensation i.e. "writing," into the brain and are gaining considerable interest as next-generation visual therapeutics.

In 2015, there were 253 million individuals (3.43% of global population) blind and moderately-to-severely visually impaired people in the world (Bourne et al., 2017). By 2050, owing to a dramatic increase in life expectancy, it is predicted that this number will rise to 703 million (7.19% of global population) (Bourne et al., 2017). Blindness is the most feared condition by the American public, more so than Alzheimer's disease, cancer and HIV/AIDS (Scott et al., 2016). Visual deficits are strongly associated with economic (Wittenborn et al., 2013), physical (McLean et al., 2014; Crews, 2016), and emotional (Stelmack, 2001; Hassell et al., 2006) detriments. While population aging is still in its early stages, large-scale communities and nations are already being challenged by the increased medical and fiscal responsibilities associated with visual impairments (Gordois et al., 2012; Wittenborn et al., 2013). In fact, the majority of public health specialists have underestimated the rapidity of this epidemiological transition and the associated need for resource reallocation (World Health Organization, 2006). Thus, it is necessary to identify new interventions to address the steep increase of visual deficits among the world population.

ELECTRODE-BASED VISUAL PROSTHESES

The traditional electrode-based visual prostheses consists of a basic set of components. A video camera is often used to convert light into electrical signals. These analog signals are digitized, and the image is processed by a portable micro-computer. The signals are then wirelessly transmitted to internal componentry with accompanying multi-electrode arrays (MEAs), which directly interface with the neural tissue.

The type of the electrode-based prostheses is dictated by the underlying pathophysiology and its location should target a region along the visual pathway that would be the most effective in restoring visual perception. Interfacing too early along the visual pathway could lead to either non-transmitted or significantly corrupted and unintelligible signals. Interfacing at a region later than necessary bypasses functional neuronal circuitry, requiring additional hardware and/or complex image-processing algorithms. There are four major prosthetic design-types, each of which are categorized based on the location of their associated MEAs. **Table 1** summarizes the advantages and limitations of the different visual prostheses and their location.

TABLE 1 | Advantages and limitations of different visual prostheses modalities with feasible interface locations.

Intervention Type	Interface Location	Advantages	Limitations	References
Electrode	Retinal Optic Nerve LGN Cortex	Efficient surgical implantation procedures Large pool of past research Biocompatible-material coatings Accessibility to deeper brain regions	Limited hermetic encapsulation Tissue and cell damage Limited spatial resolution Invasive Wireless telemetry for external hardware communication limits data transfer	Brindley and Lewin, 1968; Humayun et al., 1996; Schmidt et al., 1996; Veraart et al., 1998; Brelén et al., 2005; Pezaris and Reid, 2007; Zrenner et al., 2010; Panetsos et al., 2011; Da Cruz et al., 2013; Stingl et al., 2013; Lowery et al., 2017; Troyk, 2017; Pouratian et al., 2019
Optogenetics	Retinal Cortex	Excellent spatial resolution Excellent temporal resolution Cellular excitation or inhibition Non-invasive stimulation (retinal only) Cell specificity	No accessibility to deeper brain regions Limited cortical accessibility Phototoxicity possibility Tissue damage (cortical only) Invasive (cortical only) Need for high-power light source(s) Potential immune response	Waldvogel et al., 2000; Boyden et al., 2005; Bi et al., 2006; Chow et al., 2010; Lin et al., 2013; Reutsky-Gefen et al., 2013
Magnetic stimulation	Cortex	Non-invasive stimulation No introduction of exogeneous agents	Limited spatial resolution Limited resolution for deeper brain regions Need for high-power electromagnetic device(s)	Barker et al., 1985; Bonmassar et al., 2012; Park et al., 2013; Lee and Fried, 2016; Lee et al., 2016
Magnetic nanoparticles	Cortex	Non-invasive stimulation Cell specificity	Limited spatial resolution Limited resolution for deeper brain regions Potential cytotoxic or immune response Delivery to brain can disrupt blood–brain barrier	Hughes et al., 2007; Huang et al., 2010; Baid et al., 2013; Chen et al., 2015; Guduru et al., 2015; Munshi et al., 2018
Genetically encoded magnetic stimulation	Cortex	Non-invasive stimulation Cell specificity	Limited spatial resolution Limited resolution for deeper brain regions Potential immune response	(Wheeler et al., 2016; Krishnan et al., 2018)
Sensory substitution	Periphery	Non-invasive Suitable for any visual ailment	Limited spatial resolution Occupies another key sensory modality Requires additional training	Bach-y-Rita et al., 1969, 1998; Meijer, 1992; Chebat et al., 2007; Striem-Amit et al., 2012; Abboud et al., 2014

Retinal

Retinal prostheses offer promising rehabilitative potential for a number of retinal-based pathologies, including retinitis pigmentosa and age-related macular degeneration. In 1956, Tassicker developed and implanted the first retinal prostheses, capable of providing the recipient with crude light perception (Tassicker, 1956). Nearly 40 years later, Humayun et al. demonstrated that focal electrical excitation of the retinal surface could elicit cortical responses in animal models (Humayun et al., 1994) and localized visual percepts in human patients (Humayun et al., 1996). These preliminary experiments paved the way for retinal implants as the most common visual prostheses due to the orderly retinotopic organization, ease of surgical accessibility, and early positioning in the visual pathway. Two retinal prostheses sub-types, subretinal and epiretinal, constitute the majority of retinal prostheses-based research.

In the fovea, the most visually acute portion of the retina, there are an average of 150,000 (Shroff, 2011) and a peak density of 200,000 cone photoreceptors per mm^2 (Curcio et al., 1990). The diameters of cone outer segments and retinal ganglion cells are 3–5 μm and 6–13 μm, respectively (Hebel and Holländer, 1983; Shepherd, 2003). Although improvements in micromachining and lithography now allow for the development of precise electrode arrays, targeting each neuron independently to reproduce natural vision is still challenging. Fortunately, extrapolating from cochlear implant patients, functional vision restoration most likely requires a total electrode count that is a mere fraction of the number of retinal neurons. Moreover, patients have been observed to demonstrate a significant learning effect and task-based improvements shortly after implantation.

Subretinal

Retinal-based diseases are characterized by photoreceptor cell death that glasses and contact lenses, which only refocus light rays through the cornea and lens, cannot address. Subretinal prostheses allow for the earliest possible intervention in the visual process. The prostheses most often consists of metallic electrode contacts embedded in a biocompatible polymeric film. It is positioned within the largely degenerated photoreceptor layer and directly interface with retinal bipolar cells. Since they interact with outer-retinal tissue, subretinal prostheses retain substantial intra-retinal signal processing. This allows for the generation of more naturalistic phosphenes, serving to expedite patient training periods relative to other types of visual prostheses.

Some subretinal implants even do away with the need for an external imager altogether via the use of microphotodiode arrays (MPDAs). Early research has shown that photodiodes reliant solely on ambient light can induce neurotrophic effects, but are insufficient for phosphene generation (Chow et al., 2004; Palanker et al., 2005). By incorporating circuitry for signal amplification, significant responses were seen in animal models (Lorach et al., 2015; Prévot et al., 2019) and patients can perceive distinct phosphenes (Zrenner et al., 2010; Lorach et al., 2015). Since the image is based on incident light entering the eye instead of an externally located camera for MPDAs with electronic amplification, patients can utilize natural eye movements. This is a marked advantage over camera-based visual prostheses, which are restricted to head movements for environmental scanning. Moreover, these MPDAs preserve the functionality of microsaccadic eye movements that prevent image fading by moving stimuli into and out of adjacent neurons' receptive fields. The resultant spatial and temporal signal summation may result in more intelligible and naturalistic percepts; patients with photosensitive implants are capable of immediately recognizing shapes without any image processing (Stingl et al., 2013). A 1500 pixel MPDA subretinal implant offers visual acuity restoration up to 20/546 (Stingl et al., 2013), roughly translating to such real-world abilities as identification of office supplies and distinguishing between kitchen cutlery (Stingl et al., 2012). Some patients are even able to differentiate between large alphabet letters and combine them into words (Zrenner et al., 2010; Stingl et al., 2013). A recent study incorporated a 378-pixel array, achieving the highest visual acuity to date: 20/460. Additional testing of letter recognition and reading has already shown promising preliminary results (Palanker et al., 2019). Since MPDAs rely upon light transmittal through the cornea and lens, those with conditions that obscure light passage would not be eligible for such implants.

Research into subretinal implants has proven some initial physiological limitations, though researchers are actively seeking innovative solutions. The uneven photoreceptor density within the retina presents a major challenge. Since the density of cone photoreceptors decreases with increasing retinal eccentricity, uniform phosphene generation throughout the visual field would require MEAs with varying electrode diameters and inter-electrode spacing. Novel MEA designs that promote glial and neuronal migration may allow for lower stimulation levels and more densely packed arrays (Butterwick et al., 2009; Spira and Hai, 2013). Due to the variable thickness (Shroff, 2011) and fragility (Colodetti et al., 2007) of the degenerating retina, such designs are also surgically preferable to mitigate device-tissue contact. This prosthetic design has rehabilitative potential for millions of blind and visually-impaired individuals suffering from outer-retinal pathologies.

Epiretinal

Epiretinal prostheses interact with retinal ganglion cells. Owing to their downstream placement, epiretinal prostheses have a wider therapeutic potential than subretinal prostheses. Since extended periods of no photoreceptor input may cause signal corruption and intra-retinal neuronal degeneration, epiretinal prostheses may be the preferred visual prostheses for mid-to-late stage outer retinal pathologies. Epiretinal arrays can even selectively stimulate ganglion cells or bipolar cells based on stimulation parameters, including pulse polarity and duration (Boinagrov et al., 2014). Optimization of these features can reduce functional threshold levels, thus allowing for smaller electrode-diameters and denser MEAs before surpassing physiological safety limits. The implants are located adjacent to the spacious vitreous humor. This allows for larger electrical componentry and mitigates electrically-induced heat absorption by nearby tissue. However, unlike subretinal MEAs that are held in place by the underlying retinal pigment epithelium, the positioning of epiretinal arrays requires scleral-retinal tacks to

achieve long-term perceptual consistency. Stabilization by an individual tack induces localized damage at the tack site and can physically separate distal regions of the array from the tissue surface (Majji et al., 1999; Mahadevappa et al., 2005). Currently there is an FDA-approved retinal prostheses (Luo and Da Cruz, 2016) which consists of a 60-electrode epiretinal device that has yielded patient improvements in spatial motor tasks (Ahuja et al., 2011), motion detection (da Cruz et al., 2016), and letter-reading performance (Da Cruz et al., 2013).

Optic Nerve

Optic nerve prostheses can be efficacious for patients exhibiting retinal-based diseases or retinal detachment. Borrowing from peripheral-nerve stimulation technology (Mortimer et al., 1995), self-sizing cuff electrodes with four equidistant 200 μm^2 contacts have been implanted around the optic nerve of a human patient (Veraart et al., 1998). By varying stimulation parameters, such as pulse duration and pulse train frequency optic nerve prostheses can elicit phosphene clusters of different sizes and in various locations (Veraart et al., 2003; Brelén et al., 2005). Although selective phosphene generation is rather crude, an implanted patient successfully localized, discriminated between and grasped small specific objects (Duret et al., 2006). Moreover, optic nerve prostheses benefit from enhanced electrode-phosphene efficiency and reduced tissue damage unlike high-density arrays. Such prostheses, however, are restricted to serial stimulation (Brelén et al., 2005) and lack adjustable phosphene luminosity (Delbeke et al., 2003), a feature positively correlated with performance scores on object discrimination tasks. The surface-based electrode contacts also increase current injection thresholds and reduce nerve fiber selectivity – the 1.2 million, 1-μm diameter optic nerve fibers already makes targeting specific points in the visual field extremely challenging (Jonas et al., 1992). In an effort to enhance fiber selectivity, penetrating electrode arrays have been inserted into the optic nerve. These MEAs can elicit cortical responses in animal models (Chai et al., 2008; Li et al., 2008; Lu et al., 2013; Gaillet et al., 2019) and one penetrating array, with wire electrodes progressing through the optic disk and into the optic nerve, has been implanted in a human patient (Sakaguchi et al., 2009). Similar to retinal prostheses, optic nerve prostheses, both surface-based and penetrating, benefit from a relatively less invasive intraocular surgery.

Lateral Geniculate Nucleus (LGN)

At the optic chiasm, optic nerve fibers associated with the nasal half of each retina decussate and project to contralateral subcortical structures. Ninety percent of the retinal ganglion axons synapse at the dorsal lateral geniculate nucleus (LGN) of the thalamus (Kandel et al., 2000). An LGN prostheses has rehabilitative potential for individuals with either retinal or optic nerve pathologies.

Unlike the retina, LGN receptive fields have a consistent spatial density regardless of their visual field eccentricity. Since 60% of the LGN volume is devoted to processing the central 3° of the visual field (Schneider et al., 2004), lower-density MEAs could be used, reducing tissue damage due to mechanical insertion or electrical current delivery. Thalamic visual prostheses would require numerous electrodes to generate discrete phosphenes. One proposed method to facilitate high-density MEA uses a microwire bundle inserted via a cannula (Pezaris and Eskandar, 2009). Once the electrode nears the LGN, the microwires splay outward through the end of the cannula and penetrate the tissue at distinct locations. A model of bilateral 400-electrode implants is estimated to provide visual acuity up to 20/240 (Kyada et al., 2017). In order for such a device to be efficacious, electrode material, insertion speed and current injection levels must be optimized. As with retinal and optic nerve prostheses, intervention timing will be a key consideration to mitigate downstream neuronal degradation. Patients with severe glaucoma, for example, can show a significant progressive reduction in LGN size (Gupta et al., 2009). Although prostheses targeting the LGN have yet to be implanted in humans, animal models demonstrate device efficacy via cortical responses (Panetsos et al., 2011) and crude resolution via object localization tasks (Pezaris and Reid, 2007).

Cortex

One of the most important features of cortical prostheses is the downstream location. This offers rehabilitative potential for blind and visually-impaired individuals for which a retinal, optic nerve or LGN visual prostheses would be ineffective (Gabel, 2016). Furthermore, cortical implants have the longest window for therapeutic intervention; instead of total neural degeneration, post-injury compensatory plasticity mechanisms recruit deafferented neurons from other cortical regions, offering the possibility of stimulation well beyond the onset of injury or disease (Sadato et al., 1996; Pietrini et al., 2004). After the LGN, the optic radiations transmit signals to layer 4 of the primary visual cortex (V1). Neurons with similar receptive fields are organized into 1 mm^2 columns, which can be further subdivided into smaller columns responsive to orientation axis, color and ocular dominance. Similar to the LGN, these columns maintain a fairly consistent spatial density across the surface of V1 owing to the cortical magnification of central visual fields (Daniel and Whitteridge, 1961; Tehovnik, 1996; Dagnelie, 2011). **Figure 1** illustrates the various interfaces and their location.

The subdural electrodes used in preliminary cortical visual prostheses proved capable of eliciting phosphenes but the substantial electrode-neuron distances required milliampere-range current injection levels (Brindley and Lewin, 1968; Dobelle et al., 1974, 1976). In the 1990s, penetrating intracortical electrodes were found to exhibit vastly superior spatial resolution and induce percepts with electrical currents two to three orders of magnitude less than those of surface electrodes (Bak et al., 1990; Schmidt et al., 1996).

Cortical prostheses can comfortably access central receptive fields, which are located near the surface of the occipital lobe, but face difficulty when targeting regions corresponding to peripheral fields. The interhemispheric fissure presents an anatomical barrier for stimulating roughly 85% of V1 (Trobe, 2001) and convolutions on the surface of the brain can

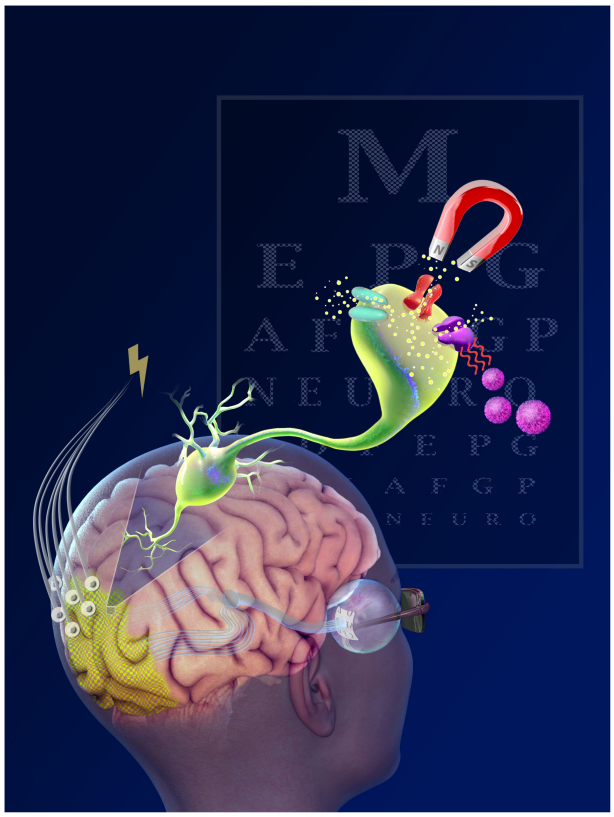

FIGURE 1 | Electrical, light and magnetic stimulation for interfacing visual processing.

bury receptive fields. However, since spatial representation is preserved and repeated multiple times across the visual cortex (Wandell et al., 2007), additional MEAs can be implanted in higher visual areas if receptive fields are inaccessible in lower regions (Dagnelie, 2011). Tertiary visual areas exhibit highly specific stimulus responsivity offering the potential for generating complex visual percepts. Early simulations for restoring functional vision via cortical prostheses estimate a total of at least 625 discrete phosphenes (Cha et al., 1992). In addition to electrode manufacturing, electronics for power and information transmission and processing must be developed. For example, one complementary metal-oxide-semiconductor chip can drive 473 electrodes independently (Wong et al., 2019), far more than is currently necessary for cortical-based MEAs.

The rapid advancement of microelectronic device fabrication and information processing has made cortical prostheses a viable rehabilitative option. There are several ongoing clinical trials testing the effectiveness and the risk associated with these implants (Fernández and Normann, 2017; Lowery et al., 2017; Troyk, 2017; Pouratian et al., 2019).

Next-generation pattern-recognition and deep-learning algorithms, especially those being investigated for computer vision will complement the complex response properties of visual areas in the brain. This could greatly expand cortical prostheses recipients' capabilities, offering depth-perception, color discrimination, figure-ground discernment, and attentional modulation.

OPTOGENETICS

A number of organisms express light-sensitive proteins (opsins) allowing them to perform vital functions, such as phototaxis (Nagel et al., 2002; Sineshchekov et al., 2002) and energy conservation (Ernst et al., 2013). Optogenetic technologies use viral vectors to deliver genes encoding for opsins into defined tissue regions and cell populations with excellent temporal and spatial resolution (Boyden et al., 2005; Han and Boyden, 2007; Chow et al., 2010). Once the proteins are expressed, the cell can be controlled using a specific wavelength of light. Though the majority of optogenetic-based research has utilized microbial opsins, animal opsins have also been explored for vision restoration. Preclinical trials have shown that most animal opsins exhibit excellent light sensitivity but poor temporal responsivity, compared to microbial opsins (Lin et al., 2008; Cehajic-Kapetanovic et al., 2015). However, a recent study utilized an alternative animal opsin to achieve high light sensitivity and quick response kinetics, both of which are imperative for visual prostheses (Berry et al., 2019). An opsin-free approach incorporates small light-sensitive molecules, deemed photoswitches, that can be bound to specific cellular proteins, such as ion channels. The physical conformation of photoswitches can be selectively altered by exposing the molecule to different wavelengths of light, causing neuronal excitation and inhibition. Intravitreal injections of photoswitch molecules have been found capable of restoring light-sensitivity in blind animal models (Caporale et al., 2011; Polosukhina et al., 2012).

The retina has constituted the majority of optogenetic-based visual research because of its accessibility and transparent nature (Bi et al., 2006). Since there are more than 60 cell types within the retina (Masland, 2012), different classes of microbial and animal opsins can be expressed in particular cell populations. By activating and silencing individual cell types, patients can experience more naturalistic visual percepts (Bi et al., 2006; Lagali et al., 2008; Busskamp et al., 2010). Optical-based stimulation technologies, including μLED matrices (Wu et al., 2015; Khan et al., 2018) and computer-generated holography (Lutz et al., 2008; Reutsky-Gefen et al., 2013; Hernandez et al., 2016; Shemesh et al., 2017), are currently being developed to enable cellular and sub-cellular spatial resolution.

Preclinical studies have yielded promising results in non-human primates (Ivanova et al., 2010; Chaffiol et al., 2017) and clinical trials for patients with a variety of retinal-based diseases are currently underway (ClinicalTrials.gov NCT02556736, NCT03293524, and NCT03326336). Though biocompatibility concerns are minimal compared to electrode-based prostheses, clinical trials will determine if any long-term immune responses are present (Busskamp et al., 2012). A limitation of any light-based modality is its restricted penetration depth through tissue, which often requires the insertion of optical fibers. Fortunately, experiments involving non-human primates have

shown that optogenetic stimulation of cortical neurons can induce visual percepts without the need to displace neural tissue (Jazayeri et al., 2012; Ju et al., 2018). Red-shifted opsins have been developed to mitigate tissue-induced light scattering as well as enable deeper stimulation and inhibition capabilities (Lin et al., 2013; Chuong et al., 2014). With the success of optogenetic-based therapies in preclinical models, it is likely that clinical trials will soon follow suit. The incorporation of these opsins may allow for the control of retinal or cortical neurons while minimizing the tissue damage characteristic of penetrating devices.

MAGNETIC STIMULATION

Magnetic fields pass through biological tissue with minimal reduction in field strength, making them desirable for non-invasive neurostimulation. Indeed, scientists have been experimenting with magnetically-induced phosphenes since the late 1800s (d'Arsonval, 1896).

The first transcranial magnetic stimulation (TMS) device was demonstrated in 1985 (Barker et al., 1985), and quickly became an important clinical and preclinical method for stimulating specific regions in the brain and spinal cord. TMS involves running an alternating current through a wire coil that is placed over a region of interest. Electromagnetic induction generates currents that are capable of stimulating neurons within the specific region. Since non-invasive stimulation of the brain reduces the risks encountered in surgical patients, such as hemorrhage, infection, and the overall cost of the procedure, TMS has recently gained interest for use in functional and behavioral research as well as rehabilitation research after brain injury (Ferbert et al., 1992; Celnik et al., 2009; Lu et al., 2015; Shin et al., 2018; Krishnan et al., 2019).

Cortical electromagnetic-based prostheses would benefit from superior coil-neuron proximity, permitting numerous small, low-power devices. Recent developments in the construction of micro-scale magnetic coils have the potential to increase the effectiveness and specificity of TMS. A number of micro-coils have demonstrated device efficacy *in vitro* (Bonmassar et al., 2012; Lee and Fried, 2016; Rizou and Prodromakis, 2018) and *in vivo* (Park et al., 2013; Minusa et al., 2017). While one major attraction of such devices is their non-invasive nature, device insertion can reduce coil-neuron distance, perceptual thresholds and necessary power input (Lee et al., 2016). Advancements in material sciences can accelerate the development of implantable micro-coils that are completely encased in biocompatible polymers to reduce electrically-induced tissue inflammation and glial scarring at the tissue-electrode interface. Additionally, the asymmetric current distribution permits selective activation of longitudinally-aligned axons (Bonmassar et al., 2012), adding a slight degree of specificity based on cellular orientation. One major limiting factor of micromagnetic stimulation is that conventional solenoid coils exhibit poor power efficiency and significant heat dissipation. Efforts into coil optimization may result in stronger magnetic flux densities and induced electric current at specific regions of interest (Bonmassar et al., 2014).

NANOPARTICLE-BASED STIMULATION

Nanoparticles are extensively utilized in the fields of drug delivery (Kumari et al., 2010), biosensing (Doria et al., 2012) and tissue imaging (Gilad et al., 2008). Recently, ferrite-based magnetic nanoparticles were attached selectively to ion channels. Applying a magnetic gradient generates a force on the nanoparticles that most likely induces a conformational change on the associated membrane channel. This method has demonstrated to induce changes in cellular activity *in vitro* upon applying an external magnetic field (Hughes et al., 2007; Tay et al., 2016).

Another method is based on magnetic hyperthermia. When exposed to an alternating field, the orientation of a nanoparticle's magnetic domain oscillates in accordance with the applied frequency. In response to weaker magnetic fields, this causes the nanoparticle to rotate and the particle-medium friction dissipates heat. With sufficient frequency, the localized heating can induce neuronal activation or inhibition via TRPV1 (Huang et al., 2010; Stanley et al., 2012; Chen et al., 2015; Munshi et al., 2017) or TMEM16A (Munshi et al., 2018) temperature-sensitive ion channels, respectively.

Voltage-gated ion channels expressed in V1 neurons can also be targeted by magnetoelectric composite nanoparticles. These nanoparticles, consisting of a magnetostrictive core and a piezoelectric shell, exhibit significant elastic coupling and magnetoelectric output (Nan et al., 2008). The magnetostrictive material can amplify a slowly varying external magnetic field, which induces a localized electric field via the piezoelectric compound. Rodent EEG recordings suggested that magnetoelectric nanoparticles offer an efficient method of neurostimulation (Guduru et al., 2015).

Nanoparticle materials are only suitable candidates for neurostimulation if they exhibit minimal cytotoxicity; little is known about the long-term health effects of nanoparticle delivery to the brain. Additionally, the method of effectively delivering nanoparticles to the central nervous system is a significant concern. Only a fraction of intravenously-injected nanoparticles successfully reach the brain and only do so by long-term endothelial cell endocytosis or by destroying their cellular membranes (Calvo et al., 2001; Yarjanli et al., 2017). However, non-invasive intranasal delivery may expedite delivery and reduce cell damage by bypassing the blood-brain barrier, which will make it more suitable for potential clinical applications.

GENETICALLY ENCODED MAGNETIC STIMULATION

Ongoing efforts have been dedicated to developing genetic-based neuromodulation technologies relying on magnetic changes. Magnetogenetics is a technology that allows cell, temporal, and location specific activation via magnetic fields and could evolve into a powerful non-invasive and effective technique for neurorehabilitation and vision restoration. These technologies mitigate concerns over cytotoxicity and tissue damage because no introduction of synthetic materials is

required. A recent work showed the development of a construct encoding for ferritin protein subunits fused to TRPV4 receptors and its effectivity in inducing neural changes (Wheeler et al., 2016). However, neuronal response times were on the order of 20–60 s. Therefore, this approach may be effective for visual rehabilitation once allowing short responses time.

Several organisms including birds (Wiltschko and Wiltschko, 2005), fish (Quinn, 1980) and bacteria (Fassbinder et al., 1990), are known to rely on the Earth's magnetic field for navigation and detection of prey and predators. Indeed, magnetic stimulation has been shown to trigger neural responses in the glass catfish, *Kryptopterus bicirrhis* (Lissmann and Machin, 1963; Struik et al., 2001). The magnetically sensitive gene has been identified and cloned, and was termed the electromagnetic-perceptive gene (EPG). *In vitro* and *in vivo* animal studies demonstrated that EPG is capable of eliciting neural responses (Krishnan et al., 2018). A number of research teams are working toward discovering the molecular structure and the signal transduction basis of this phenomenon. This will serve to expedite the optimization of stimulation parameters, including the strength and frequency of the applied magnetic field, as well as the EPG itself via artificial and targeted mutations.

SENSORY SUBSTITUTION

Stimulation devices that convert optical information into tactile and auditory sensory inputs may offer alternative sight to individuals who are visually impaired due to stroke or brain injury (Amedi et al., 2001; Poirier et al., 2006). Tactile sensory substitution systems consisting of fingertip pin arrays that vibrated according to incoming signals from a video camera were developed in the 1960s and offered limited reading capabilities (Linvill and Bliss, 1966; Bliss et al., 1970). Other devices that stimulated the patients' back extended such abilities to object recognition and differentiation (Bach-y-Rita et al., 1969; Collins, 1970).

The tongue is an excellent location for a sensory substitution device because it is densely innervated and coated in electrolytic saliva. With a tongue array consisting of over 100 electrode contacts, subjects significantly increased their visual acuity (Sampaio et al., 2001; Chebat et al., 2007). One drawback to positioning an electrode grid on the surface of the tongue, is that its usage would restrict normative tasks, such as conversing and eating. Stimulating gloves (Meers and Ward, 2005), headbands (Kajimoto et al., 2006), vests (Jones et al., 2006; Cancar et al., 2013), and belts (Van Erp et al., 2005) have also been explored for navigational, kinesthetic and vision reproduction purposes. The developments of methods such as electronic skin (Fu et al., 2018) will open new frontiers in tactile-based sensory substitution devices.

Other sensory substitution research has investigated auditory stimulation as a replacement for visual input. These devices use a number of translational parameters, including substituting pitch or frequency for vertical location, binaural intensity or time-scanning for horizontal position, loudness for brightness, and timbre for color (Meijer, 1992; Capelle et al., 1998; Abboud et al., 2014). While the development of visuoauditory systems initially lagged behind that of visuotactile, since its inception in the early 1990s (Meijer, 1992), such devices are now at the forefront of sensory substitution research. One reason for the popularization of visuoauditory devices is their increased absolute bandwidth over tactile devices; sighted individuals can recognize a total of 600 different tones (Capelle et al., 1998). Since blind individuals often exhibit enhanced auditory perception, it is feasible for the total number of tones to extend beyond the maximum estimated value. One limitation of these devices is that they restrict the ability to perceive auditory environmental cues, which is a highly preferred ability in blind individuals (Brewster and Brown, 2004).

CONCLUSION

The total number of visual ailments is increasing rapidly among the general population in both developed and developing nations. Preliminary electrode-based visual prostheses demonstrated that they could induce visual percepts by interfacing with various regions of the visual system but lacked the efficiency to be adopted by blind and visually-impaired individuals in their everyday lives. Contemporary electrode-based visual prostheses have improved substantially since early prototypes. These devices can restore a number of abilities, such as crude object recognition and spatial navigation, and are now becoming a viable therapeutic consideration for blind and visually-impaired individuals. However, even with advanced micromachining and surgical procedures, limited spatial resolution and unavoidable tissue damage may render future electrode-based devices wanting. Nevertheless, non-electrode-based means for neurostimulation are being pursued. Optogenetic technologies introduces light-responsive proteins that can be used to excite or inhibit neural activity. For example, optogenetic technologies that introduce light-responsive proteins offer excellent resolution but cortical applications are restricted by fiber implantation and tissue damage. Other stimulation modalities, such as magnetic fields, have been explored to achieve non-invasive neuromodulation. Miniature magnetic coils are currently being developed to activate select groups of neurons. The poor coupling efficiency between magnetic fields and biological tissue leads to increasing power requirements and reducing achievable resolution. Magnetically-responsive nanoparticles or exogenous proteins can significantly enhance the coupling between external electromagnetic devices and any neurons affiliated with these modifications. The need to minimize cytotoxic effects for nanoparticle-based therapies will likely restrict the number of usable materials. Nevertheless, advances in identifying and utilizing proteins that respond to magnetic fields may lead to non-invasive, cell-specific stimulation and may overcome many of the limitations that currently exist with other methods.

Finally, sensory substitution systems also serve as viable visual prostheses by converting visual input to auditory and tactile stimuli.

AUTHOR CONTRIBUTIONS

AF and GP conceptualized the manuscript, drafted the manuscript, revised and finalized it, and agreed to be accountable for all aspects of the work in ensuring that questions related to the accuracy or integrity of any part of the work are appropriately investigated and resolved.

FUNDING

This work was funded by the NIH/NINDS R01NS072171 and NIH/NINDS R01NS098231.

REFERENCES

Abboud, S., Hanassy, S., Levy-Tzedek, S., Maidenbaum, S., and Amedi, A. (2014). EyeMusic: introducing a "visual" colorful experience for the blind using auditory sensory substitution. *Restor. Neurol. Neurosci.* 32, 247–257. doi: 10.3233/RNN-130338

Ahuja, A. K., Dorn, J., Caspi, A., McMahon, M., Dagnelie, G., Stanga, P., et al. (2011). Blind subjects implanted with the Argus II retinal prosthesis are able to improve performance in a spatial-motor task. *Br. J. Ophthalmol.* 95, 539–543. doi: 10.1136/bjo.2010.179622

Amedi, A., Malach, R., Hendler, T., Peled, S., and Zohary, E. (2001). Visuo-haptic object-related activation in the ventral visual pathway. *Nat. Neurosci* 4:324. doi: 10.1038/85201

Bach-y-Rita, P., Collins, C. C., Saunders, F. A., White, B., and Scadden, L. (1969). Vision substitution by tactile image projection. *Nature* 221:963. doi: 10.1038/221963a0

Bach-y-Rita, P., Kaczmarek, K. A., Tyler, M. E., and Garcia-Lara, J. (1998). Form perception with a 49-point electrotactile stimulus array on the tongue: a technical note. *J. Rehabil. Res. Dev.* 35, 427–430.

Baid, R., Upadhyay, A. K., Shinohara, T., and Kompella, U. B. (2013). Biosynthesis, characterization, and efficacy in retinal degenerative diseases of lens epithelium-derived growth factor fragment (LEDGF1-326), a novel therapeutic protein. *J. Biol. Chem.* 288, 17372–17383. doi: 10.1074/jbc.M112.441618

Bak, M., Girvin, J., Hambrecht, F., Kufta, C., Loeb, G., and Schmidt, E. (1990). Visual sensations produced by intracortical microstimulation of the human occipital cortex. *Med. Biol. Eng. Comput.* 28, 257–259. doi: 10.1007/bf02442682

Barker, A. T., Jalinous, R., and Freeston, I. L. (1985). Non-invasive magnetic stimulation of human motor cortex. *Lancet* 325, 1106–1107. doi: 10.1016/s0140-6736(85)92413-4

Berry, M. H., Holt, A., Salari, A., Veit, J., Visel, M., Levitz, J., et al. (2019). Restoration of high-sensitivity and adapting vision with a cone opsin. *Nat. Commun.* 10:1221. doi: 10.1038/s41467-019-09124-x

Bi, A., Cui, J., Ma, Y.-P., Olshevskaya, E., Pu, M., Dizhoor, A. M., et al. (2006). Ectopic expression of a microbial-type rhodopsin restores visual responses in mice with photoreceptor degeneration. *Neuron* 50, 23–33. doi: 10.1016/j.neuron.2006.02.026

Bliss, J. C., Katcher, M. H., Rogers, C. H., and Shepard, R. P. (1970). Optical-to-tactile image conversion for the blind. *IEEE Trans. Man Mach. Syst.* 11, 58–65. doi: 10.1109/tmms.1970.299963

Boinagrov, D., Pangratz-Fuehrer, S., Goetz, G., and Palanker, D. (2014). Selectivity of direct and network-mediated stimulation of the retinal ganglion cells with epi-, sub-and intraretinal electrodes. *J. Neural Eng.* 11:026008. doi: 10.1088/1741-2560/11/2/026008

Bonmassar, G., Gale, J., and Vanduffel, W. (2014). Optimizing microscopic magnetic fields for neuronal stimulation. *Int. J. Bioelectromagn.* 16, 1–31. doi: 10.3727/096368911X600966

Bonmassar, G., Lee, S. W., Freeman, D. K., Polasek, M., Fried, S. I., and Gale, J. T. (2012). Microscopic magnetic stimulation of neural tissue. *Nat. Commun.* 3:921. doi: 10.1038/ncomms1914

Bourne, R. R., Flaxman, S. R., Braithwaite, T., Cicinelli, M. V., Das, A., Jonas, J. B., et al. (2017). Magnitude, temporal trends, and projections of the global prevalence of blindness and distance and near vision impairment: a systematic review and meta-analysis. *Lancet Global Health* 5, e888–e897.

Boyden, E. S., Zhang, F., Bamberg, E., Nagel, G., and Deisseroth, K. (2005). Millisecond-timescale, genetically targeted optical control of neural activity. *Nat. Neurosci.* 8:1263. doi: 10.1038/nn1525

Brelén, M. E., Duret, F., Gérard, B., Delbeke, J., and Veraart, C. (2005). Creating a meaningful visual perception in blind volunteers by optic nerve stimulation. *J. Neural Eng.* 2:S22.

Brewster, S., and Brown, L. M. (2004). "Tactons: structured tactile messages for non-visual information display," in *Proceedings of the Fifth Conference on Australasian User Interface-Volume*, Vol. 28, (Darlinghurst: Australian Computer Society, Inc), 15–23.

Brindley, G. S., and Lewin, W. (1968). The sensations produced by electrical stimulation of the visual cortex. *J. Physiol.* 196, 479–493. doi: 10.1113/jphysiol.1968.sp008519

Busskamp, V., Duebel, J., Balya, D., Fradot, M., Viney, T. J., Siegert, S., et al. (2010). Genetic reactivation of cone photoreceptors restores visual responses in retinitis pigmentosa. *Science* 329, 413–417. doi: 10.1126/science.1190897

Busskamp, V., Picaud, S., Sahel, J. A., and Roska, B. (2012). Optogenetic therapy for retinitis pigmentosa. *Gene Ther.* 19:169. doi: 10.1038/gt.2011.155

Butterwick, A., Huie, P., Jones, B., Marc, R., Marmor, M., and Palanker, D. (2009). Effect of shape and coating of a subretinal prosthesis on its integration with the retina. *Exp. Eye Res.* 88, 22–29. doi: 10.1016/j.exer.2008.09.018

Calvo, P., Gouritin, B., Chacun, H., Desmaële, D., D'Angelo, J., Noel, J.-P., et al. (2001). Long-circulating PEGylated polycyanoacrylate nanoparticles as new drug carrier for brain delivery. *Pharm. Res.* 18, 1157–1166.

Cancar, L., Díaz, A., Barrientos, A., Travieso, D., and Jacobs, D. M. (2013). Tactile-sight: a sensory substitution device based on distance-related vibrotactile flow. *Int. J. Adv. Rob. Syst.* 10:272. doi: 10.5772/56235

Capelle, C., Trullemans, C., Arno, P., and Veraart, C. (1998). A real-time experimental prototype for enhancement of vision rehabilitation using auditory substitution. *IEEE Trans. Biomed. Eng.* 45, 1279–1293. doi: 10.1109/10.720206

Caporale, N., Kolstad, K. D., Lee, T., Tochitsky, I., Dalkara, D., Trauner, D., et al. (2011). LiGluR restores visual responses in rodent models of inherited blindness. *Mol. Ther.* 19, 1212–1219. doi: 10.1038/mt.2011.103

Cehajic-Kapetanovic, J., Eleftheriou, C., Allen, A. E., Milosavljevic, N., Pienaar, A., Bedford, R., et al. (2015). Restoration of vision with ectopic expression of human rod opsin. *Curr. Biol.* 25, 2111–2122. doi: 10.1016/j.cub.2015.07.029

Celnik, P., Paik, N.-J., Vandermeeren, Y., Dimyan, M., and Cohen, L. G. (2009). Effects of combined peripheral nerve stimulation and brain polarization on performance of a motor sequence task after chronic stroke. *Stroke* 40, 1764–1771. doi: 10.1161/STROKEAHA.108.540500

Cha, K., Horch, K. W., and Normann, R. A. (1992). Mobility performance with a pixelized vision system. *Visi. Res.* 32, 1367–1372. doi: 10.1016/0042-6989(92)90229-c

Chaffiol, A., Caplette, R., Jaillard, C., Brazhnikova, E., Desrosiers, M., Dubus, E., et al. (2017). A new promoter allows optogenetic vision restoration with enhanced sensitivity in macaque retina. *Mol. Ther.* 25, 2546–2560. doi: 10.1016/j.ymthe.2017.07.011

Chai, X., Li, L., Wu, K., Zhou, C., Cao, P., and Ren, Q. (2008). C-sight visual prostheses for the blind. *IEEE Eng. Med. Biol. Mag.* 27, 20–28. doi: 10.1109/memb.2008.923959

Chebat, D.-R., Rainville, C., Kupers, R., and Ptito, M. (2007). Tactile–'visual'acuity of the tongue in early blind individuals. *Neuroreport* 18, 1901–1904. doi: 10.1097/wnr.0b013e3282f2a63

Chen, R., Romero, G., Christiansen, M. G., Mohr, A., and Anikeeva, P. (2015). Wireless magnetothermal deep brain stimulation. *Science* 347, 1477–1480. doi: 10.1126/science.1261821

Chow, A. Y., Chow, V. Y., Packo, K. H., Pollack, J. S., Peyman, G. A., and Schuchard, R. (2004). The artificial silicon retina microchip for the treatment of visionloss from retinitis pigmentosa. *Arch. Ophthalmol.* 122, 460–469.

Chow, B. Y., Han, X., Dobry, A. S., Qian, X., Chuong, A. S., Li, M., et al. (2010). High-performance genetically targetable optical neural silencing by light-driven proton pumps. *Nature* 463:98. doi: 10.1038/nature08652

Chuong, A. S., Miri, M. L., Busskamp, V., Matthews, G. A., Acker, L. C., Sørensen, A. T., et al. (2014). Noninvasive optical inhibition with a red-shifted microbial rhodopsin. *Nat. Neurosci.* 17:1123. doi: 10.1038/nn.3752

Collins, C. C. (1970). Tactile television-mechanical and electrical image projection. *IEEE Trans. Man Mach. Syst.* 11, 65–71. doi: 10.1109/tmms.1970.299964

Colodetti, L., Weiland, J., Colodetti, S., Ray, A., Seiler, M., Hinton, D., et al. (2007). Pathology of damaging electrical stimulation in the retina. *Exp. Eye Res.* 85, 23–33. doi: 10.1016/j.exer.2007.02.014

Crews, J. E. (2016). Falls among persons aged ≥ 65 years with and without severe vision impairment—United States, 2014. *MMWR. Morb. Mortal. Wkl. Rep.* 65, 433–437. doi: 10.15585/mmwr.mm6517a2

Curcio, C. A., Sloan, K. R., Kalina, R. E., and Hendrickson, A. E. (1990). Human photoreceptor topography. *J. Comp. Neurol.* 292, 497–523. doi: 10.1002/cne.902920402

Da Cruz, L., Coley, B. F., Dorn, J., Merlini, F., Filley, E., Christopher, P., et al. (2013). The argus II epiretinal prosthesis system allows letter and word reading and long-term function in patients with profound vision loss. *Br. J. Ophthalmol.* 97, 632–636. doi: 10.1136/bjophthalmol-2012-301525

da Cruz, L., Dorn, J. D., Humayun, M. S., Dagnelie, G., Handa, J., Barale, P.-O., et al. (2016). Five-year safety and performance results from the Argus II retinal prosthesis system clinical trial. *Ophthalmology* 123, 2248–2254. doi: 10.1016/j.ophtha.2016.06.049

Dagnelie, G. (2011). *Visual Prosthetics: Physiology, Bioengineering, Rehabilitation*. Berlin: Springer Science & Business Media.

Daniel, P., and Whitteridge, D. (1961). The representation of the visual field on the cerebral cortex in monkeys. *J. Physiol.* 159, 203–221. doi: 10.1113/jphysiol.1961.sp006803

d'Arsonval, M. (1896). Dispositifs pour la mesure des courants alternatifs de toutes fréquences. *Comput. Rend. Soc. Biol.* 3, 430–451.

Delbeke, J., Oozeer, M., and Veraart, C. (2003). Position, size and luminosity of phosphenes generated by direct optic nerve stimulation. *Vis. Res.* 43, 1091–1102. doi: 10.1016/s0042-6989(03)00013-0

Dobelle, W. H., Mladejovsky, M., and Girvin, J. (1974). Artificial vision for the blind: electrical stimulation of visual cortex offers hope for a functional prosthesis. *Science* 183, 440–444. doi: 10.1126/science.183.4123.440

Dobelle, W. H., Mladejovsky, M. G., Evans, J. R., Roberts, T., and Girvin, J. (1976). 'Braille'reading by a blind volunteer by visual cortex stimulation. *Nature* 259:111. doi: 10.1038/259111a0

Doria, G., Conde, J., Veigas, B., Giestas, L., Almeida, C., Assunção, M., et al. (2012). Noble metal nanoparticles for biosensing applications. *Sensors* 12, 1657–1687. doi: 10.3390/s120201657

Duret, F., Brelén, M. E., Lambert, V., Gérard, B., Delbeke, J., and Veraart, C. (2006). Object localization, discrimination, and grasping with the optic nerve visual prosthesis. *Restor. Neurol. Neurosci.* 24, 31–40.

Ernst, O. P., Lodowski, D. T., Elstner, M., Hegemann, P., Brown, L. S., and Kandori, H. (2013). Microbial and animal rhodopsins: structures, functions, and molecular mechanisms. *Chem. Rev.* 114, 126–163. doi: 10.1021/cr4003769

Fassbinder, J. W., Stanjekt, H., and Vali, H. (1990). Occurrence of magnetic bacteria in soil. *Nature* 343:161. doi: 10.1038/343161a0

Ferbert, A., Priori, A., Rothwell, J., Day, B., Colebatch, J., and Marsden, C. (1992). Interhemispheric inhibition of the human motor cortex. *J. Physiol.* 453, 525–546. doi: 10.1113/jphysiol.1992.sp019243

Fernández, E., and Normann, R. A. (2017). *Artificial Vision*. 191–201. Berlin: Springer.

Fu, Y., Zhang, M., Dai, Y., Zeng, H., Sun, C., Han, Y., et al. (2018). A self-powered brain multi-perception receptor for sensory-substitution application. *Nano Energy* 44, 43–52. doi: 10.1016/j.nanoen.2017.11.068

Gabel, V. P. (2016). *Artificial Vision: A Clinical Guide*. Berlin: Springer.

Gaillet, V., Cutrone, A., Artoni, F., Vagni, P., Pratiwi, A. M., Romero, S. A., et al. (2019). Spatially selective activation of the visual cortex via intraneural stimulation of the optic nerve. *Nat. Biomed. Eng.* 3, 1–14. doi: 10.1038/s41551-019-0446-8

Gilad, A. A., Walczak, P., McMahon, M. T., Na, H. B., Lee, J. H., An, K., et al. (2008). MR tracking of transplanted cells with "positive contrast" using manganese oxide nanoparticles. *Magnetic Resonance Med.*60, 1–7. doi: 10.1002/mrm.21622

Gordois, A., Cutler, H., Pezzullo, L., Gordon, K., Cruess, A., Winyard, S., et al. (2012). An estimation of the worldwide economic and health burden of visual impairment. *Global Public Health* 7, 465–481. doi: 10.1080/17441692.2011.634815

Guduru, R., Liang, P., Hong, J., Rodzinski, A., Hadjikhani, A., Horstmyer, J., et al. (2015). Magnetoelectric 'spin'on stimulating the brain. *Nanomedicine* 10, 2051–2061. doi: 10.2217/nnm.15.52

Gupta, N., Greenberg, G., De Tilly, L. N., Gray, B., Polemidiotis, M., and Yücel, Y. H. (2009). Atrophy of the lateral geniculate nucleus in human glaucoma detected by magnetic resonance imaging. *Br. J. Ophthalmol.* 93, 56–60. doi: 10.1136/bjo.2008.138172

Han, X., and Boyden, E. S. (2007). Multiple-color optical activation, silencing, and desynchronization of neural activity, with single-spike temporal resolution. *PloS One* 2:e299. doi: 10.1371/journal.pone.0000299

Hassell, J., Lamoureux, E., and Keeffe, J. (2006). Impact of age related macular degeneration on quality of life. *Br. J. Ophthalmol.* 90, 593–596.

Hebel, R., and Holländer, H. (1983). Size and distribution of ganglion cells in the human retina. *Anat. Embryol.* 168, 125–136. doi: 10.1007/bf00305404

Hernandez, O., Papagiakoumou, E., Tanese, D., Fidelin, K., Wyart, C., and Emiliani, V. (2016). Three-dimensional spatiotemporal focusing of holographic patterns. *Nat. Commun.* 7:11928. doi: 10.1038/ncomms11928

Hornig, R., Dapper, M., Le Joliff, E., Hill, R., Ishaque, K., Posch, C., et al. (2017). *Artificial Vision*. Berlin: Springer, 99–113.

Huang, H., Delikanli, S., Zeng, H., Ferkey, D. M., and Pralle, A. (2010). Remote control of ion channels, and neurons through magnetic-field heating of nanoparticles. *Nat. Nanotechnol.* 5, 602–606. doi: 10.1038/nnano.2010.125

Hughes, S., McBain, S., Dobson, J., and El Haj, A. J. (2007). Selective activation of mechanosensitive ion channels using magnetic particles. *J. R. Soc. Interface* 5, 855–863. doi: 10.1098/rsif.2007.1274

Humayun, M., Propst, R., de Juan, E., McCormick, K., and Hickingbotham, D. (1994). Bipolar surface electrical stimulation of the vertebrate retina. *Arch. Ophthalmol.* 112, 110–116.

Humayun, M. S., De Juan, E., Dagnelie, G., Greenberg, R. J., Propst, R. H., and Phillips, D. H. (1996). Visual perception elicited by electrical stimulation of retina in blind humans. *Arch. Ophthalmol.* 114, 40–46.

Humayun, M. S., Dorn, J. D., Da Cruz, L., Dagnelie, G., Sahel, J.-A., Stanga, P. E., et al. (2012). Interim results from the international trial of Second Sight's visual prosthesis. *Ophthalmology* 119, 779–788. doi: 10.1016/j.ophtha.2011.09.028

Ivanova, E., Hwang, G.-S., Pan, Z. H., and Troilo, D. (2010). Evaluation of AAV-mediated expression of Chop2-GFP in the marmoset retina. *Invest. Ophthalmol. Vis. Sci.* 51, 5288–5296. doi: 10.1167/iovs.10-5389

Jazayeri, M., Lindbloom-Brown, Z., and Horwitz, G. D. (2012). Saccadic eye movements evoked by optogenetic activation of primate V1. *Nat. Neurosci.* 15:1368. doi: 10.1038/nn.3210

Jonas, J. B., Schmidt, A. M., Müller-Bergh, J., Schlötzer-Schrehardt, U., and Naumann, G. (1992). Human optic nerve fiber count and optic disc size. *Invest. Ophthalmol. Vis. Sci.* 33, 2012–2018.

Jones, L. A., Lockyer, B., and Piateski, E. (2006). Tactile display and vibrotactile pattern recognition on the torso. *Adv. Rob.* 20, 1359–1374. doi: 10.1163/156855306778960563

Ju, N., Jiang, R., Macknik, S. L., Martinez-Conde, S., and Tang, S. (2018). Long-term all-optical interrogation of cortical neurons in awake-behaving nonhuman primates. *PLoS Biol.* 16:e2005839. doi: 10.1371/journal.pbio.2005839

Kajimoto, H., Kanno, Y., and Tachi, S. (2006). Forehead electro-tactile display for vision substitution. *Proc. EuroHaptics*.

Kandel, E. R., Schwartz, J. H., Jessell, T. M., Biochemistry, D. O., Jessell, M. B. T., Siegelbaum, S., et al. (2000). *Principles of Neural Science*, Vol. 4. New York, NY: McGraw-hill.

Khan, W., Setien, M., Purcell, E., and Li, W. (2018). Micro-reflector integrated multichannel μLED Optogenetic neurostimulator with enhanced intensity. *Front. Mech. Eng.* 4:17.

Krishnan, V., Park, S. A., Shin, S. S., Alon, L., Tressler, C. M., Stokes, W., et al. (2018). Wireless control of cellular function by activation of a novel protein responsive to electromagnetic fields. *Sci. Rep.* 8:8764. doi: 10.1038/s41598-018-27087-9

Krishnan, V. S., Shin, S. S., Belegu, V., Celnik, P., Reimers, M., Smith, K. R., et al. (2019). Multimodal evaluation of TMS-induced somatosensory plasticity and behavioral recovery in rats with contusion spinal cord injury. *Front. Neurosci.* 13:387. doi: 10.3389/fnins.2019.00387

Kumari, A., Yadav, S. K., and Yadav, S. C. (2010). Biodegradable polymeric nanoparticles based drug delivery systems. *Coll. Surf. BBiointerf.* 75, 1–18. doi: 10.1016/j.colsurfb.2009.09.001

Kyada, M. J., Killian, N. J., and Pezaris, J. S. (2017). *Artificial Vision*. Berlin: Springer, 177–189.

Lagali, P. S., Balya, D., Awatramani, G. B., Münch, T. A., Kim, D. S., Busskamp, V., et al. (2008). Light-activated channels targeted to ON bipolar cells restore visual function in retinal degeneration. *Nat Neurosci.* 11:667. doi: 10.1038/nn.2117

Lee, S. W., Fallegger, F., Casse, B. D., and Fried, S. I. (2016). Implantable microcoils for intracortical magnetic stimulation. *Sci. Adv.* 2:e1600889. doi: 10.1126/sciadv.1600889

Lee, S. W., and Fried, S. I. (2016). Enhanced control of cortical pyramidal neurons with micromagnetic stimulation. *IEEE Trans. Neural Syst Rehabil. Eng.* 25, 1375–1386. doi: 10.1109/TNSRE.2016.2631446

LeRoy, C. (1755). Où l'on rend compte de quelques tentatives que l'on a faites pour guérir plusieurs maladies par l'électricité. *Hist. Acad. Roy. Sci. Mem. Math Phys.* 60, 87–95.

Li, L., Sun, M., Cao, P., Cai, C., Chai, X., Li, X., et al. (2008). *7th Asian-Pacific Conference on Medical and Biological Engineering*. Berlin: Springer, 54–57.

Lin, B., Koizumi, A., Tanaka, N., Panda, S., and Masland, R. H. (2008). Restoration of visual function in retinal degeneration mice by ectopic expression of melanopsin. *Proc. Nal Acad. Sci. U.S.A.* 105, 16009–16014. doi: 10.1073/pnas.0806114105

Lin, J. Y., Knutsen, P. M., Muller, A., Kleinfeld, D., and Tsien, R. Y. (2013). ReaChR: a red-shifted variant of channelrhodopsin enables deep transcranial optogenetic excitation. *Nat. Neurosci.* 16:1499. doi: 10.1038/nn.3502

Linvill, J. G., and Bliss, J. C. (1966). A direct translation reading aid for the blind. *Proc. IEEE* 54, 40–51. doi: 10.1109/proc.1966.4572

Lissmann, H. W., and Machin, K. E. (1963). Electric receptors in a non-electric fish (Clarias). *Nature* 199, 88–89. doi: 10.1038/199088a0

Lorach, H., Goetz, G., Smith, R., Lei, X., Mandel, Y., Kamins, T., et al. (2015). Photovoltaic restoration of sight with high visual acuity. *Nat. Med.* 21:476. doi: 10.1038/nm.3851

Lowery, A. J., Rosenfeld, J. V., Rosa, M. G., Brunton, E., Rajan, R., Mann, C., et al. (2017). *Artificial Vision*. Berlin: Springer, 215–225.

Lu, H., Kobilo, T., Robertson, C., Tong, S., Celnik, P., and Pelled, G. (2015). Transcranial magnetic stimulation facilitates neurorehabilitation after pediatric traumatic brain injury. *Sci. Rep.* 5:14769. doi: 10.1038/srep14769

Lu, Y., Yan, Y., Chai, X., Ren, Q., Chen, Y., and Li, L. (2013). Electrical stimulation with a penetrating optic nerve electrode array elicits visuotopic cortical responses in cats. *J. Neural Eng.* 10:036022. doi: 10.1088/1741-2560/10/3/036022

Luo, Y. H. L., and Da Cruz, L. (2016). The Argus® II retinal prosthesis system. *Progr. Retin. Eye Res.* 50, 89–107. doi: 10.1016/j.preteyeres.2015.09.003

Lutz, C., Otis, T. S., DeSars, V., Charpak, S., DiGregorio, D. A., and Emiliani, V. (2008). Holographic photolysis of caged neurotransmitters. *Nat. Methods* 5:821. doi: 10.1038/nmeth.1241

Mahadevappa, M., Weiland, J. D., Yanai, D., Fine, I., Greenberg, R. J., and Humayun, M. S. (2005). Perceptual thresholds and electrode impedance in three retinal prosthesis subjects. *IEEE Trans. Neural Syst. Rehabil. Eng.* 13, 201–206. doi: 10.1109/tnsre.2005.848687

Majji, A. B., Humayun, M. S., Weiland, J. D., Suzuki, S., D'Anna, S. A., and de Juan, E. (1999). Long-term histological and electrophysiological results of an inactive epiretinal electrode array implantation in dogs. *Invest. Ophthalmol. Vis. Sci.* 40, 2073–2081.

Masland, R. H. (2012). The neuronal organization of the retina. *Neuron* 76, 266–280. doi: 10.1016/j.neuron.2012.10.002

McLean, G., Guthrie, B., Mercer, S. W., and Smith, D. J. (2014). Visual impairment is associated with physical and mental comorbidities in older adults: a cross-sectional study. *BMC Med.* 12:181. doi: 10.1186/s12916-014-0181-7

Meers, S., and Ward, K. (2005). "A substitute vision system for providing 3D perception and GPS navigation via electro-tactile stimulation," in *Proceedings of the International Conference on Sensing Technology*, (Palmerston North), 21–23.

Meijer, P. B. (1992). An experimental system for auditory image representations. *IEEE Trans. Biomed. Eng.* 39, 112–121. doi: 10.1109/10.121642

Minusa, S., Osanai, H., and Tateno, T. (2017). Micromagnetic Stimulation of the Mouse Auditory CortexIn VivoUsing an Implantable Solenoid System. *IEEE Trans. Biomed. Eng.* 65, 1301–1310. doi: 10.1109/tbme.2017.2748136

Mortimer, T., Agnew, W. F., Horch, K., Citron, P., Creasey, G., and Kantor, C. (1995). Perspectives on new electrode technology for stimulating peripheral nerves with implantable motor prostheses. *IEEE Trans. Rehabil. Eng.* 3, 145–154. doi: 10.1109/86.392373

Munshi, R., Qadri, S. M., and Pralle, A. (2018). Transient magnetothermal neuronal silencing using the chloride channel anoctamin1 (TMEM16A). *Front. Neurosci.* 12:560. doi: 10.3389/fnins.2018.00560

Munshi, R., Qadri, S. M., Zhang, Q., Rubio, I. C., del Pino, P., and Pralle, A. (2017). Magnetothermal genetic deep brain stimulation of motor behaviors in awake, freely moving mice. *Elife* 6:e27069. doi: 10.7554/eLife.27069

Nagel, G., Ollig, D., Fuhrmann, M., Kateriya, S., Musti, A. M., Bamberg, E., et al. (2002). Channelrhodopsin-1: a light-gated proton channel in green algae. *Science* 296, 2395–2398. doi: 10.1126/science.1072068

Nan, C. W., Bichurin, M., Dong, S., Viehland, D., and Srinivasan, G. (2008). Multiferroic magnetoelectric composites: historical perspective, status, and future directions. *J. Appl. Phys.* 103:1. doi: 10.2514/5.9781600866234.0001.0010

Palanker, D., Vankov, A., Huie, P., and Baccus, S. (2005). Design of a high-resolution optoelectronic retinal prosthesis. *J. Neural Eng.* 2:S105.

Palanker, D. V., Le Mer, Y., Hornig, R., Buc, G., Deterre, M., Bismuth, V., et al. (2019). Restoration of sight in geographic atrophy using a photovoltaic subretinal prosthesis. *Invest. Ophthalmol. Vis. Sci.* 60, 970–970.

Panetsos, F., Sanchez-Jimenez, A., Diaz-de Cerio, E. R., Diaz-Guemes, I., and Sanchez, F. M. (2011). Consistent phosphenes generated by electrical microstimulation of the visual thalamus. An experimental approach for thalamic visual neuroprostheses. *Front. Neurosci.* 5:84. doi: 10.3389/fnins.2011.00084

Park, H. J., Bonmassar, G., Kaltenbach, J. A., Machado, A. G., Manzoor, N. F., and Gale, J. T. (2013). Activation of the central nervous system induced by micro-magnetic stimulation. *Nat. Commun.* 4:2463. doi: 10.1038/ncomms3463

Pezaris, J. S., and Eskandar, E. N. (2009). Getting signals into the brain: visual prosthetics through thalamic microstimulation. *Neurosurg. Focus* 27:E6. doi: 10.3171/2009.4.FOCUS0986

Pezaris, J. S., and Reid, R. C. (2007). Demonstration of artificial visual percepts generated through thalamic microstimulation. *Proc. Natl. Acad. Sci. U.S.A.* 104, 7670–7675. doi: 10.1073/pnas.0608563104

Pietrini, P., Furey, M. L., Ricciardi, E., Gobbini, M. I., Wu, W. H. C., Cohen, L., et al. (2004). Beyond sensory images: object-based representation in the human ventral pathway. *Proc. Natl. Acad. Sci. U.S.A.* 101, 5658–5663. doi: 10.1073/pnas.0400707101

Poirier, C., Collignon, O., Scheiber, C., Renier, L., Vanlierde, A., Tranduy, D., et al. (2006). Auditory motion perception activates visual motion areas in early blind subjects. *Neuroimage* 31, 279–285. doi: 10.1016/j.neuroimage.2005.11.036

Polosukhina, A., Litt, J., Tochitsky, I., Nemargut, J., Sychev, Y., De Kouchkovsky, I., et al. (2012). Photochemical restoration of visual responses in blind mice. *Neuron* 75, 271–282. doi: 10.1016/j.neuron.2012.05.022

Pouratian, N., Yoshor, D., Niketeghad, S., Dornm, J., and Greenberg, R. (2019). Early feasibility study of a neurostimulator to create artificial vision. *Neurosurgery* 66:nyz310_146.

Prévot, P.-H., Gehere, K., Arcizet, F., Akolkar, H., Khoei, M. A., Blaize, K., et al. (2019). Behavioural responses to a photovoltaic subretinal prosthesis implanted in non-human primates. *Nat. Biomed. Eng.*. doi: 10.1038/s41551-019-0484-2 [Epub ahead of print].

Quinn, T. P. (1980). Evidence for celestial and magnetic compass orientation in lake migrating sockeye salmon fry. *J. Comp. Physiol.* 137, 243–248. doi: 10.1007/bf00657119

Reutsky-Gefen, I., Golan, L., Farah, N., Schejter, A., Tsur, L., Brosh, I., et al. (2013). Holographic optogenetic stimulation of patterned neuronal activity for vision restoration. *Nat. Commun.* 4:1509. doi: 10.1038/ncomms2500

Rizou, M. E., and Prodromakis, T. (2018). Magnetic stimulation in the microscale: the development of a 6 × 6 array of micro-coils for stimulation of excitable cells in vitro. *Biomed. Phys. Eng. Exp.* 4:025016. doi: 10.1088/2057-1976/aaa0dd

Sadato, N., Pascual-Leone, A., Grafman, J., Ibañez, V., Deiber, M.-P., Dold, G., et al. (1996). Activation of the primary visual cortex by Braille reading in blind subjects. *Nature* 380:526. doi: 10.1038/380526a0

Sakaguchi, H., Kamei, M., Fujikado, T., Yonezawa, E., Ozawa, M., Cecilia-Gonzalez, C., et al. (2009). Artificial vision by direct optic nerve electrode (AV-DONE) implantation in a blind patient with retinitis pigmentosa. *J, Artif. Organs* 12, 206–209. doi: 10.1007/s10047-009-0467-2

Sampaio, E., Maris, S., and Bach-y-Rita, P. (2001). Brain plasticity:'visual'acuity of blind persons via the tongue. *Brain Res.* 908, 204–207. doi: 10.1016/s0006-8993(01)02667-1

Schmidt, E., Bak, M., Hambrecht, F., Kufta, C., O'rourke, D., and Vallabhanath, P. (1996). Feasibility of a visual prosthesis for the blind based on intracortical micro stimulation of the visual cortex. *Brain* 119, 507–522. doi: 10.1093/brain/119.2.507

Schneider, K. A., Richter, M. C., and Kastner, S. (2004). Retinotopic organization and functional subdivisions of the human lateral geniculate nucleus: a high-resolution functional magnetic resonance imaging study. *J. Neurosci.* 24, 8975–8985. doi: 10.1523/jneurosci.2413-04.2004

Scott, A. W., Bressler, N. M., Ffolkes, S., Wittenborn, J. S., and Jorkasky, J. (2016). Public attitudes about eye and vision health. *JAMA Ophthalmol.* 134, 1111–1118.

Shemesh, O. A., Tanese, D., Zampini, V., Linghu, C., Piatkevich, K., Ronzitti, E., et al. (2017). Temporally precise single-cell-resolution optogenetics. *Nat. Neurosci.* 20:1796. doi: 10.1038/s41593-017-0018-8

Shepherd, G. M. (2003). *The Synaptic Organization of the Brain*. Oxford: Oxford university press.

Shin, S. S., Krishnan, V., Stokes, W., Robertson, C., Celnik, P., Chen, Y., et al. (2018). Transcranial magnetic stimulation and environmental enrichment enhances cortical excitability and functional outcomes after traumatic brain injury. *Brain Stimul.* 11, 1306–1313. doi: 10.1016/j.brs.2018.07.050

Shroff, A. (2011). *An Eye on Numbers: A Ready Reckoner in Ophthalmology*. Mumbai: Postscript Media Pvt Ltd.

Sineshchekov, O. A., Jung, K. H., and Spudich, J. L. (2002). Two rhodopsins mediate phototaxis to low-and high-intensity light in Chlamydomonas reinhardtii. *Proc. Natl. Acad. Sci.* U.S.A.99, 8689–8694. doi: 10.1073/pnas.122243399

Spira, M. E., and Hai, A. (2013). Multi-electrode array technologies for neuroscience and cardiology. *Nature Nanotechnol.* 883. doi: 10.1038/nnano.2012.265

Stanley, S. A., Gagner, J. E., Damanpour, S., Yoshida, M., Dordick, J. S., and Friedman, J. M. (2012). Radio-wave heating of iron oxide nanoparticles can regulate plasma glucose in mice. *Science* 336, 604–608. doi: 10.1126/science.1216753

Stelmack, J. (2001). Quality of life of low-vision patients and outcomes of low-vision rehabilitation. *Opt,. Vis. Sci.* 78, 335–342. doi: 10.1097/00006324-200105000-00017

Stingl, K., Bartz-Schmidt, K., Besch, D., Gekeler, F., Greppmaier, U., Hörtdörfer, G., et al. (2012). What can blind patients see in daily life with the subretinal Alpha IMS implant? Current overview from the clinical trial in Tübingen. *Ophthalmol*109, 136–141. doi: 10.1007/s00347-011-2479-6

Stingl, K., Bartz-Schmidt, K. U., Besch, D., Braun, A., Bruckmann, A., Gekeler, F., et al. (2013). Artificial vision with wirelessly powered subretinal electronic implant alpha-IMS. *Proc. R. Soc. BBiol Sci.* 280:20130077. doi: 10.1098/rspb.2013.0077

Striem-Amit, E., Guendelman, M., and Amedi, A. (2012). 'Visual'acuity of the congenitally blind using visual-to-auditory sensory substitution. *PloS One* 7:e33136. doi: 10.1371/journal.pone.0033136

Struik, M. L., Steenbergen, H. G., Koster, A. S., Bretschneider, F., and Peters, R. C. (2001). Simultaneous measurements of calcium mobilization and afferent nerve activity in electroreceptor organs of anesthetized Kryptopterus bicirrhis. *Comp. Biochem. Physiol. A Mol. Integr. Physiol.* 130, 607–613. doi: 10.1016/s1095-6433(01)00436-6

Tassicker, G. (1956). Preliminary report on a retinal stimulator. *Br. J. Physiol. Opt.* 13:102.

Tay, A., Kunze, A., Murray, C., and Di Carlo, D. (2016). Induction of calcium influx in cortical neural networks by nanomagnetic forces. *ACS Nano* 10, 2331–2341. doi: 10.1021/acsnano.5b07118

Tehovnik, E. J. (1996). Electrical stimulation of neural tissue to evoke behavioral responses. *J. Neurosci. Methods* 65, 1–17. doi: 10.1016/0165-0270(95)00131-x

Trobe, J. D. (2001). *The Neurology of Vision*. Oxford: Oxford university press.

Troyk, P. R. (2017). *Artificial Vision*. 203-214. Berlin: Springer.

Van Erp, J. B., Van Veen, H. A., Jansen, C., and Dobbins, T. (2005). Waypoint navigation with a vibrotactile waist belt. *ACM Trans. Appl. Percept.* 2, 106–117. doi: 10.1145/1060581.1060585

Veraart, C., Raftopoulos, C., Mortimer, J. T., Delbeke, J., Pins, D., Michaux, G., et al. (1998). Visual sensations produced by optic nerve stimulation using an implanted self-sizing spiral cuff electrode. *Brain Res.* 813, 181–186. doi: 10.1016/s0006-8993(98)00977-9

Veraart, C., Wanet-Defalque, M. C., Gérard, B., Vanlierde, A., and Delbeke, J. (2003). Pattern recognition with the optic nerve visual prosthesis. *Artif. Organs* 27, 996–1004. doi: 10.1046/j.1525-1594.2003.07305.x

Volta, A., and Banks, J. I. (1800). On the electricity excited by the mere contact of conducting substances of different kinds. *Philos. Mag.* 7, 289–311. doi: 10.1080/14786440008562590

Waldvogel, D., van Gelderen, P., Muellbacher, W., Ziemann, U., Immisch, I., and Hallett, M. (2000). The relative metabolic demand of inhibition and excitation. *Nature* 406, 995–998. doi: 10.1038/35023171

Wandell, B. A., Dumoulin, S. O., and Brewer, A. A. (2007). Visual field maps in human cortex. *Neuron* 56, 366–383. doi: 10.1016/j.neuron.2007.10.012

Wheeler, M. A., Smith, C. J., Ottolini, M., Barker, B. S., Purohit, A. M., Grippo, R. M., et al. (2016). Genetically targeted magnetic control of the nervous system. *Nat. Neurosci.* 19:756. doi: 10.1038/nn.4265

Wiltschko, W., and Wiltschko, R. (2005). Magnetic orientation and magnetoreception in birds and other animals. *J. Comp. Physiol. A* 191, 675–693. doi: 10.1007/s00359-005-0627-7

Wittenborn, J. S., Zhang, X., Feagan, C. W., Crouse, W. L., Shrestha, S., Kemper, A. R., et al. (2013). The economic burden of vision loss and eye disorders among the United States population younger than 40 years. *Ophthalmology* 120, 1728–1735. doi: 10.1016/j.ophtha.2013.01.068

Wong, Y. T., Feleppa, T., Mohan, A., Browne, D., Szlawski, J., Rosenfeld, J. V., et al. (2019). CMOS stimulating chips capable of wirelessly driving 473 electrodes for a cortical vision prosthesis. *J. Neural Eng.* 16:026025. doi: 10.1088/1741-2552/ab021b

World Health Organization (2006). *Neurological Disorders: Public Health Challenges*. Geneva: World Health Organization.

Wu, F., Stark, E., Ku, P.-C., Wise, K. D., Buzsáki, G., and Yoon, E. (2015). Monolithically integrated μLEDs on silicon neural probes for high-resolution optogenetic studies in behaving animals. *Neuron* 88, 1136–1148. doi: 10.1016/j.neuron.2015.10.032

Yarjanli, Z., Ghaedi, K., Esmaeili, A., Rahgozar, S., and Zarrabi, A. (2017). Iron oxide nanoparticles may damage to the neural tissue through iron accumulation, oxidative stress, and protein aggregation. *BMC Neurosci.* 18:51. doi: 10.1186/s12868-017-0369-9

Zrenner, E., Bartz-Schmidt, K. U., Benav, H., Besch, D., Bruckmann, A., Gabel, V.-P., et al. (2010). Subretinal electronic chips allow blind patients to read letters and combine them to words. *Proc. R. Soc. BBiol. Sci.* 278, 1489–1497. doi: 10.1098/rspb.2010.1747

Conflict of Interest: The authors declare that the research was conducted in the absence of any commercial or financial relationships that could be construed as a potential conflict of interest.

frontiers in Neuroscience

ORIGINAL RESEARCH
published: 07 July 2020
doi: 10.3389/fnins.2020.00582

EEG Biomarkers Related With the Functional State of Stroke Patients

Marc Sebastián-Romagosa[1,2], Esther Udina[1], Rupert Ortner[2], Josep Dinarès-Ferran[2,3], Woosang Cho[4], Nensi Murovec[4], Clara Matencio-Peralba[2], Sebastian Sieghartsleitner[4], Brendan Z. Allison[5] and Christoph Guger[2,4]*

[1] Department of Physiology, Universitat Autònoma de Barcelona, Barcelona, Spain, [2] g.tec Medical Engineering Spain SL, Barcelona, Spain, [3] Data and Signal Processing Research Group, Department of Engineering, University of Vic - Central University of Catalonia, Vic, Spain, [4] g.tec Medical Engineering GmbH, Schiedlberg, Austria, [5] Department of Cognitive Science, University of California at San Diego, La Jolla, CA, United States

Introduction: Recent studies explored promising new quantitative methods to analyze electroencephalography (EEG) signals. This paper analyzes the correlation of two EEG parameters, Brain Symmetry Index (BSI) and Laterality Coefficient (LC), with established functional scales for the stroke assessment.

Methods: Thirty-two healthy subjects and thirty-six stroke patients with upper extremity hemiparesis were recruited for this study. The stroke patients where subdivided in three groups according to the stroke location: Cortical, Subcortical, and Cortical + Subcortical. The participants performed assessment visits to record the EEG in the resting state and perform functional tests using rehabilitation scales. Then, stroke patients performed 25 sessions using a motor-imagery based Brain Computer Interface system (BCI). BSI was calculated with the EEG data in resting state and LC was calculated with the Event-Related Synchronization maps.

Results: The results of this study demonstrated significant differences in the BSI between the healthy group and Subcortical group (P = 0.001), and also between the healthy and Cortical+Subcortical group (P = 0.019). No significant differences were found between the healthy group and the Cortical group (P = 0.505). Furthermore, the BSI analysis in the healthy group based on gender showed statistical differences (P = 0.027). In the stroke group, the correlation between the BSI and the functional state of the upper extremity assessed by Fugl-Meyer Assessment (FMA) was also significant, $\rho = -0.430$ and P = 0.046. The correlation between the BSI and the FMA-Lower extremity was not significant ($\rho = -0.063$, P = 0.852). Similarly, the LC calculated in the alpha band has significative correlation with FMA of upper extremity ($\rho = -0.623$ and $P < 0.001$) and FMA of lower extremity ($\rho = -0.509$ and P = 0.026). Other important significant correlations between LC and functional scales were observed. In addition, the patients showed an improvement in the FMA-upper extremity after the BCI therapy (ΔFMA = 1 median [IQR: 0–8], P = 0.002).

Conclusion: The quantitative EEG tools used here may help support our understanding of stroke and how the brain changes during rehabilitation therapy. These tools can help identify changes in EEG biomarkers and parameters during therapy that might lead to improved therapy methods and functional prognoses.

Keywords: brain-computer interface, motor imagery, EEG, rehabilitation, Brain Symmetry Index, laterality coefficient

OPEN ACCESS

Edited by:
Ioan Opris,
University of Miami, United States

Reviewed by:
Riccardo Iandolo,
Italian Institute of Technology, Italy
Solaiman Shokur,
École Polytechnique Fédérale de Lausanne, Switzerland

****Correspondence:***
Marc Sebastián-Romagosa
sebastian@gtec.at;
marc.sebastian@e-campus.uab.cat

Specialty section:
This article was submitted to Neural Technology, a section of the journal Frontiers in Neuroscience

Received: *30 January 2020*
Accepted: *12 May 2020*
Published: *07 July 2020*

Citation:
Sebastián-Romagosa M, Udina E, Ortner R, Dinarès-Ferran J, Cho W, Murovec N, Matencio-Peralba C, Sieghartsleitner S, Allison BZ and Guger C (2020) EEG Biomarkers Related With the Functional State of Stroke Patients. Front. Neurosci. 14:582. doi: 10.3389/fnins.2020.00582

INTRODUCTION

Stroke is one of the most prevalent pathologies around the world. Stroke can cause devastating effects in survivors, including severe motor and sensory impairments that hinder their activities of daily living (Kim et al., 2020). The clinical consequences after a stroke vary, depending largely on the location and the cause of the damage (Prabhakaran et al., 2008). Diagnostic imaging tools like Computational Tomography (CT) or Functional magnetic resonance imaging (fMRI) are normally used to evaluate brain damage in the acute and sub-acute phases, offering valuable information about the diagnostic and functional prognosis for each case. Recent studies explored new methods to process and analyze brain signals acquired by conventional techniques like electroencephalography (EEG) (Kanda et al., 2009; Leon-Carrion et al., 2009; Foreman and Claassen, 2012; Rabiller et al., 2015; Wu et al., 2016) or magnetoencephalography (MEG) (Mäkelä et al., 2015; Ikkai et al., 2016; Krauss et al., 2018).

Quantitative EEG (qEEG) is a useful tool to extract features from the EEG signals and thereby help clinicians understand each patient's clinical state. qEEG parameters have shown multiple correlations with different pathologies, making qEEG an essential tool for different clinical fields (Nishida et al., 2011; Wang et al., 2013; Faust et al., 2015; Jeong et al., 2016; Muniz et al., 2016; Piano et al., 2017). One qEEG parameter is the Brain Symmetry Index (BSI), described by van Putten et al. (2004) to assess the stroke risk during carotid endarterectomy surgery in real time (van Putten et al., 2004; van Putten, 2006, 2007). Subsequently, Agius Anastasi et al. (2017) used the BSI with stroke patients and found correlations between this parameter and functional scales. The idea of the BSI is to assess the symmetry between both brain hemispheres by using the EEG.

EEG can measure brain signals with a high temporal resolution, allowing clinicians to monitor brain activity in real time (Dobkin, 2007; McFarland and Wolpaw, 2017). Brain signals can be read with a software program to provide the user with an external pathway for these brain outputs (Wolpaw, 2007). This approach has been employed in numerous Brain Computer Interface (BCI) systems providing real-time communication and control. BCIs have been used to control devices such as a wheelchair (Carlson and del, 2013), prosthesis or functional electrical stimulator (FES) (Ramos-Murguialday et al., 2013), sometimes in combination with immersive feedback relating to rehabilitation (Shokur et al., 2018). Over the past several years, many publications have combined BCI, FES and other feedback devices to increase cortical plasticity in stroke survivors helping them regain movement control (Dobkin, 2007).

In this approach to movement restoration, stroke survivors perform Motor Imagery (MI) exercises during EEG recording (Cervera et al., 2018). The decoded brain oscillations can be used to move a virtual reality avatar or trigger an FES device to reproduce the imagined movement with the paretic limb (e.g., Cho et al., 2016; Irimia et al., 2017). These types of rewarding feedback only occur if the patient imagines the desired movement, providing a closed-loop feedback system for patients and an objective means to monitor patient compliance for therapists and scientists.

During the MI tasks, the patient should concentrate on imagining a specific movement instructed by a therapist, such as wrist dorsiflexion. During MI, the contralateral motor cortex will exhibit event-related desynchronization (ERD), which is a decrease of EEG bandpower in the μ (8–13 Hz) and β (16–30 Hz) range. After the patient finishes performing MI, the contralateral motor cortex exhibits an increase in μ and lower β rhythm activity, called event-related synchronization (ERS). An ERS can also occur during MI in the ipsilateral hemisphere in the μ range, and is related to an idling state of those areas (Pfurtscheller and Aranibar, 1979; Graimann et al., 2002; Neuper et al., 2006; Kaiser et al., 2012). Many people with stroke exhibit atypical ERD/ERS activation patterns; for example, the affected cortex may be less excitable, and the changes in EEG activity may be more prominent over nearby cortical areas (Neuper et al., 2006; Kaiser et al., 2012).

Hence, stroke patients often have abnormal changes in ERD/ERS patterns resulting from MI. Kaiser et al. (2012) investigated how these abnormal patterns relate to the patient's functional state and spasticity, using a new parameter, the Laterality Coefficient (LC). For physical assessment, they used the European Stroke Scale (ESS), the Medical Research Council (MRC) and the Modified Ashworth Scale (MAS). The LC presented significant correlations with the MRC scale and MAS. The findings of Kaiser et al. (2012) showed that high percentage changes in ERD patterns in the contralesional hemisphere are related to a high degree of impairment. However, the aim of the current publication is to evaluate a novel analysis studying the correlation of LC with other functional scales like the Fugl-Meyer assessment.

Here, we explore two different qEEG parameters and their relationship with the diagnosis and functional prognosis of stroke patients. One group of healthy participants and one group of stroke patients participated in the study. Stroke patients performed functional assessment sessions, and BCI rehabilitation therapy for the upper extremity. EEG was recorded in two different situations: 8 min of resting state with open eyes (rEEG), and MI using a BCI system for motor rehabilitation. BSI perameters were analyzed with rEEG, whereas LC was calculated during the MI period. To assess each patient's functionality before and after the therapy, we primarily used the Fugl-Meyer assessment (FMA) (Gladstone et al., 2002; Woytowicz et al., 2017). We also used eight other standardized tests used in rehabilitation to assess motor function, spasticity, cognitive function, and other parameters: Fahn Tremor Rating Scale, MAS, Barthel Index, Box and Block Test, 9 Hole Peg test, 2 Point Discrimination Test, Montreal Cognitive Assessment and Self-rated questionnaire. This is the first study to employ such a broad range of tests along with analyses of BSI and other EEG-based parameters across several therapy sessions.

MATERIALS AND METHODS

Participants

Thirty-two healthy subjects and thirty-six stroke patients with upper extremity hemiparesis were recruited for this study.

All healthy participants were volunteers recruited through the Universitat de Vic, Spain. The stroke patients were recruited in the rehabilitation center RecoveriX Gym in Schiedlberg, Austria. Two patients dropped out from the study because of personal problems that prevented them from attending recording sessions. The patients' characteristics are reported in the results section.

The inclusion criteria for stroke patients were: (i) residual hemiparesis, (ii) the stroke occurred at least 4 days before the first assessment, (iii) functional restriction in the upper extremities. Additionally, for all participants, the following criteria were applied: (iv) able to understand written and spoken instructions, (v) stable neurological status, (vi) willing to participate in the study and to understand and sign the informed consent, (vii) able to attend recording sessions, (viii) no cerebellar lesions, (ix) no Botulinum toxin treatment for spasticity during the study. The participants were not recruited based on the scores of any functional assessment. Ethics approval was obtained from the Ethikkommission des Landes Oberösterreich in Austria for the patients (#D-42-17), and the ethics committee of Comitè d'Ètica de la Recerca-CER of Universitat de Vic (Spain) for the healthy controls.

Protocol

Healthy Controls

The healthy controls sat in a comfortable chair for 8 min while rEEG was collected. During this resting state assessment, participants were asked to avoid unnecessary movements and keep their eyes open, aside from normal blinking.

Stroke Patients

Each stroke patient participated in four assessment sessions and 25 therapy sessions.

Assessment: A clinician assessed each patient twice before the therapy began and twice after the last therapy session. Each of these four assessment sessions had two components: (1) the clinician recorded 8 min of rEEG with the same settings as described above for healthy controls and (2) the clinician tested the patient's motor function. The Pre1 assessment was performed 1 month before starting the therapy, and the Pre2 assessment was performed just before the therapy started. The Post1 assessment was performed just after the last session, and the Post2 assessment occurred 1 month after the last session. One hundred and and thirty six assessment sessions were performed in total (4 per patient).

Therapy: Patients completed 25 sessions, with two sessions per week.

Figures 1A,B depict different system components and the physical layout during each therapy session. At the beginning of each therapy session, the therapist talked with each patient to confirm that the patient understands the MI task and the upcoming procedure. Next, the EEG cap and FES pads were placed on the patient, and FES parameters were adjusted, as detailed below. After this preparation, the patient was seated in a comfortable chair in front of a table, facing a monitor where two virtual arms were projected in a position and orientation mimicking the subject's arms. The patient was asked to place both hands on the table and perform MI while following cues and feedback presented on the monitor. Each session contained up to three runs of 80 trials each, depending of the patient's fatigue. At the end of each session, the cap and FES pads were removed, and the skin was cleaned with a moist cloth. Each session required about 60 min total, including preparation and cleaning.

BCI System Description

The BCI system used in this study was RecoveriX (g.tec medical engineering GmbH, Austria) (Irimia et al., 2016). This system managed all EEG data recording and real-time interactions with the patient and therapist, including visual feedback using a virtual reality avatar and proprioceptive feedback using FES. Participants wore EEG caps with 16 active electrodes at positions FC5, FC1, FCZ, FC2, FC6, C5 C3, C1, CZ, C2, C4, C6, CP5, CP1, CP2, and CP6, according to the international 10/10 system (extended 10/20 system). A reference electrode was placed on the right earlobe and a ground electrode at FPZ.

Two FES electrodes were placed on the skin over the wrist extensors of the left and right forearms. The frequency was set to 50 Hz, and the pulse-width was set to 300 μs. Then, the stimulation parameters were individually adjusted for session until either (1) the optimal passive movement without pain for patients with mild or moderate muscle spasm, or (2) muscle contraction was observed in the target muscle of the paretic side for patients with severe muscle spasm.

MI Exercise

Figure 1C depicts the timing of each trial. Each trial starts with a beep, to help the participant focus on the upcoming task. Two seconds later, the system presents the instruction. For 1.5 s, the system presents an arrow pointing to the left or right on the patient's monitor and the word "left" or "right" in the participant's mother tongue via headphones. These simultaneous visual and auditory cues direct the patient to imagine dorsiflexion of the left or right wrist (in pseudorandom order). The participant is instructed to start the MI immediately after receiving the command and to continue the MI until the relax command is presented auditorily. The feedback phase starts at the same time as the instruction ends, that is 3.5 s after trial begin. The feedback devices can only be activated during this phase.

Feedback Presentation

Visual and proprioceptive FES feedback are provided in synchrony and only in the feedback phase. Classification of motor imagery is done every second. If the classified MI matches the presented command (left or right), then feedback is switched on, which means the wrist dorsiflexion is initiated by electrical stimulation and presented visually on the computer screen. During incorrect classifications, the initiated movement is done in the opposite direction. For classification, we used linear discriminant analysis (LDA) on the spatially filtered data. We followed the steps described in Irimia et al. (2018) except for a change in the electrode setup: FPZ, FP1, FP2, AF7, AF3, AFZ, AF4, AF8, F7, F5, F3, F1, FZ, F2, F4, F6, F8, FT7, FC5, FC3, FC1, FCZ, FC2, FC4, FC6, FT8, T7, C5, C3, C1, CZ, C2, C4, C6, T8, TP7, CP5, CP3, CP1, CPZ, CP2, CP4, CP6, TP8, P7, P5, P3, P1, PZ, P2, P4, P6, P8, PO7, PO3, POZ, PO4, PO8, O1, OZ, O2, O9, O10.

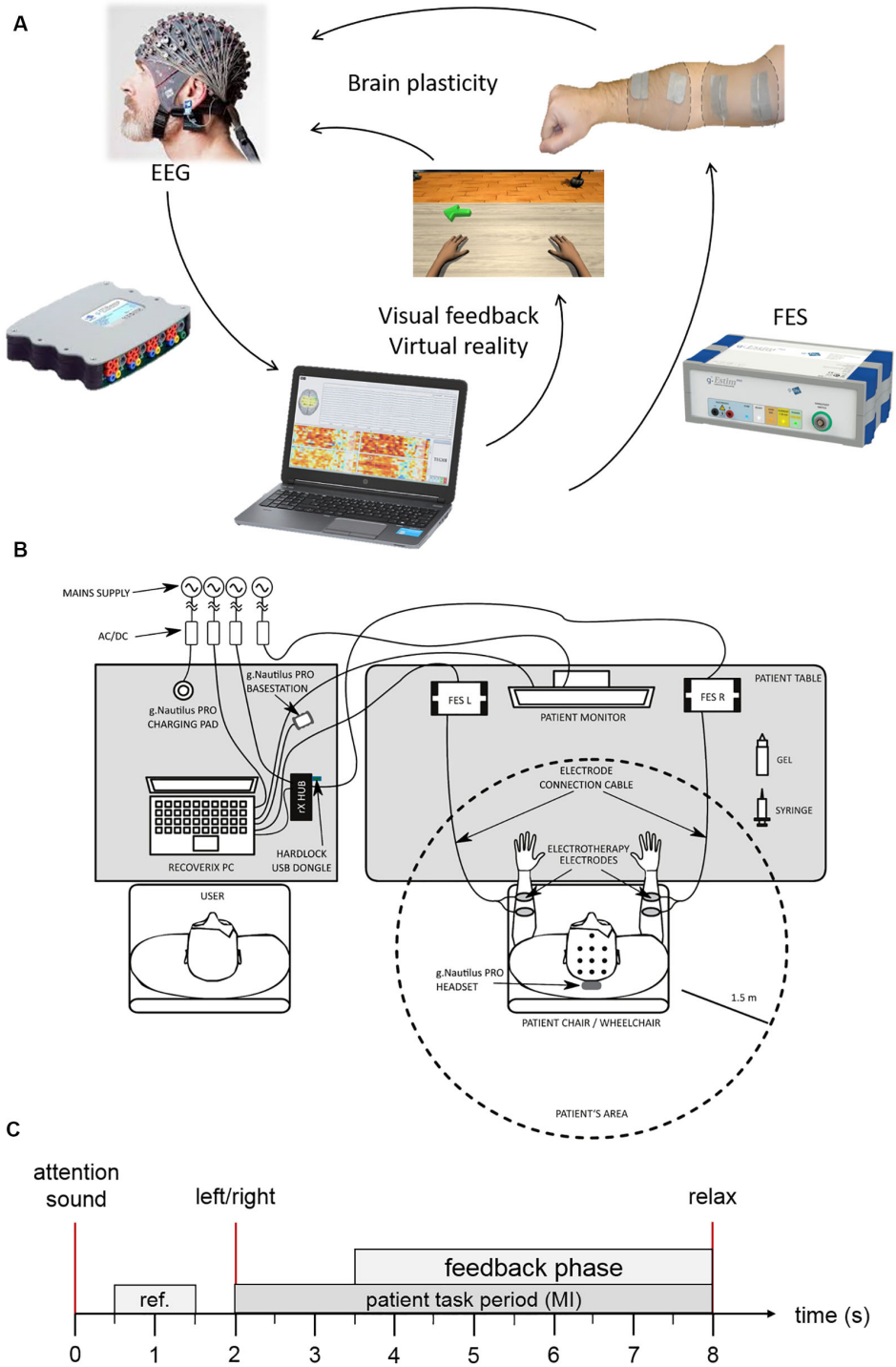

FIGURE 1 | BCI system components. **(A)** Shows the motor learning loop. **(B)** System setup. **(C)** Trial description.

Event-Related Synchronization and Desynchronization

Figure 2 presents ERD/ERS patterns that typically occur during MI. This figure was generated using the data from one BCI training session. During MI, the contralateral motor cortex produces a desynchronization (event-related desynchronization or ERD) of cortical motor neurons, showing a decrease in the bandpower of the waves with a frequency of 8–13 Hz (mu frequency rhythm). The ipsilateral motor cortex shows ERS patterns to suppress corresponding motor areas during MI of the

opposite hand side (Pfurtscheller and Aranibar, 1979; Graimann et al., 2002; Neuper et al., 2006; Kaiser et al., 2012). To create such maps, the change of EEG bandpower of several bandpass filtered frequency bands was calculated and plotted. The frequency bands chosen here ranged from 8 to 30 Hz in steps of 2 Hz. In each band, the power was calculated stepwise in windows of 16 samples (0.0625 s). Then, the bandpower of each window was compared to the bandpower of the reference period (gray area in **Figure 2**), during which the participant was in a resting state. The comparison used the following formula, in which A is the bandpower of one single window and R the bandpower within the reference period:

$$ERD = \frac{A - R}{R} * 100\%$$

Finally, a bootstrapping significance test ($\alpha = 0.05$) was done for all windows. Values that are not significant were set to 0 and are plotted in white in **Figure 2**. High ERD values (decreased bandpower) are plotted in red, whereas high ERS values (increased bandpower) are plotted in blue.

EEG Parameters

Brain Symmetry Index

The BSI is a parameter that compares the spectral power of the two hemispheres of the brain using bandpass filtered EEG signals. The BSI value ranges from 0 to 1 and is a measure of the symmetry between both hemispheres. A BSI value of 0 reflects total symmetry and 1 total asymmetry. The BSI value should be closer to 0 in healthy people and higher in stroke patients.

Method

The BSI of a segment of EEG is calculated using a revised BSI formula (van Putten, 2007), which is based on the squared value of the Fourier coefficients:

$$BSI(t) = \frac{1}{K} \sum_{n=1}^{K} \left| \frac{R_n^*(t) - L_n^*(t)}{R_n^*(t) + L_n^*(t)} \right|$$

with

$$R_n^*(t) = \frac{1}{M} \sum_{ch=1}^{M} \alpha_n^2(ch, t)$$

where $\alpha_n^2(ch, t)$ is the Fourier coefficient with index n of channel ch at time t. For the right hemisphere $R_n^*(t)$, the same formula is applied for the left hemisphere electrodes.

We collected resting state data from 16 EEG sites. For the BSI calculation, we discarded the central sites and split the remaining sites in two sets: right and left. For the left hemisphere, the electrodes were: FC3, C5, C3, C1, CP3, and CP1. For the right hemisphere, the electrodes were: FC4, C2, C4, C6, CP2, and CP4.

We processed 8 min of resting state EEG for each participant (in the healthy and stroke groups). We bandpass filtered (1–25 Hz) the whole EEG, and then we cut it in frames of 4 s, with a 2-s overlap. We used a Hamming window to prevent spectral distortion. We used an artifact detection method based on the overflow of the EEG standard deviation on each 4 s window frame. Any frame with more than 1.5 times of the total standard deviation for each channel was rejected from the BSI calculation. We did consider an algorithm for rejection of EOG related artifact, but determined that it would be unnecessary based on analysis of pilot data. The most frontal EEG electrodes are in the row of FCZ; hence, the influence of EOG was small. Furthermore, participants were asked to focus on the screen during the reference period, thus limiting eye movement. Movement related artifacts were found and rejected with our approach based on the standard deviation. Finally, the Fourier coefficient was calculated from the power density estimation using the Welch method.

Laterality Coefficient

The raw EEG data recorded during the MI sessions was used to calculate the LC parameter. The LC coefficient was calculated for each session twice: first for trials of MI of the paretic (p) hand and again for trials of the healthy (h) hand. We employed the following formula, where C and I refer to the contralateral and ipsilateral values of the ERD/ERS patterns during the MI.

$$LC_{p/h} = (C - I)/(C + I)$$

We followed six steps to calculate C and I:

(1) Band filtering (8–13 Hz or 13–30 Hz) of the EEG signal;
(2) Frame artifact rejection if a sample overflows a threshold based on the median variance among the samples of all the frames;
(3) Laplacian derivation using the surrounding electrodes;
(4) ERD/ERS patterns calculation according to (Graimann et al., 2002);
(5) Summation of all ERD/ERS values from second 2 until the end of the ERD map (second 8); and
(6) Apply the formula to obtain the LC coefficients.

Assessment Tests

We used 10 tests to assess each patient's functional capabilities during each of the four assessment sessions. All of these tests are well-established in the scientific literature and clinical practice. These ten tests each measure different aspects of motor function, other motor impairment (tremor and spasticity), cognitive function, sensory discrimination, and self-reported impact. The **Supplementary Material** provides a complete description of each test.

The scales used for the motor assessment were: Fugl-Meyer Assessment (FMA) for the upper extremity (FMAue) and for the lower extremity (FMAle), Box and Block Test (BBT) and 9 Hole Peg Test (HPT) for the healthy and paretic hand. Each patient completed the BBT and 9HPT tests with both hands to provide an individualized baselne.

The scale used to assess the tremor was the Fahn Tremor Rating Scale (FTRS). We assessed tactile discrimination with the Two Point Discrimination Test (TPDT). The spasticity of the wrists and fingers was assessed with the Modified Ashworth Scale (MAS). The Montreal Cognitive Assessment (MOCA) was used to assess the cognitive status of the patients. The Barthel Index (BI) was used to assess performance in daily life activities.

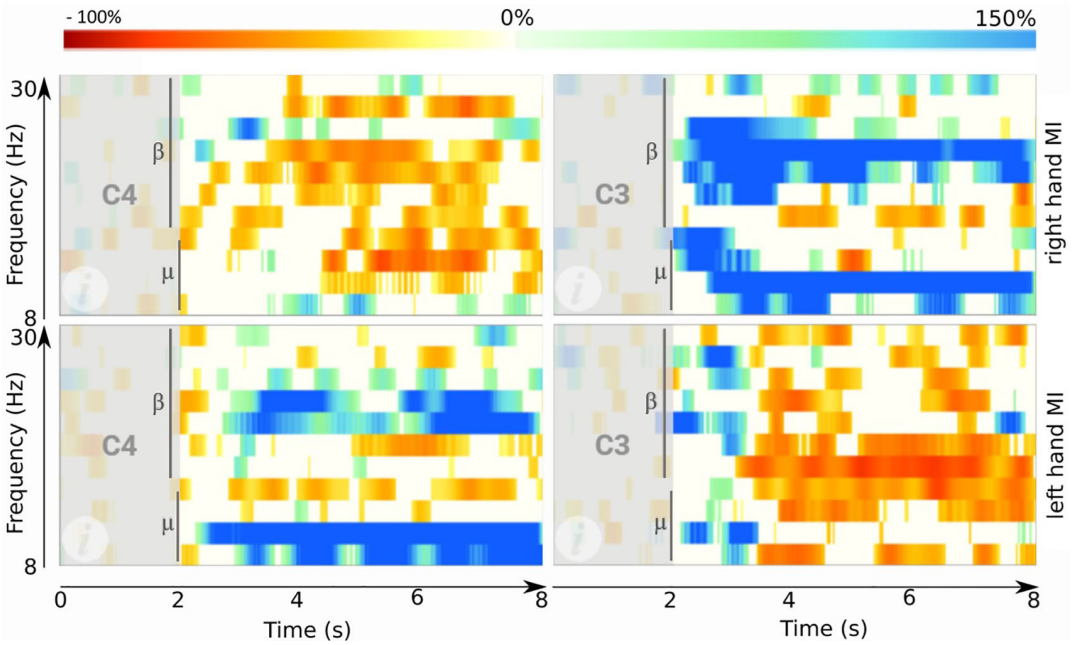

FIGURE 2 | ERD maps obtained after one session of BCI training. **Top right:** ERD map during right hand MI on site C3. **Top left:** ERD map during right hand MI on C4. **Bottom right:** ERD map during left hand MI on C3. **Bottom left:** ERD map during left hand MI on C4. Each plot shows the time from 0 to 8 s (*x*-axis) and frequencies between 8 and 30 Hz (*y*-axis). Red areas indicate high ERD. Blue areas mark the opposite: an ERS. Vertical bars indicate the cue onset at 2 s.

Patients also completed a self-rated questionnaire (SRQ) to assess pain, function, memory, thinking, mobility and the home and community, and stroke recovery.

Statistical Analysis

The sample size selection was based on the previous literature (Kaiser et al., 2012). The statistical analyses were performed using MATLAB R2017a (MathWorks Inc., United States). Normality of data was tested using the Shapiro–Wilk test. The statistical test was chosen according to the normality of the sample, the homogeneous of variance (Levene's or Brown–Forsythe test of equal variance) and sample size. Leven's test of equal variance was used if normality could be assumed; otherwise, the Brown–Forsythe test of equal variance was used. Descriptive statistics are reported as mean and the standard deviation (SD), or median and the inter-quartile range (IQR) of 0.25 and 0.75.

The correlation tests were chosen according to the results obtained by the Shapiro–Wilk test. When the normality assumption was not rejected, the correlation was made using Pearson's linear correlation test; otherwise, the correlation was done using Spearman's rank correlation test.

For the two group comparisons (for example, BSI comparison based on gender), the test was selected based on the normality and homogeneity of variance of the samples and the independence assumption. The unpaired *t*-test was used for comparisons of two independent likely normally distributed groups. For the comparisons before-and after the treatment [Pre2 vs. Post1] with measures from the same population, the paired *t*-test or the Wilcoxon test was used, depending on the normality assumption.

For comparisons between multiple groups, Welch's ANOVA was used. We used Welch's ANOVA for comparisons between multiple groups. When Welch's ANOVA yielded significant results, we conducted a *post hoc* analysis using the Single-step Games-Howell test.

A correction for multiplicity (i.e., multiple hypotheses testing) was not utilized, because no final conclusion and decision on the correlation of qEEG parameters and functional scales is drawn. Similarly, while a statistical analysis concerning the functional scales before and after BCI therapy was carried out, the goal of this paper is not to establish definitive proof on the efficacy of BCI-based therapy. Concordantly, we did not correct for multiplicity in this statistical analysis either (Bender and Lange, 2001). Additionally, Hurlbert and Lombardi (2012) recommend carrying out statistical tests without any adjustments for multiple hypothesis. This recommendation stems from the reasoning that the true probability of type I errors occurring is very small, because most null hypotheses can be expected to be false based on prior knowledge (Hurlbert and Lombardi, 2012). In the present case, one can reasonably accept this premise, based on the available literature discussed in the section "Introduction."

RESULTS

Participants' Baselines

Thirty-two healthy subjects were enrolled in the study, with 13 males and 19 females. The mean age in the healthy group was

TABLE 1 | Participants' baselines.

Group	*n*	Age (y)	*SD*	Male	Female
Healthy	32	42.3	15.4	13	19
Patient	34	65.3	14.4	22	12
Cortical	5	57.6	27.3	4	1
Subcortical	17	66.4	12.7	9	8
Cortical + Subcortical	12	67.0	09.4	9	3

TABLE 2 | Results of BSI-based age analysis.

One-way ANOVA					
	SS	**Df**	**MS**	***F***	***P***
Groups	0.000983	2	0.000492	0.3843	0.6844
Error	0.0371	29	0.0013		
Total	0.0381	31			

42.3 years (*SD* = 15.4). Thirty-four stroke patients participated (excluding two who dropped out). Twenty-two of the patients were male (64.7%), and the other 12 stroke participants were female (35.3%). The stroke patients' mean age was 65.3 years (*SD* = 14.4); this difference in age will be addressed at a later stage of this analysis.

Table 1 shows the participants' baselines. The stroke participants were classified in three groups based on their stroke diagnosis: Cortical, Subcortical, Cortical + Subcortical. The most common type of stroke was Subcortical with 17 patients (50.0%), followed by Cortical+Subcortical with 12 patients (35.3%) and Cortical with 5 patients (14.7%). Twenty-seven of these patients were in the chronic phase (79.4%), and only 7 in the subacute phase (20.6%). Twenty three patients had a stroke in the right hemisphere (67.7%), and the stroke was in the left hemisphere in 11 patients (32.4%).

Brain Symmetry Index (BSI)

BSI Differences Between Age Groups

To date, there is no evidence to demonstrate the variability of BSI with age. We performed a statistical analysis using the rEEG data from the healthy subjects. The data follows a normal distribution according to the Shapiro–Wilk test (P = 0.117). We explored the relationship between BSI and age using Pearson's method and One-way ANOVA. **Figure 3A** shows that the Pearson's correlation did not show significant correlation between BSI and age (ρ = −0.110, P = 0.548). Subsequently, we compared BSI across age groups (under 30 years, between 30 and 50 years and over 50 years). The variance of each group, using Levene's test, did not show significant results (df = 29.00, F = 1.338, P = 0.278). The analysis of variance shows that there is no significant difference in the BSI parameter based on the three age groups (F = 0.3843, P = 0.684). See **Figure 3B** and **Table 2**.

BSI Based on Gender

Figure 4 presents the results of this subgroup analysis. Both groups have similar variance (Levene's test results: df = 30.00, F = 1.733, P = 0.198). The result of this analysis shows that there is a statistical difference in BSI based on gender, according to the unpaired t-test (t-value = | 2.333|, P = 0.027).

BSI Between Groups

Since the results obtained in the BSI based on age did not show significant differences in the healthy group, we compared the BSI between groups (stroke and healthy) despite the age difference.

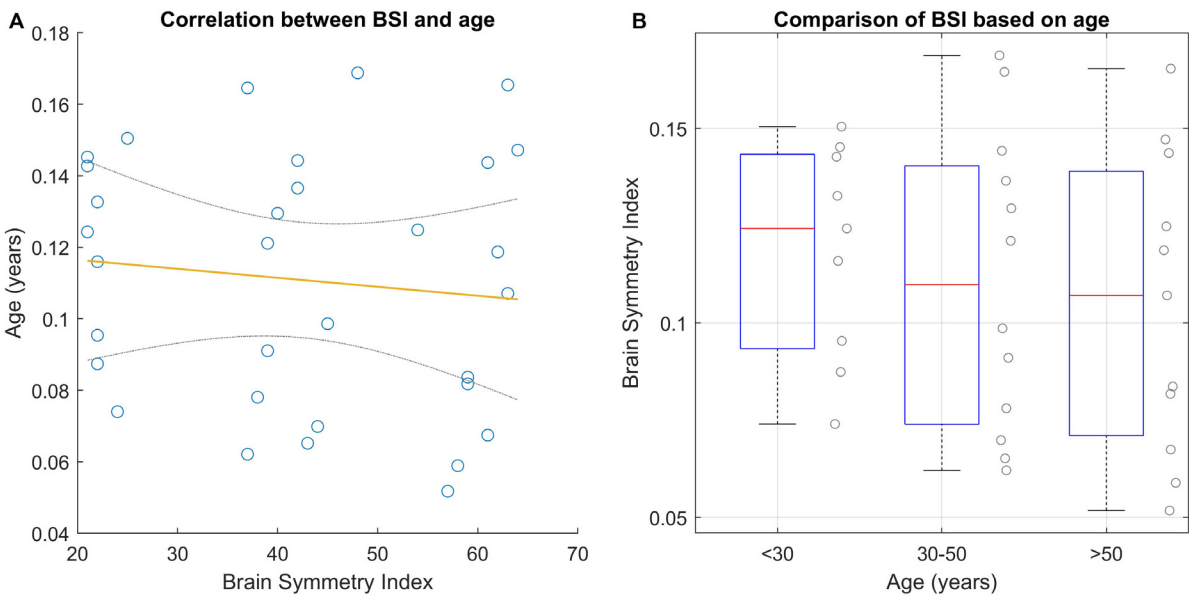

FIGURE 3 | BSI analyses based on age. **(A)** Shows the correlation between age and BSI using Pearson's method. The yellow line is the regression line and the gray lines are the CI at 95%. **(B)** Shows the BSI results based on three clusters.

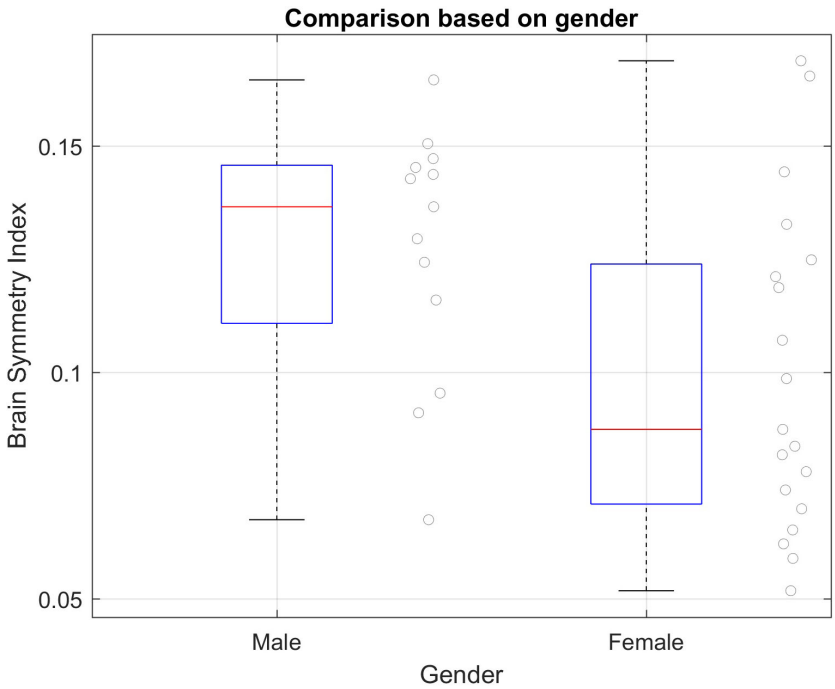

FIGURE 4 | BSI subgroup analyses based on gender in the healthy group. Mean and SD of each group: Male = 0.1272 (*SD* = 0.0278); Female = 0.0997 (*SD* = 0.0357). Significant difference between groups using unpaired *t*-test; *t*-value = | 2.333| *P* = 0.027.

We first analyzed the resting state data collected during the assessments, consisting of 136 assessment sessions from 34 stroke patients and 32 EEG recordings from 32 healthy subjects. We calculated the BSI of each assessment (Pre1, Pre2, Post1, Post2) from each patient's rEEG data. For this analysis, we used the median of Pre2 and Post1. In one case, the BSI could not be calculated due the corruption of the EEG data recordings (this patient belongs to Cortical group). The first step was the normality testing of each group. The first three datasets did not attain significance using the Shapiro–Wilk Test, hence, a normal distribution can be assumed. Group 4 (cortex + subcortex) is the only one that is not normally distributed. The equality of the variances cannot be assumed (Levene's Test results: df = 61.00, $F = 5.798$, $P = 0.001$). We used Welch's ANOVA test to compare the BSI parameter across the four groups, because this method is reasonably robust to deviations of normality, when the variances are substantially different and even if the sample sizes are unequal (Kohr and Games, 1974; Tomarken and Serlin, 1986). **Table 3** summarizes results from each group. Welch's ANOVA test found an associated probability of $P = 0.003$ and $F = 8.929$, so the hypothesis of equal sample means was rejected. As the Welch's ANOVA test showed significant results, the Games-Howell test was used to complete the analysis. The single-step Games-Howell test (see **Table 4**) shows significant differences between group 1 (healthy group) and both group 3 (subcortex group) and group 4 (cortex + subcortex group). **Figure 5** shows the BSI values for each group.

TABLE 3 | BSI analysis summary statistic.

Group	Size	Mean	Variance
1	32	0.1109	0.0012
2	4	0.1789	0.0098
3	17	0.1580	0.0011
4	12	0.1931	0.0061

Group numbers: 1 – Healthy, 2 – Cortical, 3 – Subcortical, 4 – Cortical + Subcortical.

Correlations Between BSI and Functional Tests

Figure 6 shows a significant correlation between BSI and patients' outcomes on the FMAue scale. The correlation coefficient of this

TABLE 4 | Single-step Games-Howell test.

Comparison		Delta	*SE*	Df	*P*	*H*	lb	ub
1	2	−0.068	0.045	4.157	0.505	0	−0.246	0.110
1	3	−0.047	0.010	33.870	0.001	1	−0.075	−0.019
1	4	−0.082	0.023	12.708	0.019	1	−0.151	−0.013
2	3	0.021	0.045	4.275	0.965	0	−0.156	0.198
2	4	−0.014	0.050	6.171	0.992	0	−0.185	0.156
3	4	−0.035	0.024	13.937	0.481	0	−0.105	0.035

Result of group comparison based on BSI values using Games-Howell test. The first column shows the group code; 1 – Healthy group, 2 – Cortical group, 3 – Subcortical group, 4 – Cortex + Subcortex group. The column 'H' shows the significant (H = 1) and non-significant (H = 0) differences at alpha level, and the column 'P' shows the significance level of these comparisons.

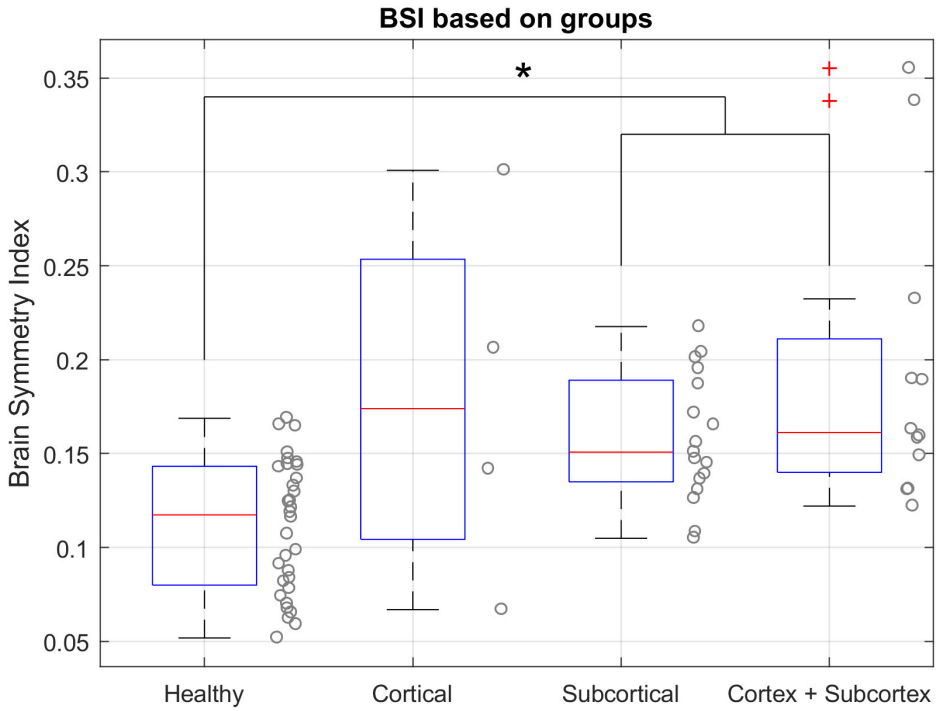

FIGURE 5 | BSI values in resting state with open eyes for each group. (*) Indicates the significant differences based on the Games-Howell test. The BSI of the healthy group is significantly different from the subcortical group and cortex + subcortex group. Healthy group median = 0.1173, IQR = 0.0799 – 0.1432. Cortical group = 0.1739, IQR = 0.1043–0.2534. Subcortical group = 0.1507, IQR = 0.1349–0.1890. Cortex + Subcortex group = 0.1612, IQR = 0.1400–0.2110.

relationship is −0.430 and $P = 0.046$. Lower BSI values are related to better functionality.

Laterality Coefficient

The LC was calculated separately for the MI tasks of the healthy (LCh) and paretic (LCp) hand. We calculated the LC for the alpha (LChα and LCpα) and beta (LChβ and LCpβ) bands. We explored the LC (α and β) between groups (Cortical, Subcortical, and Cortical + Subcortical), and found no significant differences of LC between groups (Welch ANOVA, $F = 0.36$, $P = 0.7033$).

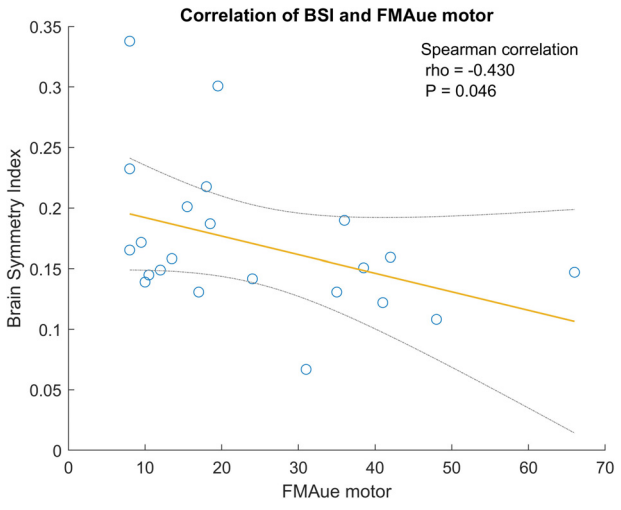

FIGURE 6 | Correlation between BSI and FMA upper extremity. The gray lines are the confidence interval at 95%.

In this part of the analysis, we correlated the LC mean of the 25 BCI therapy sessions against the mean of the results from motor tests collected in the Pre2 and Post1 assessment visits. The Shapiro–Wilk Test shows that the data are likely not normally distributed at alpha level. The Spearman test has been used for the correlation analysis. **Table 5** shows the correlation's results of LC against the functional scales.

Alpha Band

The LC calculated during the MI task with the healthy hand (LChα) is the parameter that shows the highest correlation with functional scales. In general terms, the results show that LC values near 0 are related to better functionality and less tremor in the paretic upper extremity (see **Figure 7**).

Tremor of the paretic hand assessed by FTRS shows a significant correlation with the LChα. The correlation coefficient is positive ($\rho = 0.450$ and $P = 0.008$). Thus, low degrees of tremor are related to LChα values near to 0.

In the BBT of the paretic hand, there is a stable correlation with all the LC parameters and bands. Here, the LChα shows a correlation but with a negative sign. The correlation is strong ($\rho = -0.616$ and $P < 0.001$). This correlation shows that good scores in the grasp ability, as assessed by BBT, are related to low values of LChα.

TABLE 5 | Significant correlations between LC and functional scales using Spearman Correlation are colored red.

Scale		Laterality Coefficient							
		α				β			
		LC_h		LC_p		LC_h		LC_p	
Name	Side	ρ	*P*	ρ	*P*	ρ	*P*	ρ	*P*
BI	–	−0.260	0.138	0.058	0.743	−0.154	0.383	0.184	0.296
FTRS	Healthy	−0.038	0.829	0.105	0.555	−0.093	0.600	0.060	0.734
	Paretic	0.450	0.008	−0.245	0.162	0.336	0.052	−0.490	0.003
MAS	Wrist	0.076	0.670	−0.216	0.220	−0.116	0.514	0.034	0.848
	Fingers	0.237	0.176	−0.262	0.134	0.109	0.539	−0.099	0.579
BBT	Healthy	0.102	0.566	−0.154	0.386	0.059	0.741	−0.141	0.425
	Paretic	−0.616	<0.001	0.354	0.043	−0.418	0.016	0.569	0.001
9HPT	Healthy	−0.042	0.813	0.036	0.839	−0.167	0.345	0.186	0.291
	Paretic	0.536	0.236	−0.357	0.444	0.714	0.088	−0.607	0.167
TPDT	Thumb *H*	−0.169	0.340	0.031	0.862	0.038	0.830	−0.005	0.979
	Index *H*	−0.010	0.956	0.041	0.820	−0.053	0.765	0.157	0.374
	Thumb *P*	0.000	0.999	−0.067	0.746	−0.139	0.499	0.152	0.459
	Index *P*	0.065	0.751	−0.079	0.701	−0.082	0.689	−0.125	0.543
FMAue	–	−0.706	<0.001	0.400	0.019	−0.440	0.009	0.384	0.025
FMAle	–	−0.601	0.006	0.271	0.261	−0.252	0.298	−0.057	0.817
SRQ	Pain	0.287	0.100	−0.157	0.374	0.095	0.591	−0.115	0.518
	Function	−0.427	0.012	0.316	0.069	−0.488	0.003	0.447	0.008
	Memory	−0.068	0.704	−0.130	0.465	−0.226	0.198	−0.033	0.855
	Mobility	−0.216	0.219	−0.034	0.849	−0.150	0.396	0.033	0.855
	Recovery	0.065	0.717	−0.205	0.245	0.083	0.642	0.061	0.732
MOCA	–	0.005	0.982	−0.032	0.884	−0.232	0.288	0.043	0.847

Also, the LChα parameter showed significant correlations with the FMA upper and lower extremity. The FMAue correlation has a stronger correlation coefficient ($\rho = -0.706$ and $P < 0.001$) than the FMAle ($\rho = -0.601$ and $P = 0.006$). The correlation coefficient is negative in both cases, and these results are consistent with the other relationships explained above – better motor function in the lower and upper extremity, as assessed by FMA, is related to LChα values near to 0.

Finally, the LChα is also correlated with the function score of the SRQ ($\rho = -0.427$ and $P = 0.0212$). The function score of SRQ is based on the subjective opinion of the patient doing different motor tasks. The negative correlation shows that good scores in the function score of SRQ are related to low values of LChα.

Other similar correlations with opposite signs have been found for the LCpα. In this case, LCp values near to 0 are related to better performance in the FMAue score ($\rho = 0.400$ and $P = 0.019$) and also in the BBT of the paretic hand ($\rho = 0.354$ and $P = 0.043$).

Beta Band

LChβ and LCpβ also presented some interesting correlations with the functional scales. In general, the correlations found in this frequency band are weaker than the correlations found in the alpha band. The low tremor degree in the paretic hand assessed by FTRS (higher scores in this scale) is correlated with values near to 0 in LCpβ ($\rho = -0.490$ and $P = 0.003$). The good grasp ability in the paretic hand, assessed by BBT (BBT_p), is also correlated with low values of LChβ ($\rho = -0.418$ and $P = 0.016$) and values near 0 in LCpβ ($\rho = 0.569$ and $P = 0.001$). The general motor function of the upper extremity, assessed by FMA, is also correlated with LChβ ($\rho = -0.440$ and $P = 0.009$), and with LCpβ ($\rho = 0.384$ and $P = 0.025$).

Finally, the last significant correlation is between the function scale part of SRQ and LChβ ($\rho = -0.488$ and $P = 0.003$) and LCpβ ($\rho = 0.447$ and $P = 0.008$). Again, the best functionality is related to values near to 0 of both LC parameters. All correlation results regarding the LC and functional scales can be seen in **Table 5**.

Assessment Tests Before and After BCI Treatment

The results in this section summarize differences from the Pre2 to Post1 assessments across different tests. We used the Wilcoxon signed rank test for statistical analysis, since the data did not present a normal distribution (see **Table 6**). The improvement of each scale is presented using the median and IQR, and the mean and SD are also provided if differences are significant.

Fugl-Meyer Assessment

The FMAue test has a score range of 0–66. One of the 34 patients had only slight hemiparesis and attained the maximum FMAue score in the pre-assessment. The Wilcoxon signed rank test shows that there is a significant improvement in FMAue after the therapy (ΔFMAue = 1 [0–8], $P = 0.002$). The mean

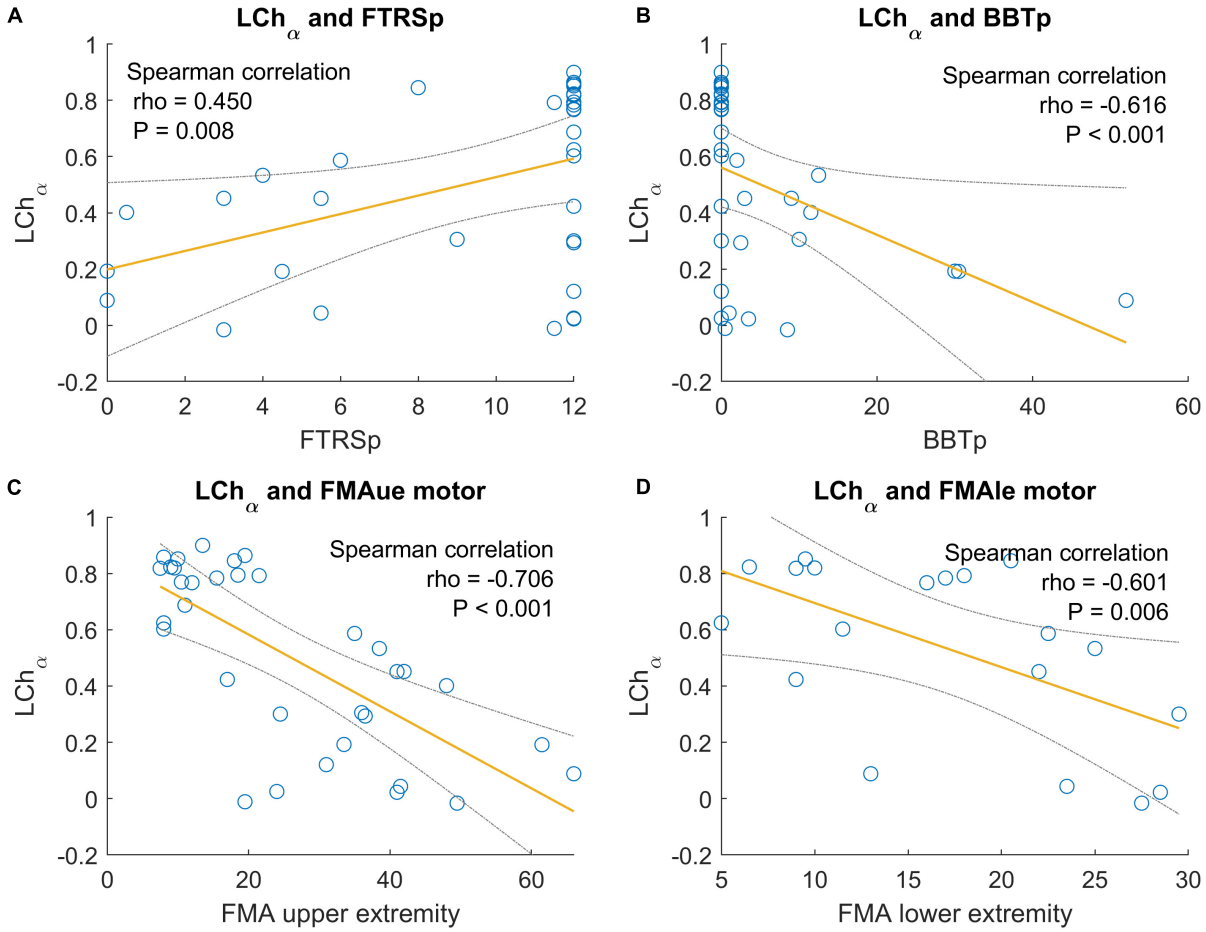

FIGURE 7 | Significant correlations between LC of the paretic hand in alpha band and functional scales. The gray lines are the confidence interval at 95%. **(A)** Correlation between LChα and BBT of the paretic hand. **(B)** Correlation between LChα and FTRS of the paretic hand. **(C)** Correlation between LChα and FMAue of the motor part. **(D)** Correlation between LChα and FMAle of the motor part.

improvement is 3.12 (*SD* = 5.1). Twenty one patients (61.8%) improved at least 1 point in the FMA score. Among patients who improved, the mean improvement was 5.76 points (*SD* = 4.61). Six patients (17.7%) decreased at least 1 point in FMA score, and the mean decrease in this group was −2.5 points (*SD* = 1.76). The remaining 6 patients (17.7%) had an improvement equal to 0.

Barthel Index

The BI did not show significant improvements after the therapy (ΔBI = 0 [0–5], *P* = 0.480). The BI score decreased in 7 patients (20.6%), 11 patients (32.4%) reported positive changes in the BI after the therapy, and 16 patients (47.1%) did not show changes in this parameter.

Fahn Tremor Rating Scale

The FTRS for the healthy hand (FTRS_h) did not show a significant difference before versus after the BCI therapy (ΔFTRS_h = 0 [0–0], *P* = 0.984). The FTRS in the paretic hand (FTRS_p) did show a significant improvement (ΔFTRS_p = 0 [−1-0], *P* = 0.018). The mean improvement of FTRS_p is −0.65 (*SD* = 1.5). Thirty two of the 34 patients (94.1%) reported some degree of tremor in the paretic hand (FTRS_p) before the therapy. After the therapy, 10 of these 32 patients (31.3%) exhibited a decreased tremor in the paretic hand. One of these 32 patients (3.1%) showed an increase of tremor after the therapy. The other patients did not report any changes.

Modified Ashworth Scale

The MAS scale showed a statistical reduction of the spasticity in the wrist [ΔMAS_w = 0 [-1-0], *P* = 0.003, mean improvement −0.37 (*SD* = 0.69)], and in the fingers [ΔMAS_f = 0 [-1-0], *P* = 0.001, mean improvement −0.41 (*SD* = 0.63)]. Twenty three of the 34 patients (67.7%) reported some spasticity in the wrist (MAS > 0), and 25 patients (73.5%) reported some spasticity in the fingers. Twelve of the 23 patients (52.2%) who reported wrist spasticity prior to therapy reported a decrease after therapy. Fourteen of the 25 patients (56.0%) who reported finger spasticity prior to therapy reported a decrease after therapy.

Box and Block Test

We observed a statistical improvement of BBT in the healthy hand [ΔBBT_h = 2 [1–8] and *P* = 0.005, mean improvement 3.64

TABLE 6 | Changes in the functional scales.

Scale	SWT		Pre	Post	Δ		P
	H	P	Median [IQR]	Median [IQR]	Median [IQR]	Mean (SD)	
BI	1	0.001	85 [70–95]	85 [65–100]	0 [0-5]	0.29 (6.15)	0.480
FTRS_h	1	<0.001	0 [0–0]	0 [0–0]	0 [0-0]	−0.03 (0.83)	0.984
FTRS_p	1	<0.001	12 [7–12]	12 [4–12]	0 [-1-0]	−0.65 (1.52)	0.018
MAS_w	1	<0.001	1.25 [0–3]	1 [0–2]	0 [-1-0]	−0.37 (0.69)	0.003
MAS_f	1	0.001	2 [0–3]	1 [0–2]	0 [-1-0]	−0.41 (0.63)	0.001
BBT_h	0	0.346	54 [44–68.75]	54.5 [47–73]	2 [1-8]	3.64 (7.4)	0.005
BBT_p	1	<0.001	0 [0–3.5]	0 [0–4.25]	0 [0-1]	1.22 (3.5)	0.034
9HPT_h	1	<0.001	23 [18.75–27.25]	23 [20–26]	−1 [-2-2]	−1.06 (4.6)	0.325
9HPT_p	1	0.046	164 [76–346.25]	135.5 [93–324]	−24.5 [-70-2]	−34 (45.35)	0.375
TPDT_h_t	1	<0.001	3 [2–4]	3 [2–4]	0 [-0.75-1]	0.06 (1.34)	0.720
TPDT_h_i	1	0.001	3 [3–4]	3 [3–4]	0 [-1-0.5]	−0.09 (1)	0.667
TPDT_p_t	0	0.127	4 [3–5]	4 [3–5]	0 [-1.25-1]	−0.08 (1.75)	0.888
TPDT_p_i	1	0.001	3 [3–4.5]	4 [3–4.75]	1 [-0.25-1]	0.46 (1.66)	0.324
FMAue_m	1	0.003	19 [10–37]	23 [12–41]	1 [0-8]	3.12 (5.06)	0.002
FMAle_m	0	0.443	17 [9.75–24.25]	19 [9–25]	−0.5 [-2-2.5]	0.56 (4.1)	0.856
Pain	0	0.275	25 [16–37]	21 [15.5–36.5]	−2 [-7.5-6]	−3.75 (11.93)	0.285
Function	1	<0.001	3 [0–12]	6 [0–12]	0 [0-4]	−3.46 (16.71)	0.444
Memory	1	0.003	55 [39.75–70]	59 [43.5–68]	0 [-3-6.5]	1.63 (12.89)	0.614
Mobility	1	0.023	67 [35–79]	70.5 [43.5–81.5]	5 [-3-10.5]	5.93 (17.54)	0.056
Recovery	0	0.174	5 [4–8]	6 [5–7]	0 [-2-3]	0.6 (2.91)	0.311
MOCA_Total	1	0.043	24.5 [17–27]	26 [21–27.75]	2.5 [0-6]	2.71 (3.29)	0.012

The first column shows the results of the Shapiro–Wilk Test (SWT), to assess the normality of the dependent variable. The last column (P) presents the probability results of the paired test, with statistically significant differences colored red.

(*SD* = 7.4)]. The changes in the paretic hand are also significant [ΔBBT_p = 0 [0–1] and *P* = 0.034, mean improvement 1.22 (*SD* = 3.5)]. Ten patients (29.4%) improved the BBT score with the paretic hand, 2 patients (5.89%) decreased the BBT score with the paretic hand, and 22 patients (64.7%) did not change from the initial BBT score. In three cases (8.8%), it was impossible to perform the BBT before the therapy due to the severity of the motor impairment, but after the therapy, these patients could move at least 1 block in the BBT.

9HPT

The 9HPT in the paretic hand is one of the most commonly used tests of grasp function. Only five patients (14.7%) could perform the test before the therapy, and six patients (20.6%) could perform this test after the treatment. No significant improvements were observed after the therapy in the healthy hand (Δ9HPT_h = −1 [-2-2], *P* = 0.325), or in the paretic hand (Δ9HPT_p = −24.5 [-70-2], *P* = 0.375). The results show that the time in the healthy hand has slightly decreased, and in the affected hand the decrease in time was great.

Two Point Discrimination Test

This test did not show significant changes before vs. after the therapy in the thumb or index of the healthy hand (ΔTPDT_h_t = 0 [-0.75-1], *P* = 0.720; ΔTPDT_h_i = 0 [-1-0.5], *P* = 0.667). The paretic hand did not show a significant improvement either (ΔTPDT_p_t = 0 [-1.25-1], *P* = 0.888; ΔTPDT_p_i = 1 [-0.25-1], *P* = 0.324). Eight patients (23.5%) improved the discrimination between two points in the healthy thumb by at least 1 mm, and nine patients (26.5%) improved in the healthy index finger. Six patients (17.7%) improved in the TPDT at least by 1 mm in the paretic thumb, and three patients (8.8%) reported at least 1 mm of improvement in the paretic index.

SRQ

Sixteen patients (47.1%) reported at least 1 point of pain reduction, and 11 patients (32.4%) reported at least 1 point of pain increase. Thirteen patients (38.2%) reported an improvement in the ability to perform ADLs, and six patients (17.7%) reported a decrease in ADL performance. Eleven patients (32.4%) reported an improvement in the memory part, and 11 patients (32.4%) reported a decrease in memory. Sixteen patients (47.1%) reported an improvement in the mobility part of the questionnaire, while 11 patients (32.4%) reported a decrease in mobility. Finally, 12 patients (35.3%) reported a better general recovery after BCI therapy, and 10 patients (29.4%) reported a worse recovery after BCI therapy. There are no significant changes in any part of SRQ (ΔPain = −2 [-7.5-6], *P* = 0.285; ΔFunction = 0 [0-4], *P* = 0.444; ΔMemory = 0 [-3-6.5], *P* = 0.614; ΔMobility = 5 [-3-10.5], *P* = 0.056; ΔRecovery = 0 [-2-3], *P* = 0.311).

MOCA

The comparison between before and after the therapy showed a significant improvement in cognitive function, ΔMOCA = 2.5 [0-6], *P* = 0.012, with a mean improvement of 2.71 (*SD* = 3.29). Ten patients (29.4%) improved by at least one point after therapy, and the MOCA score decreased in two patients (5.9%). The remaining patients reported no change.

DISCUSSION

The objective of this experiment was to explore how two EEG-based parameters relate to different facets of stroke diagnosis and functional prognosis during BCI-based stroke rehabilitation therapy. The BSI was derived from EEG data recorded during the assessment visits in the resting state, while the LC was based on EEG data recorded during MI exercises.

BSI, Age, and Gender

The analysis of the BSI in healthy subjects based on age suggests that this parameter does not change with age. However, this issue needs to be further explored in larger studies. The results show significant difference in BSI based on gender; males usually have higher BSI values than females. These results could help our understanding of the BSI parameter in healthy conditions, improve detection of pathological values correlated with different brain affectations that can help with diagnosis of stroke and other conditions, and support further research involving gender differences.

BSI and Stroke Diagnoses

Stroke patients were divided into three different groups based on stroke location; Cortical, Subcortical and Cortical + Subcortical. The Cortical group was the smallest group with only five patients and exhibited the highest BSI variability. Prior work found similar results, with an almost identical boxplot distribution but a smaller sample size (Agius Anastasi et al., 2017). Our results show that healthy participants had significantly lower BSI values than stroke patients of the Subcortical group ($P = 0.001$) and the Cortex + Subcortex group ($P = 0.019$); see **Table 4** and **Figure 5**. The high variability in the Cortical group may be due to small size of this subgroup. Moreover, in these patients the location of the lesion is very peripheral, and most of the neural activity observable via EEG originates from the cortex; consequently, the aberrant neural activity is more apparent in these patients than in the ones with other stroke locations.

Hence, despite the high variability in the Cortical group, the BSI parameter did differ significantly between the healthy control vs. stroke groups Subcortical and Cortex + Subcortex. Results were consistent with prior work (Agius Anastasi et al., 2017). With further research, the BSI could become a tool to support stroke diagnosis, including stroke location and severity.

BSI and Functional Impairment

We also analyzed the correlations between the values of BSI and the patient's functional state (**Figure 6**). The most noteworthy correlations observed showed that patients with lowest BSI have better motor function in the upper extremities (FMAue). The correlation between BSI and FMAue was also observed in prior studies; lower BSI values were correlated with higher functionality in the upper extremity (Agius Anastasi et al., 2017). Thus, the BSI could be a useful parameter to assess functional impairment during stroke assessment and rehabilitation.

LC in Alpha Band

We calculated the LC using the event-related synchronization and desynchronization patterns generated during the MI task (Kaiser et al., 2012). The LC is derived in a similar manner as the BSI, but the LC yields results from −1 to 1. We calculated the LC in two frequency bands, 8–13 Hz (α band, mu frequency rhythm) and 13–30 Hz (β band) and found the most relevant results in the alpha band. In general, LC values calculated during the MI tasks with the healthy hand (LCh) were between 0 and 1, while LC values of the paretic hand MI tasks (LCp) were between −1 and 0. The LCh in alpha band presented numerous significant correlations with functional scales. We also observed most of these significant correlations with the LCp parameter, but with the opposite sign.

The LC values for the healthy hand presented noteworthy correlations with four dependent variables. LCh values near 0 were related with a higher BBT score in the paretic hand, which indicates better grasp function ($\rho = -0.616$ and $P < 0.001$). The LCh was also significantly correlated with tremor, assessed by FTRS. Participants with LCh values near 1 tended to have a higher FTRS score (reflecting greater tremor) in the paretic hand ($\rho = 0.450$ and $P = 0.008$). Finally, the LCh parameter was significantly correlated with the FMAue and FMAle. LCh values closer to 0 reflect better motor functionality for the upper extremity (FMAue, $\rho = -0.706$ and $P < 0.001$) and for the lower extremity (FMAle, $\rho = -0.601$ and $P = 0.006$).

The correlations between the LCp and the functional scales are less common than the LCh. This could occur because the affected hemisphere does not present a normal activation pattern due the stroke, but the healthy hemisphere maintains the normal patterns of desynchronization during the ipsilateral motor movements (originated in the affected hemisphere). The ERD/ERS patterns observed in the healthy hemisphere should be more stable than the ERD/ERS patterns observed in the affected side of the brain.

LC in Beta Band

The LC calculated in the β band showed similar correlations (see **Table 5**). Interestingly, LCβ shows significant correlations with the scales where more mental concentration is required (FTRS and BBT). In both scales, values near 0 in LCβ (healthy and paretic) are correlated with better grasp ability and less tremor. Other studies showed correlations between the EEG activity in beta band and concentration (Janssen et al., 2017; Kiiski et al., 2020).

Clinical Improvements Before vs. After BCI Therapy

The main objective of the study was not to demonstrate the efficacy of the BCI system in neurorehabilitation, nor to compare BCI-based therapy to other forms of therapy. The relationship between BCI stroke therapy and functional outcomes has been addressed in numerous studies (Ramos-Murguialday et al., 2013; Pichiorri et al., 2015; Remsik et al., 2016; Biasiucci et al., 2018;

Cho et al., 2018). However, we would like to add to the existing literature by discussing our observations.

FMAue was the primary measure of motor function in this study. When assessing the motor function of the upper extremity by FMAue, we found the most important significant clinical improvement (ΔFMAue = 1 [0-8] and $P = 0.002$). On average, the stroke patients improved by 3.21 points ($SD = 5.1$) in the FMAue with the BCI therapy. After the therapy, the patients also presented a significant reduction in tremor (FTRS), spasticity (MAS), and increase on the grasp ability (BBT) and in the cognitive state (MOCA).

In general, the first sign that patients reported during the therapy was a reduction in spasticity, followed with improvement in motor function. The reduced spasticity may drive the improved range of motion and reduced tremor, something that can explain the improvements on FTRS, BBT and FMAue.

The MOCA scale also showed significant improvement, which may be related to the need for concentration during the BCI sessions in order to get positive feedback. The patients have to learn to maintain concentration during the sessions to improve their motor skills using BCI.

GENERAL DISCUSSION

The BSI parameter can be calculated in real-time using portable and practical EEG tools, and thus could be used during stroke diagnosis or ongoing monitoring of patients' brain activity during stroke rehabilitation and recovery. More broadly, the BSI and LC parameters might contribute to other neurological assessments and ongoing monitoring of brain damage and recovery.

One limitation of this study is the absence of a healthy group that performed the same BCI training as the patient group, which prevents us from comparing LC between these groups. The study may also be limited by the unequal numbers of participants across the three stroke subgroups, and additional work is needed to identify any age differences between the control and stroke groups. Overcoming these limitations will require substantial additional work with more participants in a larger study, which we are currently exploring. Additionally, a great number of hypotheses tests were carried out in the present study. Therefore, results referred to as "statistically significant" may have been obtained by chance and we strongly recommend considering the obtained *p*-values and effect sizes when interpreting the results of this study.

In addition to broader work with more participants, future research could: explore variants of the different measures that we used that might be more informative; identify correlations with other types of diagnoses and therapies relating to motor (and perhaps other) impairment and recovery; evaluate these and other parameters in tandem with other methods to treat stroke, such as medications or non-invasive brain stimulation; measure long-term changes via longitudinal follow-up assessments; and compare the utility of these measures to other tools.

DATA AVAILABILITY STATEMENT

The datasets for this manuscript are not publicly available because: Patients' data need to be treated according to current data protection laws and ethical guidelines. Requests to access the datasets should be directed to MS-R, sebastian@gtec.at.

ETHICS STATEMENT

The studies involving human participants were reviewed and approved by Ethikkommission des Landes Oberösterreich. The patients/participants provided their written informed consent to participate in this study.

AUTHOR CONTRIBUTIONS

MS-R participated in the data acquisition, performed the analysis, and did the main contribution to the manuscript writing. EU supervised the data analysis and assisted in the manuscript preparation. RO supervised the whole process, data acquisition, analysis, and manuscript revision. JD-F supervised the signal processing methods. NM participated to the data acquisition from stroke participants. CM-P did the acquisition of healthy subjects. SS participated in the data analysis. BA provided scientific input and contributed to the manuscript writing. CG supervised the whole project and reviewed the manuscript. WC contributed to the data analysis.

FUNDING

We appreciate the collaboration of the Government of Catalonia that partially supported this study with the Industrial Doctorates Plan (2017/DI/065). This study was also supported by the EEG-DDS project (E! 12274 – EUROSTARS), the SeizureAI project (E! 12946 – EUROSTARS), and MSCA-RISE grant Pro-Gait (No. 778043).

SUPPLEMENTARY MATERIAL

The Supplementary Material for this article can be found online at: https://www.frontiersin.org/articles/10.3389/fnins.2020.00582/full#supplementary-material

REFERENCES

Agius Anastasi, A., Falzon, O., Camilleri, K., Vella, M., and Muscat, R. (2017). Brain symmetry index in healthy and stroke patients for assessment and prognosis. *Stroke Res. Treat.* 2017, 1–9. doi: 10.1155/2017/8276136

Bender, R., and Lange, S. (2001). Adjusting for multiple testing—when and how? *J. Clin. Epidemiol.* 54, 343–349. doi: 10.1016/S0895-4356(00)00314-0

Biasiucci, A., Leeb, R., Iturrate, I., Perdikis, S., Al-Khodairy, A., Corbet, T., et al. (2018). Brain-actuated functional electrical stimulation elicits lasting arm motor recovery after stroke. *Nat. Commun.* 9:2421. doi: 10.1038/s41467-018-04673-z

Carlson, T., and del, R. M. J. (2013). Brain-controlled wheelchairs: a robotic architecture. *IEEE Robot. Autom. Mag.* 20, 65–73. doi: 10.1109/MRA.2012.2229936

Cervera, M. A., Soekadar, S. R., Ushiba, J., del, R. M. J., Liu, M., Birbaumer, N., et al. (2018). Brain-computer interfaces for post-stroke motor rehabilitation: a meta-analysis. *Ann. Clin. Transl. Neurol.* 5, 651–663. doi: 10.1002/acn3.544

Cho, W., Guger, C., Heilinger, A., Ortner, R., Murovec, N., Xu, R., et al. (2018). "Motor rehabilitation for hemiparetic stroke patients using a brain-computer interface method," in *Proceedings of the 2018 IEEE International Conference on Systems, Man, and Cybernetics (SMC)*, (Piscataway, NJ: IEEE), 1001–1005. doi: 10.1109/SMC.2018.00178

Cho, W., Sabathiel, N., Ortner, R., Lechner, A., Irimia, D. C., Allison, B. Z., et al. (2016). Paired associative stimulation using brain-computer interfaces for stroke rehabilitation: a pilot study. *Eur. J. Transl. Myol.* 26:6132. doi: 10.4081/ejtm.2016.6132

Dobkin, B. H. (2007). Brain-computer interface technology as a tool to augment plasticity and outcomes for neurological rehabilitation. *J. Physiol.* 579, 637–642. doi: 10.1113/jphysiol.2006.123067

Faust, O., Acharya, U. R., Adeli, H., and Adeli, A. (2015). Wavelet-based EEG processing for computer-aided seizure detection and epilepsy diagnosis. *Seizure* 26, 56–64. doi: 10.1016/j.seizure.2015.01.012

Foreman, B., and Claassen, J. (2012). Quantitative EEG for the detection of brain ischemia. *Crit. Care* 16:216. doi: 10.1186/cc11230

Gladstone, D. J., Danells, C. J., and Black, S. E. (2002). The Fugl-meyer assessment of motor recovery after stroke: a critical review of its measurement properties. *Neurorehabil. Neural Repair* 16, 232–240. doi: 10.1177/154596802401105171

Graimann, B., Huggins, J., Levine, S., and Pfurtscheller, G. (2002). Visualization of significant ERD/ERS patterns in multichannel EEG and ECoG data. *Clin. Neurophysiol.* 113, 43–47. doi: 10.1016/S1388-2457(01)00697-6

Hurlbert, S. H., and Lombardi, C. M. (2012). Lopsided reasoning on lopsided tests and multiple comparisons. *Aust. New Zeal. J. Stat.* 54, 23–42. doi: 10.1111/j.1467-842X.2012.00652.x

Ikkai, A., Dandekar, S., and Curtis, C. E. (2016). Lateralization in Alpha-band oscillations predicts the locus and spatial distribution of attention. *PLoS One* 11:e0154796. doi: 10.1371/journal.pone.0154796

Irimia, D., Sabathiel, N., Ortner, R., Poboroniuc, M., Coon, W., Allison, B. Z., et al. (2016). "recoveriX: a new BCI-based technology for persons with stroke," in *Proceedings of the 2016 38th Annual International Conference of the IEEE Engineering in Medicine and Biology Society (EMBC*, (Piscataway, NJ: IEEE), 1504–1507. doi: 10.1109/EMBC.2016.7590995

Irimia, D. C., Cho, W., Ortner, R., Allison, B. Z., Ignat, B. E., Edlinger, G., et al. (2017). Brain-computer interfaces with multi-sensory feedback for stroke rehabilitation: a case study. *Artif. Organs* 41, E178–E184. doi: 10.1111/aor.13054

Irimia, D. C., Ortner, R., Poboroniuc, M. S., Ignat, B. E., and Guger, C. (2018). High classification accuracy of a motor imagery based brain-computer interface for stroke rehabilitation training. *Front. Robot. AI* 5. doi: 10.3389/frobt.2018.00130

Janssen, T. W. P., Hillebrand, A., Gouw, A., Geladé, K., Van Mourik, R., Maras, A., et al. (2017). Neural network topology in ADHD; evidence for maturational delay and default-mode network alterations. *Clin. Neurophysiol.* 128, 2258–2267. doi: 10.1016/j.clinph.2017.09.004

Jeong, D. H., Kim, Y., Do Song, I. U., Chung, Y. A., and Jeong, J. (2016). Wavelet energy and wavelet coherence as eeg biomarkers for the diagnosis of Parkinson's disease-related dementia and Alzheimer's disease. *Entropy* 18:8. doi: 10.3390/e18010008

Kaiser, V., Daly, I., Pichiorri, F., Mattia, D., Müller-Putz, G. R., and Neuper, C. (2012). Relationship between electrical brain responses to motor imagery and motor impairment in stroke. *Stroke* 43, 2735–2740. doi: 10.1161/STROKEAHA.112.665489

Kanda, P. A., de, M., Anghinah, R., Smidth, M. T., and Silva, J. M. (2009). The clinical use of quantitative EEG in cognitive disorders. *Dement. Neuropsychol.* 3, 195–203. doi: 10.1590/S1980-57642009DN30300004

Kiiski, H., Rueda-Delgado, L. M., Bennett, M., Knight, R., Rai, L., Roddy, D., et al. (2020). Functional EEG connectivity is a neuromarker for adult attention deficit hyperactivity disorder symptoms. *Clin. Neurophysiol.* 131, 330–342. doi: 10.1016/j.clinph.2019.08.010

Kim, J., Thayabaranathan, T., Donnan, G. A., Howard, G., Howard, V. J., Rothwell, P. M., et al. (2020). Global Stroke Statistics 2019. *Int. J. Stroke* 139:174749302090954. doi: 10.1177/1747493020909545

Kohr, R. L., and Games, P. A. (1974). Robustness of the analysis of variance, the welch procedure and a box procedure to heterogeneous variances. *J. Exp. Educ.* 43, 61–69. doi: 10.1080/00220973.1974.10806305

Krauss, P., Metzner, C., Schilling, A., Tziridis, K., Traxdorf, M., Wollbrink, A., et al. (2018). A statistical method for analyzing and comparing spatiotemporal cortical activation patterns. *Sci. Rep.* 8:5433. doi: 10.1038/s41598-018-23765-w

Leon-Carrion, J., Martin-Rodriguez, J. F., Damas-Lopez, J., Barroso y Martin, J. M., and Dominguez-Morales, M. R. (2009). Delta–alpha ratio correlates with level of recovery after neurorehabilitation in patients with acquired brain injury. *Clin. Neurophysiol.* 120, 1039–1045. doi: 10.1016/j.clinph.2009.01.021

Mäkelä, J. P., Lioumis, P., Laaksonen, K., Forss, N., Tatlisumak, T., Kaste, M., et al. (2015). Cortical excitability measured with nTMS and MEG during Stroke recovery. *Neural Plast.* 2015, 1–8. doi: 10.1155/2015/309546

McFarland, D. J., and Wolpaw, J. R. (2017). EEG-based brain–computer interfaces. *Curr. Opin. Biomed. Eng.* 4, 194–200. doi: 10.1016/j.cobme.2017.11.004

Muniz, C. F., Shenoy, A. V., O'Connor, K. L., Bechek, S. C., Boyle, E. J., Guanci, M. M., et al. (2016). Clinical development and implementation of an institutional guideline for prospective EEG monitoring and reporting of delayed cerebral ischemia. *J. Clin. Neurophysiol.* 33, 217–226. doi: 10.1097/WNP.0000000000000281

Neuper, C., Wörtz, M., and Pfurtscheller, G. (2006). "ERD/ERS patterns reflecting sensorimotor activation and deactivation," in *Progress in Brain Research*, eds S. Waxman, D. G. Stein, D. Swaab, and H. Fields, (Amsterdam: Elsevier), 211–222. doi: 10.1016/S0079-6123(06)59014-4

Nishida, K., Yoshimura, M., Isotani, T., Yoshida, T., Kitaura, Y., Saito, A., et al. (2011). Differences in quantitative EEG between frontotemporal dementia and Alzheimer's disease as revealed by LORETA. *Clin. Neurophysiol.* 122, 1718–1725. doi: 10.1016/j.clinph.2011.02.011

Pfurtscheller, G., and Aranibar, A. (1979). Evaluation of event-related desynchronization (ERD) preceding and following voluntary self-paced movement. *Electroencephalogr. Clin. Neurophysiol.* 46, 138–146. doi: 10.1016/0013-4694(79)90063-4

Piano, C., Mazzucchi, E., Bentivoglio, A. R., Losurdo, A., Calandra Buonaura, G., Imperatori, C., et al. (2017). Wake and sleep EEG in patients with Huntington disease. *Clin. EEG Neurosci.* 48, 60–71. doi: 10.1177/1550059416632413

Pichiorri, F., Morone, G., Petti, M., Toppi, J., Pisotta, I., Molinari, M., et al. (2015). Brain-computer interface boosts motor imagery practice during stroke recovery. *Ann. Neurol.* 77, 851–865. doi: 10.1002/ana.24390

Prabhakaran, S., Zarahn, E., Riley, C., Speizer, A., Chong, J. Y., Lazar, R. M., et al. (2008). Inter-individual variability in the capacity for motor recovery after ischemic stroke. *Neurorehabil. Neural Repair* 22, 64–71. doi: 10.1177/1545968307305302

Rabiller, G., He, J. W., Nishijima, Y., Wong, A., and Liu, J. (2015). Perturbation of brain oscillations after Ischemic stroke: a potential biomarker for post-stroke function and therapy. *Int. J. Mol. Sci.* 16, 25605–25640. doi: 10.3390/ijms161025605

Ramos-Murguialday, A., Broetz, D., Rea, M., Läer, L., Yilmaz, Ö, Brasil, F. L., et al. (2013). Brain-machine interface in chronic stroke rehabilitation: a controlled study. *Ann. Neurol.* 74, 100–108. doi: 10.1002/ana.23879

Remsik, A., Young, B., Vermilyea, R., Kiekhoefer, L., Abrams, J., Evander Elmore, S., et al. (2016). A review of the progression and future implications of brain-computer interface therapies for restoration of distal upper extremity motor function after stroke. *Expert Rev. Med. Devices* 13, 445–454. doi: 10.1080/17434440.2016.1174572

Shokur, S., Donati, A. R. C., Campos, D. S. F., Gitti, C., Bao, G., Fischer, D., et al. (2018). Training with brain-machine interfaces, visuo-tactile feedback and assisted locomotion improves sensorimotor, visceral, and psychological signs in chronic paraplegic patients. *PLoS One* 13:e0206464. doi: 10.1371/journal.pone.0206464

Tomarken, A. J., and Serlin, R. C. (1986). Comparison of ANOVA alternatives under variance heterogeneity and specific noncentrality structures. *Psychol. Bull.* 99, 90–99. doi: 10.1037/0033-2909.99.1.90

van Putten, M. J. A. M. (2006). Extended BSI for continuous EEG monitoring in carotid endarterectomy. *Clin. Neurophysiol.* 117, 2661–2666. doi: 10.1016/j.clinph.2006.08.007

van Putten, M. J. A. M. (2007). The revised brain symmetry index. *Clin. Neurophysiol.* 118, 2362–2367. doi: 10.1016/j.clinph.2007.07.019

van Putten, M. J. A. M., Peters, J. M., Mulder, S. M., de Haas, J. A. M., Bruijninckx, C., and Tavy, D. L. J. (2004). A brain symmetry index (BSI) for online EEG monitoring in carotid endarterectomy. *Clin. Neurophysiol.* 115, 1189–1194. doi: 10.1016/j.clinph.2003.12.002

Wang, J., Barstein, J., Ethridge, L. E., Mosconi, M. W., Takarae, Y., and Sweeney, J. A. (2013). Resting state EEG abnormalities in autism spectrum disorders. *J. Neurodev. Disord.* 5:24. doi: 10.1186/1866-1955-5-24

Wolpaw, J. R. (2007). Brain-computer interfaces as new brain output pathways. *J. Physiol.* 579, 613–619. doi: 10.1113/jphysiol.2006.125948

Woytowicz, E. J., Rietschel, J. C., Goodman, R. N., Conroy, S. S., Sorkin, J. D., Whitall, J., et al. (2017). Determining levels of upper extremity movement impairment by applying a cluster analysis to the Fugl-Meyer assessment of the upper extremity in chronic stroke. *Arch. Phys. Med. Rehabil.* 98, 456–462. doi: 10.1016/j.apmr.2016.06.023

Wu, J., Srinivasan, R., Burke Quinlan, E., Solodkin, A., Small, S. L., and Cramer, S. C. (2016). Utility of EEG measures of brain function in patients with acute stroke. *J. Neurophysiol.* 115, 2399–2405. doi: 10.1152/jn.00978.2015

Conflict of Interest: MS-R, RO, JD-F, CM-P, and CG are employed at g.tec medical engineering Spain SL and CG is CEO of g.tec medical engineering Spain SL and g.tec medical engineering GmbH. This study was conducted primarily as a component of a Ph.D. program, and our motivation for conducting the study to explore different methods was entirely scientific. However, the described algorithms may be commercialized by g.tec medical engineering GmbH in the future.

The remaining authors declare that the research was conducted in the absence of any commercial or financial relationships that could be construed as a potential conflict of interest.

frontiers in Neuroscience

REVIEW
published: 09 July 2020
doi: 10.3389/fnins.2020.00724

Functional Near-Infrared Spectroscopy and Its Clinical Application in the Field of Neuroscience: Advances and Future Directions

*Wei-Liang Chen[1,2,3], Julie Wagner[4], Nicholas Heugel[4], Jeffrey Sugar[1], Yu-Wen Lee[1,2], Lisa Conant[1], Marsha Malloy[1,2], Joseph Heffernan[1], Brendan Quirk[1], Anthony Zinos[1,4], Scott A. Beardsley[1,4], Robert Prost[1] and Harry T. Whelan[1,2]**

[1] Department of Neurology, Medical College of Wisconsin, Milwaukee, WI, United States, [2] Department of Neurology, Children's Hospital of Wisconsin, Milwaukee, WI, United States, [3] School of Medicine, University of Washington, Seattle, WA, United States, [4] Department of Biochemical Engineering, Marquette University and Medical College of Wisconsin, Milwaukee, WI, United States

OPEN ACCESS

Edited by:
Ulrich G. Hofmann, Medical Center – University of Freiburg, Germany

Reviewed by:
Wei-Peng Teo, National Institute of Education, Nanyang Technological University, Singapore
Keum-Shik Hong, Pusan National University, South Korea

***Correspondence:**
Harry T. Whelan
hwhelan@mcw.edu

Specialty section:
This article was submitted to Neural Technology, a section of the journal Frontiers in Neuroscience

Received: 11 March 2020
Accepted: 17 June 2020
Published: 09 July 2020

Citation:
Chen W-L, Wagner J, Heugel N, Sugar J, Lee Y-W, Conant L, Malloy M, Heffernan J, Quirk B, Zinos A, Beardsley SA, Prost R and Whelan HT (2020) Functional Near-Infrared Spectroscopy and Its Clinical Application in the Field of Neuroscience: Advances and Future Directions. Front. Neurosci. 14:724. doi: 10.3389/fnins.2020.00724

Similar to functional magnetic resonance imaging (fMRI), functional near-infrared spectroscopy (fNIRS) detects the changes of hemoglobin species inside the brain, but via differences in optical absorption. Within the near-infrared spectrum, light can penetrate biological tissues and be absorbed by chromophores, such as oxyhemoglobin and deoxyhemoglobin. What makes fNIRS more advantageous is its portability and potential for long-term monitoring. This paper reviews the basic mechanisms of fNIRS and its current clinical applications, the limitations toward more widespread clinical usage of fNIRS, and current efforts to improve the temporal and spatial resolution of fNIRS toward robust clinical usage within subjects. Oligochannel fNIRS is adequate for estimating global cerebral function and it has become an important tool in the critical care setting for evaluating cerebral oxygenation and autoregulation in patients with stroke and traumatic brain injury. When it comes to a more sophisticated utilization, spatial and temporal resolution becomes critical. Multichannel NIRS has improved the spatial resolution of fNIRS for brain mapping in certain task modalities, such as language mapping. However, averaging and group analysis are currently required, limiting its clinical use for monitoring and real-time event detection in individual subjects. Advances in signal processing have moved fNIRS toward individual clinical use for detecting certain types of seizures, assessing autonomic function and cortical spreading depression. However, its lack of accuracy and precision has been the major obstacle toward more sophisticated clinical use of fNIRS. The use of high-density whole head optode arrays, precise sensor locations relative to the head, anatomical co-registration, short-distance channels, and multi-dimensional signal processing can be combined to improve the sensitivity of fNIRS and increase its use as a wide-spread clinical tool for the robust assessment of brain function.

Keywords: functional NIRS, near-infrared spectroscopy, functional MRI, cytochrome c oxidase, epilepsy, migraine, autonomic dysfunction, cerebral autoregulation

INTRODUCTION

Functional near-infrared spectroscopy (fNIRS) is a well-established non-invasive tool to continuously assess regional tissue oxygenation at bed-side. It was first described by Jöbsis 40 years ago (Jobsis, 1977) and has been utilized in different clinical settings, especially in the field of neuroscience (Obrig, 2014; Hong and Yaqub, 2019). The current review aims to discuss the mechanism of fNIRS, its advantages and limitations in detecting brain activity, the current status of fNIRS clinical applications, and the future directions for developing fNIRS into a more widespread clinical tool.

The brain is a high energy-demand organ and neuronal activation correlates with increases in cerebral blood flow and volume. This so-called "neurovascular" coupling is the fundament of many functional neuroimaging techniques, including fNIRS, functional magnetic resonance imaging (fMRI), positron emission tomography (PET) and single-photon emission computerized tomography (SPECT). By measuring changes in the light absorption of different hemoglobin species, temporal changes in cerebral blood flow can be calculated with fNIRS. Several features of fNIRS, including portability, non-invasiveness, cost effectiveness and tolerability, make it an advantageous tool in both clinical care and neuroscience research. Concurrent monitoring of other real-time physiological parameters, such as EEG (Hong and Khan, 2017; Khan and Hong, 2017; Hong et al., 2018; Khan et al., 2018), can further enhance its temporal resolution, making it an ideal tool for the study of epilepsy, autonomic function, and physiologic phenomena.

Indeed, fNIRS has become a tool for standard care in pediatric ICUs to assess regional oxygenation, such as somatic (Balakrishnan et al., 2018) and cerebral oxygenation (Hoffman et al., 2017), in real-time. It is also widely used to assess task-related cortical function. By using a block design, regional cerebral blood flow signals can be enhanced to characterize task-based cortical function (see (Hong and Yaqub, 2019) for a comprehensive review). In this review we will focus on language mapping which has been the main interest of neurologists and neurosurgeons.

When it comes to more sophisticated measurement in real-time, fNIRS has encountered several limitations. First, oligochannel fNIRS used in most of clinical settings lacks spatial resolution which is crucial for functional localization in cognitive tests and source localization in seizure detection. Second, although the development of multichannel fNIRS greatly increases the spatial resolution of this technology, individual event analysis remains challenging due to the reduced signal-to-noise ratio (SNR) of fNIRS. Group analysis and signal processing can increase the SNR, but it is still unable to analyze individual events, such as seizures, in real-time. Techniques such as vector diagram analysis to detect the initial dip in the hemodynamic response have helped to tackle this problem (Zafar and Hong, 2018). Third, compared with EEG, the temporal resolution of fNIRS may be suboptimal to capture individual neurologic events. Seizures spread quickly between neurons on a millisecond timescale and can require a high sampling rate for accurate source localization (Coelli et al., 2019; Vespa et al., 2020). Sampling rates of clinical EEG are typically between 256 to 1024 Hz, whereas the sampling rate of fNIRS is an order of magnitude lower. Finally, reproducibility in the spatial localization of fNIRS is often limited by a lack of co-registration between individual subject's anatomy and sensor placement. Co-registration of standardized optode placement to individual subject anatomy and individualized generation of forward models of fNIRS signal propagation, coupled with fMRI validation, could help address this issue.

With appropriate selection of light wavelengths, fNIRS characterization of neurovascular coupling can be expanded to also include metabolic function, for example using cytochrome c oxidase (CCO) (Bale et al., 2018; Holper and Mann, 2018; Lange et al., 2019). Coupled with the ability to simultaneously measure fNIRS together with other neuroimaging analysis techniques such as EEG and neural network learning (Yang et al., 2019) fNIRS has the potential for widespread clinical applications in neuroscience.

NEUROVASCULAR COUPLING

The lack of an energy storage capability in neurons means that increased metabolic activity associated with neuronal communication requires a ready supply of glucose and oxygen. Fox and Raichle (1984) demonstrated with PET that volitional tasks caused an increase in local glucose utilization as well as local oxygen utilization in the brain regions associated with the functional task. In the resting state, neurons have a relatively constant oxygen extraction fraction, resulting in a steady ratio of oxygenated to deoxygenated blood in the capillary bed surrounding the neurons. When going from a resting state to an active one, the local oxygen extraction fraction increases, which first increases the concentration of deoxyhemoglobin. Shortly after this begins, sphincters in the arterioles located just before the capillary bed dilate, flooding the capillaries with oxyhemoglobin. MRI detects this change as a change in the magnetic state of the blood. Oxyhemoglobin is diamagnetic, but when it releases its bound oxygen atoms to become deoxyhemoglobin, it becomes paramagnetic. The local change in the magnetic susceptibility of the tissues surrounding the capillary bed changes the T2* relaxation rate of the visible hydrogen nuclei. In the first 1–2 s of activation, the excess of deoxyhemoglobin decreases T2*, causing the intensity of the voxel to decrease (initial dip). This phenomenon is not as reliably detected as the subsequent, and typically larger, increase in oxyhemoglobin concentration, which increases the T2* of the tissue and the corresponding intensity of voxels within the MR image.

Functional MRI, which measures changes in blood oxygenation/deoxygenation in the brain vis-à-vis the blood-oxygen-level-dependent (BOLD) response, has become a cornerstone of functional neuroimaging. While fMRI has been widely used to characterize neuronal activity in both healthy volunteers and patients, it has several limitations. The first is that the detection of brain activity is indirect. Because fMRI measures changes in blood oxygenation rather than neuronal activity directly, the effect can be extinguished or precluded by other vasoactive processes. A second important limitation is the need for a high-field-strength MRI system. The subject is

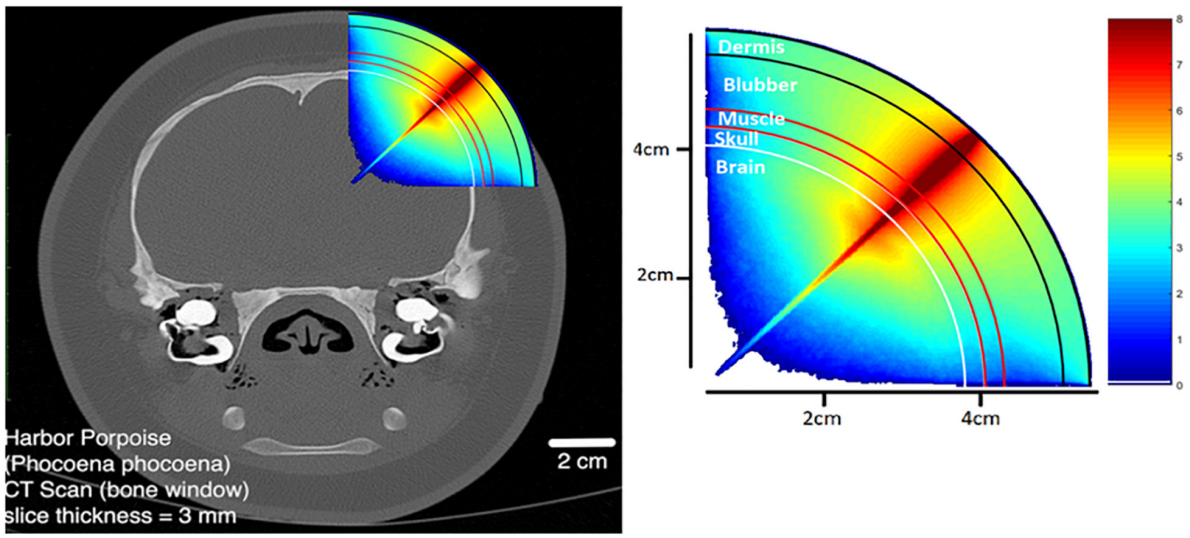

FIGURE 1 | Monte Carlo photon propagation simulation using a point LED source incident at an angle normal to the scalp. Anatomy modeled on the harbor porpoise.

confined in a magnet, and both the subject and any experimental apparatus must be magnet-safe. A final limitation is that the BOLD response measured with fMRI is based on the ratio of oxy- to deoxy-hemoglobin. These two moieties of hemoglobin are not individually detected.

Unlike fMRI, fNIRS measures the two hemoglobin species separately. The differentiation between hemoglobin species facilitates the use of differential analysis techniques, such as vector diagram analysis, using 2 (oxy- and deoxyhemoglobins) or 4 (oxy-, deoxyhemoglobin, the difference between them and the total hemoglobin) components to better define the initial dip in the hemodynamic response (Zafar and Hong, 2017, 2018). Moreover, fNIRS is portable, tolerable and cost effective. Timely bed-side assessment of cerebral oxygen can be performed more easily with fNIRS than fMRI. Functional NIRS is also a safe technology for patients with non-MR compatible implanted devices such as a vagal nerve stimulator (VNS), deep brain stimulator (DBS), or pacemaker.

MECHANISMS OF fNIRS

Near-infrared spectroscopy in the brain is made possible by the relative transparency of biological tissues (including bone) to light for infrared wavelengths ranging from 650 to 925 nm. Light in this range is absorbed by oxyhemoglobin and deoxyhemoglobin much more strongly than surrounding and overlying tissues. The absorption of infrared light as a function of wavelength is different for these two chromophores, with deoxyhemoglobin absorbing more strongly below 790 nm and oxyhemoglobin more strongly above 790 nm.

By detecting the changes in the relative concentrations of different light-absorbing molecules, fNIRS allows the analysis of energy metabolism in the brain. For example, fNIRS can measure changes of oxygenated and deoxygenated hemoglobin in a manner similar to fMRI, and thus reflect regional changes in neuronal activation. In order to do so, sufficient near-infrared light must be incident on the cortical surface. The attenuation of light by the skull, scalp and meninges can be predicted by Monte Carlo simulation (Hiraoka et al., 1993) as shown in **Figure 1**, to account for the static light-absorbing properties of the surrounding tissue.

Commercial fNIRS systems utilize separate illumination sources and detectors. Typical source-detector separation is on the order of 1.5–3 cm in children and 2.5–5 cm in adults depending on head circumference, although it is recommended that separation does not exceed 3.5 cm in adults. In recent years, the use of short separation channels, <1 cm separation from source to detector, have been incorporated in studies to estimate and remove the blood flow contribution of the scalp in typical source-detector channels. Thus, models of light absorption by the surrounding tissues must also account for the path that the light takes to reach the cortex and be reflected back to the detector. This situation is shown in **Figure 2**.

NOISE REDUCTION AND SIGNALING PROCESSING

Multiple sources of signal interference (i.e., noise) can complicate interpretation of the fNIRS signal and has been a major challenge in clinical settings. Sources of noise can include head motion, variations in coupling over time due to changes in the distances between optodes (sources and detectors) on the scalp, and changes to blood flow unrelated to neuronal activity. Whereas fMRI measures the ratio of oxy- to deoxy-hemoglobin as a result of changes in bulk magnetic properties, fNIRS measures oxyhemoglobin and deoxyhemoglobin separately which can be confounded by changes in heart rate and blood flow. Since the

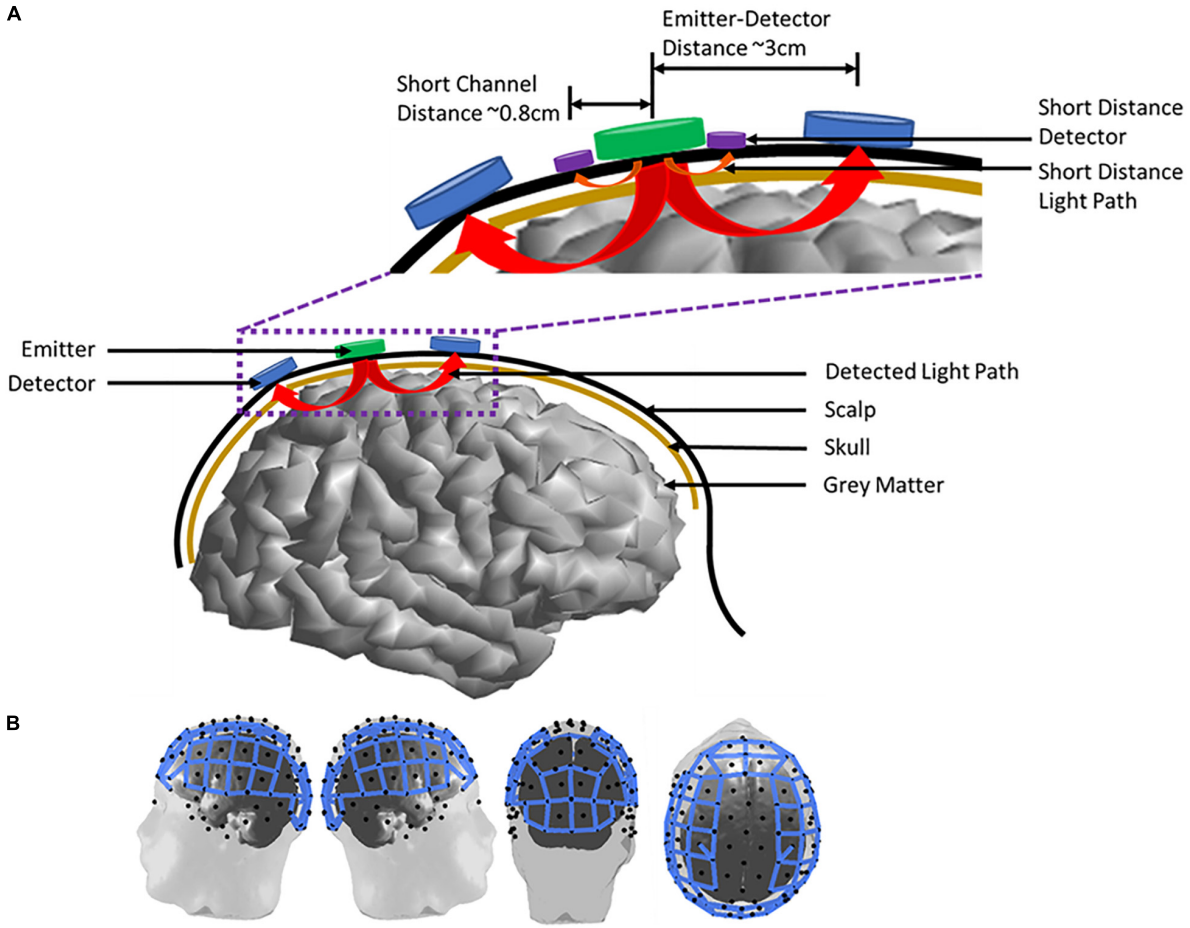

FIGURE 2 | Emitter and detector arrangement on an adult human subject. **(A)** A two channel emitter-detector pair placement on the scalp. Arrows from the emitter to the detectors indicate the measured light path of each channel. The inset highlights emitter-detector distances and the incorporation of short-distance channels to measure scalp blood flow. **(B)** Full head imaging cap example on an adult human subject. Blue lines represent measurement channels (n = 102 channels) between emitter (n = 32) and detector (n = 32) pairs.

near-infrared wavelengths must first pass through the meninges, skull, and scalp, physiologic changes in these tissues can induce changes in the light absorption between the source and detector that may not be related to functional changes in neuronal activity. Moreover, like fMRI, the response of the fNIRS signals to changes in neuronal activity are convolved with a hemodynamic response function which describes the latencies, overshoots and undershoots of the arteriole sphincters that control blood flow into the capillary beds in responses to changes in metabolic demand of the neuronal tissue (Osharina et al., 2010).

A number of signal processing techniques have been developed to separate task related signals from noise. The following sub-sections provide a brief overview of current approaches for reducing sources of physiological noise and motion artifacts.

Reducing Physiologic Sources of Interference in fNIRS

The sources of physiological noise present in fNIRS include heart rate, blood pressure fluctuations, respiratory rate, and scalp blood flow. Several approaches have been used to identify and remove physiologic noise including digital filtering, prewhitening, adaptive filtering, data driven methods such as principle component analysis (PCA) and independent component analysis (ICA), and the use of short separation channels. Since different biological functions typically occur over different ranges of frequencies (Cordes et al., 2001; Blanco et al., 2018) digital filtering can be used to reduce or remove sources of interference that occur at temporal frequencies distinct from the task-related measures of brain activity (Cordes et al., 2001; Liu et al., 2017). However, blood pressure fluctuations (0.08–0.12 Hz) and resting heart rate (1–1.5 Hz) can overlap in frequency with the signals of interest and confound task-related signals presented in certain types of block designs (Huppert, 2016).

Another option is to remove physiological noise is through prewhitening. Prewhitening can be used to remove temporally autocorrelated signals, such as heart rate, by decorrelating physiologic signals not associated with the task (Barker et al., 2013). To determine the optimal prewhitening filter coefficients, Barker et al. (2013) and Blanco et al. (2018) used an iterative

autoregressive model to reduce the residual error in the task-related activity estimated from a general linear model analysis. Prewhitening accuracy can be can be affected by motion artifacts (Blanco et al., 2018). Therefore, before prewhitening is applied any motion artifacts present in the signal should be removed (see section "Noise Reduction of Motion Artifacts" below).

Adaptive filtering techniques use a system of linear functions within either an open or closed loop control model. Nguyen et al. (2018) applied this principle to reduce the amount of physiological noise present in fNIRS during a finger tapping task through the linear combination of the expected hemodynamic responses to the prescribed stimuli, short separation channel signals to detect extra-cortical noise, Fourier approximations of physiological noise (heart rate, respiratory, and blood pressure fluctuations), and baseline drift. Unknown model coefficients were estimated using a recursive least-square estimator to produce an adaptive filter that was able to reduce on average 77% of noise in oxyhemoglobin and 99% of noise in deoxyhemoglobin (Nguyen et al., 2018). Some limitations of this type of filtering include parameter tuning, the need to define noise distributions, and biased estimations if the filter is not closed loop (Abdelnour and Huppert, 2009).

Changes in fNIRS due to global blood flow at the scalp can pose an additional signal confound especially in more demanding functional tasks. Spatial analyses, such as PCA, can be used to remove global blood flow not associated with a functional task (Zhang et al., 2016). PCA can be particularly effective when there is one dominant source of variation, such as either global blood flow or motion artifacts, but can fail if there are multiple sources driving the overall variation (Zhang et al., 2016). Furthermore, PCA approaches require multiple channels to reliably parse the global blood flow from physiologic signals of interest. Gaussian kernel approaches, similar to those used in fMRI, have also been shown to remove global blood flow at the scalp when applied spatially across channels (Zhang et al., 2016) although the ability to account for more localized spatial changes in blood flow produced by large vasculature is not well accounted for. Lastly, ICA (Hyvarinen and Oja, 2000), has been used to remove global blood flow during gait experiments by leveraging the temporal coherence between channels to identify large signal component(s) with a high coefficient of spatial uniformity (Kohno et al., 2007). While the use of ICA for artifact removal in EEG is well-established, its application to fNIRS has been limited.

More recently, short separation channels (∼8 mm source-detector distance) have been used to directly measure and remove scalp blood flow from fNIRS (Gagnon et al., 2014; Funane et al., 2015; Nguyen et al., 2018). The short distance between the light emitters and detectors prevents light penetration to the cortical surface, limiting blood flow measurements to the scalp. Funane et al. (2015) showed that hemoglobin signals obtained with short distances channels (∼1.5 cm) were better correlated with laser-doppler flowmetry measures of scalp blood flow than signals obtained from standard emitter/detector distances (∼3 cm) targeted to measurements of blood flow in adult cortex. Additionally, Nguyen et al. (2018) showed there was no correlation ($r < 0.38$) of short separation channels to other physiological noises present in long range separation channels. Thus, the inclusion of short separation channels as a regressor in fNIRS analyses can reduce signal interference from scalp blood flow.

Noise Reduction of Motion Artifacts

Motion artifacts can occur from talking or movements of the face, head, and/or upper body (Izzetoglu et al., 2010; Jahani et al., 2018). Typically when these movements are made, the optodes on the scalp become displaced resulting in sharp high frequency displacements, slow wave drifts, or baseline shift in the fNIRS signal (Jahani et al., 2018). Various methods have been used to remove motion artifacts including wavelet-based filtering, spline interpolation, and Kalman filtering. Wavelets can be particularly efficient at removing motion artifacts due to their time-frequency localization properties. Wavelet-based methods decompose the fNIRS signal into wavelet coefficients and removes those that fall outside of a predefined distribution, like a Gaussian distribution, under the assumption that they are related to motion artifacts (Robertson et al., 2010; Molavi and Dumont, 2012). Molavi and Dumont (2012) reported a reduction in motion artifacts in fNIRS collected from infants after using wavelets. Although they are efficient at removing spike artifacts, wavelet-based methods can produce an added baseline shift into the data around the spike artifact. Additionally, if artifacts do not meet the threshold criteria, they can continue to corrupt the signal.

Spline interpolation methods model motion artifacts as a series of spline functions and subtracts them from the data (Scholkmann et al., 2010). Scholkmann et al. (2010) reported an average 89.8% decrease in root mean square error between NIRS signals before and after spline interpolation. Although they found a reduction in motion artifacts, residual high frequency spikes remained following the spline interpolation (Scholkmann et al., 2010). In a comparison study, Jahani et al. (2018) showed that combining spline interpolations with the Savitzky–Golay filter or a robust locally weighted regression smoothing (RLOESS) was able to correct for baseline shifts and high frequency spikes without introducing additional artifacts into the signal. Even though both methods, spline-Savitzky–Golay and spline-RLOESS, produced similar results with respect to artifact removal (i.e., mean square error between the true and estimated hemodynamic response functions: 0.44 ± 0.06 and 0.56 ± 0.08 for spline-Savitzky–Golay and spline-RLOESS respectfully), the spline-Savitzky–Golay method had significantly faster processing time (16 sec), versus the spline-RLOESS (1800 sec), for 51 channels (Jahani et al., 2018).

Kalman filtering recursively improves the estimate of a signal with additional information added over time. Izzetoglu et al. (2010) compared the effectiveness of a Kalman filter, versus an adaptive filter and Wiener filter, for removing motion artifacts in fNIRS data of 11 subjects performing various speed head movements. They found that the Kalman filter significantly increased the signal to noise ratio (SNR) of fNIRS signals (SNR = [6.63 8.51]) compared to the adaptive filter (SNR = [2.79 4.17]) while no statistical difference was found between the Kalman filter and the Wiener filter

(SNR = [5.25 9.05]). This is important as the Kalman filter can be applied to real time analysis without the additional sensors required for adaptive filters and does not require fNIRS signals to be statistically stationarity as with a Wiener filter (Izzetoglu et al., 2010). However, caution is warranted when using the Kalman filter for motion artifact removal as the accumulation of error over time due to instabilities if the filter is not set up properly, non-modeled system dynamics, or non-linearities in the data can impact performance (Izzetoglu et al., 2010).

REDOX STATES OF CYTOCHROME C OXIDASE

Aside from physiologic signal confounds and motion artifacts present in most imaging measures of brain activity, measuring variations in the hemodynamic response via changes in oxyhemoglobin and deoxyhemoglobin has inherent limitations. It is not sensitive enough to determine the cerebral metabolic rate of oxygen (CMRO2). Hemoglobin provides information on cerebral circulation and intravascular oxygenation but its concentration does not reflect the tissue's ability on oxygen utilization. On the other hand, mitochondria are responsible for most of immediate cellular oxygen metabolism. Hence, CMRO2 directly relates to mitochondrial function and could help identify the clinical significance of hemodynamic change. CMRO2 can be calculated by combining cerebral oxygenation and arterial oxygenation with cerebral blood flow (CBF), assuming the arteriovenous blood volume ratio is fixed (Verdecchia et al., 2013). However, it has proven challenging to measure cerebral oxygenation in many clinical settings due to its invasiveness. Therefore, researchers have been focusing on a third chromophore, cytochrome c oxidase (CCO), which is a key element in oxidative metabolism in mitochondria, the "power station" of neurons.

Cytochrome c oxidase plays a crucial role in the oxidative metabolism of glucose. Glycolysis metabolizes glucose into pyruvate in which the adenosine triphosphate (ATP) and nicotinamide adenine dinucleotide (NADH) are generated. The pyruvate is later transported into the mitochondria and converted to acetyl CoA. Acetyl CoA enters the tricarboxylic acid (TCA) cycle to generate more ATP and NADH. NADH is an electron donor in the electron transfer chain (ETC) (**Figure 3**); a series of protein complexes (known as complex I-V) that reside in the inner membrane of the mitochondria. Complexes I and II accept electrons from NADH and succinate, respectively, from the TCA cycle and transfer them to the soluble electron carrier coenzyme Q (CoQ). CoQ is oxidized by complex III, in the process the electrons used to reduce cytochrome c. Cytochrome c as a receiver for the electrons in the mitochondrial ETC is then oxidized by CCO (complex IV), which is a heme protein containing a binuclear copper center (CuA), a heme a, and a binuclear Fe-Cu center (heme a_3-Fe) (Bale et al., 2016). The electron accepted from the cytochrome c is ultimately transferred to molecular oxygen, which is reduced to water. This process generates an electrochemical potential, which drives ATP synthesis via ATP synthase (complex V) in mitochondria. ATP is the ultimate energy source for cells.

All of these redox changes have associated optical transitions. In the range of near-infrared, the CuA center in CCO contributes the most to the absorption spectrum, around 830 to 840 nm. In theory, three wavelengths are required to simultaneously measure changes of CCO, oxyhemoglobin and deoxyhemoglobin. However, traditional continuous-wave fNIRS, which uses 2 to 3 wavelengths for hemoglobin species, is not suitable to quantify the change of CCO due to lower concentration of CCO and crosstalk between CCO, oxyhemoglobin, and deoxyhemoglobin in those wavelengths. Using multiple wavelength combinations is therefore important to accurately quantify the change of CCO and distinguish it from hemoglobin species. Although minimalistic approaches using fewer wavelengths are subject to noise and crosstalk, using too many wavelengths can be computationally prohibitive. Current advances in wavelength optimization suggest that with 8 wavelength combinations, the error rate for estimating changes of CCO can be reduced to less than 2% (Arifler et al., 2015). Redox changes in CCO may therefore allow fNIRS to detect changes in the electron transport of a heme protein, which absorbs light in the near-infrared spectrum and reflects mitochondrial energy metabolism.

Unlike hemoglobin species, CCO concentration does not change over a short time period.

The systemic fluctuation of blood pressure has little impact on CCO. Therefore, it is not influenced by the change of regional blood flow outside the brain as hemoglobins are. The redox state of CCO is not interfered by hemoglobin species and regional cerebral oxygenation (Springett et al., 2000). In theory, measuring the change of mitochondrial CCO better reflects cellular metabolism and viability. Potential clinical application of CCO will be further discussed in the next section.

CLINICAL APPLICATION OF fNIRS

Language Mapping

Language is the most sophisticated high cortical function and the most important functional domain to localize during brain surgeries for tumor resection and epilepsy (Binder, 2011). Language mapping strongly correlates with the prognosis and outcomes of brain surgeries (Janecek et al., 2013b). Functional MRI has been the main tool for language mapping extra-operatively. It has high sensitivity but very low specificity (Rolinski et al., 2019). Therefore, invasive mapping such as direct cortical stimulation and Wada (intracarotid sodium amobarbital testing) test are inevitable in patients with bilateral or equivocal language representation in fMRI (Janecek et al., 2013a,b). Epileptologists, neurosurgeons and neuropsychologists have been looking for a non-invasive alternative and fNIRS has been studied for this purpose. Several lines of evidence have shown that fNIRS is a validated tool for neurocognitive functions (Hong and Yaqub, 2019). For example, research in human subjects suggests that the increase of prefrontal cerebral blood flow while performing cognitive tests can be detected

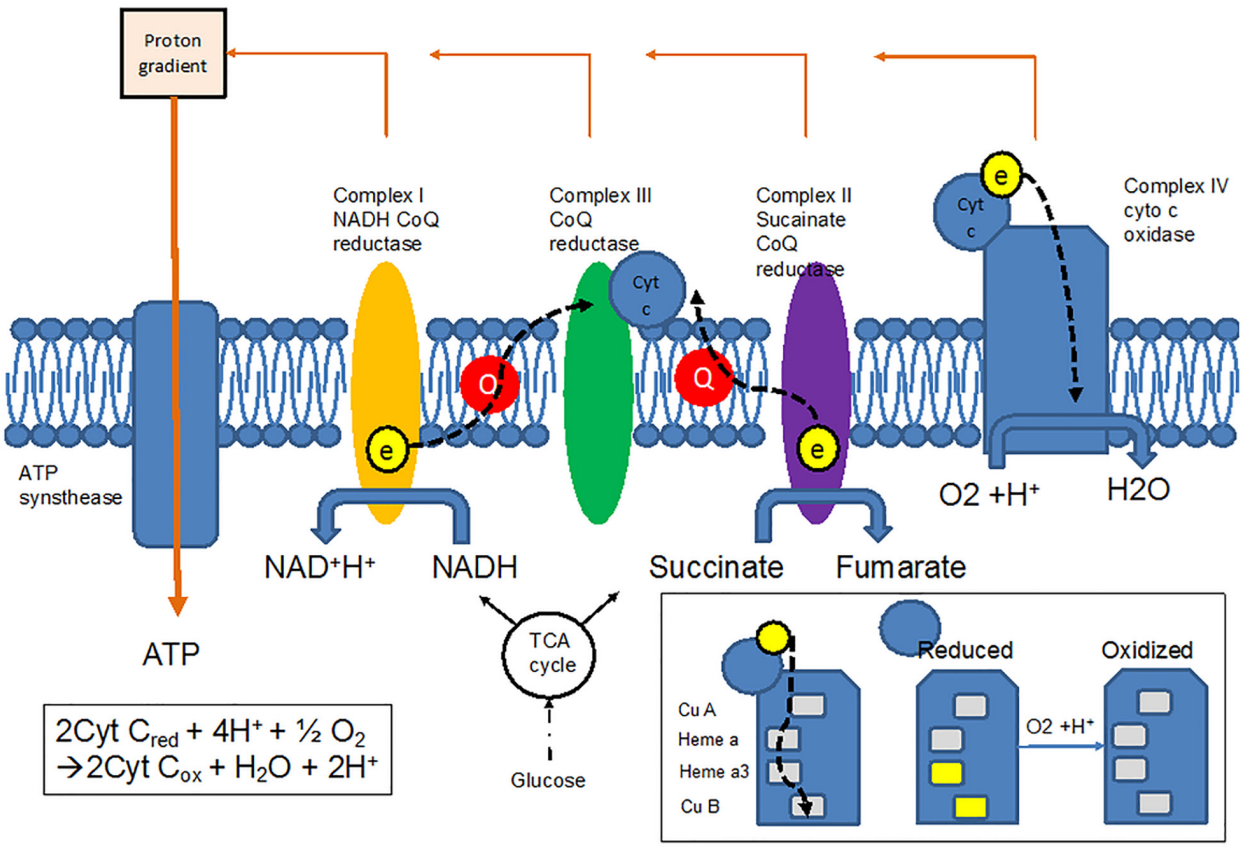

FIGURE 3 | Electron transfer chain allows electrons to be transferred from the TCA cycle to oxygen via cytochrome c oxidase (CCO), resulting in changes in the redox states of CCO.

by fNIRS (Masataka et al., 2015). Presurgical evaluations for refractory epilepsies have shown the reliability of fNIRS for language lateralization (Watanabe et al., 1998). Lateralization of inferior frontal activation during a written word-generation task was found to be consistent with handedness in a small study involving 11 healthy adults and 6 patients with medication-resistant epilepsy. The six patients with epilepsy had undergone the Wada test and showed the same lateralization for language as obtained with fNIRS (Watanabe et al., 1998). Another study using a category fluency task also suggested qualitative alignment of lateralization between fNIRS and either fMRI or Wada test results in small samples of adult and pediatric patients with epilepsy (Gallagher et al., 2007). Using a letter-fluency task administered to bilingual speakers in both Japanese and English, multichannel fNIRS showed additional areas of activation when performing the task in the later-acquired language, and this additional activation was correlated with second-language proficiency (Wroblewski et al., 2017).

Functional NIRS has its inherent limitations for language mapping and has not been used in a clinical setting. Limited temporal resolution and depth resolution of fNIRS pose the main obstacles for language mapping. Furthermore, fNIRS lacks anatomic specificity, which is crucial for surgical planning. Increasing the density of optodes and co-registration with other imaging modalities (e.g., MRI) could improve the anatomic specificity.

Neurocritical Care

Anatomic specificity becomes less an issue in the setting of neurocritical care where timely measurements of global cerebral oxygenation is the main purpose. Functional NIRS has been widely used for this purpose given its non-invasiveness and good temporal resolution for hemodynamic changes. Several lines of evidence have shown that fNIRS has the potential to monitor cerebral hemodynamic change and cerebral autoregulation (CA) in the subacute phase of stroke. An early trial with a small number of patients (n = 10) revealed that the hypercapnia-induced increase in regional cerebral blood flow was impaired in the hemisphere affected by ischemic stroke (Vernieri et al., 1999). The authors concluded that dysfunctional CA played a pivotal role in the finding. A large-scale prospective trial (n = 98) suggests that dysfunctional CA correlated with delayed ischemic stroke after subarachnoid hemorrhage (SAH) (Budohoski et al., 2012). All patients had acute (<5 days) aneurysmal SAH and were treated according to the current clinical guidelines. Transcranial Doppler (TCD) was performed on each patient every 1–2 days to screen for vasospasm. Digital subtraction angiography was used to supplement the diagnosis. Bilateral frontal tissue oxygenation

index (TOI) was obtained via cerebral fNIRS (NIRO-200). CA was calculated with both fNIRS and TCD as the linear correlation coefficient between arterial blood pressure (ABP) and TOI, and between ABP and middle cerebral artery flow velocity. The primary end point was cerebral ischemia within 21 days after SAH. In those who developed cerebral ischemia, TCD flow velocity failed to predict the development of cerebral ischemia while the autoregulation index showed changes 5 and 4 days before the ischemia, via fNIRS and TCD, respectively. This phenomenon suggests that fNIRS was able to demonstrate dysfunctional autoregulation 1 day earlier than TCD, which could make it a promising clinical tool for predicting the development of delayed ischemic stroke. Further research using continuous real-time fNIRS-generated CA indices might generate more clinically relevant utilization.

Frequency-domain fNIRS is another emerging tool for assessing CA in stroke patients. Low (LFO) and very-low frequency oscillation (VLFO) of oxyhemoglobin are found to be robust parameter for evaluating CA (Andersen et al., 2018; Su et al., 2018). Based on the cerebral oscillation theory, LFO and VLFO are associated with cerebral sympathetic activity. Furthermore, LFO reflects the myogenic component of CA; whereas VLFO reflects neurogenic (larger vasculature) and metabolic (microcirculation). Analysis of amplitudes and the interhemispheric synchronization of LFO and VLFO is a well-established method to assess the CA (see review (Andersen et al., 2018)). In patients with acute ischemic stroke (<5 days), the decrease in amplitudes of LFOs in the ischemic hemisphere and interhemispheric desynchronization were seen (Phillip et al., 2014). The effect of stroke on LFO and VLFO can last up to 12 months (Li et al., 2010).

Cerebral autoregulation is an increasingly recognized parameter in managing traumatic brain injury (TBI). Traditionally, intracranial pressure (ICP) and cerebral perfusion pressure (CPP) guide the pressure treatment in severe TBI. However, this concept is possibly oversimplified considering the individual differences between patients. Unlike ICP and CPP, CA is believed to be a more physiologic parameter and allows more flexible blood pressure management. Impaired CA results in secondary brain damage, which is an independent risk factor for fatality (Czosnyka et al., 2009). Therefore, autoregulation indices have been developed to identify the most optimal CPP (CPP_{opt}) in the patient with severe TBI. The CPP_{opt} is determined by the correlation coefficient between the slow fluctuation in mean ABP and the ICP. This correlation coefficient is called the pressure reactivity index (PRx) in the field of neurocritical care, and a negative PRx is associated with favorable outcome. In a given patient, the CPP range in which the PRx is lowest is defined as "CPP_{opt}." Researchers have shown the correlation between the CPP_{opt} and patient morbidity and mortality (see review (Zeiler et al., 2017)). Typically, invasive ABP and ICP measurements are required to calculate PRx and optimal CPP, however, efforts have been made to find non-invasive alternatives to reliably calculate them (Dias et al., 2015; Bindra et al., 2016). For example, a recent prospective trial used multimodal brain monitoring, including ICP, CPP, bilateral transcranial cerebral oximetry with fNIRS, brain tissue oxygenation and cerebral blood flow, to assess the CPP_{opt} in patients with severe TBI. A total of 18 patients were included with a median Glasgow Coma Scale of 6. The CPP_{opt} was displayed every minute at bedside based on the CPP_{opt} curve calculated with invasive ABP and ICP data in the past 4 h. Therefore, the CPP_{opt} was monitored in virtual real-time for each patient, and the amount of time in which patients spent in impaired CA (PRx > 0.25) could be calculated. The ABP and ICP were managed based on the CPP_{opt} when it was available. Those who had high PRx and a longer period with PRx > 0.25 had statistically significantly poorer short-term and long-term outcomes. Further *post hoc* analysis suggested that PRx generated by transcranial cerebral oximetry with fNIRS showed the best degree of agreement with optimal CPP calculated by invasive PRx (Dias et al., 2015). These findings indicate that fNIRS can reliably supplement, or even replace, invasive ICP in terms of calculating CPP_{opt}. Another trial of 19 patients with different critical neurological conditions including TBI used a similar approach to compare the validity of invasive and non-invasive Finometer photoplethysmograph ABP in calculating PRx (Bindra et al., 2016). This trial suggests that PRx can be obtained via an entirely non-invasive method (Finometer and fNIRS) in patients with critical neurological pathologies.

Oxygen saturation typically cannot be reliably estimated by continuous-wave fNIRS due to the unknown scattering coefficients in each patient. New fNIRS technologies allow researchers to assess the concentrations of hemoglobin species, rather than changes in them. For example, time-domain fNIRS has been used to investigate the cerebral oxygenation in patients with ischemic stroke (Giacalone et al., 2019). The result shows increased total hemoglobin but decreased oxyhemoglobin (namely, decreased oxygen saturation) in the ischemic hemisphere of large vessel stroke. Furthermore, a new approach combining measurements for hemoglobin species and CCO with time-domain fNIRS (Lange et al., 2019) can substantially enhance our understanding of dynamic neuronal oxygen metabolism in different cerebral pathologies. The non-invasiveness and the ability to measure the real-time physiological changes of fNIRS can also inspire researchers to further explore its potential for different clinical settings. Seizure detection is one of the most studied applications.

Epilepsy

In the past decades, animal studies suggest that increased cerebral blood flow and oxygenation corresponding to epileptic spikes and high-frequency oscillation can be detected by fNIRS (Hoshi et al., 2001; Zhang et al., 2014). These changes identified by fNIRS can precede the appearance of spikes induced by bicuculline methiodide by about 5 s (Osharina et al., 2010). These findings have inspired many subsequent clinical studies in the field of epilepsy. The oxygenation response to seizures has been investigated extensively. There seem to be differences between focal and generalized seizure. For example, an early clinical case study revealed consistent ictal increase of oxygenation on the epileptic hemisphere relative to the non-epileptic hemisphere in patients with temporal and extratemporal lobe epilepsies (Monrad et al., 2015). This pilot study sheds light on further understandings about metabolic and hemodynamic change

during seizure, such as uncoupling of oxidative phosphorylation, or alterations in cerebrovascular autoregulation. Other groups also suggest similar findings in focal-onset seizures (Villringer et al., 1994; Adelson et al., 1999; Sokol et al., 2000). In generalized epilepsies and secondary generalized seizures, regional frontal oxygenation has been shown to decrease during seizure (Sokol et al., 2000; Buchheim et al., 2004). Despite the small sample size of the studies (n = 2–8) and the use of oligo-channel fNIRS (1–2 channels), these preliminary findings paved the way for later larger-scale multi-channel trials.

Unlike other applications of fNIRS, precise localization and spatial resolution are crucial in epilepsy care and management. One of the current advances in fNIRS research is the development of multi-channel fNIRS devices. Multi-channel fNIRS is aimed at increasing spatial resolution, which has been the major obstacle of oligo-channel fNIRS. In the past decades, several case reports or series (n = 1–4) have been published. Differential increase in regional oxygenation or blood flow has been noted in SMA seizures (Sato et al., 2013), mesial temporal epilepsy (Rizki et al., 2015) and other focal seizures (Yucel et al., 2014). Utilizing multichannel fNIRS together with long-term EEG would allow epileptologists to better understand the hemodynamic changes during different phases of seizures (preictal, ictal, postictal and interictal phases) and improve seizure detection and localization. However, co-registering EEG, fNIRS or even MRI data requires advanced experimental skill sets and signal processing techniques to obtain and fuse multimodal imaging datasets. For example, placing multiple optodes and standard EEG electrodes simultaneously can be challenging for both patients and the electrodiagnostic technologists. Specialized software capable of displaying fNIRS and EEG recordings in real time is not yet commercially available. Analyzing small changes of hemoglobin species in the context of significant noise in fNIRS can be extremely challenging. The significant difference of sampling rates between fNIRS (tens of Hz) and EEG (∼500–2000 Hz) requires sophisticated mathematical techniques and computer power to temporally synchronize the recordings.

One of the pioneer trials, with a total of three presurgical patients, has overcome some of the technical issues (Nguyen et al., 2012). The customized electrode-optode combined cap allowed more efficient and comfortable placement of the sensors. The authors used a low frequency filter to minimize the cardiac artifact and a simple statistic tool (student's t-test) to differentiate significant signal changes from the background. Selected fNIRS channels were averaged during the seizures to assess the overall variation. The authors found that total hemoglobin and oxyhemoglobin increased in the epileptogenic zone during the seizure, and deoxyhemoglobin exhibited a biphasic response with an initial decrement and later increment in the concentration. However, the lack of trials with larger patient numbers prevent the generalization of this practice. Furthermore, this trial did not show that the fNIRS provided additional localization value for seizure management. Indeed, one of the current clinical trials using portable multichannel fNIRS in 15 epileptic patients failed to show a significant seizure detection rate (Jeppesen et al., 2015). Only 6–18% of a total of 34 focal seizures exhibited significant changes in hemoglobin species. In addition, none of the clinical studies have yet shown an ability to use fNIRS at bedside for real-time monitoring. All the fNIRS data required later analysis.

Due to the inconsistent seizure detection rate, fNIRS has not been widely used in epilepsy clinical practice. This might reflect the fact that the theory of neurovascular coupling is a secondary phenomenon of primary neuronal hyperexcitability, which is subjected to further temporal delay on event capture. Therefore, targets other than hemoglobin species, such as CCO, may be more useful. CCO, as discussed earlier, is a mitochondrial complex that generates electrochemical potential, which drives ATP synthesis via ATP synthase. As the energy demand increases in hyperexcited neurons, intracellular ATP and corresponding oxidized CCO concentrations will change as well. In our institution, tens of patients have undergone simultaneous EEG and fNIRS monitoring with a custom-made device that is able to detect the change of hemoglobin species and CCO (Kadamati J. et al., 2018). This technology is well-tolerated, and there is no interference between the EEG and fNIRS. This pilot study sheds light on further understanding about metabolic and hemodynamic change during seizure. It potentially can offer an additional clinical parameter for more accurate earlier seizure detection and localization.

Vector diagram analysis to detect the initial dip in the hemodynamic response (Hong and Naseer, 2016), might also improve the temporal detection of seizure onset with fNIRS. However, the need for a higher sampling rate with fNIRS remains an obstacle, particularly for whole-head multi-channel systems. A new fNIRS device equipped with a sampling rate up to 100 Hz could result in comparable temporal resolution to EEG.

Autonomic Functions

Other than assessing physiological changes of well-known cerebral phenomenon, fNIRS also can be a useful research tool for those diseases whose mechanisms are not fully explored. Autonomic dysfunction is one example. Our previous study has suggested that fNIRS can be utilized as a tool to assess autonomic dysfunction (Kadamati P. et al., 2018). A total of 12 subjects were recruited; 6 healthy controls, and 6 diagnosed with postural orthopedic tachycardia syndrome (POTS). Muscle oxygenation of lower extremities was measured via a commercial fNIRS device (INVOS 5100B) and custom-built optodes concomitantly. Expectedly, the subjects with POTS showed a higher degree of venous pooling (increased amount of total hemoglobin) in the lower extremities during 70-degree tilting. Furthermore, the responding time of the oxyhemoglobin and deoxyhemoglobin was faster in the healthy subjects than the POTS group, which suggests both neural reflexes and vascular compliance play roles in this group. These new findings from our study shed light on the mechanisms of POTS, and also of orthostatic intolerance in which patients do not have typical heart rate responses to tilting but have similar orthostatic symptoms.

Many other studies have also used fNIRS to investigate the cerebral hemodynamic dysregulation in patients with dysautonomia (Lankford et al., 2015), orthostatic intolerance (Tanaka et al., 2002) and vasovagal syncope (Ayers and Lawrence, 2015). For example, decreased temporal regional cerebral saturation was noticed to precede other changes of

vital signs during vasovagal syncope (Ayers and Lawrence, 2015). Functional NIRS also yields a more reliable result for continuous cerebral blood flow. By analyzing the pattern of the dynamic change of cerebral blood flow, it is possible to expand the spectrum and the mechanism of orthostatic intolerance (Lankford et al., 2015). Therefore, fNIRS could potentially be a new biomarker for autonomic dysfunction. Moreover, diseases which are associated with cerebral hemodynamic dysregulation such as migraine can also be further studied with fNIRS.

Migraine

A few groups have focused on the application of fNIRS to the detection of cortical spreading depression (CSD) in migraine. CSD is hypothesized as the main electrophysiological feature of migraine aura (see review (Goadsby et al., 2017)). In animal models, CSD is characterized by a short period of influx of sodium and calcium and intense depolarization of neurons and glias followed by a long-lasting "depression" of neuronal activity and decrease in regional cerebral blood flow (Lauritzen, 1994). Studying the regional oxygenation saturation and cerebral blood flow in migraine can provide more information about the mechanisms of migraine. Combining with TCD, in a self-controlled trial fNIRS has showed hypoperfusion secondary to decreased oxygen demand in the regions where aura and CSD presumably occur (Viola et al., 2010).

Several other groups have utilized fNIRS to evaluate cerebrovascular reactivity in patients with migraine. Delays in and reduced amplitude of peak oxyhemoglobin and total blood flow were observed in a patient with migraine during hypercapnia induced by breath-holding (Akin and Bilensoy, 2006). These findings suggest the possibility of impaired cerebrovascular reactivities in patients with migraine. Using different methods, similar conclusions were drawn by Shinoura and Yamada (2005). Specifically, transient positional intracranial hypertension resulted in less cerebrovascular reactivity in patients with migraine. Functional NIRS can be a potential biomarker to assess treatment responses to medication in patients with migraine. A more recent study has shown differences in hemodynamic changes between patients who received valproic acid, magnesium sulfate and dihydroergotamine suggesting their distinctive mechanisms for migraine treatment (Pourshoghi et al., 2015). In the next subsection, the potential of fNIRS as a diagnostic biomarker is further illustrated in mild cognitive impairment.

Mild Cognitive Impairment

Mild cognitive impairment is characterized by cognitive decline that falls between that associated with normal aging and the more serious decline of dementia. It affects at least one of the cognitive domains, such as memory or complex thinking, but not activities of daily life. MCI is an etiologically heterogenous entity and about 15–20% of patients with MCI go on to develop clinical Alzheimer disease (AD) (Jessen et al., 2010). Neuropsychological testing has been the main biomarker used to distinguish patients with MCI, who eventually develop AD, from those with MCI who do not (Mueller et al., 2018; Meilan et al., 2020). Like other non-invasive neuroimaging modalities, fNIRS has been explored as a potential biomarker to differentiate MCI and AD (Hong and Yaqub, 2019). Recent fNIRS studies of MCI have shown a smaller increase in oxyhemoglobin (i.e., hypoactivation) in bilateral prefrontal lobes during working memory (Yeung et al., 2016; Vermeij et al., 2017) and in dorsolateral prefrontal cortices during memory retrieval (Uemura et al., 2016). However, the accuracy, on average 60–70%, has been too low to reliably identify MCI patients (Yang et al., 2019). Moreover, fNIRS has shown inconsistent results suggesting that patients with MCI have an increased oxyhemoglobin response in regions of interest compared with the healthy control group (Yoo and Hong, 2019). Therefore, the hemodynamic response detected by fNIRS is unlikely to be sensitive and specific enough for clinical practice.

More recently, the focus on non-invasive neuroimaging biomarkers for MCI and AD have shifted to functional connectivity. A recent systemic review including 36 articles over the past two decades suggests that patients with MCI and AD have impaired frontal and long-range connectivity in the resting state fMRI (Yeung and Chan, 2020), which was also observed in a recent study (Yoo and Hong, 2019). Task-related functional connectivity analysis suggests that the number and strength of prefrontal functional connections increased during a working memory task (Yu et al., 2020) but left and inter-hemispheric connectivity during a verbal fluency test were lower (Nguyen et al., 2019) in the patients with MCI compared to healthy controls. This could indicate the use of compensatory mechanisms in the prefrontal cortex as a result of impaired default connectivity in MCI patients. More research is needed to validate fNIRS against fMRI for use as a tool to characterize functional connectivity in patients with MCI.

fMRI VALIDATION OF fNIRS

When it comes to widespread clinical use, such as for MCI, reproducibility (accuracy and precision) is a minimal requirement. It has been challenging to obtain consistent inter- and intra-subject results with continuous-wave fNIRS due to its relatively low SNR and the variability in scattering coefficients among subjects over time. Time- and frequency-domain fNIRS can be used to estimate the scattering coefficients in exchange of cost effectiveness and temporal resolution, making continuous-wave fNIRS more practical for use in a clinical setting.

Several studies have worked to validate fNIRS measures of oxy-, deoxy-, and total hemoglobin with fMRI, either simultaneously (Huppert et al., 2006; Steinbrink et al., 2006; Cui et al., 2011; Heinzel et al., 2013; Moriguchi et al., 2017; Wijeakumar et al., 2017) or separately (Okamoto et al., 2004; Maggioni et al., 2015). Using a cluster of voxels or a region of interest analysis, most fMRI studies have reported positive correlations ($r > 0.4$) between the BOLD response and fNIRS measures of deoxyhemoglobin (Huppert et al., 2006; Maggioni et al., 2015; Wijeakumar et al., 2017), while others have found stronger correlations between the BOLD response and fNIRS measures of oxyhemoglobin (Cui et al., 2011). The increased correlation between deoxyhemoglobin and the fMRI-BOLD response has been associated with the indirect measurement of task-dependent changes in deoxyhemoglobin due to metabolic

demand (Huppert et al., 2006). Interestingly, Moriguchi et al. (2017) reported a stronger correlation in total hemoglobin (r = 0.33) compared to oxy- (r = 0.26) or deoxyhemoglobin (r = −0.2) using a bivariate correlation between fNIRS hemodynamic states and BOLD response during an n-back working memory task (Moriguchi et al., 2017). The reduced correlations across hemodynamic states could be related to task difficulty. Simple visual or motor based tasks have both shown increased correlations (r > 0.5) for oxy- and deoxyhemoglobin (Cui et al., 2011; Maggioni et al., 2015; Huppert, 2016; Wijeakumar et al., 2017). For example, during a finger tapping task with 14 fNIRS channels placed over the contralateral motor area, Huppert et al. (2006) reported a Pearson's correlation of 0.71, 0.98, and 0.53 for zero-lag cross correlations between group averaged (n = 11) changes in the BOLD response to oxy-, deoxy-, and total hemoglobin respectfully.

While most validation studies have focused on group analysis, some have reported within subject results. In a finger tapping experiment, Huppert et al. (2006) showed similar correlations between hemoglobin concentrations and the BOLD response on an individual subject level. During a visual task, Maggioni et al. (2015) report correlations between oxy-, deoxy-, and total hemoglobin concentrations and the BOLD response measured within a 1 cm spherical radius projected below the fNIRS channel for 8 subjects (Maggioni et al., 2015). For deoxyhemoglobin, task-based correlations ranged from 0.26 to 0.83 across subjects. The high inter-subject variability could help explain why more complicated tasks, such as working memory, show decreased correlations in group analyses (Cooper et al., 1997; Huppert et al., 2006; Cui et al., 2011; Maggioni et al., 2015).

Techniques that account for subject-specific differences in anatomy and sensor positioning can improve the correspondence between fNIRS and fMRI measures of task related activity within subject. The impact of subject variability can be reduced by projecting fNIRS channel data onto subject specific anatomy. This has recently been done by Wijeakumar et al. (2017) who showed that the mapping of fNIRS channel data onto subject specific anatomy and projection from the fNIRS channel space to the fMRI voxel space improved the correlation between fNIRS and fMRI measures of task activity. Using a voxel cluster correlation, they reported correlations ranging from 0.62 to 0.99 for both oxy- and deoxyhemoglobin.

LIMITATIONS OF fNIRS AND FUTURE DIRECTIONS

In summary, fNIRS is an appealing technology in the field of neuroscience due to its portability, tolerability, non-invasiveness, cost effectiveness, and ability for long-term real-time monitoring. However, fNIRS has, so far, had limited clinical use due to the lack of anatomic specificity, suboptimal temporal resolution, and low intra-subject reproducibility for individual analysis. The spatial resolution of fNIRS is also less than that of fMRI. Whereas fMRI provides homogeneous resolutions of 1–3 mm, the spatial resolution of fNIRS is limited by the number of detector optodes and the physics of light scatter from the emitter to the detector. Current systems uses detectors spaced ∼3 cm apart from an illuminating optode that inform on brain activity along a curved path from the emitter to the detector, increasing the spatial uncertainty of the signal source both laterally (between the emitter/detector pair) and in depth.

Increasing optode density, such as multichannel fNIRS, can greatly improve the anatomic specificity. Multichannel has been widely used increasingly in research (Hong and Yaqub, 2019). However, multichannel fNIRS optode caps can become uncomfortable to wear over time, due to the weight of the cables and the pressure of the optodes on the subject's scalp. Reducing cable weight by using an armature can help reduce discomfort for prolonged recordings. In addition to the tolerability concern, multichannel fNIRS could impact concurrent EEG monitoring. Hybrid EEG-fNIRS caps are designed to tackle this problem (Hong and Khan, 2017). However, in many clinic settings including pediatric populations and for patients with cranial

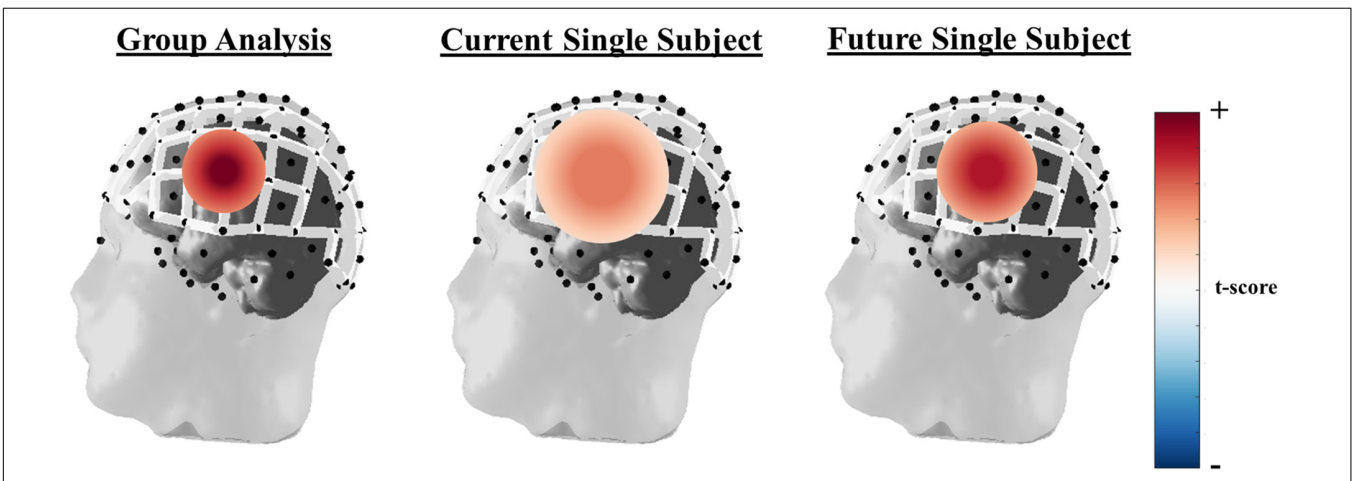

FIGURE 4 | Idealized GLM output for a right-hand finger tapping task at the group **(left)**, current single subject fNIRS analysis capabilities **(middle)**, and where single subject fNIRS analysis needs to be in order to be clinically relevant **(right)**. The example of oxyhemoglobin is used in this depiction.

defects or abnormalities, the hybrid cap with fixed electrode placement can dramatically decrease the accuracy of EEG.

An additional limitation of fNIRS is the lack of access to cortical regions not adjacent to the scalp. The ventral surface of the frontal cortex, the basal ganglia and much of the cerebellum cannot be readily measured with fNIRS due to the increased light absorption with distance from the scalp. Variations in the thickness of the skull and adjacent tissues can affect the inter-subject sensitivity of fNIRS, especially in adults. Time-domain and frequency-domain fNIRS can increase depth sensitivity (Lange et al., 2019) and have proved to be reliable for detecting oxygenation in deep tissue at the cost of sampling rate, instrument cost effectiveness and computational tolerability. At present, optimum processing of fNIRS signals requires advanced knowledge of computer science, signaling processing, and engineering, which can reduce the perceived accessibility of the fNIRS for use in the clinical environment.

Another way to increase the anatomic specificity is through co-registration of fNIRS sensor locations to individual subject's anatomy (via MRI). If anatomical MR scans are available, the use of subject specific parameters, such as partial path length, skull thickness, and skull curvature could be measured and used to account for individual differences in the forward model of fNIRS signal propagation. For patients with neurologic dysfunction, full head imaging could prove especially important for spatial localization and identification of eloquent cortex before surgical intervention.

Compared with EEG, the lower temporal resolution of fNIRS restricts its clinical application. The physiological window for hemodynamic change occurs over seconds while the electrical changes occur over tens to hundreds of milliseconds. Minimally sampling rates of 100 Hz are required for EEG, and most clinical laboratories sample at more than 512 Hz. Commonly used sampling rates for fNIRS are in the tens of Hertz and are even lower for whole-head multi-channel systems. Newer machines using higher sampling rates of ∼100 Hz would provide comparable temporal resolution to clinical EEG. Functional NIRS with higher sampling rates could be particularly useful for CCO detection since it directly responds to increases in cellular metabolism secondary to neuronal activity.

The intrasubject reproducibility is determined by a variety of environmental factors including the presence of ambient light, skull thickness, hair density and color (dense dark hair can block light transmission and reduce signal strength), and head motion. For some factors, experimental preparation to reduce ambient light and separate hair follicles during sensor placement can mitigate their impact prior to data collection, while others, such as head motion, can often be corrected during post-processing by leveraging techniques developed for fMRI and EEG analyses.

Recent advances in neural network learning has increased the accuracy of fNIRS (Yang et al., 2019) and could improve its utility for online monitoring of patients. Processing techniques, such as adaptive filtering, can be used online to provide real-time feedback on neurological conditions (Izzetoglu et al., 2010; Nguyen et al., 2018) but will require computational refinement for online processing during full head imaging.

Finally, fNIRS studies report results at the group level to increase statistical power. While this approach enables the use of fNIRS for neuroimaging research into brain function, its limits the clinical utility for individual diagnosis. In order for fNIRS to be used in clinical assessment of brain function, such as identifying language lateralization in epileptic patients before surgical resection, consistent and robust results need to be obtained at the individual level. An idealized general linear model (GLM) example of the differences in group versus individual subject level analysis can be seen in **Figure 4**. Here the depiction shows strong statistical increase in t-scores over a specific set of channels known to be active during a right hand finger tapping task at the group level, while the current capabilities of individual subject analysis shows a more broad region with a smaller increase in t-scores. In order to be more clinically relevant, advanced processing and hardware configurations, such as those mentioned in this review, are critical. Further developments of the field are needed to identify a more spatially localized and significant result then what is currently being done. The use of high-density whole head optode arrays, precise sensor locations relative to the head, co-registration with anatomic scans, short-distance channels, and improvements in signal processing can be combined to improve within subject analyses.

AUTHOR CONTRIBUTIONS

All authors contributed extensively to the work presented in this manuscript. W-LC and JW wrote the first draft of the manuscript. JW, NH, JS, and SB wrote additional sections of the manuscript. All authors reviewed and edited the manuscript.

FUNDING

This work was supported by the Bleser Endowed Chair in Neurology (to HW), the Baumann Research Endowment (to HW) and Office of Naval Research Grant No: N00014-19-1-2560 (to HW).

REFERENCES

Abdelnour, A. F., and Huppert, T. (2009). Real-time imaging of human brain function by near-infrared spectroscopy using an adaptive general linear model. *Neuroimage* 46, 133–143. doi: 10.1016/j.neuroimage.2009.01.033

Adelson, P. D., Nemoto, E., Scheuer, M., Painter, M., Morgan, J., and Yonas, H. (1999). Noninvasive continuous monitoring of cerebral oxygenation periictally using near-infrared spectroscopy: a preliminary report. *Epilepsia* 40, 1484–1489.

Akin, A., and Bilensoy, D. (2006). Cerebrovascular reactivity to hypercapnia in migraine patients measured with near-infrared spectroscopy. *Brain Res.* 1107, 206–214. doi: 10.1016/j.brainres.2006.06.002

Andersen, A. V., Simonsen, S. A., Schytz, H. W., and Iversen, H. K. (2018). Assessing low-frequency oscillations in cerebrovascular diseases and related conditions with near-infrared spectroscopy: a plausible method for evaluating cerebral autoregulation? *Neurophotonics* 5:030901. doi: 10.1117/1.NPh.5.3.030901

Arifler, D., Zhu, T., Madaan, S., and Tachtsidis, I. (2015). Optimal wavelength combinations for near-infrared spectroscopic monitoring of changes in brain tissue hemoglobin and cytochrome c oxidase concentrations. *Biomed. Opt. Express* 6, 933–947. doi: 10.1364/BOE.6.000933

Ayers, M. D., and Lawrence, D. K. (2015). Near-infrared spectroscopy to assess cerebral perfusion during head-up tilt-table test in patients with syncope. *Congenit. Heart Dis.* 10, 333–339. doi: 10.1111/chd.12236

Balakrishnan, B., Dasgupta, M., Gajewski, K., Hoffmann, R. G., Simpson, P. M., Havens, P. L., et al. (2018). Low near infrared spectroscopic somatic oxygen saturation at admission is associated with need for lifesaving interventions among unplanned admissions to the pediatric intensive care unit. *J. Clin. Monit. Comput.* 32, 89–96. doi: 10.1007/s10877-017-0007-1

Bale, G., Elwell, C. E., and Tachtsidis, I. (2016). From Jobsis to the present day: a review of clinical near-infrared spectroscopy measurements of cerebral cytochrome-c-oxidase. *J. Biomed. Opt.* 21:091307. doi: 10.1117/1.JBO.21.9.091307

Bale, G., Rajaram, A., Kewin, M., Morrison, L., Bainbridge, A., Diop, M., et al. (2018). Broadband NIRS cerebral cytochrome-C-oxidase response to anoxia before and after hypoxic-ischaemic injury in piglets. *Adv. Exp. Med. Biol.* 1072, 151–156. doi: 10.1007/978-3-319-91287-5_24

Barker, J. W., Arabi, A., and Huppert, T. J. (2013). Autoregressive model based algorithm for correcting motion and serially correlated errors in fNIRS. *Biomed. Opt. Express* 4, 1366–1379.

Binder, J. R. (2011). Functional MRI is a valid noninvasive alternative to Wada testing. *Epilepsy Behav.* 20, 214–222. doi: 10.1016/j.yebeh.2010.08.004

Bindra, J., Pham, P., Aneman, A., Chuan, A., and Jaeger, M. (2016). Non-invasive monitoring of dynamic cerebrovascular autoregulation using near infrared spectroscopy and the finometer photoplethysmograph. *Neurocrit. Care* 24, 442–447. doi: 10.1007/s12028-015-0200-3

Blanco, B., Molnar, M., and Caballero-Gaudes, C. (2018). Effect of prewhitening in resting-state functional near-infrared spectroscopy data. *Neurophotonics* 5:040401. doi: 10.1117/1.NPh.5.4.040401

Buchheim, K., Obrig, H., v Pannwitz, W., Muller, A., Heekeren, H., Villringer, A., et al. (2004). Decrease in haemoglobin oxygenation during absence seizures in adult humans. *Neurosci. Lett.* 354, 119–122.

Budohoski, K. P., Czosnyka, M., Smielewski, P., Kasprowicz, M., Helmy, A., Bulters, D., et al. (2012). Impairment of cerebral autoregulation predicts delayed cerebral ischemia after subarachnoid hemorrhage: a prospective observational study. *Stroke* 43, 3230–3237. doi: 10.1161/STROKEAHA.112.669788

Coelli, S., Nobili, L., Boly, M., Riedner, B., and Bianchi, A. M. (2019). Optimization of the Cortical Traveling Wave Analysis framework for feasibility in Stereo-Electroencephalography. *Conf. Proc. IEEE Eng. Med. Biol. Soc.* 2019, 3854–3857. doi: 10.1109/EMBC.2019.8857664

Cooper, C. E., Cope, M., Quaresima, V., Ferrari, M., Nemoto, E., Springett, R., et al. (1997). Measurement of cytochrome oxidase redox state by near infrared spectroscopy. *Adv. Exp. Med. Biol.* 413, 63–73. doi: 10.1007/978-1-4899-0056-2_7

Cordes, D., Haughton, V. M., Arfanakis, K., Carew, J. D., Turski, P. A., Moritz, C. H., et al. (2001). Frequencies contributing to functional connectivity in the cerebral cortex in "resting-state" data. *AJNR Am. J. Neuroradiol.* 22, 1326–1333.

Cui, X., Bray, S., Bryant, D. M., Glover, G. H., and Reiss, A. L. (2011). A quantitative comparison of NIRS and fMRI across multiple cognitive tasks. *Neuroimage* 54, 2808–2821. doi: 10.1016/j.neuroimage.2010.10.069

Czosnyka, M., Brady, K., Reinhard, M., Smielewski, P., and Steiner, L. A. (2009). Monitoring of cerebrovascular autoregulation: facts, myths, and missing links. *Neurocrit. Care* 10, 373–386. doi: 10.1007/s12028-008-9175-7

Dias, C., Silva, M. J., Pereira, E., Monteiro, E., Maia, I., Barbosa, S., et al. (2015). Optimal cerebral perfusion pressure management at bedside: a single-center pilot study. *Neurocrit. Care* 23, 92–102. doi: 10.1007/s12028-014-0103-8

Fox, P. T., and Raichle, M. E. (1984). Stimulus rate dependence of regional cerebral blood flow in human striate cortex, demonstrated by positron emission tomography. *J. Neurophysiol.* 51, 1109–1120. doi: 10.1152/jn.1984.51.5.1109

Funane, T., Sato, H., Yahata, N., Takizawa, R., Nishimura, Y., Kinoshita, A., et al. (2015). Concurrent fNIRS-fMRI measurement to validate a method for separating deep and shallow fNIRS signals by using multidistance optodes. *Neurophotonics* 2:015003. doi: 10.1117/1.NPh.2.1.015003

Gagnon, L., Yucel, M. A., Boas, D. A., and Cooper, R. J. (2014). Further improvement in reducing superficial contamination in NIRS using double short separation measurements. *Neuroimage* 85(Pt 1), 127–135. doi: 10.1016/j.neuroimage.2013.01.073

Gallagher, A., Theriault, M., Maclin, E., Low, K., Gratton, G., Fabiani, M., et al. (2007). Near-infrared spectroscopy as an alternative to the Wada test for language mapping in children, adults and special populations. *Epileptic Disord.* 9, 241–255. doi: 10.1684/epd.2007.0118

Giacalone, G., Zanoletti, M., Re, R., Germinario, B., Contini, D., Spinelli, L., et al. (2019). Time-domain near-infrared spectroscopy in acute ischemic stroke patients. *Neurophotonics* 6:015003. doi: 10.1117/1.NPh.6.1.015003

Goadsby, P. J., Holland, P. R., Martins-Oliveira, M., Hoffmann, J., Schankin, C., and Akerman, S. (2017). Pathophysiology of migraine: a disorder of sensory processing. *Physiol. Rev.* 97, 553–622. doi: 10.1152/physrev.00034.2015

Heinzel, S., Haeussinger, F. B., Hahn, T., Ehlis, A. C., Plichta, M. M., and Fallgatter, A. J. (2013). Variability of (functional) hemodynamics as measured with simultaneous fNIRS and fMRI during intertemporal choice. *Neuroimage* 71, 125–134. doi: 10.1016/j.neuroimage.2012.12.074

Hiraoka, M., Firbank, M., Essenpreis, M., Cope, M., Arridge, S. R., van der Zee, P., et al. (1993). A Monte Carlo investigation of optical pathlength in inhomogeneous tissue and its application to near-infrared spectroscopy. *Phys. Med. Biol.* 38, 1859–1876. doi: 10.1088/0031-9155/38/12/011

Hoffman, G. M., Ghanayem, N. S., Scott, J. P., Tweddell, J. S., Mitchell, M. E., and Mussatto, K. A. (2017). Postoperative cerebral and somatic near-infrared spectroscopy saturations and outcome in hypoplastic left heart syndrome. *Ann. Thorac. Surg.* 103, 1527–1535. doi: 10.1016/j.athoracsur.2016.09.100

Holper, L., and Mann, J. J. (2018). Test-retest reliability of brain mitochondrial cytochrome-c-oxidase assessed by functional near-infrared spectroscopy. *J. Biomed. Opt.* 23, 1–9. doi: 10.1117/1.JBO.23.5.056006

Hong, K. S., and Khan, M. J. (2017). Hybrid brain-computer interface techniques for improved classification accuracy and increased number of commands: a review. *Front. Neurorobot.* 11:35. doi: 10.3389/fnbot.2017.00035

Hong, K. S., Khan, M. J., and Hong, M. J. (2018). Feature extraction and classification methods for hybrid fNIRS-EEG brain-computer interfaces. *Front Hum Neurosci* 12:246. doi: 10.3389/fnhum.2018.00246

Hong, K. S., and Naseer, N. (2016). Reduction of delay in detecting initial dips from functional near-infrared spectroscopy signals using vector-based phase analysis. *Int. J. Neural Syst.* 26:1650012. doi: 10.1142/S012906571650012X

Hong, K. S., and Yaqub, M. A. (2019). Application of functional near-infrared spectroscopy in the healthcare industry: a review. *J. Innov. Opt. Health Sci.* 12:1930012.

Hoshi, Y., Kobayashi, N., and Tamura, M. (2001). Interpretation of near-infrared spectroscopy signals: a study with a newly developed perfused rat brain model. *J. Appl. Physiol.* 90, 1657–1662. doi: 10.1152/jappl.2001.90.5.1657

Huppert, T. J. (2016). Commentary on the statistical properties of noise and its implication on general linear models in functional near-infrared spectroscopy. *Neurophotonics* 3:010401. doi: 10.1117/1.NPh.3.1.010401

Huppert, T. J., Hoge, R. D., Diamond, S. G., Franceschini, M. A., and Boas, D. A. (2006). A temporal comparison of BOLD, ASL, and NIRS hemodynamic responses to motor stimuli in adult humans. *Neuroimage* 29, 368–382. doi: 10.1016/j.neuroimage.2005.08.065

Hyvarinen, A., and Oja, E. (2000). Independent component analysis: algorithms and applications. *Neural Netw.* 13, 411–430. doi: 10.1016/s0893-6080(00)00026-5

Izzetoglu, M., Chitrapu, P., Bunce, S., and Onaral, B. (2010). Motion artifact cancellation in NIR spectroscopy using discrete Kalman filtering. *Biomed. Eng. Online* 9:16. doi: 10.1186/1475-925X-9-16

Jahani, S., Setarehdan, S. K., Boas, D. A., and Yucel, M. A. (2018). Motion artifact detection and correction in functional near-infrared spectroscopy: a new hybrid method based on spline interpolation method and Savitzky-Golay filtering. *Neurophotonics* 5:015003. doi: 10.1117/1.NPh.5.1.015003

Janecek, J. K., Swanson, S. J., Sabsevitz, D. S., Hammeke, T. A., Raghavan, M., Mueller, W., et al. (2013a). Naming outcome prediction in patients with discordant Wada and fMRI language lateralization. *Epilepsy Behav.* 27, 399–403. doi: 10.1016/j.yebeh.2013.02.030

Janecek, J. K., Winstanley, F. S., Sabsevitz, D. S., Raghavan, M., Mueller, W., Binder, J. R., et al. (2013b). Naming outcome after left or right temporal lobectomy in patients with bilateral language representation by Wada testing. *Epilepsy Behav.* 28, 95–98. doi: 10.1016/j.yebeh.2013.04.006

Jeppesen, J., Beniczky, S., Johansen, P., Sidenius, P., and Fuglsang-Frederiksen, A. (2015). Exploring the capability of wireless near infrared spectroscopy as a portable seizure detection device for epilepsy patients. *Seizure* 26, 43–48. doi: 10.1016/j.seizure.2015.01.015

Jessen, F., Wiese, B., Bachmann, C., Eifflaender-Gorfer, S., Haller, F., Kolsch, H., et al. (2010). Prediction of dementia by subjective memory impairment: effects of severity and temporal association with cognitive impairment. *Arch. Gen. Psychiatry* 67, 414–422. doi: 10.1001/archgenpsychiatry.2010.30

Jobsis, F. F. (1977). Noninvasive, infrared monitoring of cerebral and myocardial oxygen sufficiency and circulatory parameters. *Science* 198, 1264–1267.

Kadamati, J., Sugar, M. R., Sannagowdara, K., Malloy, M., Chen, W., Quirk, B., et al. (2018). "Cerebral oxygen saturation and cytochrome oxidase redox state in children with epilepsy: a pilot study -MULTICHANNEL NIRS for epilepsy seizure detection," in *Proceedings of the International Congress of Clinical Neurophysiology*, Washington, DC.

Kadamati, P., Sugar, J. J., Quirk, B. J., Mehrvar, S., Chelimsky, G. G., Whelan, H. T., et al. (2018). Near-infrared spectroscopy muscle oximetry of patients with postural orthostatic tachycardia syndrome. *J. Innov. Opt. Health Sci.* 11:1850026. doi: 10.1142/S1793545818500268

Khan, M. J., Ghafoor, U., and Hong, K. S. (2018). Early detection of hemodynamic responses using EEG: a hybrid EEG-fNIRS study. *Front. Hum. Neurosci.* 12:479. doi: 10.3389/fnhum.2018.00479

Khan, M. J., and Hong, K. S. (2017). Hybrid EEG-fNIRS-based eight-command decoding for BCI: application to Quadcopter control. *Front. Neurorobot.* 11:6. doi: 10.3389/fnbot.2017.00006

Kohno, S., Miyai, I., Seiyama, A., Oda, I., Ishikawa, A., Tsuneishi, S., et al. (2007). Removal of the skin blood flow artifact in functional near-infrared spectroscopic imaging datathrough independent component analysis. *J. Biomed. Opt.* 12, 0621111–0621119.

Lange, F., Dunne, L., Hale, L., and Tachtsidis, I. (2019). MAESTROS: a multiwavelength time-domain NIRS system to monitor changes in oxygenation and oxidation state of cytochrome-C-oxidase. *IEEE J. Sel. Top. Quantum Electron.* 25:7100312. doi: 10.1109/JSTQE.2018.2833205

Lankford, J., Numan, M., Hashmi, S. S., Gourishankar, A., and Butler, I. J. (2015). Cerebral blood flow during HUTT in young patients with orthostatic intolerance. *Clin. Auton. Res.* 25, 277–284. doi: 10.1007/s10286-015-0295-9

Lauritzen, M. (1994). Pathophysiology of the migraine aura. The spreading depression theory. *Brain* 117(Pt 1), 199–210. doi: 10.1093/brain/117.1.199

Li, Z., Wang, Y., Li, Y., Wang, Y., Li, J., and Zhang, L. (2010). Wavelet analysis of cerebral oxygenation signal measured by near infrared spectroscopy in subjects with cerebral infarction. *Microvasc. Res.* 80, 142–147. doi: 10.1016/j.mvr.2010.02.004

Liu, Y., Ayaz, H., and Shewokis, P. A. (2017). Multisubject "Learning" for mental workload classification using concurrent EEG, fNIRS, and physiological measures. *Front. Hum. Neurosci.* 11:389. doi: 10.3389/fnhum.2017.00389

Maggioni, E., Molteni, E., Zucca, C., Reni, G., Cerutti, S., Triulzi, F. M., et al. (2015). Investigation of negative BOLD responses in human brain through NIRS technique. A visual stimulation study. *Neuroimage* 108, 410–422. doi: 10.1016/j.neuroimage.2014.12.074

Masataka, N., Perlovsky, L., and Hiraki, K. (2015). Near-infrared spectroscopy (NIRS) in functional research of prefrontal cortex. *Front. Hum. Neurosci.* 9:274. doi: 10.3389/fnhum.2015.00274

Meilan, J. J. G., Martinez-Sanchez, F., Martinez-Nicolas, I., Llorente, T. E., and Carro, J. (2020). Changes in the rhythm of speech difference between people with nondegenerative mild cognitive impairment and with preclinical dementia. *Behav. Neurol.* 2020:4683573. doi: 10.1155/2020/4683573

Molavi, B., and Dumont, G. A. (2012). Wavelet-based motion artifact removal for functional near-infrared spectroscopy. *Physiol. Meas.* 33, 259–270. doi: 10.1088/0967-3334/33/2/259

Monrad, P., Sannagowdara, K., Bozarth, X., Bhosrekar, S., Hecox, K., Nwosu, M., et al. (2015). Haemodynamic response associated with both ictal and interictal epileptiform activity using simultaneous video electroencephalography/near infrared spectroscopy in a within-subject study. *J. Near Infrared Spectrosc.* 23, 209–218. doi: 10.1255/jnirs.1170

Moriguchi, Y., Noda, T., Nakayashiki, K., Takata, Y., Setoyama, S., Kawasaki, S., et al. (2017). Validation of brain-derived signals in near-infrared spectroscopy through multivoxel analysis of concurrent functional magnetic resonance imaging. *Hum. Brain Mapp.* 38, 5274–5291. doi: 10.1002/hbm.23734

Mueller, K. D., Hermann, B., Mecollari, J., and Turkstra, L. S. (2018). Connected speech and language in mild cognitive impairment and Alzheimer's disease: a review of picture description tasks. *J. Clin. Exp. Neuropsychol.* 40, 917–939. doi: 10.1080/13803395.2018.1446513

Nguyen, D. K., Tremblay, J., Pouliot, P., Vannasing, P., Florea, O., Carmant, L., et al. (2012). Non-invasive continuous EEG-fNIRS recording of temporal lobe seizures. *Epilepsy Res.* 99, 112–126. doi: 10.1016/j.eplepsyres.2011.10.035

Nguyen, H. D., Yoo, S. H., Bhutta, M. R., and Hong, K. S. (2018). Adaptive filtering of physiological noises in fNIRS data. *Biomed. Eng. Online* 17:180. doi: 10.1186/s12938-018-0613-2

Nguyen, T., Kim, M., Gwak, J., Lee, J. J., Choi, K. Y., Lee, K. H., et al. (2019). Investigation of brain functional connectivity in patients with mild cognitive impairment: a functional near-infrared spectroscopy (fNIRS) study. *J. Biophotonics* 12:e201800298. doi: 10.1002/jbio.201800298

Obrig, H. (2014). NIRS in clinical neurology - a 'promising' tool? *Neuroimage* 85(Pt 1), 535–546. doi: 10.1016/j.neuroimage.2013.03.045

Okamoto, M., Dan, H., Sakamoto, K., Takeo, K., Shimizu, K., Kohno, S., et al. (2004). Three-dimensional probabilistic anatomical cranio-cerebral correlation via the international 10-20 system oriented for transcranial functional brain mapping. *Neuroimage* 21, 99–111. doi: 10.1016/j.neuroimage.2003.08.026

Osharina, V., Ponchel, E., Aarabi, A., Grebe, R., and Wallois, F. (2010). Local haemodynamic changes preceding interictal spikes: a simultaneous electrocorticography (ECoG) and near-infrared spectroscopy (NIRS) analysis in rats. *Neuroimage* 50, 600–607. doi: 10.1016/j.neuroimage.2010.01.009

Phillip, D., Schytz, H. W., Iversen, H. K., Selb, J., Boas, D. A., and Ashina, M. (2014). Spontaneous low frequency oscillations in acute ischemic stroke – a near infrared spectroscopy (NIRS) study. *J. Neurol. Neurophysiol.* 5:241. doi: 10.4172/2155-9562.1000241

Pourshoghi, A., Danesh, A., Tabby, D. S., Grothusen, J., and Pourrezaei, K. (2015). Cerebral reactivity in migraine patients measured with functional near-infrared spectroscopy. *Eur. J. Med. Res.* 20:96. doi: 10.1186/s40001-015-0190-9

Rizki, E. E., Uga, M., Dan, I., Dan, H., Tsuzuki, D., Yokota, H., et al. (2015). Determination of epileptic focus side in mesial temporal lobe epilepsy using long-term noninvasive fNIRS/EEG monitoring for presurgical evaluation. *Neurophotonics* 2:025003. doi: 10.1117/1.NPh.2.2.025003

Robertson, F. C., Douglas, T. S., and Meintjes, E. M. (2010). Motion artifact removal for functional near infrared spectroscopy: a comparison of methods. *IEEE Trans. Biomed. Eng.* 57, 1377–1387. doi: 10.1109/TBME.2009.2038667

Rolinski, R., Austermuehle, A., Wiggs, E., Agrawal, S., Sepeta, L. N., Gaillard, W. D., et al. (2019). Functional MRI and direct cortical stimulation: prediction of postoperative language decline. *Epilepsia* 60, 560–570. doi: 10.1111/epi.14666

Sato, Y., Fukuda, M., Oishi, M., Shirasawa, A., and Fujii, Y. (2013). Ictal near-infrared spectroscopy and electrocorticography study of supplementary motor area seizures. *J. Biomed. Opt.* 18:76022. doi: 10.1117/1.JBO.18.7.076022

Scholkmann, F., Spichtig, S., Muehlemann, T., and Wolf, M. (2010). How to detect and reduce movement artifacts in near-infrared imaging using moving standard deviation and spline interpolation. *Physiol. Meas.* 31, 649–662. doi: 10.1088/0967-3334/31/5/004

Shinoura, N., and Yamada, R. (2005). Decreased vasoreactivity to right cerebral hemisphere pressure in migraine without aura: a near-infrared spectroscopy study. *Clin. Neurophysiol.* 116, 1280–1285. doi: 10.1016/j.clinph.2005.01.016

Sokol, D. K., Markand, O. N., Daly, E. C., Luerssen, T. G., and Malkoff, M. D. (2000). Near infrared spectroscopy (NIRS) distinguishes seizure types. *Seizure* 9, 323–327. doi: 10.1053/seiz.2000.0406

Springett, R., Newman, J., Cope, M., and Delpy, D. T. (2000). Oxygen dependency and precision of cytochrome oxidase signal from full spectral NIRS of the piglet brain. *Am. J. Physiol. Heart Circ. Physiol.* 279, H2202–H2209. doi: 10.1152/ajpheart.2000.279.5.H2202

Steinbrink, J., Villringer, A., Kempf, F., Haux, D., Boden, S., and Obrig, H. (2006). Illuminating the BOLD signal: combined fMRI-fNIRS studies. *Magn. Reson. Imaging* 24, 495–505. doi: 10.1016/j.mri.2005.12.034

Su, H., Huo, C., Wang, B., Li, W., Xu, G., Liu, Q., et al. (2018). Alterations in the coupling functions between cerebral oxyhaemoglobin and arterial blood pressure signals in post-stroke subjects. *PLoS One* 13:e0195936. doi: 10.1371/journal.pone.0195936

Tanaka, H., Matsushima, R., Tamai, H., and Kajimoto, Y. (2002). Impaired postural cerebral hemodynamics in young patients with chronic fatigue with and

without orthostatic intolerance. *J. Pediatr.* 140, 412–417. doi: 10.1067/mpd.2002.122725

Uemura, K., Shimada, H., Doi, T., Makizako, H., Tsutsumimoto, K., Park, H., et al. (2016). Reduced prefrontal oxygenation in mild cognitive impairment during memory retrieval. *Int. J. Geriatr. Psychiatry* 31, 583–591. doi: 10.1002/gps.4363

Verdecchia, K., Diop, M., Lee, T. Y., and St Lawrence, K. (2013). Quantifying the cerebral metabolic rate of oxygen by combining diffuse correlation spectroscopy and time-resolved near-infrared spectroscopy. *J. Biomed. Opt.* 18:27007. doi: 10.1117/1.JBO.18.2.027007

Vermeij, A., Kessels, R. P. C., Heskamp, L., Simons, E. M. F., Dautzenberg, P. L. J., and Claassen, J. (2017). Prefrontal activation may predict working-memory training gain in normal aging and mild cognitive impairment. *Brain Imaging Behav.* 11, 141–154. doi: 10.1007/s11682-016-9508-7

Vernieri, F., Rosato, N., Pauri, F., Tibuzzi, F., Passarelli, F., and Rossini, P. M. (1999). Near infrared spectroscopy and transcranial Doppler in monohemispheric stroke. *Eur. Neurol.* 41, 159–162. doi: 10.1159/000008041

Vespa, S., Baroumand, A. G., Ferrao Santos, S., Vrielynck, P., de Tourtchaninoff, M., Feys, O., et al. (2020). Ictal EEG source imaging and connectivity to localize the seizure onset zone in extratemporal lobe epilepsy. *Seizure* 78, 18–30. doi: 10.1016/j.seizure.2020.03.001

Villringer, A., Planck, J., Stodieck, S., Botzel, K., Schleinkofer, L., and Dirnagl, U. (1994). Noninvasive assessment of cerebral hemodynamics and tissue oxygenation during activation of brain cell function in human adults using near infrared spectroscopy. *Adv. Exp. Med. Biol.* 345, 559–565.

Viola, S., Viola, P., Litterio, P., Buongarzone, M. P., and Fiorelli, L. (2010). Pathophysiology of migraine attack with prolonged aura revealed by transcranial Doppler and near infrared spectroscopy. *Neurol. Sci.* 31(Suppl. 1), S165–S166. doi: 10.1007/s10072-010-0318-1

Watanabe, E., Maki, A., Kawaguchi, F., Takashiro, K., Yamashita, Y., Koizumi, H., et al. (1998). Non-invasive assessment of language dominance with near-infrared spectroscopic mapping. *Neurosci. Lett.* 256, 49–52.

Wijeakumar, S., Huppert, T. J., Magnotta, V. A., Buss, A. T., and Spencer, J. P. (2017). Validating an image-based fNIRS approach with fMRI and a working memory task. *Neuroimage* 147, 204–218. doi: 10.1016/j.neuroimage.2016.12.007

Wroblewski, G. J., Matsuo, K., Hirata, K., Matsubara, T., Harada, K., Watanabe, Y., et al. (2017). Effects of task language and second-language proficiency on the neural correlates of phonemic fluency in native Japanese speakers: a functional near-infrared spectroscopy study. *Neuroreport* 28, 884–889. doi: 10.1097/WNR.0000000000000852

Yang, D., Hong, K. S., Yoo, S. H., and Kim, C. S. (2019). Evaluation of neural degeneration biomarkers in the prefrontal cortex for early identification of patients with mild cognitive impairment: an fNIRS study. *Front. Hum. Neurosci.* 13:317. doi: 10.3389/fnhum.2019.00317

Yeung, M. K., and Chan, A. S. (2020). Functional near-infrared spectroscopy reveals decreased resting oxygenation levels and task-related oxygenation changes in mild cognitive impairment and dementia: a systematic review. *J. Psychiatr. Res.* 124, 58–76. doi: 10.1016/j.jpsychires.2020.02.017

Yeung, M. K., Sze, S. L., Woo, J., Kwok, T., Shum, D. H., Yu, R., et al. (2016). Reduced frontal activations at high working memory load in mild cognitive impairment: near-infrared spectroscopy. *Dement. Geriatr. Cogn. Disord.* 42, 278–296. doi: 10.1159/000450993

Yoo, S. H., and Hong, K. S. (2019). Hemodynamics analysis of patients with mild cognitive impairment during working memory tasks. *Conf. Proc. IEEE Eng. Med. Biol. Soc.* 2019, 4470–4473. doi: 10.1109/EMBC.2019.8856956

Yu, J. W., Lim, S. H., Kim, B., Kim, E., Kim, K., Kyu Park, S., et al. (2020). Prefrontal functional connectivity analysis of cognitive decline for early diagnosis of mild cognitive impairment: a functional near-infrared spectroscopy study. *Biomed. Opt. Express* 11, 1725–1741. doi: 10.1364/BOE.382197

Yucel, M. A., Selb, J., Boas, D. A., Cash, S. S., and Cooper, R. J. (2014). Reducing motion artifacts for long-term clinical NIRS monitoring using collodion-fixed prism-based optical fibers. *Neuroimage* 85(Pt 1), 192–201. doi: 10.1016/j.neuroimage.2013.06.054

Zafar, A., and Hong, K. S. (2017). Detection and classification of three-class initial dips from prefrontal cortex. *Biomed. Opt. Express* 8, 367–383. doi: 10.1364/BOE.8.000367

Zafar, A., and Hong, K. S. (2018). Neuronal activation detection using vector phase analysis with dual threshold circles: a functional near-infrared spectroscopy study. *Int. J. Neural Syst.* 28:1850031. doi: 10.1142/S0129065718500314

Zeiler, F. A., Donnelly, J., Calviello, L., Smielewski, P., Menon, D. K., and Czosnyka, M. (2017). Pressure autoregulation measurement techniques in adult traumatic brain injury, Part II: a scoping review of continuous methods. *J. Neurotrauma* 34, 3224–3237. doi: 10.1089/neu.2017.5086

Zhang, T., Zhou, J., Jiang, R., Yang, H., Carney, P. R., and Jiang, H. (2014). Pre-seizure state identified by diffuse optical tomography. *Sci. Rep.* 4:3798. doi: 10.1038/srep03798

Zhang, X., Noah, J. A., and Hirsch, J. (2016). Separation of the global and local components in functional near-infrared spectroscopy signals using principal component spatial filtering. *Neurophotonics* 3:015004. doi: 10.1117/1.NPh.3.1.015004

Conflict of Interest: The authors declare that the research was conducted in the absence of any commercial or financial relationships that could be construed as a potential conflict of interest.

Advantages of publishing in Frontiers

OPEN ACCESS
Articles are free to read for greatest visibility and readership

FAST PUBLICATION
Around 90 days from submission to decision

HIGH QUALITY PEER-REVIEW
Rigorous, collaborative, and constructive peer-review

TRANSPARENT PEER-REVIEW
Editors and reviewers acknowledged by name on published articles

Frontiers
Avenue du Tribunal-Fédéral 34
1005 Lausanne | Switzerland

Visit us: www.frontiersin.org
Contact us: frontiersin.org/about/contact

REPRODUCIBILITY OF RESEARCH
Support open data and methods to enhance research reproducibility

DIGITAL PUBLISHING
Articles designed for optimal readership across devices

FOLLOW US
@frontiersin

IMPACT METRICS
Advanced article metrics track visibility across digital media

EXTENSIVE PROMOTION
Marketing and promotion of impactful research

LOOP RESEARCH NETWORK
Our network increases your article's readership